The University of Nottingham
School of Physics & Astronomy



INVESTIGATION OF THE OPTICAL AND ELECTRICAL PROPERTIES OF DILUTE NITRIDE COMPOUND SEMICONDUCTORS BASED ON GaP

by

HIND MOHAMMED ALBALAWI

M. Sc (Renewable Energy and Architecture)

Thesis submitted to The University of Nottingham
for the degree of Doctor of Philosophy
March 2019

ABSTRACT

The effect of nitrogen (N) incorporation on the optical properties of Gallium phosphide $GaP_{1-x}N_x$ (x= 1.4%, 2.1%, and 2.7%) alloys grown by MBE, have been investigated in this thesis. In addition, the influence of adding arsnic (As) and indium (In) on the optical properties of $GaAs_{0.1}P_{0.89}N_{0.01}$ and $In_{0.07}Ga_{0.93}P_{0.99}N_{0.01}$ alloys have been studied. The PL measurements demonstrated the change of the bandgap nature from indirect to pseudo-direct in all the above devices. PL intensity decreased with increasing N concentrations as well as the bandgap energy. $GaAs_{0.1}P_{0.89}N_{0.01}$ alloy has shown better PL intensity, FWHM and reached the target bandgap of solar cells materials based on Si substrate which is 1.8 eV compared to $In_{0.07}Ga_{0.93}P_{0.99}N_{0.01}$ alloy. Furthermore, the effect of different epilayer thickness (100 nm and 1 μm) on the optical properties of $GaAs_{0.1}P_{0.89}N_{0.01}$ alloys have been studied. Increasing the thickness allowed to enhance the optical efficiency by increasing the PL intensity, reducing the FWHM and raising the activation energy. However, the bandgap shifted towards higher energy (higher than 1.8 eV)

Also in this thesis, the effect of RTA on the optical and structural properties of $GaP_{0.986}N_{0.014}$, $GaAs_{0.1}P_{0.89}N_{0.01}$ and $In_{0.07}Ga_{0.93}P_{0.99}N_{0.01}$ devices have been examined. From an optical point of view, all samples had a blue shift in their bandgap energy after annealing. It increased also the PL intensities as well as the activation energies for all alloys. The S-shape behaviour was not affected much by annealing these materials. However, the FWHM showed smaller values after annealing the samples, indicating that RTA reduced the defects. From a structural perspective, RTA decreased the surface roughness of $GaP_{0.986}N_{0.014}$, however, no change in N-induced in vertical lattice spacing was observed. A small reduction of vertical lattice parameter and an increase of the surface roughness were caused by annealing for both $GaAs_{0.1}P_{0.89}N_{0.01}$ and $In_{0.07}Ga_{0.93}P_{0.99}N_{0.01}$ alloys.

Moreover, I-V, C-V, DLTS, and Laplace DLTS measurement techniques were used to investigate the effect of RTA on the electrical properties of p-i-n GaAsPN solar structure materials grown by MBE. This study showed a noticeable effect of annealing on the samples and was correlated to the creation of new defects. RTA improved the electrical properties of this material by reducing the concentration and /or capture cross-section values of major defects. Overall, rapid thermal annealing is an effective treatment process to improve the optical, structural and electrical properties of different semiconductor structures and devices.

PUBLICATIONS

1. *High-performance organic/inorganic hybrid heterojunction based on Gallium Arsenide (GaAs) substrates and a conjugated polymer.*
   D. A. Jameel, J.F. Felix, M. Aziza, N. Al Saqri, D. Taylor, W.M. de Azevedo, E.F. da Silva Jr., **H. Albalawi**, H. Alghamdi, F. Al Mashary, M. Henini.

   Journal: Applied Surface Science 357, 2189–2197 (2015) (Impact Factor 3.150).

2. *Electrical performance of conducting polymer (SPAN) grown on GaAs with different substrate orientations.*
   D. A. Jameel, M. Aziza, J.F. Felix, N. Al Saqri, D. Taylor, W.M. de Azevedo, E.F. da Silva Jr., **H. Albalawi**, H. Alghamdi, F. Al Mashary, M. Henini.

   Journal: Applied Surface Science 387, 228-236 (2016) (Impact Factor 3.150).

3. *Investigation of the Effects of Gamma Radiation on the Electrical Properties of Dilute $GaAs_{1-x}N_x$ Layers Grown by Molecular Beam Epitaxy.*
   N Al Saqri, JF Felix, M Aziz, D Jameel, CIL de Araujo, **H Albalawi**, F Al Mashary, H Alghamdi, D Taylor, M Henini.

   Journal: Current Applied Physics 15, 1230 (2015) (Impact Factor 2.212).

4. *Investigation of the Effects of Gamma Radiation on the Electrical Properties of Dilute $GaAs_{1-x}N_x$ Layers Grown by Molecular Beam Epitaxy.*
   N Al Saqri, JF Felix, M Aziz, D Jameel, CIL de Araujo, **H Albalawi**, F Al Mashary, H Alghamdi, D Taylor, M Henini.

   Journal: Current Applied Physics 15, 1230 (2015) (Impact Factor 2.212).

5. *Rapid thermal annealing: An efficient method to improve the electrical properties of tellurium compensated Interfacial Misfit GaSb/GaAs heterostructures.*
   Mohsin Aziz, Jorlandio F Felix, Dler Jameel, Noor Al Saqri, Faisal S Al Mashary, Haifaa M Alghamdi, **Hind MA Albalawi**, David Taylor, Mohamed Henini.

   Journal: Superlattices and Microstructures 88, 80 (2015) (Impact Factor 2.097).

6. *Electrical Behavior of MBE Grown Interfacial Misfit GaSb/GaAs Heterostructures With and Without Te-Doped Interfaces.*

Mohsin Aziz, Jorlandio Francisco Felix, Noor Al Saqri, Dler Jameel, Faisal Saleh Al Mashary, **Hind Mohammed Albalawi**, Haifaa Mohammed Abdullah Alghamdi, David Taylor, Mohamed Henini.

Journal: IEEE Transactions on Electron Devices, 62, 3980 (2015) (Impact Factor 2.472).

7. *Effect of rapid thermal annealing on the electrical properties of dilute GaAsPN based diodes.*
   H.A. Alburaih , **H. Albalawi**, M. Henini, Submitted to Journal of Alloys and Compounds (2019) (impact factor 3.779).

8. *Effects of Nitrogen incorporation and thermal annealing on the optical and spin properties of GaPN dilute nitride alloys.*
   M. A. G. Balanta, P. B. A. de Oliveira, **H Albalawi**, Y.Galvão Gobato, H. V. A. Galeti, F.Iikawa, A.D.Rodriges, M.Henini, S. Almosni, C. Robert, A. Balocchi, Y. Léger, H. Carrère, M. Bahri, G. Patriarche, X. Marie, C. Cornet.

   Submitted to Journal of Alloys and Compounds (2019) (impact factor 3.779).

9. *Effects of thermal annealing on the optical properties of GaAsPN dilute nitride alloy.*
   H.A. Alburaih , **H. Albalawi**, M. Henini.

   Submitted to Journal of Semiconductor Science and Technology (2019) (impact factor 2.280).

10. *Effects of epitaxial layer thickness variation on the optical properties of dilute nitride GaAsPN.*
    H. Albalawi, Vanessa Orsi Gordo, Samy Almosni, Noor Al Saqri, Dler Jameel, Olivier Durand, David Taylor, Mohamed Henini.

    Submitted to Journal of Alloys and Compounds (2019) (impact factor 3.779).

CONFERENCE PRESENTATIONS

ORAL PRESENTATIONS

- "Investigation of the Effect of Thermal Annealing on the Optical Properties of Dilute Nitride GaPN Alloys"
  International Semiconductor Science and Technology Conference (ISSTC-2015), Kuşadası/Aydın, Turkey, 11-13 May, (2015).

- "Investigation of the Effect of Adding As on the Optical Properties of Dilute Nitride GaAsPN Alloys"
  Nanostructure Materials for Photovoltaic Applications Workshop (NMPA-2015), SVU, Qena, Egypt, 21-26 November, (2015).

- "Investigation of Optical Properties of Dilute Nitride GaAsPN and InGaPN Alloys after rapid thermal annealing"
  Nano-semiconductors for Optoelectronics and Solar Cell Devices Workshop, Nottingham, UK, September, (2016).

- "Investigation of the Effect of Thermal Annealing on the Optical Properties of Dilute Nitride GaAsPN Alloys"
  4th International NANO TODAY CONFERENCE, Dubai, UAE, 6-10 December, (2016).

- "Investigation of the Effect of Adding Nitrogen on the Optical Properties of Dilute Nitride $GaP_{1-x}N_x$ Alloys"
  20th International Conference on Advanced Nanotechnology, Amsterdam, Netherlands, 11-12 September, (2017).

- "Investigation of the Effect of Adding indium on the Optical Properties of Dilute Nitride InGaPN Alloys and Thermal Annealing Effect"
  5th Nano Today Conference Nano Today, Hawaii, USA, 6-10 December, (2017).

- "Study the Effect of Different V-III BEP ratio on the Optical Properties of GaPN alloys"
  23rd International Conference on Nanomaterials and Nanotechnology, London, UK, 15-16 March, (2018).

POSTER PRESENTATIONS

- "Rapid Thermal Annealing Effect on the Optical Properties of GaPN Alloys with Different III-V BEP ratios"
- Defects - Recognition, Imaging and Physics in Semiconductors (DRIP XVIII), Berlin, Germany, September 8 -12, (2015).

- "Investigation of the Effect of Incorporation of N:As on the Optical Properties of GaP Alloys Grown by MBE"
  The 40th WOCSDICE - Workshop on Compound Semiconductor Devices and Integrated Circuits held in Europe & 13th EXMATEC - Expert Evaluation and Control of Compound Semiconductor Materials and Technologies, Aveiro, Portugal, 06 -10 June, (2016).

- "Effects of Nitrogen Incorporation and Thermal Annealing on the Optical and Spin Properties of GaPN Dilute Nitride Alloys".
  The International Conference on Extended Defects in Semiconductors, Les Issambres, France, 25-29 September, (2016).

- "Effects of Epi-Layer Thickness on the Optical Properties of GaAsPN Dilute Nitride Alloys".
  Global Summit & Expo on Nanotechnology and Material Science, Dubai, UAE, 04-06 December, (2017).

- "Investigation of Electrically Active Defects in p-i-n GaAsPN Solar Cells After Rapid Thermal Annealing"
  28th International Conference and Expo on Nanosciences and Nanotechnology, Barcelona, Spain, 26-28 November, (2018).

ACKNOWLEDGMENT

"**All praise is due to Allah**, **the Lord of the Worlds"**

I would like to deeply thank my supervisors Prof. **Mohamed Henini** for his help and continuous support as I owe him all the knowledge and academic growth I acquired these past years. During my study at Nottingham University I worked with academic and non-academic members in the physics department and international institutions, who were always of great of help, therefore I thank them all.

I would like to thank **Princess Norah University (PNU)** in Riyadh for thr provision of a studentship.

My deepest gratitude to my friends who were the fuel of this journey, **Nourah Alshalawi, Tahani Aledwani, Shahd Alfadhli, Nora Alsaffar, Munairah Aldwosari, Maer Alanazi, Fatimah Albalawi, Sarah AlOtaibi, Amjad Almunyif, and Maryam Alhuwayz.**

A special gratitude to my aunt **Mona Alhandi**, thank you for all the joy and the care you offer.

To the soul of my brother, **Abdullah**, may he rests in peace, I am blessed because of his encouragements and prayers.

I thank my brothers; **Ziyad**, **Abdulaziz**, and **Abdulmajeed** and my sisters; **Khulud**, **Ohood**, **Hanadi**, **Sarah, Duaa** and **Reem** for endless love and supports.

My appreciation for my loving husband **Musab Alruthia**, for being my peace and comfort in the UK.

I would like to dedicate this thesis to my great father **Mohammed Albalawi** and my soulful mother **Thanwa Alma'aitah**, who are my role models in the life, my motive to be greater than myself, and the real reasons for my success.

TABLE OF CONTENTS

CHAPTER 1: INTRODUCTION....1

1.1 INTRODUCTION 1

1.2 MOTIVATION 4

1.3 SCHEME OF THE THESIS 5

REFERENCES 7

CHAPTER 2: FUNDAMENTAL CONCEPTS OF SEMICONDUCTORS....9

2.1 SEMICONDUCTORS 9

2.1.1 UNDOPED AND DOPED SEMICONDUCTORS 10

2.2 CRYSTAL STRUCTURES AND PROPERTIES 11

2.2.1 CRYSTAL STRUCTURES 11

2.2.2 ENERGY BANDGAPS 14

2.2.3 DIRECT AND INDIRECT ENERGY BANDGAPS 15

2.2.4 TEMPERATURE DEPENDENT ENERGY BANDGAPS 16

2.2.5 DENSITY OF STATES 16

2.3 HETEROJUNCTION STRUCTURES 18

2.3.1 LATTICE MISMATCH 18

2.3.2 ATOM SIZE AND ELECTRONEGATIVITY 19

2.3.3 BAND ALIGNMENTS 20

2.4 OPTICAL PROPERTIES OF SEMICONDUCTORS 22

2.4.1 ABSORPTION PROCESSES 22

2.4.2 EMISSION PROCESSES 24

2.5 CLASSIFICATION OF DEFECTS 27

2.5.1 POINT DEFECTS 27

2.5.2 COMPLEXES OF POINT DEFECTS 28

2.5.3 LINEAR DEFECTS 29

2.6 DEFECTS AND THEIR CARRIER KINETICS 30

2.6.1 SHALLOW LEVELS AND DEEP LEVELS DEFECTS 30

2.6.2 SHOCLEY-READ-HALL THEORY 31

2.7 GENERAL PROPERTIES OF SELECTED SEMICONDUCTOR MATERIALS34

2.7.1 GaP 34

2.7.2 GaAs 36

2.7.3 DILUTE GaPN 37

2.7.3.1 THE BAND ANTICROSSING (BAC) MODEL **38**
2.7.4 DILUTE GaAsN *39*
2.7.4.1 THE BAND ANTICROSSING (BAC) MODEL **40**
2.7.4.2 SOME IMPORTANT PROPERTIES OF GaAsN **41**
2.7.5 S-SHAPE IN DILUTE NITRIDES *42*
2.8 DEFECTS IN SELECTED SEMICONDUCTORS **43**
2.8.1 DEFECTS IN GaAs *43*
2.8.2 DEFECTS IN DILUTES GaAsN *44*
2.8.3 DEFECTS IN GaP *46*
2.8.4 DEFECTS IN DILUTES GaPN *47*
2.8.5 EFFECTS OF RAPID THERMAL ANNEALING (RTA) *49*
2.9 P-N JUNCTION **50**
2.9.1 P-N JUNCTION UNDER BIAS CONDITIONS *51*
2.9.2 DEPLETION LAYER CAPACITANCE *53*
2.9.3. CAPACETANCE IN P-I-N JUNCTION *55*
2.10 PHOTOVOLTAIC CELL **55**
REFERENCES **57**
CHAPTER 3: EXPERIMENTAL WORK **64**
3.1 SAMPLES USED IN THIS STUDY **64**
3.2 MEASUREMENT DETAILS **65**
3.2.1 PHOTOLUMINESCENCE MEASUREMENTS *65*
3.2.2 I-V MEASUREMENTS *66*
3.2.3 C-V MEASUREMENTS *66*
3.2.4 DLTS MEASUREMENTS *66*
3.3 PHOTOLUMINESCENCE **67**
3.3.1 SYSTEM HARDWARE IMPLEMENTATION *69*
3.3.1.1 SPECTROMETER **69**
3.3.1.2 LASERS, LIGHT CHOPPER AND OPTICS **70**
3.3.1.3 DETECTORS **71**
3.3.1.4 SPECTRACQ2 **71**
3.3.1.5 LOCK-IN AMPLIFIER **72**
3.3.1.6 CRYOSTAT AND TEMPERATURE CONTROLLER **72**
3.3.1.7 COMPUTER INTERFACE **73**
3.3.1.8 SYSTEM CONTROLLING SOFTWARE **73**

3.4 CURRENT- VOLTAGE CHARACTERISATION 73
3.5 DEEP LEVEL TRANSIENT SPECTROSCOPY (DLTS) 76
3.5.1 CAPACITANCE TRANSIENTS 76
3.5.2 CONVENTIONAL DLTS 80
3.6 LAPLACE DLTS SPECTROSCOPY 82
3.7 SYSTEM HARDWARE IMPLEMENTATION 86
3.7.1 DESCRIPTION OF SYSTEM HARDWARE 86
3.7.1.1 CRYOSTAT AND TEMPERATURE CONTROLLER 86
3.7.1.2 CAPACITANCE METER 87
3.7.1.3 CURRENT-VOLTAGE SOURCE METER 87
3.7.1.4 DATA ACQUISITION AND BNC-2100 CONNECTOR 88
3.7.1.5 COMPUTER INTERFACE 88
3.8 SYSTEM SOFTWARE 88
3.8.1 CONVENTIONAL DLTS MEASUREMENTS MODE 88
3.8.2 LAPLACE TRANSIENT PROCESSING MODE 89
REFERENCES 90

CHAPTER 4: INVESTIGATION OF THE EFFECTS OF NITROGEN INCORPORATION AND THERMAL ANNEALING ON THE OPTICAL PROPERTIES OF $GAP_{1-X}N_X$ DILUTE NITRIDES 92

4.1 INTRODUCTION 92
4.2 SAMPLES DETAILS 95
4.3 RESULTS AND DISCUSSION 96
4.3.1 INVESTIGATION OF STRUCTURAL PROPERTIES OF AS-GROWN AND ANNEALED $GaP_{0.986}N_{0.014}$ 96
4.3.2 INVESTIGATION OF THE EFFECT OF NITROGEN CONTENT ON THE OPTICAL PROPERTIES OF $GaP_{1-X}N_X$ 100
4.3.3 INVESTIGATION OF RAPID THERMAL ANNEALING ON THE OPTICAL PROPERTIES OF $GaP_{1-X}N_X$ 105
4.4 SUMMERY 113
REFERENCES 114

CHAPTER 5: INVESTIGATION OF THE EFFECTS OF ARSENIC AND INDIUM INCORPORATION AND THERMAL ANNEALING ON THE STRUCTURAL AND OPTICAL PROPERTIES OF $GAP_{0.99}N_{0.01}$.....118

5.1 INTRODUCTION **118**

5.2 SAMPLES DETAILS **122**

5.3 RESULTS AND DISCUSSION **123**

5.3.1 INVESTIGATION OF STRUCTURAL PROPERTIES OF AS-GROWN AND ANNEALED $GaAs_{0.1}P_{0.89}N_{0.01}$ and $In_{0.07}Ga_{0.93}P_{0.99}N_{0.01}$ ***123***

5.3.2 OPTICAL PROPERTIES OF $GaAs_{0.1}P_{0.89}N_{0.01}$ and $In_{0.07}Ga_{0.93}P_{0.99}N_{0.01}$ ***126***

5.3.3 INVESTIGATION OF RTA EFFECT ON THE OPTICAL PROPERTIES OF $GaAs_{0.1}P_{0.89}N_{0.01}$, AND $In_{0.07}Ga_{0.93}P_{0.99}N_{0.01}$ ***130***

5.3.3.1 **THE $GaAs_{0.1}P_{0.89}N_{0.01}$ CASE** **130**

5.3.3.2 **THE $In_{0.07}Ga_{0.93}P_{0.99}N_{0.01}$ CASE** **135**

5.4 SUMMERY **140**

REFERENCES **142**

CHAPTER 6: INVESTIGATION OF THE EFFECT OF DIFFERENT THICKNESSES AND THERMAL ANNEALING ON THE OPTICAL PROPERTIES OF $GAAS_{0.1}P_{0.89}N_{0.01}$ ALLOYS GROWN ON GAP SUBSTRATES.....145

6.1 INTRODUCTION **145**

6.2 SAMPLE DETAILS **148**

6.3 EFFECT OF EPILAYER THICKNESS ON THE OPTICAL PROPERTIES OF $GAAs_{0.1}P_{0.89}N_{0.01.}$ **148**

6.4 EFFECT OF RAPID THERMAL ANNEALING ON THE 1 MM $GAAs_{0.1}P_{0.89}N_{0.01.}$ **152**

6.5 SUMMERY **158**

REFERENCES **159**

CHAPTER 7: INVESTIGATION OF THE EFFECT OF RAPID THERMAL ANNEALING ON THE ELECTRICALLY ACTIVE DEFECTS IN GAASPN P-I-N SOLAR CELLS USING DEEP LEVEL TRANSIENT SPECTROSCOPY TECHNIQUE 161

7.1 INTRODUCTION **161**

7.2 SAMPLE DETAILS **162**

7.3 RESULTS AND DISCUSSION **164**

7.3.1 INVESTIGATION OF THE RTA EFFECT ON THE CURRENT (I) – VOLTAGE (V) CHARACTERISTICS OF P-I-N GaAsPN SOLAR CELLS ***164***

7.3.2 INVESTIGATION OF THE RTA EFFECT ON THE CAPACITANCE (C) – VOLTAGE (V) CHARACTERISTICS OF P-I-N GaAsPN SOLAR CELLS *169*

7.3.3 DLTS AND LAPLACE DLTS CHARACTERISTICS *170*

7.4 SUMMERY **173**

REFERENCES **174**

CHAPTER 8: CONCLUSION AND FUTURE WORK 178

8.1 CONCLUSION **178**

8.2 FUTURE WORK SUGGESTIONS **180**

CHAPTER 1: INTRODUCTION

1.1 INTRODUCTION

With regard of numerous governmental and non- governmental scientific reports, population is facing serious issues such as global warming, the rarefaction of fossil energy resources, and a worldwide energy consumption growth [1]. These difficulties are all linked to our balance of production and consumption of energy which is not in equilibrium with the earth natural resources, considering the available technologies. Tremendous development has been achieved in the technology of renewable energy, especially the photovoltaic (PV) energy. PV is one of the most efficient way to harvest solar energy for electricity production, i.e. converting sunlight directly into electricity using solar cells (SCs). In addition, solar energy is one of the most promising because it is abundant, clean, almost eternal, easy accessibility, and has the potential to cover a significant share of the energy needs of humanity [2]. One of the primary motivation for the development of high efficiency solar cells is to decrease the use of non-renewable energy which has been the main responsible for causing global warming and raising a serious environmental concern for future commercial development of electricity mass production.

Currently, solar cells based on crystalline, polycrystalline and amorphous silicon represent more than 90% of the world production and the energy conversion mechanism in these devices reach efficiencies in the range of 12-16% and 17-29%, respectively [3]. The Si solar cells work most efficiently in the 950–1100 nm (1.3-1.1 eV) spectral region, but they show very low spectral response to the short-wavelength (high energy) sunlight as shown in Fig. 1.1 [4]. Utilization of light-converting materials has been considered as an attractive strategy to improve light harvesting abilities.

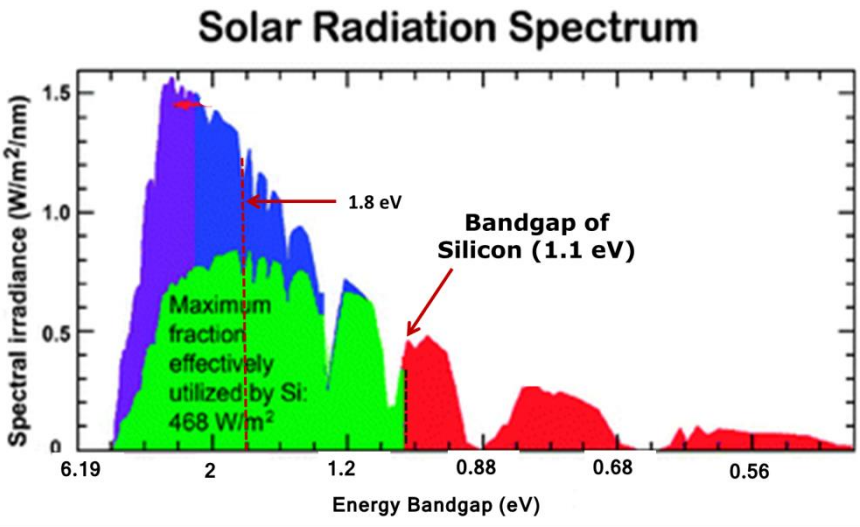


Fig. 1.1. Spectral distribution of sunlight at Air Mass 1.5 global (AM 1.5G) showing the fraction (highlighted in green) absorbed by a typical silicon-based PV cell [4].

One of this class of materials is dilute III-V nitride alloys which have recently attracted a great deal of attention for applications in optoelectronics particularly for solar cells [5-6]. Among these alloys, GaPN is an interesting material for pseudomorphic integration of photonics with silicon [7-8]. Furthermore, recently it was found that GaNP-based nanowires are a promising material for innovative device applications due to their beneficial properties related to their architecture [9-10]. Gallium phosphide (GaP) has the smallest lattice mismatch with silicon (0.37% at room temperature) amongst all binary III–V compound semiconductors. Fig. 1.2 shows the bandgaps of some of selected III-V semiconductors with their lattice constants. However, the residual strain due to this lattice mismatch can be compensated by the incorporation of a few per cent of nitrogen in GaP [11-12]. Incorporating a small percentage of nitrogen atoms into dilute III-V nitride semiconductors causes a considerable reduction of their band gap. The control of the band gap helps tailor their optical and electronic properties [13].

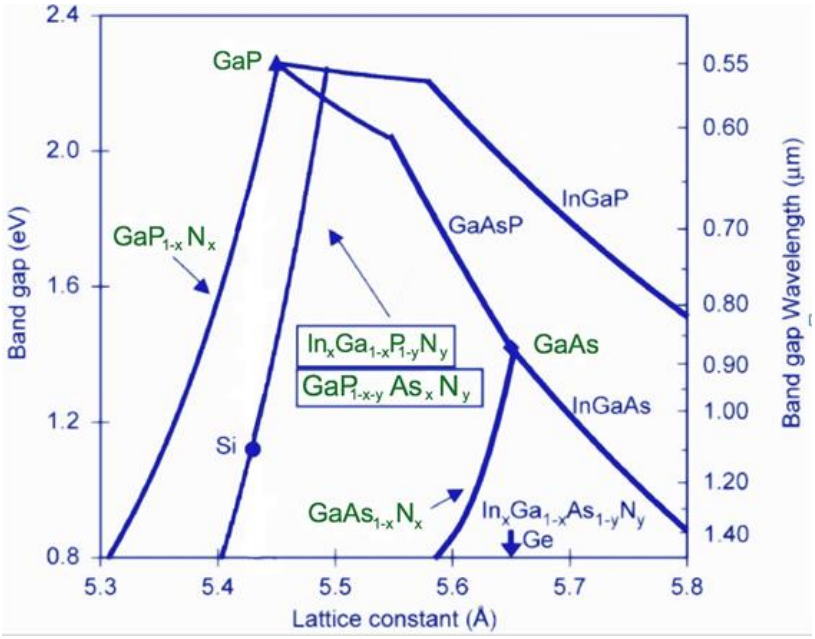


Fig. 1.2. Energy bandgap as a function of the lattice constant of selected III-V semiconductors [14].

However, the optical efficiency of GaPN material decreases with increasing nitrogen content. Potentially, this problem may be alleviated by incorporating arsenic (As) and indium (In) into GaPN host lattice to enhance the optical quality by increasing the PL intensity and reducing the Full Width at Half Maximum (FWHM). This incorporation modifies the conduction band structure, suggesting that the band gap of the alloys namely (GaAsPN and InGaPN) can be adjusted to the desired wavelengths required for several applications, for example achieving 1.8 eV bandgap material lattice matched to Si for solar cell devices. These novel and exciting III-V-N materials systems have been proposed as good candidates to fabricate solar cells with high efficiency. In addition, there are new opportunities to further develop this material system by epitaxially growing with different epilayer thickness [15]. The thickness of the epilayer has a strong influence on the optical and electronic properties of III-V-N materials.

However, the incorporation of nitrogen, arsenic and indium into the host lattice of GaP as well as a change in epilayer thickness lead to the creation of deep and shallow defects [16]. Defects, in the form of deep levels in the bandgap of semiconductors, have detrimental

effects on the device's performance because they act as efficient recombination centres. A number of studies have made efforts to reduce these defects. Rapid thermal annealing has been used in order to improve the optical and electrical efficiency of III-V-N dilute nitrides [17]. Nevertheless, a study of the effect of the rapid thermal annealing (RTA) on the structural, optical and electrical properties of GaPN-based semiconductors has not been reported.

Photoluminescence (PL), which is a very powerful optical characterisation technique, has been used to assess the optical quality of the as-grown and annealed semiconductors. In particular, significant parameters such as PL intensity, bandgap energy and full width at half maximum (FWHM) can be determined using PL. Moreover, to characterise and identify deep levels defects, also referred to as electrically active defects and traps, deep level transient spectroscopy (DLTS) which is a unique electrical technique has been employed. Particularly, fundamental defect parameters such as activation energy, capture cross-section and concentration can be obtained from DLTS measurements [18].

1.2 MOTIVATION

The main source of renewable energy is solar radiation, i.e. sunlight. The constantly sunny weather in Saudi Arabia has a greater potential for solar power application more than any other place in the world. Saudi Arabia ranges from Azimuth 50 to Azimuth 35 and from latitude 17 in the south to latitude 32 in the north [19]. Renewable energy is one of the important strategic theme of Saudi Arabia national priorities and the objectives of Vision 2030. It is worth pointing out that the market of solar cells nowadays has varity of solar cells materials such as colloidal quantum dots and GaAs [20]. However, further materials and development are required to reduce the cost of the solar cells and increase the efficiency of their work. Furthermore, a 1.8 eV band gap material lattice matched to Si (1.1 eV) for tandem solar cell applications is required as a top junction absorber to achieve very high conversion

efficiencies. The main motivation of this thesis is, therefore, to study the optical and electrical properties of GaP based materials grown by Molecular Beam Epitaxy (MBE) to reach the target 1.8 eV bandgap energy for the top junction. Moreover, this work aims to investigate the effect of annealing on these potential materials, namely GaPN, GaAsPN and InGaPN.

PL characterisation technique is employed to study the optical properties of as-grown and annealed $GaP_{1-X}N_X$ alloys (x= 1.4%, 2.1% and 2.7%). It is also used to investigate the optical properties of as-grown and annealed $GaAs_{0.1}P_{0.89}N_{0.01}$ and $In_{0.07}Ga_{0.93}P_{0.99}N_{0.01}$ quaternary alloys as well as the effect of different epilayer thickness (100nm and 1μm) on the optical properties of $GaAs_{0.1}P_{0.89}N_{0.01}$. Additionally, Current – Voltage (I-V), Capacitance – Voltage (C-V), conventional DLTS, and Laplace DLTS characterisation techniques are performed to study the electrical properties of as-grown and annealed p-i-n GaAsPN solar cells.

1.3 SCHEME OF THE THESIS

This thesis is arranged as follows:

Chapter 1 presents the research motivations and thesis structure.

Chapter 2 describes the semiconductors fundamental concepts, the structure of the crystal, the principles of heterostructure devices. It also covers the properties of GaP, GaAs, GaPN, and GaAsN dilute nitrides materials.

Chapter 3 provides information on the crystal defects and theoretical background of carrier kinetics.

Chapter 4 discusses the experimental techniques used in this thesis including PL, I-V, C-V, DLTS, and Laplace DLTS. The hardware and software required to perform these systems are also illustrated.

Chapter 5 covers the samples used in this work and explains briefly the details of the measurements set up.

Chapter 6 investigates the effect of adding different N concentrations ranging from 1.4 to 2.7% on the optical properties of $GaP_{1-X}N_X$ alloys grown by Molecular Beam Epitaxy (MBE) using PL measurements. RTA effects on these samples are also discussed.

Chapter 7 discusses the effect of adding 10% of As and 7% of In on the optical properties of as-grown and annealed dilute $GaAs_{0.1}P_{0.89}N_{0.01}$ and $In_{0.07}Ga_{0.93}P_{0.99}N_{0.01}$ alloys.

Chapter 8 describes the effect of the epilayer thickness (100 nm and 1 μm) on the optical properties of $GaAs_{0.1}P_{0.89}N_{0.01}$. The effect of annealing on 1 μm $GaAs_{0.1}P_{0.89}N_{0.01}$ is also reported in this chapter.

Chapter 9 presents a study of electrically active defects in p-i-n GaAsPN solar cell structures, and the effect of RTA on their electrical properties.

Chapter 10 gives a summary of the research work performed in this thesis and proposes future work suggestions.

REFERENCES

[1] C. Team, (http://www.ipcc.ch/pdf/assessment-report/ar4/syr/ar4_syr.pdf).

[2] D. MacKay, and D. Mackay, Sustainable Energy: Without the Hot Air Cambridge, [Online], (2017).

[3] V. Badescu, J. Appl. Phys. Lett. **102**, 073102 (2007).

[4] H. Xiaoyong, Chem. Soc. Rev. **42**, 173 (2013).

[5] S. Almosni, P. Rale, C. Cornet, M. Perrin, L. Lombez , A. Létoublon, K. Tavernier , C. Levallois, T. Rohel, N. Bertru, J. Guillemoles, and O. Durand. Solar Energy Materials and Solar Cells. Elsevier, **147**, pp.53 (2016).

[6] M. Wiemer, V. Sabnis, and H. Yuen, Proc. SPIE **8108**, 810804 (2011).

[7] K. Kharel, and A. Freundlich, J. Appl. Phys. Lett. **124**, 095104 (2018).

[8] S. Almosni, C. Robert, T. Nguyen Thanh, C. Cornet, A. Létoublon, T. Quinci, C. Levallois, M. Perrin, J. Kuyyalil, L. Pedesseau, A. Balocchi, P. Barate, J. Even, J. Jancu, N. Bertru, X. Marie, O. Durand, and A. Le Corre. J. Appl. Phys. Lett. **113**, 123509 (2013).

[9] M. Steidl, M. Wu, K. Peh, P. Kleinschmidt, E. Spiecker, and T. Hannappel. Nanoscale Research Letters **13**, 1, 417 (2018).

[10] S. Filippov, M. Jansson, J. Stehr, J. Palisaitis, P. PO, F. Ishikawa, W. Chen, and I. Buyanova. Nanoscale **8**, 15939 (2016).

[11] A. Lazarenko, E. Nikitina, M. Sobolev, E. Pirogov, D. Denisov, and A. Egorov. Semiconductors **49**, 479 (2015).

[12] S. Shokhovets, O. Supplie, C. Koppka, S. Krischok, and T. Hannappel. Phys. Rev. Lett. B **98**, 075205. (2018).

[13] J. Olson, S. Kurtz, A. Kibbler, and P. Faine, J. Appl. Phys. Lett. **56**, 623 (1990).

[14] M. Henini, Dilute Nitride Semiconductors (2005).

[15] P. Blood, and J. W. Orton, Reports on Progress in Physics **41** (2), 157 (1978).

[16] Y. Jin, R. Jock, H. Cheng, Y. He, A. Mintarov, Y. Wang, C. Kurdak, J. Merz, and R.S. Goldman. J. Appl. Phys. Lett. **95**, 062109 (2009).

[17] Y. Kuang, S. Chen, H. Li, S. Sinha, and C. Tu, Journal of Vacuum Science & Technology B **30**, 121 (2012).

[18] D. Lang, J. Appl. Phys. Lett. **45** (7), 3023 (1974).

[19] O. Alnatheer, Energy Policy **33**, 2298 (2005).

[20] http://www.altenergy.org/renewables/solar/latest-solar-technology.html [online 06/05/2019].

CHAPTER 2: FUNDAMENTAL CONCEPTS OF SEMICONDUCTORS

This chapter describes the basics, fundamentals and properties of semiconductors. It includes semiconductors crystal structure, energy bandgaps, direct and indirect bandgaps and density of states. Furthermore, this chapter will provide details of heterostructure materials and their structural and electrical properties such as lattice mismatch, atom size, atom electronegativity, and band alignment. The optical properties of III-V semiconductors will be also discussed. The defects in the crystalline structure of semiconductors caused by foreign impurities and trapping centres are discussed also in this chapter. The theory of deep level defects and their carrier kinetics processes are also described. The chapter will provides a discussion of the basic features of GaP, GaAs, and dilute GaPN and GaAsN materials. Additionally, a review of the defects in GaP, GaAs and dilute nitrides GaPN and GaAsN semiconductor materials and their properties is presented. A brief introduction to annealing effects on semiconductor materials will be iullestrated.The chapter will conclude by providing basics of pn, pin and photovoltaic.

2.1 SEMICONDUCTORS

For the last few decades, modern electronic and optical technologies have been built on semiconductor materials which allowed the fabrication of numerous components for optoelectronic and electronic applications [1]. There are many examples of such devices which can be found in computers (memories, Central processing units (CPUs)), optical storage hardwares (lasers for CDs and DVDs), network infrastructures (laser and photo-detectors for optical-fiber technology), solar cells with high efficiency, display devices (thin film transistors, LEDs), projectors (laser diodes), lights (LEDs) [2] etc.

Semiconductors can be defined by their conductivity which lies between insulators and conductors. A material with an electrical resistivity in the range of 10^{-2} to 10^{9} Ω.cm is considered

semiconducting. Semiconductors are known either as elementaries, which are made of a single element, or as compounds, which are made of two or more elements. Elementary semiconductors in the periodic table belong to group IV such as silicon (Si) and germanium (Ge). Compound semiconductors can be formed by combining elements from groups III and V, or II and VI elements. Gallium phosphide (GaP) and gallium arsenide (GaAs) are semiconducting compounds made of only two elements and are classified binary compounds. If a compound semiconductor is made of three elements, it is known as ternary compound such as gallium phosphide nitride (GaPN) and gallium arsenide nitride (GaAsN). Quaternary compounds are those semiconductors made of four elements, for example InGaAsN and GaAsPN.

2.1.1 UNDOPED AND DOPED SEMICONDUCTORS

An essential classification of semiconductors is based on the type of the material doping. Undoped or intrinsic semiconductors are classifications for pure semiconductors. Usually, intrinsic semiconductors are very pure with an insignificant amount of impurities, which could in some cases affect the electronic properties. An alternative identification of pure semiconductors is made when the number of negative charge carriers (electrons) in the conduction band is equal to the number of positive charge carriers (holes) in the valence band. Intrinsic semiconductors have the ability to behave as insulator at zero absolute temperature due to the position of the Fermi level between the filled valence band and the empty conduction band. Thus, in this hallmark feature there is no flow of free electrons and thereby no conductivity. If such semiconductor is subject to a thermal or a photonic excitation, the material conductivity increases.

The doping process is one of the most popular approaches to change the properties of semiconductors. If a pure semiconductor is doped with a small percentage of impurity atoms then it is classified as an extrinsic semiconductor. If the dopant atom causes the number of electrons to exceed the number of holes, then the resulting semiconductor is called n-type. A

good example of the n-type doping process is the addition of pentavalent impurity material from group V in the periodic table (such as As) to an element from IV group (such as Si). Arsenic has five electrons in its valence band while Si has four. Adding As to Si causes the formation of four bonds between 4 electrons from each element and one electron will always be free, thus the material has n-type behaviour. Likewise, if an element of III group (e.g Boron) is added to pure Si, three covalent bonds are formed between the three valence electrons in B with three of Si valence electrons, leaving one hole free. Thus, the dopant atoms introduce more holes than electrons and therefore creating p-type behaviour, hence p-type semiconductor.

2.2 CRYSTAL STRUCTURES AND PROPERTIES

The features and properties of semiconductors, as other solid materials, are determined by their crystal structure. Crystal structure refers to the arrangement of atoms into periodic crystals.

2.2.1 CRYSTAL STRUCTURES

The crystal structure of a material is the product of a unit cell, which represents an infinite periodic building unit composed of a set of atoms in a well-defined arrangement. There are many forms of crystal structures. Fig 2.1 shows three types of periodic crystal structures known as simple cubic (sc), body-centred cubic (bcc), and face centred cubic (fcc).

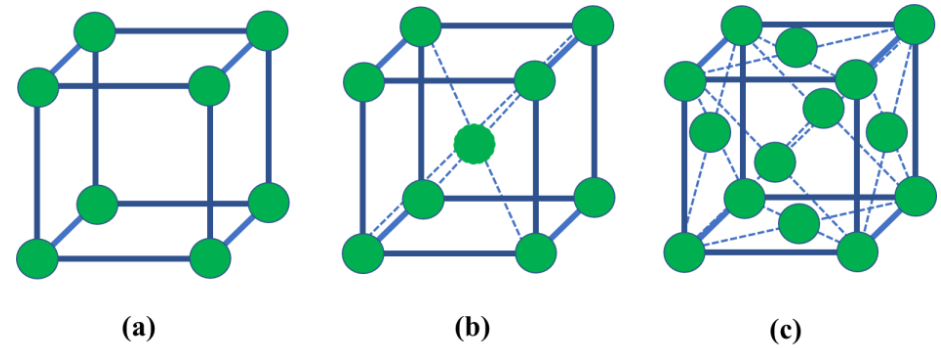


Fig. 2.1. Crystal structure of **(a)** simple cubic lattice **(b)** body centred cubic lattice and **(c)** face centred cubic lattice

The simple cubic is the simplest crystal structure, where each cubic corner represents an atomic site (Fig 2.1 (a)). The closest similar arrangement is the body centred cubic structure, which is basically a simple cubic structure with an additional atom site at the centre of the cube (Fig 2.1 (b)). The face centred cube has simple cubic atomic sites in addition to one atom at the centre of each cubic face as illustrated in Fig 2.1 (c).

Some crystal structures are more common than others in semiconductor materials such as diamond crystal structure (Fig 2.2 (a)) and zincblende structure (Fig 2.2 (b)). Each atom in these two structures forms four covalent bonds with four neighbouring atoms in a tetrahedron configuration, which can be viewed as two overlapped fcc lattices. All the atoms in the diamond crystal structure are of the same type. In zincblende structure the atomic sites are occupied by two different kinds of atoms. The semiconducting elements Si, Ge and C have diamond structured crystals, whereas the III-V compounds such as GaAs, GaP and InAs have zincblende crystal structure.

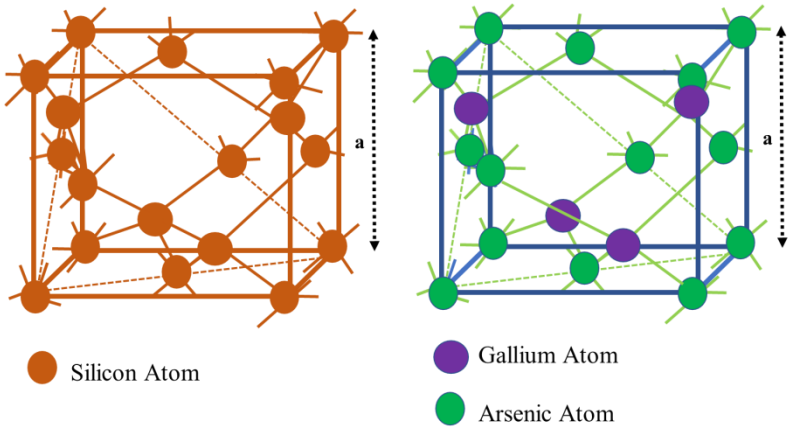


Fig. 2.2. Presentation of **(a)** diamond structure for Si where both types of atomic sites are occupied by Si and **(b)** zincblende structure for GaAs where the sites are occupied by Ga and As atoms, a is the lattice constant [3].

The lattice configuration and its surface properties are essential requirements in the semiconductor's fabrication processes. One of the lattice parameters are called Miller indices, which can be considered as the coordinates of lattice planes. Therefore, Miller indices

indicate the orientation of the semiconductor crystal. The lattice is constructed from three primitive basis vectors $\boldsymbol{a}, \boldsymbol{b}$ and $\boldsymbol{c}$, which can be used to determine Miller indices. Figure 2.3 shows an example of a lattice plane orientation described by Miller indices (100).

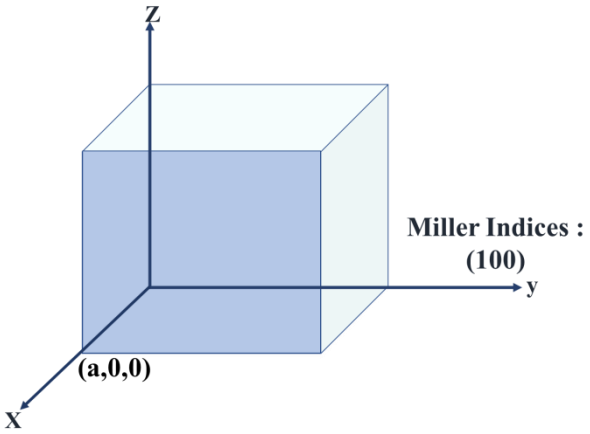


Fig. 2.3. Illustration of a plane having Miller indices (100).

The crystalline solid can be described by three primitive basis vectors, which are determined by the primitive cell. Through these vectors, the crystal structure is invariant under transformation of the lattice position vector $\boldsymbol{R}$, which is given by the sum of integers multiples of $\boldsymbol{a}, \boldsymbol{b}$ and $\boldsymbol{c}$, *as:*

$$\boldsymbol{R} = m\boldsymbol{a} + n\boldsymbol{b} + p\boldsymbol{c} \qquad (2.1)$$

where m, n and p are integers and $\boldsymbol{a}, \boldsymbol{b}$ *and* $\boldsymbol{c}$ are vectors. If a point on the crystal structure is translated through the vector **R**, then the point is transformed to an identical site, and therefore the lattice looks exactly the same.

If the lattice undergoes Fourier transformation, hence transformed to the reciprocal space, then the reciprocal lattice basis vectors $\boldsymbol{a}^*, \boldsymbol{b}^*$ and $\boldsymbol{c}^*$ can be written in term of direct lattice vectors $\boldsymbol{a}, \boldsymbol{b}$ and $\boldsymbol{c}$ as:

$$\boldsymbol{a}^* = \boldsymbol{2\pi}\,[(\boldsymbol{b} \times \boldsymbol{c})/(\boldsymbol{a}.\boldsymbol{b} \times \boldsymbol{c})] \qquad (2.2)$$

$$\boldsymbol{b}^* = \boldsymbol{2\pi}\,[(\boldsymbol{c} \times \boldsymbol{a})/(\boldsymbol{a}.\boldsymbol{b} \times \boldsymbol{c})] \qquad (2.3)$$

$$\boldsymbol{c}^* = \boldsymbol{2\pi}\,[(\boldsymbol{a} \times \boldsymbol{b})/(\boldsymbol{a}.\boldsymbol{b} \times \boldsymbol{c})] \qquad (2.4)$$

where $\boldsymbol{a}^*.\boldsymbol{a} = 2\pi$ and $\boldsymbol{a}.\boldsymbol{b}^* = 0$ and so on, taking in consideration that the volume included by these vectors = $\boldsymbol{a}.\boldsymbol{b} \times \boldsymbol{c} = \boldsymbol{b}.\boldsymbol{c} \times \boldsymbol{a} = \boldsymbol{c}.\boldsymbol{a} \times \boldsymbol{b}$.

In the reciprocal space, the position vector is defined as:

$$\boldsymbol{G} = h\boldsymbol{a}^* + k\boldsymbol{b}^* + l\boldsymbol{c}^* \qquad (2.5)$$

where h, k and l are integers. The vector $\boldsymbol{G}$ is given by the basic transformation between the direct lattice and the reciprocal lattice which is:

$$\boldsymbol{G}.\boldsymbol{R} = 2\pi \times integer \qquad (2.6)$$

2.2.2 ENERGY BANDGAPS

The energy bandgap (E_g) is a key parameter in solid state physics concerning the materials properties which are determined by the energy band structure. $E_g$is defined as the difference in energy between the valence band (VB) energy (E_V) and the conduction band (CB) energy (E_C) as shown in Fig 2.4. The size of the energy gap determines the type of the material, being either an insulator or a metal. Metals have energy gap close to zero ($E_g \sim 0\ eV$), while insulators have a very high energy gap ($E_g > \sim 6\ eV$). Semiconductor materials have a bandgap that fits in between, in particular E_g is within the range of $\sim 0.5\ to\ \sim 3\ eV$ [4].

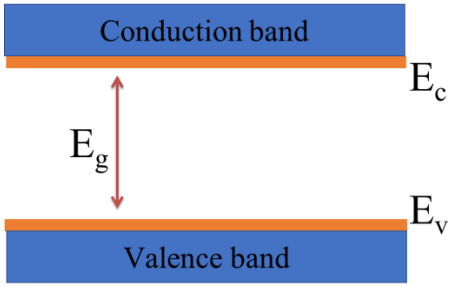


Fig. 2.4. Energy bands diagram of a semiconductor.

The dispersion relation of the bandgap in semiconductor is determined in respect to the wave vector k, where the relationship between the energy and the wave vector is illustrated in Fig

2.5. At $k = 0$, close to zero energy the valence and the conduction energies have parabolic dependence as described by the following equation:

$$E_C = E_g + \frac{h^2k^2}{8\pi^2 m_e^*}, \quad E_V = -\frac{h^2k^2}{8\pi^2 m_h^*} \qquad (2.7)$$

where E_C and E_V are the energy levels of the conduction and the valence bands, respectively, h is Plank's constants, k is Boltzman constant, m_e^* and m_h^* are the effective masses of electron and holes. At low temperatures~0 K, the valence electrons are confined within the outer band due to the absence of excitation energy. Consequently, intrinsic semiconductors exhibit insulating behaviour at very low temperatures.

2.2.3 DIRECT AND INDIRECT ENERGY BANDGAPS

Semiconductor materials have two different types of bandgap, namely a direct bandgap or an indirect bandgap. This classification is based on the positioning of the valence and conduction energy band with respect to each other as functions of wave vector k. When the minimum of the conduction band and the maximum of the valence band occur at $k = 0$ the semiconductor has a direct bandgap. The most common direct bandgap semiconductor is GaAs. The indirect bandgap on the other hand represents the case where one of the bands has a shifted momentum, thus the vertices are placed at different momentum values, such as in Si, which is the most common indirect semiconductor. Fig 2.5 shows the $E - k$ relationship of the two types of bandgaps.

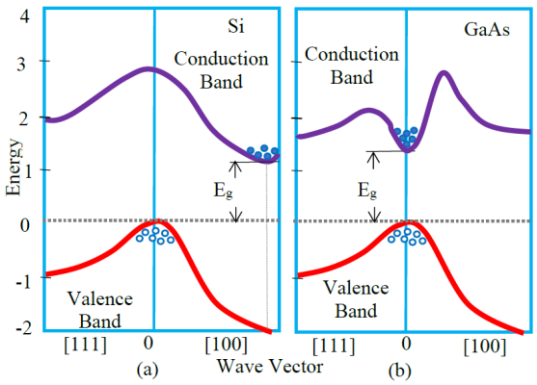


Fig. 2.5. Energy-band structure of **(a)** Si that has an indirect bandgap and **(b)** GaAs that has a direct bandgap [3]. The full and open circles represent electrons and holes, respectively.

2.2.4 TEMPERATURE DEPENDENT ENERGY BANDGAPS

The energy of the bandgap of semiconducting materials is temperature dependent. This dependence is related to the thermal vibrational energy, which results in an increase in the amplitude of the atomic vibrations. Such effect extends the interatomic spacing which in turn reduces the potential experienced by the electrons in the semiconductor. Consequently, the size of the energy gap is reduced.

The temperature dependence of the energy bandgap can be constructed from the empirical relationship, which was formulated by Varshni [5] as:

$$E_g(T) = E_g(0) - \frac{\alpha T^2}{\beta + T} \qquad (2.8)$$

where $E_g(0)$ is the energy bandgap at 0 K, and α and β are the empirical parameters for the material. Table 2.1 shows the empirical parameters for GaAs, GaP, $GaP_{1-X}N_x$ (x= 1.3%) and $GaAs_{1-x}N_x$ (x= 2.97%).

Table 2.1. Empirical parameters for temperature dependency of GaP, GaAs, GaPN and GaAsN bandgaps.

Parameter	GaP [6]	GaAs [6]	GaPN (N= 1.3%) [7]	GaAsN (N=2.97%) [8]
α (meV/K)	0.5	0.5	0.36	0.61
β (K)	372	220	372	560

2.2.5 DENSITY OF STATES

The density of states identifies the distribution of charge carriers by considering the number of vacancies in the electron states at each energy level. The interatomic interaction in solids is determined by the atoms electric fields due to the tight positioning of atoms in solid materials. Therefore, energy levels split into infinite number of electronic states [9]. Electrons have the tendency to occupy the lowest energy states possible, causing the energy sublevels close

to zero to be filled up first, thus, the valence and the conduction bands are formed. In semiconductors the conductivity means that electrons are transferred from the valence band to the conduction band due to an energy excitation. The absence of electrons from the valence band creates positive charges, i.e. holes. In semiconductors, the number of states that are available to be occupied is known as the density of states ($N(E)$) at a certain energy level. This density is dependent on two factors namely the degree of charge carriers freedom and their confinement. The degree of freedom is determined by the energy level splitting and the confinement within the dimensions of the material. For instance, in three-dimensional (3D) systems $N(E)$ has a square root dependence with energy (Fig 2.6 (a)). Likewise, in 2D materials $N(E)$ forms a step like function with respect to energy (Fig 2.6 (b)). Whereas in 1D systems $N(E)$ is proportional to $(E)^{-\frac{1}{2}}$ as $\left(\text{Fig 2.6 (c)}\right)$ presented, and it is dependent on (delta function) energy in 0D systems as (Fig 2.6 (d)) illustrated.

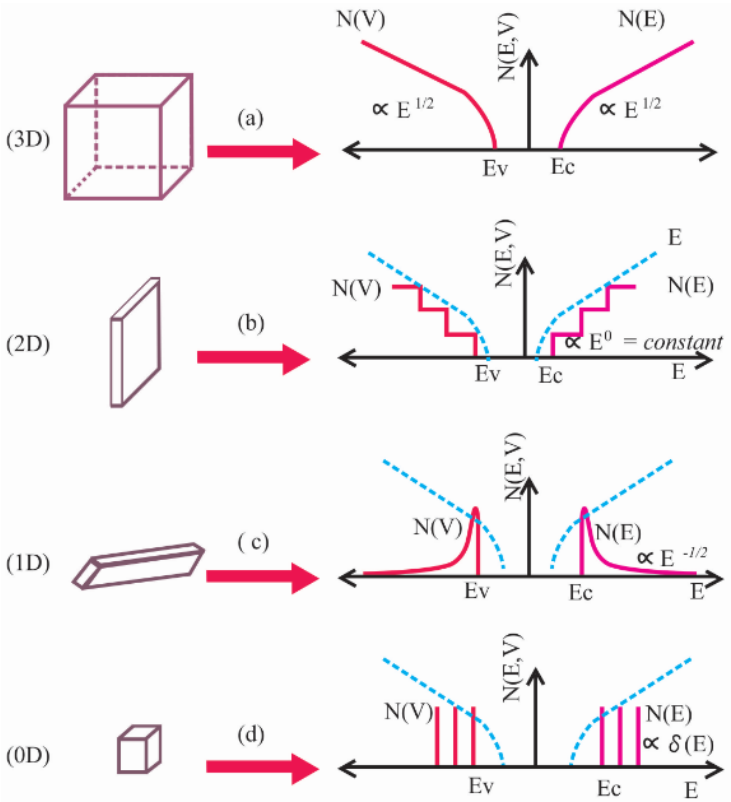


Fig. 2.6. Density of states for **(a)** bulk semiconductor or three dimensional system (3D), **(b)** two dimensional systems (2D), **(c)** one dimensional systems (1D), and **(d)** zero dimensional systems (0D) [3].

2.3 HETEROJUNCTION STRUCTURES

Semiconductor structures can be produced in a number of configurations such as homojunction and heterojunction structures. When two layers of similar semiconductor crystals are grown on top of each, the structure is called homojunction. If the two layers are made of different materials the structure is termed Heterojunction.

The homojunction semiconductors have the same bandgap (Fig 2.7 (a)), yet each layer could have a different doping. In heterojunction structures the two layers could have different bandgaps (Fig 2.7 (b)) and/or different lattice constants.

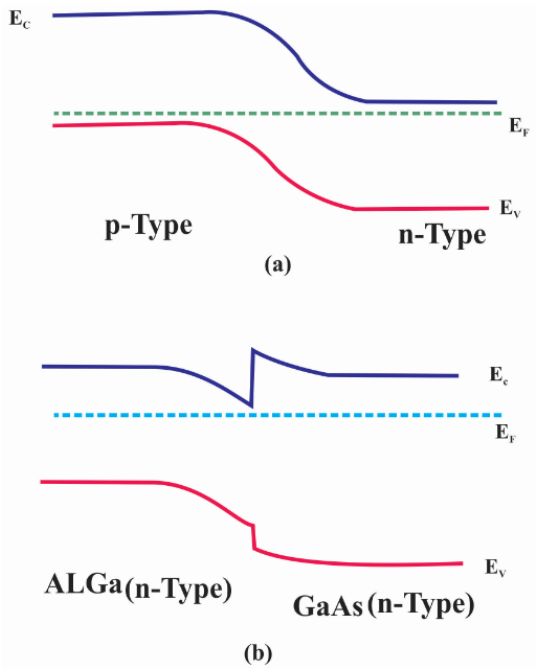


Fig. 2.7. Schematic illustration of **(a)** a homojunction structure and **(b)** a heterojunction structure.

2.3.1 LATTICE MISMATCH

Lattice matching can be obtained by growing two layers of materials on top of each other while both have the same lattice constant (Fig 2.8 (a)). Contrarily, if the two materials grown on top of each other have different lattice constants, then the formed structure is called mismatched. The lattice mismatch is determined by:

$$\frac{\Delta a}{a} = \frac{a_{layer} - a_{sub}}{a_{sub}} \qquad (2.9)$$

where a_{layer} and a_{sub} represent the lattice constants of layer and substrate, respectively. During the growth process of the heterojunction structure, defects emerge at the interface. As the difference between a_{layer} and a_{sub} increases, the creation of defects would increase. Two types of strains may occur in the mismatched system, namely compressive and tensile strains.

Fig 2.8 (b) illustrates a compressive strain caused by placing a material of a larger lattice constant than that of the substrate. On the other hand, if the top layer has a smaller lattice constant than the substrate, the mismatched system will experience a tensile stain as demonstrated in Fig 2.8 (c).

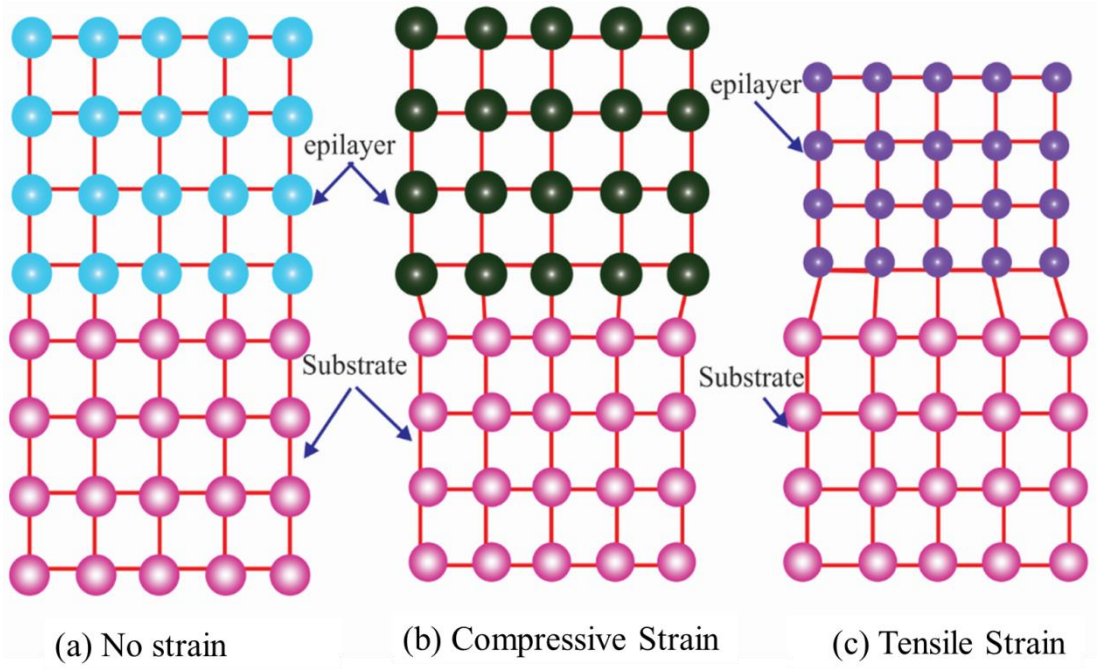


Fig. 2.8. Schematic illustration of **(a)** lattice matched structure, **(b)** Compression strain (lattice mismatched structure) and **(c)** Tensile strain (lattice mismatched structure).

2.3.2 ATOM SIZE AND ELECTRONEGATIVITY

During the creation process of a heterojunction structure, a number of factors have key influence on the mismatched system. The growth process can be affected by the different atoms

sizes of the two different materials, atoms electronegativity (χ), and the alignment of the energy band of the two layers, in addition to the mismatching factor. The growth of two layers of materials which have different atoms sizes results in strain. The formation of chemical bonds during the growth process depends on the atom's electronegativity, which is a unitless feature that allows the atom to attract electrons for bonding. This atom property is usually referred to as Pauling scale, as Linus Pauling was the first to demonstrate the principal of electronegativity in 1932 [10]. If two materials A and B are layered together to form a heterostructure, then the difference in the electronegativity can be calculated via Pauling's theory as:

$$\chi_A - \chi_B = (eV)^{-\frac{1}{2}} \sqrt{E_D(AB) - \frac{[E_D(AA)+E_D(BB)]}{2}} \qquad (2.10)$$

where E_D (in eV) is the dissociation energy between atoms by type ($AB, AA \,\&BB$). The introduction of the $(eV)^{-\frac{1}{2}}$ to the equation is to balance the units so $\chi_A - \chi_B$ would be unitless. This difference in Pauling electronegativity, if found to be large, indicates a major change in the electronic structure.

2.3.3 BAND ALIGNMENTS

The fabrication of heterojunctions is dependent on the band alignment of the layered materials. Fig. 2.9 shows a schematic illustration of three different band alignments categorised as type I, type II and type III alignments. Type I alignment is referred to as the straddled alignment, where one material (e.g. material B) has a smaller energy gap than material A. The bands are aligned such that the valance band of B lies within the valence band of material A, and the conduction band of B lies within the conduction band of A. Common semiconductors with such alignment are InGaAs/InP and AlGaAs/GaAs structures.

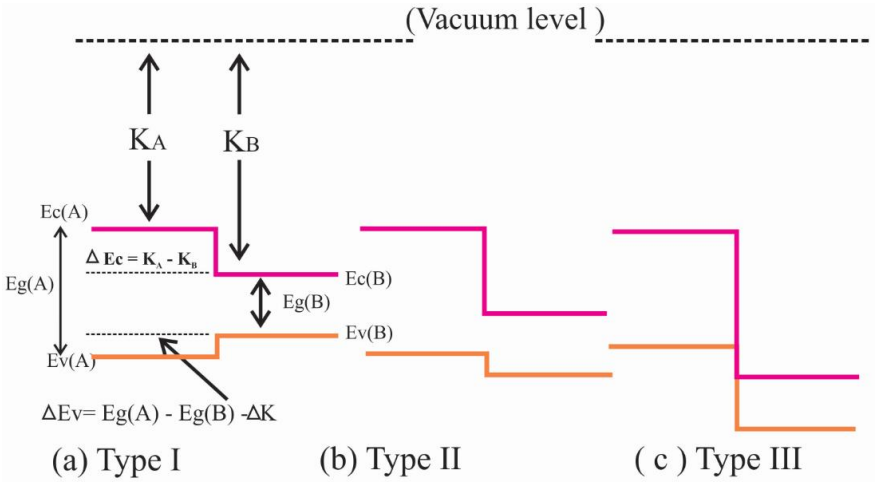


Fig. 2.9. Types of energy bands alignments in heterojunctions, where E_C, E_V, Eg, ΔE_C, ΔE_V are the conduction band, valence band, energy gap, conduction band offset, and valence band offset, respectively. κ_A and κ_B are electron affinity of materials A and B, respectively.

In a type II band alignment, the edges of the valence and conduction bands of larger bandgap material A are above the corresponding edges of valence and conduction bands of smaller bandgap material B. This type is called staggered alignment and it can be produced in hetero-junctions such as GaSb/GaAs. The third type of alignment (type III band alignment) is known as broken gap alignment such in GaSb/InAs heterostructures. This alignment is arranged such as the edge of conduction band of B is aligned below the edge of valence band in material A.

To calculate the band offset of a typical heterostructure in semiconductors the theoretical approach of electron affinity can be considered. This theoretical model was designed by Anderson in 1962 [11]. The conduction band (ΔE_C) and the valence band (ΔE_V) can be found to experience an additional offset as a result of the difference in affinities of electrons in two different materials ($\kappa_A - \kappa_B$), which is determined by:

$$\kappa_A - \Delta E_C - \kappa_B = 0 \qquad (2.11)$$

$$\Delta E_V = \Delta E_g - \Delta E_C \qquad (2.12)$$

where E_g is the energy gap.

Nevertheless, this rule only includes electron affinity but does not include states of defect, surface interface and dislocation. Therefore, this model is limited. Furthermore, the rule con-

siders intrinsic semiconductors so donor or acceptor charges cannot be taken into consideration.

2.4 OPTICAL PROPERTIES OF SEMICONDUCTORS

Semiconducting surfaces interact with incident photons in many processes as they may be reflected from the surface, transmitted through it or/and be absorbed in the material. If the incidence is of high energy photons, they could excite an electron allowing its transfer from valence band to conduction band. The optical interaction could contribute to atoms vibrations or localized defects. Therefore, detection of optical response of semiconductor materials provides empirical data of the properties of the material.

2.4.1 ABSORPTION PROCESSES

Illumination of semiconductors with high energy photons can be used to produce an electron-hole pair only if the photons energy is greater than the energy bandgap of the semiconductor. Fig. 2.10 illustrates the illumination process of a semiconductor which can cause band-to-band transition as shown in process (A) where the electron is excited by photon absorption and transferred to conduction band, thus creating a hole in the valence band. Processes (B) and (C) show the transition of electron to/from impurity atom leaving behind an electron charge vacancy (i.e. hole). The transition can also be experienced between two impurity atoms as process (D) shows.

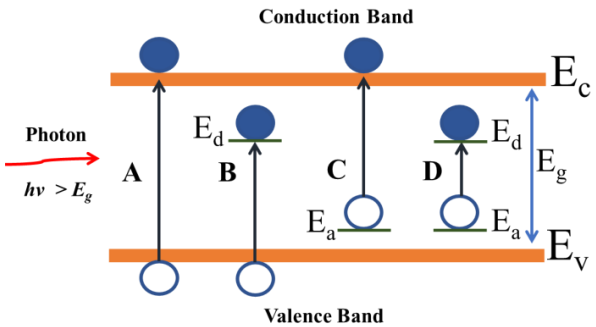


Fig.2.10. Main optical processes involved in absorption mechanism in semiconductors.

Measurement of optical absorption of a semiconductor material is a basic method to probe the band structure of the material. If a light with wavelength λ and intensity I_0 is incident on a semiconductor surface of thickness t, the transmitted light with intensity I(λ,t) can be detected form the other side as:

$$I(\lambda, t) = [1 - R(\lambda)]I_0(\lambda)e^{-\alpha(\lambda)t} \qquad (2.13)$$

where $R(\lambda)$ is the reflection coefficient at the interface and $\alpha(\lambda)$ is the absorption coefficient of the material.

The absorption coefficient $\alpha(\lambda)$ of semiconductors with direct bandgap such as GaAs, can be determined using the following relationship [12]:

$$\alpha(\lambda) = A\left(h\nu - E_g\right)^{1/2} \qquad (2.14)$$

where $h\nu$ is the energy of the incident photon (in our case is a blue laser with 2.62 eV) and A is dependant on the material properties.

Phonons are not involved in direct optical transition processes, while in the indirect optical transitions a single photon is either emitted or absorbed with the transition to conserve the momentum. The energy of the phonon is given by E_p, where the absorption coefficient $\alpha(\lambda)$ includes the absorption of a phonon α_a and emission of the phonon α_e. $\alpha(\lambda)$ is given by:

$$\alpha = \alpha_a + \alpha_e \qquad (2.15)$$

Thus, if the transition electron absorbs a phonon, the absorption coefficient α_a is calculated as:

$$\alpha_a = B\left(h\nu - E_g + E_p\right)^2 \qquad (2.16)$$

where $h\nu > E_g - E_p$, and B is a constant that can be determined from the materials properties and temperature,

If the transition process involves a phonon emission, then the absorption coefficient is

$$\alpha_e = C\left(h\nu - E_g - E_p\right)^2 \qquad (2.17)$$

where $h\nu > E_g + E_p$, and the value of the constant C depends on the materials.

2.4.2 EMISSION PROCESSES

The creation of an electron-hole pair in the transition process results from the absorption of photons. In the emission process, the formed electron-hole pair recombines and hence a photon is emitted. Therefore, the absorption phenomenon is the inverse of the emission process. Emission of the photon can be radiative, where the electron in a high energy level transit to a lower energy level. The released quantized energy is given by the difference in energy between the two levels, therefore the radiated electromagnetic wave keeps the momentum conserved. The following section illustrates some of the important radiative transitions in semiconductors.

i) BAND-TO-BAND TRANSITIONS

In direct bandgap semiconductor, a band-to-band recombination transition can occur such that the thermalisation of a free electron in the conduction band and a free hole in the valence band results in their full recombination. The radiative recombination of the electron-hole is of high probability in direct bandgap semiconductor. One of the strong light emitters is GaAs compound which has a direct gap and is usually used in light emitting diodes (LEDs).

Indirect band-to-band transitions can occur from all occupied states in the conduction band to all empty states in the valence band. However, these can only occur if the momentum is conserved. In the occurrence of this transition phonons are emitted. Indirect semiconductors processes are non-radiative and therefore, the probability of radiative transition in these semiconductors is small.

ii) FREE EXCITON EMISSION

Excitons are quasi particles that are formed by the binding of free electrons and holes under Coulombic interaction. These quasi particles have the ability to move freely through the crys-

tal as excitons do not form any localized states. The quasi energy of an exciton is a combination of two energy forms, the translational kinetic energy and Coulombic interaction energy. Excitons are part of radiative recombination process, where excitons are annihilated thus the momentum is reduced by an amount equal to the momentum of the emitted excitons. In direct gap materials, the emitted photon through this process is given by the energy of exciton E_x as [13]:

$$h\nu \approx E_g - E_x \qquad (2.18)$$

While in the indirect bandgap materials, the energy of the emitted photon in the free exciton radiative recombination is given by:

$$h\nu \approx E_g - E_x - E_p \qquad (2.19)$$

iii) BOUND-EXCITON EMISSION

Another form of emission could result from the interaction of impurity atoms with an exciton. The atom attracts the exciton via van der Waals interaction, which results in reducing the exciton energy [14]. Photons are emitted as a result of this energy variation. If the semiconductor is doped with neutral impurities, then the probability of forming a bound-exciton emission is high as these impurities are efficient in trapping excitons. This type of emission produces a photon with an energy lower than the photon emitted from free excitons.

The bound-exciton can form a number of complexes with impurities such as: (D^o, X) is an exciton (X) bounded to neutral donor (D^o), (A^o, X) is a bound-exciton to neutral accepter (A^o), (D^+, X) is an exciton bounded to ionized donor (D^+), and (A^-, X) bounded to ionized accepter (A^-) [15].

iv) DONOR-ACCEPTOR PAIR TRANSITIONS

If donors and acceptors both exist in a semiconductor, it is known as compensated semiconductor. In such type, some donor electrons are captured by acceptors, thus compensated. Hence, compensated semiconductor contains both ionized-donors (D^+) and ionized-acceptors (A^-).

Through optical excitation, electrons can be transferred to conduction band while holes are created in the valence band. Ionized-donors (D^+) and ionized-acceptors (A^-) can trap those charge carriers, resulting in the formation of neutral donor (D^o) and acceptor (A^o). If the material is restoring its equilibrium, neutral-donors electrons are radiatively recombined with neutral acceptors holes, thus allowing donor-acceptor pair (DAP) transition. This process can be demonstrated by:

$$D^0 + A^0 \rightarrow h\nu + D^+ + A^- \qquad (2.20)$$

where the emitted photon energy is expressed as:

$$h\nu = E_g - (E_A + E_D) + \frac{q^2}{\varepsilon r_{da}} \qquad (2.21)$$

where E_g is the bandgap energy, E_A is the acceptor binding energy and E_D is the donor binding energy. Coloumbic interaction is given by $\frac{q^2}{\varepsilon r_{da}}$ between ionized donors and acceptors with an r_{da} distance from each other. The r_{da} is a discrete radii when the acceptor and donor are substitutional. The dielectric constant of the material is ε. If the donor and acceptor are far apart such that r_{da} is very large, then the Coulombic interaction is small and can be neglected. Therefore, the energy of the emitted photon becomes:

$$h\nu = E_g - (E_A + E_D) \qquad (2.22)$$

v) FREE -TO- BOUND TRANSITIONS

At high temperatures, band-to-band transition is of higher probability as surface donors and acceptors are ionised. On the other hand, impurities' charge carriers are frozen at relatively low temperatures. Trapped holes on acceptors can be accumulated with free electrons due to

photon excitation. Such recombination can be radiative and in some cases non-radiative. This type of transition is called free-to-bound transition, involving the emission of a photon with energy:

$$h\nu \approx E_g - E_A - E_p \qquad (2.23)$$

where $\boldsymbol{E_A}$ is the acceptor level energy and $\boldsymbol{E_p}$ is the released phonon energy in the crystal to conserve the momentum.

2.5 CLASSIFICATION OF DEFECTS

A perfect crystalline structure has identical periodic arrangement of repeated unit cells along the crystal orientation. Such crystals are considered as ideal [16-17]. However, practically there are a number of defects existing in many forms such as point, complexes, and extended defects. The following section highlights the most common defects in details.

2.5.1 POINT DEFECTS

A point defect refers to a disorder caused by a single atom, which is placed in an irregular site in the lattice structure. Points defects have zero dimension, thus the interruption of the crystal structure caused by these defects is at isolated sites. This type of defect can be present in different forms such as vacancy, substitutional, interstitial and antisite impurities. If an atom is missing from a lattice site in the crystal, a vacancy defect is created as shown in Fig 2.11 (a). In some cases, one of the basis atoms of a certain crystal structure is replaced by a foreign atom impurity. This form of defect is known as substitutional defect, where an impurity atom is placed in a lattice site in the host semiconductor (Fig 2.11 (b)). If one of the host atoms is substituted by another host atom, this kind of substitutional defects is called an antisite defect. For example, Fig 2.11 (c) shows an antisite defect in GaAs semiconductor, where one As atom is substituted by one Ga atom [As antisite (Ga_{As})]. If the atoms are reversed such that As occupies a Ga site then a Ga antisite (As_{Ga}) is created.

Another type of point defects is interstitial impurity shown in Fig 2.11 (d). This defect is generated by an atom occupying the space between two atomic sites. If the atom is of the same type as the host material atoms, then the defect is called self-interstitial. However, if the interstitial atom is foreign from the regular crystal, the defect is known as foreign-interstitial.

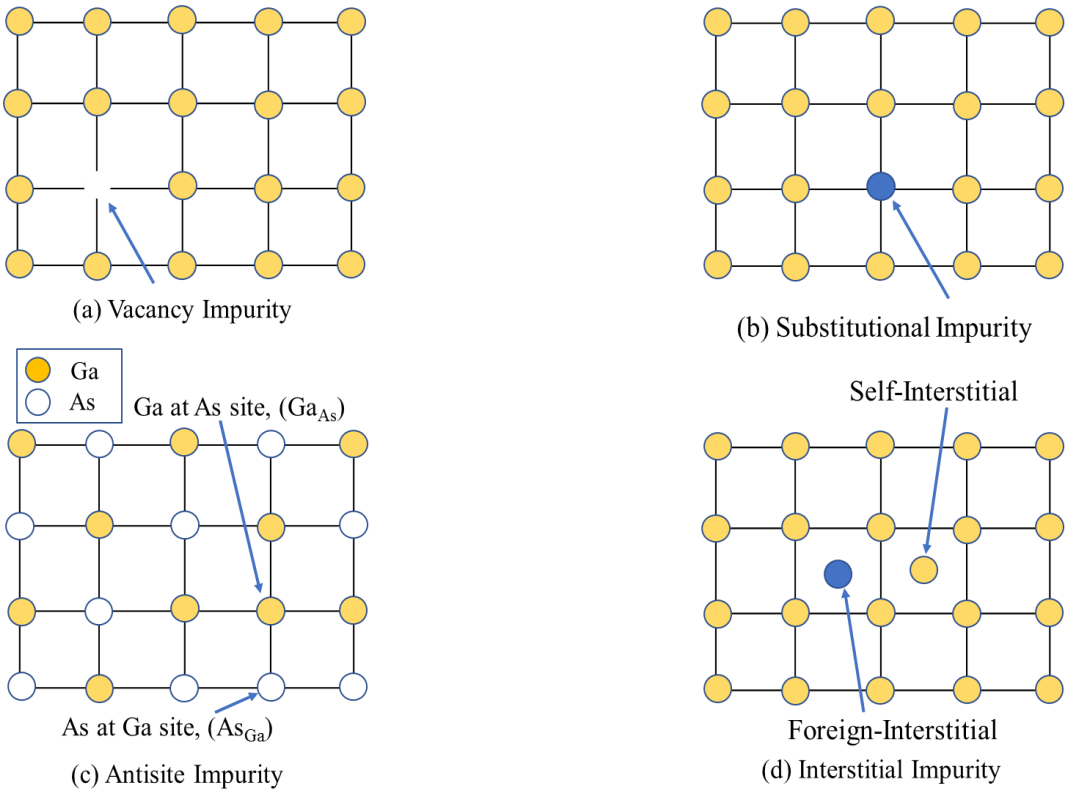


Fig. 2.11. Illustration of different forms of point defects in crystalline semiconductors: **(a)** Vacancy impurity; **(b)** Substitutional impurity; **(c)** Antisite impurity and **(d)** Interstitial impurity.

2.5.2 COMPLEXES OF POINT DEFECTS

Complexes of point defects can occur when more than one point defect are bounded to each other in a way similar to bounded atoms in molecules. If more than one point defect is introduced in the crystal, then these defects can interact and produce pairs of complex defects. If the complex point defect is produced by pairing of two interstitials atoms, the defect is called split-interstitials defect which is illustrated in Fig 2.12 (a). The split-interstitial defect can be the product of two interstitial atoms of the same host material

forming a pair, or two impurity interstitials atoms pair. A complex point defect can also be created by vacancy defects in the crystal structure as shown in Fig 2.12 (b). Many kinds of complexes can be formed, for example if two vacancies form a pair, then the defect is called Di-vacancy. If the pair is formed by self-interstitial atoms, the defect is then called Frenkel defect. Furthermore, if the pair is produced by the interaction of foreign-interstitial, then the formed complex defect is called vacancy-impurity complex. In addition, a complex pair can be formed by vacancies and interstitial atoms producing a split vacancy. Another kind of complex defect emerges from two point defects where one is substitutional impurity atom and the other is an interstitial impurity atom forming impurity-pair defect as shown in Fig 2.12 (c).

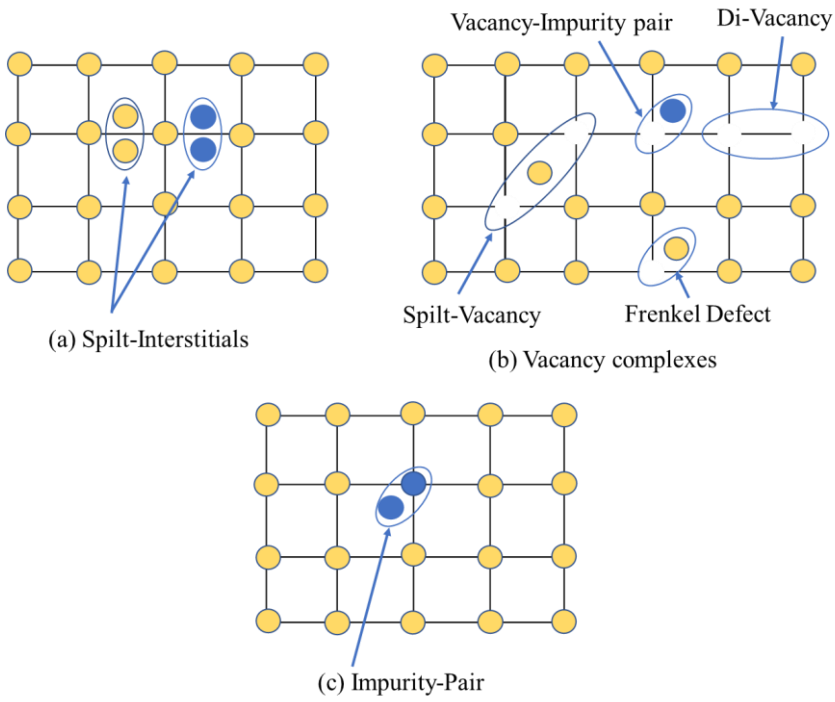


Fig. 2.12. Illustration of different forms of complex defects: **(a)** spilt-interstitials, **(b)** vacancy complexes, and **(c)** complexes of impurity-pair.

2.5.3 LINEAR DEFECTS

Linear defects refer to a line of atoms which are dislocated from their original positions in the crystal. This type of defect is one dimensional, and can be classified as edge dislocation and

screw dislocation. Fig 2.13 (a) illustrates the edge dislocation which is formed by insertion of a half plane of atoms to the lattice forcing a distortion in the nearby atoms. On the other hand, the screw dislocation is shown in Fig 2.13 (b), where a shift is applied to one part of the crystal lattice only.

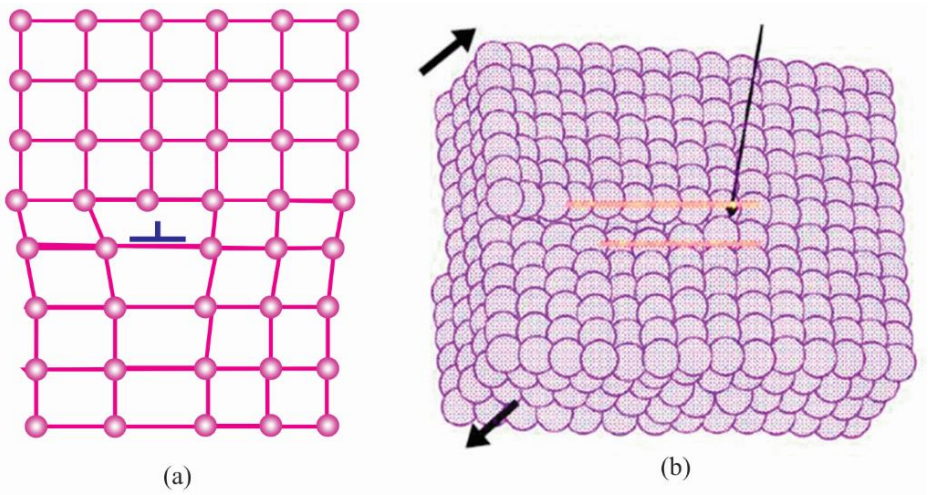


Fig. 2.13. Illustration of different forms of linear defects: **(a)** edge dislocations and **(b)** screw dislocations.

2.6 DEFECTS AND THEIR CARRIER KINETICS

2.6.1 SHALLOW LEVELS AND DEEP LEVELS DEFECTS

The creation of defects in a material is associated with an energy change introduced to the bandgap of the host material. This change in energy can be used to classify defects. If the defects are located near the valence band or the conduction band, then the defects represent impurities which are shallow levels impurities as shown in Fig 2.14. Although these defects are known as dopant impurities, they actually include two kinds, namely shallow donor levels for atoms donating electrons to the conduction band (E_C) and shallow acceptor levels for atoms donating holes to the valence band (E_V) [18]. Shallow levels basically have ionisation energy of 5-10 meV, which is considerably low. Hence, shallow levels can be ionised at room temperature, and therefore they contribute to increasing the conductivity of semiconductors.

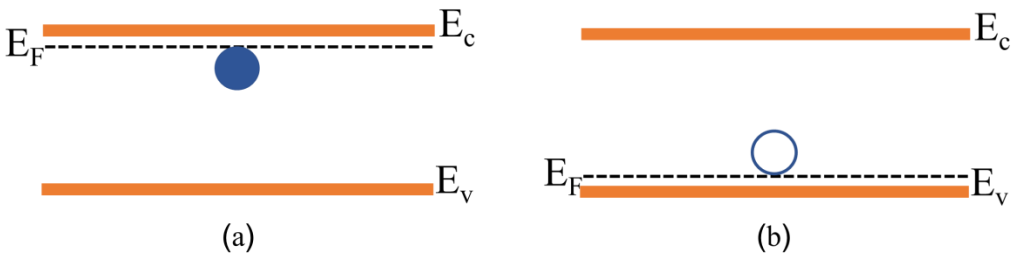


Fig. 2.14. Schematic diagram of **(a)** shallow donor level, and **(b)** shallow acceptor level. E_c, E_v and E_F represent conduction band energy, valence band energy and Fermi level, respectively.

On the contrary to the shallow level defects, deep level defects are formed away from the edge of the bandgap (Fig. 2.15). Deep levels are considered to have energies larger than 100 meV and they are known as recombination-generation centres. The presence of deep level impurities could affect the electrical and optical properties of semiconductors. The conduction mechanism involving impurities levels are discussed in the next section.

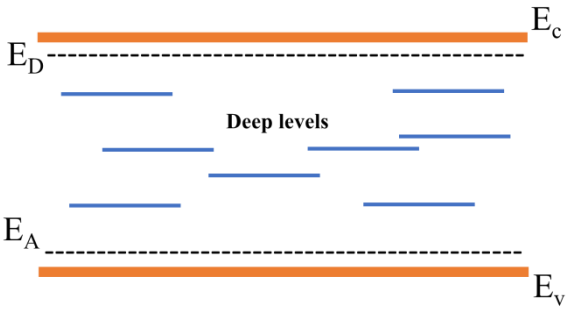


Fig. 2.15. Schematic diagram of deep level defects in semiconductors. E_D and E_A represent shallow donor level and shallow acceptor level, respectively.

2.6.2 SHOCLEY-READ-HALL THEORY

Once an electron occupies a vacant energy state, a number of recombination phenomena appear in the covalent bond. For an example, generation of an electron-hole pair is a result of an electron with an energy high enough to become free from the covalent bond, resulting in a free hole in the valence. The rates of generation and recombination processes are balanced at

thermodynamic equilibrium where the concentration of holes and electrons is constant. This balance is affected by external sources of energies such as incident light which increases the carriers' concentration leading to unequal generation and recombination processes. Such a system is known to be in non-equilibrium [19].

Understanding the charge carriers' emission and capture rates at equilibrium assists in determining the occupancy of recombination-generation centres (G-R centres). A defect with an energy E_T in the bandgap provides the possibility of four sub-processes as described in the following [19]:

(i) Electron capture: an electron from the conduction band is captured by an empty trap with an electron capture coefficient c_n (Fig. 2.16 (a)).

(ii) Electron emission: a trapped electron is retransferred from level E_T to the conduction band (Fig. 2.16 (b)) where e_n is the electron emission rate.

(iii) Hole capture: a hole from the valence band is captured by a trapped electron providing a hole capture coefficient c_p (Fig. 2.16 (c)).

(iv) Hole emission: a hole is emitted by an empty trap from level E_T to the valence band (one of the valence electrons is trapped in the conduction band leaving a hole in the valence band) as shown in Fig. 2.16 (d) where e_p is the hole emission rate.

In Fig 2.16 n and p are the electron and hole density, respectively, p_T is a G-R centre occupied by a hole, and n_T is a G-R centre occupied by an electron.

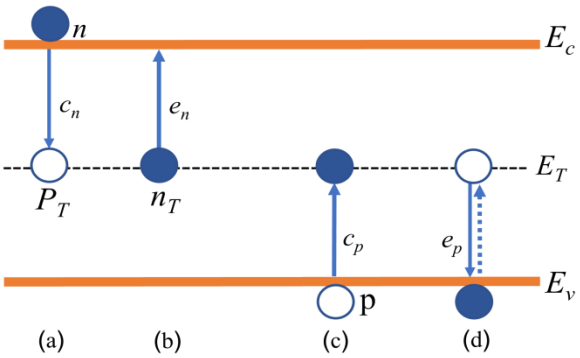


Fig. 2.16. Schematic diagram of capture and emission processes: **(a)** capture of electron **(b)** emission of electron **(c)** capture of hole and **(d)** emission of hole.

For a donor G-R centre, the state p_T holds a positive charge and the state n_T is neutral. However, in an acceptor G-R centre, p_T becomes neutral and the state n_T is negatively charged. G-R centres are occupied by both electrons n_T and holes p_T, with a total density N_T given by:

$$N_T = n_T + p_T \tag{2.24}$$

The density of electrons in the conduction band is given by n and the density of holes in the valence band is p, where their states in the G-R centers are given by n_T and p_T, respectively. When an electron or hole is created by a center or recombine in a center the densities of electrons in conduction band and holes in valence band (n) and (p), respectively, and charges states of the centers n_T and p_T change with time. The rate of change with time of the electron density for instance is expressed by:

$$\frac{d_n}{d_t}|_{G-R} = (b) - (a) = e_n n_T - c_n n p_T \tag{2.25}$$

The number of electrons emitted per second by the G-R centre to the conduction band is referred to as the emission rate e_n. The concentration of the trap occupied by electrons is given by n_T. From equation (2.25), it can be evident that the only parameters affecting the electron emission are e_n and n_T. Also from this equation, it is obvious that the electron capture pro-

cess depends on the presence of electrons in the conduction band n, the electron capture rate c_n, and the concentration of the traps that are occupied by holes p_T.

In a similar way to equation (2.25), the change in holes density per time is given by [19]:

$$\frac{d_p}{d_t}|_{G-R} = (d) - (c) = e_p p_T - c_p p n_T \quad (2.26)$$

The coefficient of the capture process of electron c_n is affected by the electron thermal velocity υ_{th} and the capture cross-section σ_n of electron capture by G-R centre. This dependence is expressed by:

$$c_n = \upsilon_{th}\sigma_n \quad (2.27)$$

2.7 GENERAL PROPERTIES OF SELECTED SEMICONDUCTOR MATERIALS

This following section reviews some of the properties of semiconductors which are investigated in this thesis.

2.7.1 GaP

Gallium phosphide is a III-V semiconductor compound widely known for its potential and promising applications due to its wide bandgap and thermal stability. III-V compounds are formed by the combination of an atom from group III (Ga) and an atom from group V (P) in the periodic table. GaP is commercially promoted for its important applications in optoelectronics and electroluminescent devices. The energy bandgap structure of GaP is shown in Fig. 2.17. The atomic configuration outside the core of gallium and phosphorus atoms is respectively (s^2p^1 and s^2p^3) showing that Ga has 3 electrons in the outer shell while P has 5 electrons. If Ga and P are combined, then binding can be formed by an average of four valence electrons per atom. Thus, allowing three different binding possibilities being (i) covalent, (ii) ionic and (iii) neutral.

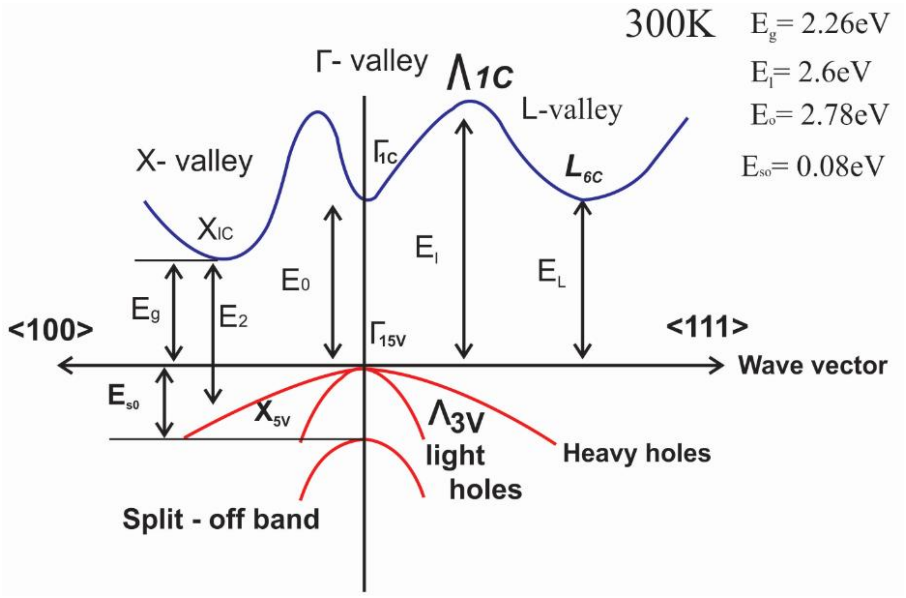


Fig. 2.17. Energy bandgap structure of GaP. E_{SO}, E_X, E_L are energy of spin-orbital splitting, energy of X-valley and energy of L-valley, respectively [20].

For GaP to form covalent bonding, four phosphorus atoms contribute with an electron each to gallium atom, which has four valence electrons available for bonding. The produced bonds are sp^3 hybrid and tetrahedral bond. If gallium donates 3 electrons to phosphorus, the two atoms become ionised as Ga^{+3} and P^{3-}, allowing the formation of pure ionic bond. The ions of Ga and P have two symmetrical closed shells configurations which are bonded by electrostatic forces.

Ionic formation of a material is determined by the atomic properties such as electronegativity. This feature allows atoms to attract, thus transfer charges depending on the electronegativity of the two atoms. If the atoms retain their electrons while bonding, they form a neutral bond with no difference in charge between the gallium and phosphorus.

Indirect transitions processes refer to transitions that occur between indirect band-to-band. GaP is found to be an appropriate material to study the optical processes occurring indirect bandgap semiconductors. GaP compound is an indirect bandgap where the gap size is dependent on the temperature such as at 0 K E_g = 2.338 eV, while at 300 K E_g = 2.26 eV.

Table 2.2. Some important properties of intrinsic GaP at 300K. h_h and l_h represent heavy hole and light hole, respectively [21].

Parameter	GaP
Crystal Structure	Zincblende
Lattice constant (Å)	5.4505
Crystal density (g/cm3)	4.14
Energy bandgap (eV)	2.26
Band type	Indirect
Electron effective mass	$1.12m_o$
Hole effective mass	$0.79m_o(h_h)$ $0.14m_o(l_h)$
Dielectric constant (static)	11.1
Electron affinity (eV)	3.8

2.7.2 GaAs

Gallium arsenide (GaAs), a III-V compound, is one of the most known materials and the next important semiconductor after Si. The properties of this compound were understood 30 years after it was first demonstrated by Goldschmidt in 1920. This compound has a direct bandgap as shown in Fig. 2.18, where the conduction and the valence bands vertices are at $k = 0$. Therefore, electrons transfer between the conduction band and the valence band with conservation of momentum. GaAs has many applications in optoelectronic devices because of its direct bandgap.

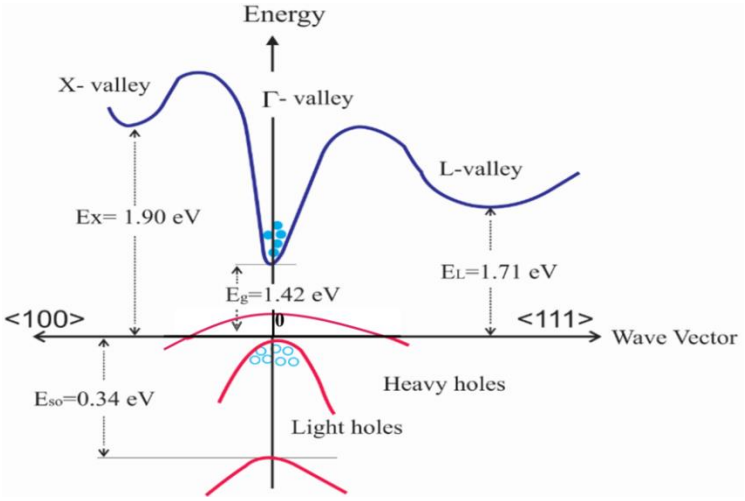


Fig. 2.18. Energy band diagram of GaAs. E_{SO}, E_X, E_L are energy of spin-orbital splitting, energy of X-valley and energy of L-valley, respectively.

In comparison with Si, GaAs had a direct bandgap where Si has an indirect bandgap. Additionally, GaAs has a resistivity of around 10^8 Ω-cm, which higher than Si resistivity of ~ 6.4×10^2 Ω-cm. As a result, GaAs has less parasitic capacitive effects which make it suitable for the use in high frequency integrated circuits as a semi-insulating substrate. The energy gap of GaAs is larger than Si, and thus the compound is stable for high temperature applications. Some important intrinsic GaAs properties at room temperature (300 K) are provided in Table 2.3.

Table 2.3. Some important properties of intrinsic GaAs at 300K. h_h and l_h represent heavy hole and light hole, respectively, and m_0 is the effective mass of electron at rest [21].

Parameter	GaAs
Crystal Structure	Zincblende
Lattice constant (Å)	5.6533
Crystal density (g/cm3)	5.360
Energy band gap (eV)	1.42
Band type	Direct
Electron effective mass	0.063 m_o
Hole effective mass	0.51 m_o (h_h) 0.082 m_o (l_h)
Dielectric constant (static)	12.85
Electron affinity (eV)	4.07

2.7.3 DILUTE GaPN

In 1990s the first epitaxial growth of dilute nitride semiconductor materials was demonstrated [22-23]. These materials have uncommon physical properties which make them acceptable for use in technological applications such as optical amplifiers, solar cells, LEDs, laser diodes [24-25].

Among these materials, GaPN is an interesting material for pseudomorphic integration of photonics on silicon. The gallium phosphide (GaP) has the smallest lattice mismatch to silicon among binary III–V compound semiconductors (0.37% at room temperature). In addition, the residual strain due to this lattice mismatch can be compensated by the

incorporation of a few per cent of nitrogen in GaP [26]. Particularly, lattice-matching with Si can be achieved by adding a 2.2% nitrogen into GaP(N). In fact, the doping of GaP semiconductor, which is an indirect bandgap semiconductor (2.26 eV), with nitrogen (N) isoelectronic impurity has been widely used in the past to improve its radiative efficiency, and thus, making it suitable for optoelectronic applications. It has been shown that the incorporation of nitrogen in GaP leads to an extremely large band-gap bowing and N-induced transformation from an indirect to a pseudo-direct bandgap which is less than that of GaP by approximately 0.1 eV with one percent of nitrogen. This type of transition in GaPN was previously explained by the band anticrossing model (BAC model), due to the interaction between heavily localized N states and extended states of the conduction band minimum that splits the conduction band into two subbands and leads to a reduction of its fundamental band gap [27]. Kent and Zunger [28] have pointed out that all the localized levels which are related to isolated N, N-N pairs, N triplets or N chains are located below the conduction band minimum (CBM) of GaP. In other words, the incorporation of N breaks the translational symmetry of the host crystal perturbing the conduction states of the host crystal at the Γ, L and X points. The degradation of the conduction band minimum (CBM) is described by repulsion between these perturbed host states. With large N content, the interaction between the CBM and the deepest cluster states becomes stronger; therefore the wavefunction results in a mix of localized and further delocalized levels.

2.7.3.1 THE BAND ANTICROSSING (BAC) MODEL

In order to understand the results of adding N into GaP with the expected bandgap shrinking due to the N incorporation, the Band Anti Crossing (BAC) model [29] is used. The BAC model is an oversimplified description of the band structure changes induced by isovalent N atom in a III-V host matrix. However, it predicts accurately bandgap energies and gives reasonable explanation of increase of electron effective mass for low N quantities. In GaPN, the

N level lies about 600 meV below the Γ minimum of the conduction band. The interaction between these two levels leads to the formation of a Γ-like band and a pseudo-direct band gap transition. As for GaAsN, two subbands emerge [30 - 31] and their energies can be given by:

$$E_{\pm}^{GaPN} = (1/2)\left[\left(E_{M\Gamma}^{GaP}(k) + E_N\right) \pm \sqrt{\left(E_{M\Gamma}^{GaP}(k) = E_N\right)^2 + 4xC_{NM}^{GaP^2}}\right] \qquad (2.\ 27)$$

with $E_N(GaP) = 2.18eV$ and $C_{NM}^{GaP} = 3.05eV$. The GaP conduction band minima values are: $E_G^{\Gamma} = 2.78eV$, $E_G^{X} = 2.26eV$ and $E_G^{L} = 2.60eV$.

Following the previous equation (2. 27), the conduction band minimum (CBM) reaches E- =2.05 *eV*, which corresponds to a reduction of the band gap $\Delta E_C = E_G^X(GaP) - E_G^{\Gamma}(GaPN) = 0.216eV$.

These results are in very good agreement with the observed PL peak position at room temperature confirming the successful incorporation of N in GaP layers. However, the new fundamental conduction states are strongly localized, the projection of the wavefunction on the Γ states being of the order of 10%. When the nitrogen fraction is increased, the Γ character is more pronounced, reaching a value of about 25% for 3% of nitrogen. However, the strong localized character of this ternary makes it questionable for high efficiency light emitting devices. When GaPN is pseudomorphically grown on GaP or Si substrates, it experiences a slight tensile strain, leading to a reduction of the band gap energy and a splitting of heavy/light hole levels.

2.7.4 DILUTE GaAsN

In the case of isovalent impurity atoms substitute a host atom of the same valency, semiconductor alloys are created that leads to produce weak perturbations in the host crystal band structure. When the isovalent impurity atoms and the host atoms have different

properties, the host band structure can be changed significantly such as atomic radii, electronegativity, etc.

For example, GaAs band structure changes partially when an impurity atom such as phosphorus (P) substitutes As or indium (In) substitutes Ga in GaAs. However, when nitrogen (N) atoms are incorporated into GaAs, the band structure of GaAs changes significantly due to the formation of single GaAsN crystal. The energy gap of GaAs reduces by approximately 0.1eV for each percent of N in the alloy. In fact a significant local potential is generated due to the large differences in atom size and electronegativity of N atoms and host anions [32]. Thus, this creates N-related localized states near the conduction band edge which leads to the reduction of the band gap and other associated effects. The band anticrossing model (BAC) has been introduced by Shan *et al*. [29] which has been used extensively to interpret the characteristics of GaAsN. This model is described briefly below.

2.7.4.1 THE BAND ANTICROSSING (BAC) MODEL

The interaction between the localized state of nitrogen and the extended conduction band states of the host semiconductor matrix is used in the BAC model [29-33] to explain the electronic structure of N-alloys. This interaction leads the conduction band to split into the E_- and E_+ bands, and a decrease of the fundamental bandgap which is dependent on the nitrogen composition.

Fig. 2.19 demonstrates the anticrossing behaviour between the N-related state (E_N) and conduction band edge (E_{CB}) of GaAs. The N related states are spread over the reciprocal space with constant energy because they have localised nature. E_N and E_{CB} energy states are shown in Fig. 2.19 by dotted lines. According to the BAC model, the energy of these two states resulting from their interaction is given by:

$$E_{\pm} = \frac{1}{2}\left(E_N + E_{CB} \pm \sqrt{(E_N - E_{CB})^2 + 4V_{CB,N}^2} \right) \qquad (2.\ 28)$$

where $V_{CB,N}$ is the coupling parameter describing the strength of interaction between the localized N states and extended CB states which is given by:

$$V_{CB,N} = Cx^{1/2} \qquad (2.\ 29)$$

where C is a constant whose value depends on the semiconductor host and x is the nitrogen fraction in the alloy.

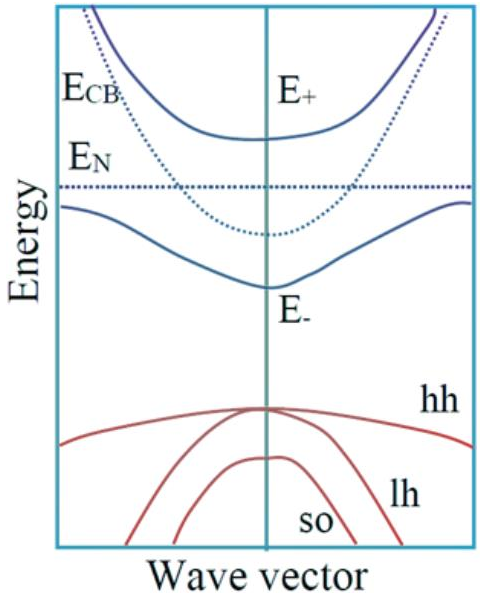


Fig. 2.19. Schematic diagram of band anticrossing model of GaAsN.

The BAC model is a non-ideal model as it does not consider the broadening of the energy levels or splitting of L-conduction band extrema, and only describes the interaction between a single isovalent impurity level and the conduction band edge. In spite of all its shortcomings, the BAC model has been a popular and most cited model in dilute nitride literature because of its simplicity and satisfactory fit for many characteristics of the alloy.

2.7.4.2 SOME IMPORTANT PROPERTIES OF GaAsN

Dilute nitride GaAsN has shown unusual properties such as a large band gap reduction, enhancement of the effective mass, low charge carrier mobility, and small lifetime of the charge carriers. Some of these properties are illustrated below.

Considerable studies of dilute nitrides alloys have reported a different group of values of the effective mass of the electron ranging from $m_e^* \sim 0.8m_o$ to $0.1m_o$ (m_o is the mass of the electron at rest). In dilute nitride materials the increased effective mass (GaAs: $m_e^* \sim 0.0663m_o$) and large alloy scattering lead to the degradation of mobility of electrons and holes. For example, Ptak *et al.* [34] noted a significant degradation of hole mobility in both molecular beam epitaxy (MBE) and metal organic chemical vapour deposition (MOCVD) grown GaAsN samples. In a similar way, a reduction in electron mobility is observed and is correlated to the increase of the electron effective mass [35].

The lifetime of the charge carriers in light emitting devices is considered to be a significant parameter. In dilute nitride materials, carrier lifetimes have smaller values because of the high defect densities. Ahrenkiel *et al.* [36] have observed that at room temperature with one percent of nitrogen in GaAsN, the lifetime of the carriers is less than 1ns.

Undoped dilute nitrides materials grown by MBE or by MOCVD are in general p-type [37]. However, Kurtz *et al*. [38] have noted the conversion of the conductivity type when they annealed their samples. They have attributed this transformation of conductivity type to nitrogen-hydrogen defects which were formed after annealing.

2.7.5 S-SHAPE IN DILUTE NITRIDES

One of the most common behaviour that has been observed while studying the bandgap of dilute III-V-N is called S-shape [39]. For example, by analysing the temperature dependence of photoluminescence (PL) measurements, it was observed that at low temperatures the bandgap energy decreases and then increases as the temperature increases. At high temperatures the bandgap decreased again. [40]. This S-shape behaviour can be explained as follows. Firstly, at low temperatures the electron-hole pairs (excitons) of higher energy are gradually redistributed into low energy, which causes a decrease in the PL peak energy. Secondly, when the temperature is increased, more thermal energy is transferred to excitons which are

then activated into delocalized states, resulting in a rapid increase in bandgap energy. Finally, all excitons are delocalized and the PL peak energy is reduced as a consequence of the bandgap bowing with temperature [41].

2.8 DEFECTS IN SELECTED SEMICONDUCTORS

Most of modern electronic devices are based on the use of semiconductor materials which leads to a significant development in the semiconductors industries. The major difficulties in these industries are to fabricate perfect crystals. In fact, all crystals have impurities and defects when foreign atoms have the ability to enter the crystal structure or/and some atoms can be missing in crystal structures or lattices [18]. In general, the presence of these impurities and defects in devices affects their performance by changing their electrical and optical properties. Therefore, it is essential to identify and characterise the defects created during growth and processing of these materials and devices to understand their roles that could affect the performance of these devices [19]. In the following section a brief literature review of defects in GaAs, GaAsN, GaP and GaPN materials will be presented.

2.8.1 DEFECTS IN GaAs

Gallium arsenide compound is a III-V semiconductor which has gained huge interest for its properties that allow applications in electronics and optoelectronics devices. During the growth of GaAs compound different kinds of native defects can be formed in the structure of the compound, such as vacancies, interstitials, and antisite defects. The main intrinsic defect in GaAs is *EL2*, which is associated with energy level in the range of 0.70 eV to 0.85 eV [42]. This defect is usually present with a concentration of ~ 10^{16} cm^{-3} in bulks and ~ 10^{14} cm^{-3} in epitaxially grown materials [43]. The formation of *EL2* defect corresponds to isolated Arsenic antisite defect (As_{Ga}) [44-45] or complex defect including As_{Ga} and arsenic interstitial [46-47]. Another common defect in GaAs is *EL3* trap, which has an energy level of ~0.575 eV [48]. Substituting oxygen on arsenic sites (oc-O_{As}) causes off-centre complexes,

which are usually responsible of the occurrence of such traps [49]. In addition, *EL5* and *EL6* defects are found in GaAs with energy levels of ~0.43 eV and ~0.35 eV, respectively [48]. The *EL5* defect is related to complexes with As interstitials- Ga vacancies (As_iV_{Ga}) [50], while *EL6* is associated with complexes involving arsenic antisite defect (As_{Ga}) and arsenic vacancy (V_{As}) [51]. Moreover, *EL10* trap defect can be formed in GaAs with an energy around ~0.18eV [48]. This low energy trap is assigned to an arsenic vacancy (V_{As}) complex defect involving an impurity [52-53].

2.8.2 DEFECTS IN DILUTES GaAsN

If nitrogen atoms are incorporated into the GaAs crystal, they introduce a general perturbation in the electronic band structure. In the crystalline structure of GaAs, when As atoms are substituted by nitrogen atoms they create localised energy states at the edge of the conduction band [54]. As a result, the bandgap of the semiconductors is reduced significantly [55]. Such reduction changes the electrical and optical properties of the material [56]. On the other hand, N atoms in non-substitutional sites in the lattice of GaAs create defects which degrade the quality of the crystal, and consequently resulting in a reduction of the carrier lifetime and low optical efficiency [57-58].

In this dilute nitride semiconductor, many types of point defects can be formed such as N-interstitials, As-antisites and Ga-vacancies as demonstrated by a number of studies. For example, Zhang and Wei [59] reported the presence of substitutional N, N–N spilt interstitial and Ga vacancies through thermodynamic calculations. These defects are likely to occur in GaAsN materials grown by MBE and MOVPE [60]. Fig 2.20 demonstrates such types of defects. It has been reported by T. Ahlgren *et al.* [61] that as the composition of N increases in GaAsN, the N substitutional concentration increases. However, they have shown that the N interstitials concentration did not change (2.3×10^{19} cm^{-3}) with the increase of N contents

from 0.7% to 3%. They determined that these non-radiative recombination centers could have a major degrading effect on the optical efficiency of nitride materials.

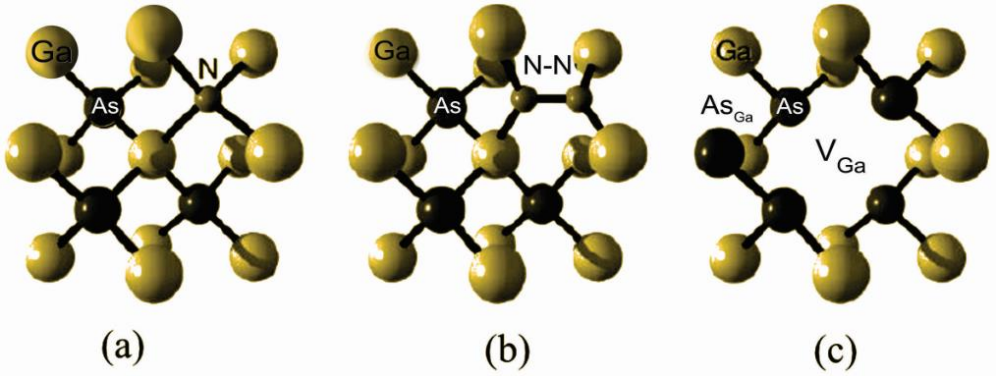


Fig. 2.20. Configurations of nitrogen in GaAsN; **(a)** substitutional N; **(b)** N–N split interstitial; **(c)** Ga vacancy and As antisite (after Zhang and Wei [59]).

Deep Level Transient Spectroscopy (DLTS) technique is usually implemented to characterise defects in GaAsN, in particular defects that are electrically active. For example, P. Krispin *et al.* [62] deployed DLTS measurements in MBE grown p-type GaAsN samples, and reported the existence of HK1 (0.16 eV), HK2 (0.39 eV), HK3 (0.35 eV), HK4 (0.45 – 0.55 eV) and HK5 (0.69 eV) hole traps in the samples. They demonstrated that the highest concentration of HK1 trap is at the interface of GaAsN/GaAs. They also suggested that HK2 and HK5 traps could be associated with Ga_{As} antisites (Ga on As site) observed in GaAs grown by liquid phase epitaxy (LPE). On the other hand, HK3 and HK4 were associated with copper and iron related defects, which are connected with the operation of the nitrogen plasma cell during GaAsN growth. Additionally, P. Kripsin *et al.* [63] also reported the presence of two N-related electron traps in Si-doped GaAsN samples. These traps have been assigned to (N-N) and (As-N) split interstitials having thermal activation energies of 0.8 eV and 1.1 eV, respectively, located above the valence band edge. The EL2, EL3, EL6 and EN3 defects are well-known in GaAs; the same defects were also detected in GaAsN or GaInNAs structures [64]. Optically detected magnetic resonance (ODMR) measurements [65-66] have indicated the

presence of As antisites in Ga(In)NAs alloys. Arsenic antisites (As_{Ga}) have been found to be attracted by substitutional N in GaAs, resulting in the creation of efficient non-radiative centres of (N_{As}–As_{Ga}) complex defects [67-68].

2.8.3 DEFECTS IN GaP

GaP substrate has been found to contain impurities that are very degrading for the photovoltaic (PV) properties. For example, isoelectronic nearest neighbour Zn-O pair is a defect that behaves as recombination center reducing the efficiency of GaP solar cells to 4% or below [69, 70, 71, 72, 73]. Furthermore, it has been shown that O impurities can appear even in epitaxial layers of GaP grown in a solid source MBE chamber, as a result of the phosphorus cracker temperature which is above 800°C [74]. Additionally, GaP surface has a high recombination velocity which prevents its use as a window layer as it requires to be passivated [70-75].

D. G. Thomas *et al.* [76] investigated defects in GaP. The photoluminescence signal has been observed for GaP crystals, which were grown from gallium solution at 20 K. The obtained spectra have shown several sharp lines. Such lines are mostly caused by the radiative recombination of trapped electrons and holes at donors and acceptors. Some of the lines result from excitons bound to point defects.

R. Krause et al. [77] performed positron lifetime and Hall effect measurements to identify vacancy defects in GaP. In their study, Ga vacancies have not been found, while P vacancies have always been present in as-grown material with a concentration in the order of 10^{16} cm^{-3}. The study also demonstrated that within the upper half of the bandgap there are at least two ionization levels identified as V_P^+/V_P^0 at $E_C - E_D > 400\ meV$ and V_P^0/V_P^- at $E_C = E_D = 250 \pm 30\ meV$, respectively.

2.8.4 DEFECTS IN DILUTES GaPN

Recently, systems of dilute nitride materials have gained a great interest due to the exceptional properties of such materials. One of such properties is the strong downward bowing of the bandgap if incorporated with a small percentage of nitrogen [78]. In particular, GaP:N material has been massively studied in the recent years. Such material has been usually studied as an alloy in order to determine its physical properties [79]. Nevertheless, due to the large bandgap reduction and massive bowing caused by N doping into this material, it has been considered an abnormal alloy. Typically, host semiconductors which incorporate isoelectronic impurities are considered alloys [80]. The influence of isoelectronic impurities can be neglected in the dilute limit if the impurities do not introduce bound states in the host material [81]. Nevertheless, there are a few remarkable cases where induced isoelectronic impurities produce bound states. Such bound states are either "donor-like" such as in GaP:Bi and/or "acceptor-like" as in GaP:N [82].

Nevertheless, a number of studies illustrated that such systems can be viewed in the framework of heavily doped semiconductors rather than alloys [83, 84, 85]. Accordingly, heavy doping allows the creation of an impurity band that is basically positioned under the intrinsic bandgap of the host. This induced band reduces the bandgap significantly and results in several other phenomena, for example, the semiconductor could go through the so-called Mott transition. Incorporation of N into GaP has been achievable since the early 1990's, where non-equilibrium growth techniques such as MBE allowed for much larger amounts of N to be incorporated. Baillargeon et al. [86-87] and Liu et al. [88] showed that doping GaP with about 1% N results in a large red shift of the absorption edge. The bandgap is therefore reduced which indicates the creation of a N induced impurity band in GaP. It was later shown by Xin et al. [89] that if the N concentrations exceeds 1%, then the absorption edge in GaP:N becomes similar to the energy of a direct gap semiconductor, showing the same $\sqrt{E - E_g}$ dependence. This result indicated that this material could be suitable for LED devices.

The doping range of GaP:N is relatively large being in the impurity limit range ($\sim 10^{15}$ – $20^{20} cm^3$). In addition, the material has a high-critical concentration leading to the creation of an impurity band [85]. Therefore, GaP:N is a unique system which provides an opportunity to explore the effects of the impurity band which results from heavy isoelectronic doping. In the 60's to the 80's, it was founded that N acts as an isoelectronic trap in materials such as GaP and GaAs [89, 90, 91]. In both these materials, thermodynamic calculations [92] suggested that N was insoluble. While other studies showed that in bulk crystals grown by Liquid Phase Epitaxy (LPE), it was only possible to incorporate N with doping levels less than10^{19}, which resulted in the demonstration of N induced trap levels in these semiconductors [83-85].

It has been reported [86] that at a very low-doping level ([N] $< 10^{17}\ cm^3$), only one emission line namely (*A*-line) can be observed from the exciton bound to isolated N center [86]. For higher doping levels (up to [N]$\sim 10^{19}\ cm^3$) different N-N pairs introduce a series of emission lines (NN_i lines, i=1, 2, 3 etc.) with their phonon sidebands in an energy range of 140 meV below the bandgap [89]. The deepest N-N pair bound state is NN_1, which was recently found to be present up to concentrations of [N] $\sim 1 \times 10^{20}\ cm^3$ or $x = 0.43\%$ [87, 88, 93, 94]. At a higher N concentration, no structures were observed as the spectrum was considerably broadened.

Overall, heavy N doping in GaP introduces a huge bandgap "bowing" phenomenon, redshifts in the photoluminescence, and impurity band levels in the band structure.

Further studies have reported [95-96] that several structural defects exist in dilute nitride materials such as point defects, alloys fluctuations and phase separation. Those defects are believed to be caused degradation in optical and electrical properties of GaPN-based alloys. The origins of these defects are still not fully understood, however, they are usually attributed to N composition, N clusters, P_{Ga} antisite, Ga_i interstitial and Ga_v defects [97, 98, 99].

2.8.5 EFFECTS OF RAPID THERMAL ANNEALING (RTA)

To improve the quality of the dilute nitride alloys, post-growth thermal annealing has to be monitored in order to produce materials with better optical and electrical properties [100-101]. This mandatory process allows atoms to migrate and reduces many of the defects that emerge during the growth [102, 103, 104]. For example, intrinsic point defects in GaIn(N)As and GaPN were identified as As_{Ga} antisites, N interstitials, and Ga vacancies [105-106]. Annealed dilute nitride materials show an improved PL intensity [107], higher quenching temperature and a narrower Full Width at Half Maximum (FWHM) [108-109]. In addition, a blueshift occurs in the PL signal due to modification of the electronic band structure caused by interdiffusion process, when nitrogen transit from interstitial to substitutional site, thus forming a defect [110]. The amount of such effects is highly dependent on the annealing parameters (time, temperature and atmosphere), as well as the growth conditions [111]. Past studies concerning GaInNAs(Sb)/GaAs Quantum Well (QW) materials showed that via annealing the S-shape behaviour observed in PL can be reduced with respect to temperature [112]. As mentioned previously, the S-shape emission is one of the dilute nitride properties that depends on the induced N states to the bandgap of III-V materials [113]. If the S-shape emission is reduced, then this indicates that the annealing process has successfully reduced the effect of the N localized states [114]. Therefore, the S-shape is a non-monotonous change in the PL peak energy. It is widely suggested that annealing assists in the reorganisation of N atoms in the lattice, therefore resulting in reduction of alloy fluctuations [115]. The S-shape behaviour can be eliminated by controlling the growth and annealing of the dilute nitride, thus reducing the N localized states that caused the S-shape emission in the as-grown materials.

2.9 P-N JUNCTION

A p-n junction refers to joining two materials where one is of p-type and the other is of n-type [116]. The junction is formed when electrons of the n-type flow to the p-type material and holes from the p-type to the n-type. This in turn creates a depletion region that prevents any further carrier flow from the two different sides of the junction, hence acting as a barrier. A schematic illustration of a p-n junction and its energy bands is shown in Fig 2.21 where the figure shows the change in the energy levels before and after the creation of the junction where the transitions are considered under thermal equilibrium with no application of applied bias. As the p-n junction is formed, Fermi levels of n and p sides (E_{Fn} and E_{Fp} respectively) change with respect to the conduction band energy, valence band energy and intrinsic Fermi level (E_c, E_v, and E_{Fi} respectively). The potential difference between Fermi level and intrinsic Fermi level in n-region and p-region are represented as V_n and V_p, respectively, where qV_{bi} is the built-in potential. χ_s is the electron affinity of the semiconductor material and x_n and x_p are the widths of the depletion layer regions in the *n* and *p* sides, respectively [117-118]. The Fermi level of the p-n junction is created as soon as the junction is formed, and at thermodynamic equilibrium E_F remains constant [117-119] as seen in Fig 2.21 (b). Moreover, in Fig. 2.21 (b), the n and p doped regions are considered to be uniformly doped and there is an abrupt transition between these two regions. Thus this leads to the formation of an abrupt junction (or step junction). In contrast, a linearly graded junction is formed when the doping concentration is not uniform across the p-n junction regions. Fig. 2.21 (a, b and c) illustrates three separate regions in a p-n junction, which are the quasi-neutral p and n regions (QNR) away from the metallurgical junction, and the space-charge (or depletion) region (SCR), which is occupied by ionized shallow acceptors in the p-depletion region and ionized shallow donors in the n-depletion region.

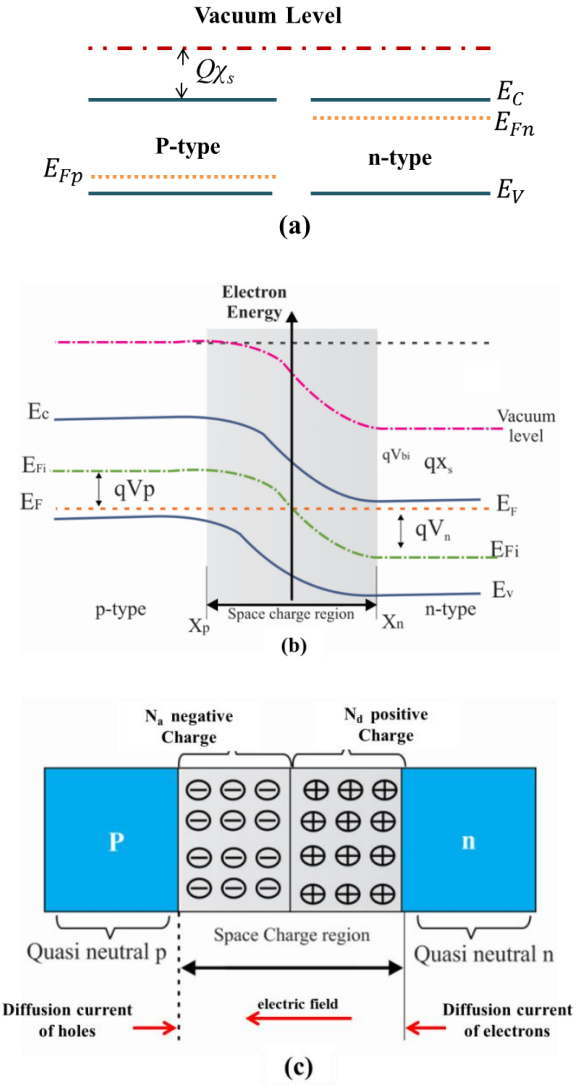


Fig. 2.21. Schematically diagram of a p-n junction: **(a)** the energy band structure of a p-type and n-type semiconductors before forming the junction **(b)** the energy band structure after the formation of the junction **(c)** p-n junction showing the depletion region (or space charge region).

2.9.1 P-N JUNCTION UNDER BIAS CONDITIONS

The equilibrium condition of a p-n junction can be disturbed by an external bias voltage, which is usually applied between p and n regions. As a result, charge carriers start flowing via the junction. The direction of the current is determined by the polarity of the applied external biases, which are either forward bias or reverse bias conditions. Applying a reverse bias voltage results in pushing the charge carriers (electrons and holes) away from the junction and thus it is difficult for them to cross the depletio n region. Fig 2.22 illustrates the changes

in the band structure of a p-n junction before and after the external bias. Fig 2.22 (a) shows Fermi energy at zero bias to be constant across the junction. If a forward bias voltage is applied across the junction as shown in (Fig 2.22 (b)) the potential barrier across the junction lowers to $(V_{bi} - V)$ and the depletion width decreases. As a result, high current flows through the junction. In this case, the Fermi level in the n side E_{Fn} is shifted down by half its value at equilibrium while the Fermi level in the p side E_{Fp} does the reverse. The application of a reverse bias voltage causes the Fermi level of the n region to be shifted lower than the Fermi level of the p region as shown in Fig 2.22 (c), hence increasing the potential barrier to $(V_{bi} + V)$. The depletion width expands and as a result the current flow through the junction becomes very small. This means in a reverse-bias condition, the current flows only by thermal effects.

By neglecting the voltage drop in p and n quasi-neutral regions and modifying the solution of the Poisson's equation at zero bias with $(V_{bi} \pm V)$ instead of V_{bi}, one can get the depletion width for abrupt junction under bias condition to be:

$$W = \left(\frac{2\varepsilon_S (N_A + N_D)}{q N_A N_D} (V_{bi} \pm V) \right)^{1/2} \qquad (2.30)$$

Reverse and forward bias conditions are indicated by the plus and minus signs, respectively.

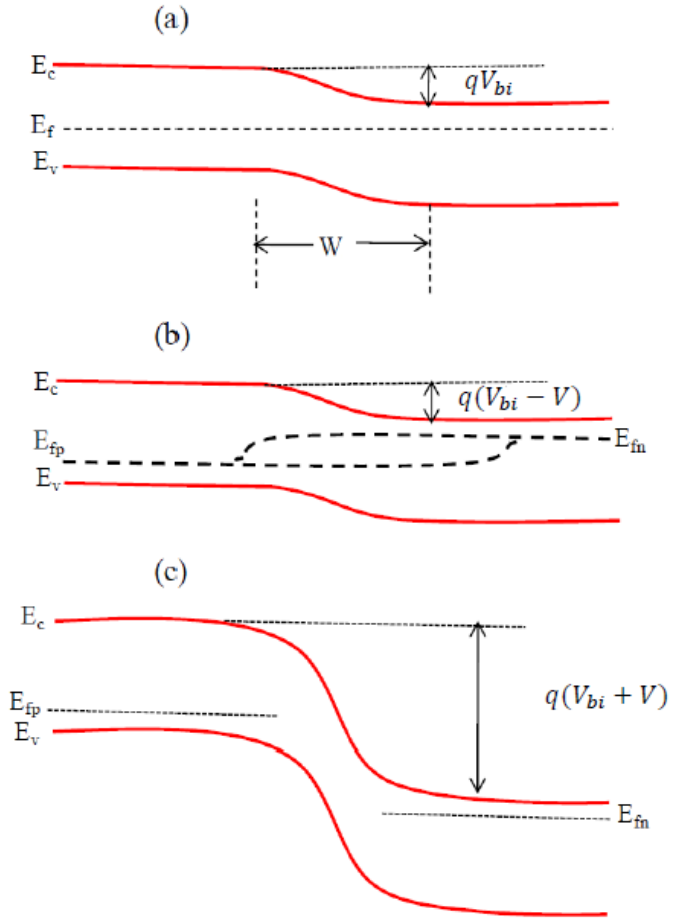


Fig. 2.22. Schematic diagram of the energy band structure of a p-n junction under **(a)** a zero-bias, **(b)** a forward bias, and **(c)** a reversed bias condition [120].

2.9.2 DEPLETION LAYER CAPACITANCE

One of the key parameters of the p-n junction is the depletion capacitance of the space charge region, which is an important parameter that helps to understand and characterize the p-n junction. The measurements of the capacitance of a device as a function of reverse-bias voltages help to determine the built-in potential of a junction. Moreover, the capacitance-voltage analysis is a standard method used to estimate the carrier density profile of a Schottky diode or p-n junction [120]. Since a p-n junction is composed of a double layer of donors (with positive charges) and acceptors (with negative charges), its related capacitance is expressed as [121]:

$$C = \frac{dQ}{dV} = \frac{d(qN_A x_p)}{dV} = \frac{d(q\, n_D x_n)}{dV} \qquad (2.31)$$

where dQ represents the charge in the depletion region and dV is the applied voltage. Moreover, this capacitance can be given as a function of the junction depletion width as:

$$C = \frac{A\varepsilon_S}{W} \tag{2.32}$$

where A the area of the junction and ε_S is the permittivity of the semiconductor. Considering $N_A \gg N_D$ and using Equations (2.31) and (2.32), the one side abrupt junction capacitance can be written as:

$$C = \frac{dQ}{dV} = \frac{A}{2}\left[\frac{2\varepsilon_S q N_D}{V_{bi} \pm V}\right]^{1/2} \tag{2.33}$$

From this equation, it is evident that as the applied reverse bias is increased, the capacitance of the diode decreases. Hence, a linear relationship can be seen in the plot of the inverse of the capacitance square, $(1/C^2)$, as a function of applied voltage, V, as illustrated in Fig. 2.23. The doping concentration of the lightly doped semiconductor is found from the slope of the line, and the x-intercept of this line (at $1/C^2 = 0$) gives the built-in potential across the junction [120-121].

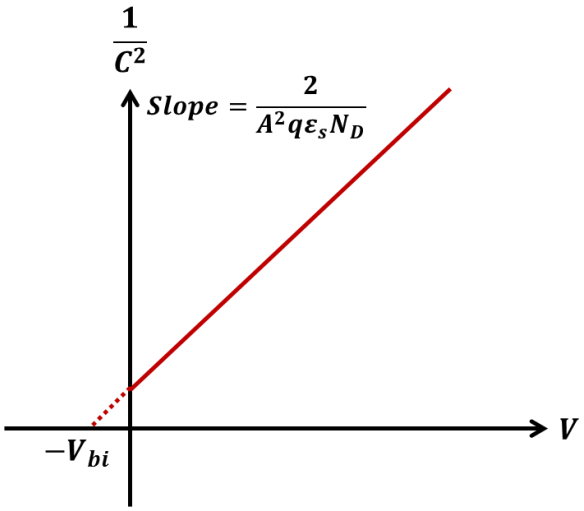


Fig. 2.23. A typical plot of $1/C^2$ versus applied reverse-bias voltage for a one step- junction diode.

2.9.3. CAPACETANCE IN P-I-N JUNCTION

For a p-i-n junction the total potential of the diode take the following form [121]:

$$\phi_n + \phi_p + \phi_u = \phi_i - V_a \tag{2.34}$$

Where V_a is the applied voltage. $\emptyset_n$, $\emptyset_p$, $\emptyset_u$ are the potential across n, p and middle of un-doped regions of the diode, which are expressed as:

$$\phi_n = \frac{qN_d x_n^2}{2\varepsilon_s}, \phi_p = \frac{qN_a x_p^2}{2\varepsilon_s} \text{ and } \phi_u = \frac{qN_a x_p d}{\varepsilon_s} \tag{2.35}$$

where:

$$qN_a x_p = qN_d x_n$$

where x_n and x_p are the deplion regions width, d is the thickness of the middle undoped re-gion. ε_s is the electric charge density.

As the capacitance of a p-i-n diode can be obtained from the series connection of the capaci-tances of each region, therefore, it is simply can be expressed by adding both depletion layer widths and the undoped region width, and given as:

$$C_j = \frac{\varepsilon_s}{x_n + x_p + d} = \frac{\varepsilon_s}{x_d} \tag{2.36}$$

2.10 PHOTOVOLTAIC CELL

The principle of a photovoltaic cell or a solar cell is the transformation of the energy from sunlight into electricity directly as shown in Fig. 2.24. The physics of such transformation is based on photons absorbed by a semiconductor p-n junction, forming electron-hole pairs (EHPs), as shown in Fig. 2.24. This in turn results in an electrical current flow [122].

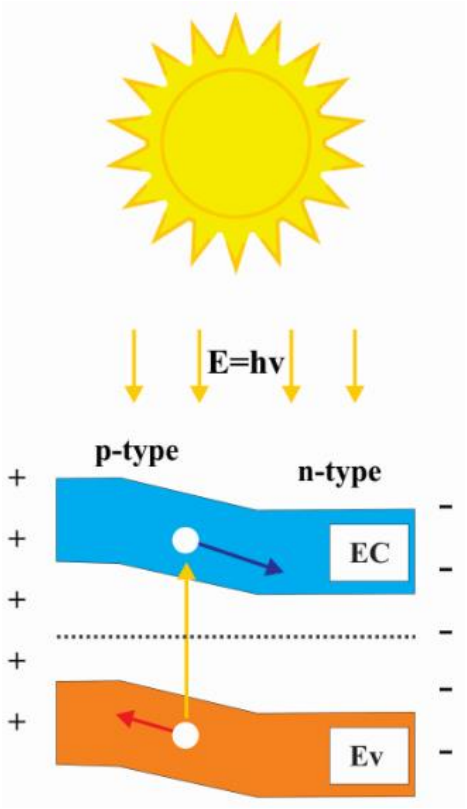


Fig. 2.24. Operation principle of a solar cell. *E and v* are energy and frequency of the photon [122].

The efficiency of a solar cell (η) depends on the absorption and the temperature of the solar cell. Thus, the chose of the optimum energy bandgap for a semiconductor used for solar cells fabrication is very significant to reach high efficiency solar cells by increasing the absorption process [123]. The fill factor (FF) also a significant parameter in solar cells. The relation between the FF and η as given in (2.37) simply indicates that increase the FF leads to enhance the efficiency of the solar cells [123].

$$\eta = \frac{FF \times V_{OC} \times I_{SC}}{P_{in}} \times 100\% \qquad (2.37)$$

where FF represents the fill factor, V_{OC} is the open-circuit voltage, and I_{SC} is the short-circuit current.

REFERENCES

[1] M. Grundmann, The physics of semiconductors, Springer (2006).

[2] B. Sapoval, C. Hermann and C. Hermann, Physics of semiconductors. Springer, (2003).

[3] S. M. Sze and K. K. Ng, Physics of semiconductor devices. John Wiley & Sons, (2006).

[4] B. Sapoval, C. Hermann and C. Hermann, Physics of semiconductors. Springer, (2001).

[5] Y. P. Varshni, Physica **34** (1), 149 (1967).

[6] P. Wang, S. Holmes, T. Le, R. Stradling, I. Ferguson and A. De Oliveira, Semiconductor science and technology **7** (6), 767 (1992).

[7] Ch. Zhen, T. Wei, N. Li, Sh. Wang and K. Lu, Physica B **427**, 58, (2013).

[8] K. Uesugi, I. Suemune, T. Hasegawa, T. Akutagawa and T. Nakamura, Applied Physics Letters **76** (10), 1285 (2000).

[9] I. Vurgaftman and J. Meyer, Journal of Applied Physics **94** (6), 3675, (2003).

[10] D. Wood, *Optoelectronic semiconductor devices*. (Prentice Hall, 1994).

[11] L. Pauling, Journal of the American Chemical Society **54** (9), 3570 (1932).

[12] R. Anderson, IBM Journal of Research and Development **4** (3), 283 (1960).

[13] J. Essick and R. Mather, Am. J. Phys. **61**, 7 (1993).

[14] F. Askary, P.Y. Yu, Solid State Commun. **47**, 241 (1983).

[15] S. Ding, S. Barman, K. Horn, H. Yang, B. Yang, O. Brandt and K. Ploog, Appl. Phys. Lett. **70**, 2407 (1997).

[16] W. Shockley and W. Read, Phys. Rev. **87**, 835 (1952).

[17] R. Hall, Phys. Rev. **87**, 387 (1952).

[18] M. McCluskey and E. Haller, *Dopants and defects in semiconductors*. (CRC Press, 2012).

[19] D. Schroder, *Semiconductor material and device characterization*. (John Wiley & Sons, 2006).

[20] G. Gilliland, Materials Science and Engineering, R**18**, 99 (1997).

[21] M. Weyers, M. Sato and H. Ando, Jap. J. of Appl. Phys. **31** (7A), L853 (1992).

[22] M. Kondow, K. Uomi, T. Kitatani, S. Watahiki and Y. Yazawa, Journal of Crystal Growth **164** (1), 175 (1996).

[23] S. R. Kurtz, A. Allerman, E. Jones, J. Gee, J. Banas and B. Hammons, Appl. Phys. Lett. **74** (5) (1999).

[24] P. Thijs, L. Tiemeijer, P. Kuindersma, J. Binsma and T. Van Dongen, IEEE Journal of Quantum Electronics **27** (6), 1426 (1991).

[25] H. Jussila, **47**, 075106 (2014).

[26] R. Roperto, Appl. Phys. Lett. **100**, 111901 (2012).

[27] P. Kent and A. Zunger, Phys. Rev. Lett. B **64**, 115208 (2001).

[28] W. Shan, W. Walukiewicz, J. Ager, III, E. Haller, J. Geisz, D. Friedman, J. Olson, and S. Kurtz, Phys. Rev. Lett. **82**, 1221 (1999).

[29] J. Wu, W. Shan, and W. Walukiewicz, Semicond. Sci. Technol. **17**, 860 (2002).

[30] E. O'Reilly, A. Lindsay, P. Klar, A. Polimeni, and M. Capizzi, Semicond. Sci. Technol. **24**, 033001 (2009).

[31] H. Hjalmarson, P. Vogl, D. Wolford and J. Dow, Phys. Rev. Lett. **44** (12), 810 (1980).

[32] A. Lindsay and E. O'Reilly, Solid State Communications **112** (8), 443 (1999).

[33] A. Ptak, S. Johnston, S. Kurtz, D. Friedman and W. Metzger, Journal of Crystal Growth **251** (1), 392 (2003).

[34] C. Skierbiszewski, P. Perlin, P. Wisniewski, T. Suski, W. Walukiewicz, W. Shan, J. Ager, E. Haller, J. Geisz and D. Friedman, physica status solidi (b) **216** (1), 135 (1999).

[35] R. Ahrenkiel, S. Johnston, B. Keyes, D. Friedman and S. Vernon, Appl. Phys. Lett. **77** (23), 3794 (2000).

[36] J. Geisz and D. Friedman, Semicond. Sci. Technol. **17** (8), 769 (2002).

[37] S. Kurtz, J. Geisz, D. Friedman, W. Metzger, R. King and N. Karam, J. of Appl. Phys. Lett. **95** (5), 2505 (2004).

[38] S. Bank, M. Wistey, H. Yuen, V. Lordi, V. Gambin, and J. Harris, J. Vac. Sci. Technol. B Microelectron. Nanometer Struct. **23**, 1320 (2005).

[39] R. Kudrawiec, M. Latkowska, M. Baranowski, J. Misiewicz, L.H. Li, and J.C. Harmand, Phys. Rev. B **88**, 125201 (2013).

[40] S. Mazzucato, R. Potter, A. Erol, N. Balkan, P.R. Chalker, T.B. Joyce, T.J. Bullough, X. Marie, H. Carrère, E. Bedel, G. Lacoste, A. Arnoult, and C. Fontaine, Phys. E Low-Dimens. Syst. Nanostructures **17**, 242 (2003).

[41] H. Xiaoyong et al., Chem. Soc. Rev. **42**, 173 (2013).

[42] J. Bourgoin and T. Neffati, Solid-State Electron. **43** (1), 153 (1999).

[43] H. Von Bardeleben, D. Stievenard, D. Deresmes, A. Huber and J. Bourgoin, Phys. Rev. Lett. B **34** (10), 7192 (1986).

[44] J. Lagowski, M. Kaminska, J. Parsey Jr, H. Gatos and M. Lichtensteiger, Appl. Phys. Lett. **41** (11), 1078 (1982).

[45] M. Baeumler, U. Kaufmann and J. Windscheif, Appl. Phys. Lett. **46** (8), 781 (1985).

[46] A. Irvine and D. Palmer, Phys. Rev. Lett. **68** (14), 2168 (1992).

[47] M. Kaminska and E. Weber, Semiconductors and Semimetals **38**, 59 (1993).

[48] G. Martin, A. Mitonneau and A. Mircea, Electronics Letters **13** (7), 191 (1977).

[49] U. Kaufmann, E. Klausmann, J. Schneider and H. Alt, Phys. Rev. Lett. B **43** (14), 12106 (1991).

[50] R. Yakimova, T. Paskova and C. Hardalov, J. of Appl. Phys. Lett. **74** (10), 6170 (1993).

[51] K. Yokota, H. Kuchii, K. Nakamura, M. Sakaguchi, H. Takano and Y. Ando, J. of Appl. Phys. Lett. **88** (9), 5017 (2000).

[52] D. V. Lang, A. Y. Cho, A. Gossard, M. Ilegems and W. Wiegmann, J. of Appl. Phys. Lett. **47** (6), 2558 (1976).

[53] P. Blood and J. Harris, J. of Appl. Phys. Lett. **56** (4), 993 (1984).

[54] A. Erol, Materials Science **105** (2008).

[55] L. Bellaiche, S. Wei and A. Zunger, Phys.l Rev. Lett. B **54** (24), 17568 (1996).

[56] S. Ding, S. Barman, K. Horn, H. Yang, B. Yang, O. Brandt and K. Ploog, J. of Appl. Phys. Lett. **70**, 2407 (1997).

[57] I. Buyanova, W. Chen, B. Monemar, H. Xin and C. Tu, J. of Appl. Phys. Lett. **75** (24), 3781 (1999).

[58] S. Kurtz, J. Klem, A. Allerman, R. M. Sieg, C. Seager and E. Jones, J. of Appl. Phys. Lett. **80** (8), 1379 (2002).

[59] A. Fleck, B. Robinson and D. Thompson, J. of Appl. Phys. Lett. **78**, 1694 (2001).

[60] S. Zhang and S. Wei, Phys. Rev. Lett. **86** (9), 1789 (2001).

[61] W. Li, M. Pessa, T. Ahlgren and J. Decker, J. of Appl. Phys. Lett. **79** (8), 1094 (2001).

[62] T. Ahlgren, E. Vainonen-Ahlgren, J. Likonen, W. Li and M. Pessa, J. of Appl. Phys. Lett. **80**, 2314 (2002).

[63] P. Krispin, S. Spruytte, J. Harris and K. Ploog, J. of Appl. Phys. Lett. **89** (11), 6294 (2001).

[64] P. Krispin, V. Gambin, J. Harris and K. Ploog, J. of Appl. Phys. Lett. **93** (10), 6095 (2003).

[65] N. Al Saqri, J. Felix, M. Aziz, D. Jameel, C. de Araujo, H. Albalawi, F. Al Mashary, H. Alghamdi, D. Taylor and M. Henini, Current Applied Physics **15** (10), 1230 (2015).

[66] W. Wei, S. Zhang and S. Huai, Phys. Rev. Lett. **86**, 1789 (2001).

[67] N. Thinh, I. Buyanova, P. Hai, W. Chen, H. Xin and C. Tu, Phys. Rev. B, **63**, 033203 (2001).

[68] N. Thinh, I. Buyanova, W. Chen, H. P. Xin and C. Tu, Appl. Phys. Lett. **79**, 3089 (2001)

[69] K. Montgomery, C. Allen, I. Wildeson, J. Jeon, A. Ramdas, and J. Woodall, J. Electron. Mater. **40**, 1457 (2011).

[70] M. Gershenzon and R. Mikulyak, Appl. Phys. Lett. **8**, 245 (1966).

[71] P. Dean, J. Lumin. 1, 398 (1970).

[72] A. Epstein and W. Groves, Adv. Energy Convers. **5**, 161 (1965).

[73] C. Allen, J. Woodall, and J. Jeon, Sol. Energy Mater. Sol. Cells **95**, 2655 (2011).

[74] G. Wicks, M. Koch, J. Varriano, F. Johnson, C. Wie, H. Kim, and P. Colombo, Appl. Phys. Lett. **59**, 342 (1991).

[75] O. Sulima, P. Sims, J. Cox, M. Mauk, R. Mueller, J. Reedy, A. Khammadov, P. Paulson, and G. Landis, Photovolt. Energy Convers. Proc. 3rd World Conf., pp. 737, Vol. **1** (2003).

[76] D. Thomas, M. Gershenzon, and F. Trumbore. Phys. Rev. Lett. **133**, A269, (1964).

[77] R. Krause, A. Polity, W. Siegel and G. Kuhnel. Semicond. Sci. Technol. **8**, 290, (1993).

[78] S. Almosni, Growth, structural and electro-optical properties of GaP/Si and GaAsPN/ GaP single junctions for lattice-matched tandem solar cells on silicon, PhD, INSA de Rennes, France (2015).

[79] Y. Zhang, B. Fluegel, A. Mascarenhas, H. Xin and C. Tu, Phys. Rev. Lett. B, vol. **62**, no. 7, pp. 4493, (2000).

[80] A. Chen and A. Sher, Semiconductor alloys. New York: Plenum Press, (1995).

[81] J. Laurenti, P. Roentgen, K. Wolter, K. Seibert, H. Kurz and J. Camassel, Phys. Rev. Lett. B, vol. **37**, no. 8, pp. 4155, (1988).

[82] J. Hopfield, D. Thomas and R. Lynch, Phys. Rev. Lett., vol. **17**, no. 6, pp. 312, (1966).

[83] Y. Zhang and W. Ge, Journal of Luminescence, vol. **85**, no. 4, pp. 247, (2000).

[84] Y. Zhang, A. Mascarenhas, H. Xin and C. Tu, Phys. Rev. Lett.B, vol. **61**, no. 7, pp. 4433, (2000).

[85] Y. Zhang, A. Mascarenhas, H. Xin and C. Tu, Phys. Rev. Lett. B, vol. **61**, no. 11, pp. 7479, (2000).

[86] A. Mascarenhas, Y. Zhang and M. Seong, physica status solidi (b), vol. **228**, no. 1, pp. 243, (2001).

[87] J. Baillargeon, K. Cheng, G. Hofler, P. Pearah and K. Hsieh, J. Appl. Phys. Lett., vol. **60**, no. 20, pp. 2540, (1992).

[88] X. Liu, S. Bishop, J. Baillargeon and K. Cheng, J. Appl. Phys. Lett., vol. **63**, no. 2, pp. 208, (1993).

[89] H. Xin, C. Tu, Y. Zhang and A. Mascarenhas, J. Appl. Phys. Lett. vol. **76**, no. 10, pp. 1267, (2000).

[90] D. Thomas and J. Hopfield, Phys. Rev. Lett., vol. **150**, no. 2, pp. 680, (1966).

[91] D. Wolford, J. Bradley, K. Fry, J. Thompson, and H. King. Phys. Conf. Ser, no. **65**, pp. 501, (1982).

[92] X. Liu, M. Pistol, L. Samuelson, S. Schwetlick and W. Seifert, J. Appl. Phys. Lett., vol. **56**, no. 15, pp. 1451, (1990).

[93] I. Ho and G. Stringfellow, Journal of Crystal Growth, vol. **178**, no. 1, pp. 1, (1997).

[94] S. Miyoshi, H. Yuguchi, K. Onabe, R. Ito and Y. Shiraki, Journal of Crystal Growth, vol. **145**, no. 1, pp. 87, (1994).

[95] H. Yaguchi, S. Miyoshi, G. Biwa, M. Kibune, K. Onabe, Y. Shiraki and R. Ito, Journal of Crystal Growth, vol. **170**, no. 1, pp. 353, (1997).

[96] Y. Furukawa, H. Yonezu, K. Ojima, K. Samonji, Y. Fujimoto, K. Momose, and K. Aiki, Jpn. J. Appl. Phys. **41**, 528 (2002).

[97] B. Kunert, D. Trusheim, V. Voßebürger, K. Volz, and W. Stolz, Phys. Status Solidi A **205**, 114 (2008).

[98] P. Kent and A. Zunger, Phys. Rev. Lett. B **64**, 115208 (2001).

[99] W. Chen, I. Buyanova, C. Tu, and H. Yonezu, Phys. B Condens. Matter 376, 545 (2006).

[100] J. Geisz, D. Friedman, and S. Kurtz, pp. 864. IEEE, (2002).

[101] J. Harris, R. Kudrawiec, H. Yuen, S. Bank, H. Bae, M. Wistey, D. Jackrel, E. Pickett, T. Sarmiento, L. Goddard, V. Lordi, and T. Gugov, Phys. Status Solidi B **244**, 2707 (2007).

[102] J. Even, F. Doré, C. Cornet, L. Pedesseau, A. Schliwa, and D. Bimberg, Appl. Phys. Lett. **91**, 122112 (2007).

[103] C. Cornet, A. Schliwa, J. Even, F. Doré, C. Celebi, A. Létoublon, E. Macé, C. Paranthoën, A. Simon, P.M. Koenraad, N. Bertru, D. Bimberg, and S. Loualiche, Phys. Rev. Lett. B **74**, 035312 (2006).

[104] F. Doré, Emetteurs à Îlots Quantiques Pour Le Moyen-infrarouge, Thèse INSA Rennes, (2008).

[105] B. Kunert, D. Trusheim, V. Voßebürger, K. Volz, and W. Stolz, Phys. Status Solidi A **205**, 114 (2008).

[106] M. Izadifard, I. Buyanova, J. Bergman, W. Chen, A. Utsumi, Y. Furukawa, A. Wakahara, and H. Yonezu, Semicond. Sci. Technol. **20**, 353 (2005).

[107] X. Chen, D. Zhang, Y. Jin, J. Li, J. Teng, and N. Yakovlev, Jornal of Crystal Growth **362**, 197 (2013).

[108] S. Mazzucato, R. Potter, A. Erol, N. Balkan, P. Chalker, T. Joyce, T. Bullough, X. Marie, H. Carrère, E. Bedel, G. Lacoste, A. Arnoult, and C. Fontaine, Phys. E Low-Dimens. Syst. Nanostructures **17**, 242 (2003).

[109] N. Thinh, I. Buyanova, P. Hai, W. Chen, H. Xin, and C. Tu, Phys. Rev. Lett. B **63**, (2001).

[110] O. Rumyantsev, P. Brunkov, E. Pirogov, and A. Egorov, Semiconductors **44**, 893 (2010).

[111] H. Jussila, S. Sintonen, M. Sopanen, H. Lipsanen, and T.O. Tuomi, (2013).

[112] H. Jussila, K.M. Yu, J. Kujala, F. Tuomisto, S. Nagarajan, J. Lemettinen, T. Huhtio, T.O. Tuomi, H. Lipsanen, and M. Sopanen, J. Phys. Appl. Phys. **47**, 075106 (2014).

[113] Y. Lin, T. Ma, H. Lin, J.Wu, and Y. Huang, J. Appl. Phys. Lett. **96**, 011903 (2010).

[114] M. Baranowski, R. Kudrawiec, M. Syperek, J. Misiewicz, T. Sarmiento, and J. Harris, Nanoscale Res. Lett. **9**, 81 (2014).

[115] L. Grenouillet, C. Chevallier, G. Guillot, P. Gilet, P. Ballet, P. Duvaut, G. Rolland, and A. Million, J. Appl. Phys. Lett. **91**, 5902 (2002).

[116] L. Dobaczewski, A. Peaker and K. B. Nielsen, J. Appl. Phys. Lett. **96** (9), 4689 (2004).

[117] T. Gfroerer, Encyclopedia of Analytical Chemistry R.A. Meyers, John Wiley & Sons Ltd, Chichester, 9209 (2000).

[118] B. G. Yacobi, Semiconductor materials: an introduction to basic principles. (Springer, 2003).

[119] J. Colinge and C. Colinge, Physics of semiconductor devices. (Springer, 2002).

[120] S. Sze and K. Ng, Physics of semiconductor devices. (John Wiley & Sons, 2006).

[121] D. Neamen and B. Pevzner, Semiconductor physics and devices: basic principles. (McGraw-Hill New York, 2003).

[122] V. Bormashov, S. Troschiev, A. Volkov, S. Tarelkin, E. Korostylev, A. Golovanov, M. Kuznetsov, D. Teteruk, N. Kornilov and S. Terentiev, physica status solidi (a) 212 (11), 2539 (2015).

[123] L. Olsen, (1993).

CHAPTER 3: EXPERIMENTAL WORK

The purpose of this chapter is to provide a brief description of the samples used in this study. The equipment and experimental setup used for the measurements carried out for the optical and electrical characterization of semiconductor materials will be briefly illustrated. This chapter presents also the experimental methods used to investigate the optical and electronic properties of the semiconductor structures studied in this thesis. Photoluminescence (PL) spectroscopy, current-voltage (I-V), capacitance-voltage (C-V), deep level transient spectroscopy (DLTS) and Laplace DLTS techniques will be discussed. This chapter also illustrates the hardware and software used in this study.

3.1 SAMPLES USED IN THIS STUDY

The samples investigated in this thesis were grown and processed by the French group at the University of Rennes, INSA Rennes, CNRS, Institut FOTON, France.

The main motivation of this thesis is to investigate (i) the optical properties of different materials structures for optoelectronic and photovoltaic applications and (ii) the electrically active defects present in these devices and their effects on their electrical properties.

In this thesis four groups of materials have been investigated using different structures:

i. $GaP_{1-x}N_x$ epilayers grown on GaP substrates with nitrogen concentrations ranging from x=1.4 to 2.7%. The samples were annealed at 800 °C for 5 minutes under a forming gas atmosphere using a rapid thermal annealer (RTA). The aim was to understand the effect of nitrogen composition and rapid thermal annealing on the optical properties of $GaP_{1-x}N_x$.

ii. Dilute GaAsPN (As= 10%) and InGaPN (In= 7%) epilayers grown on GaP substrates with nitrogen concentration of 1%. The samples were annealed at 800 °C for 5

minutes using RTA. The aim was to understand the effect of arsenic and indium, and rapid thermal annealing on the optical properties of $GaAs_{0.1}P_{0.89}N_{0.01}$ and $In_{0.07}Ga_{0.93}P_{0.99}N_{0.01}$.

iii. Dilute $GaAs_{0.1}P_{0.89}N_{0.01}$ thin films grown on GaP substrates with two epilayer thicknesses, namely100 nm to 1 μm. The samples were also annealed by RTA at 800 °C for 5 minutes. The aim was to investigate the effect of epilayer thickness and thermal annealing process on the optical properties of these devices.

iv. Dilute GaAsPN-based P-I-N solar cell structures where the I region is p doped. Similar RTA procedure and conditions were used to anneal these devices. The aim was to investigate the electrically active defects in order to understand the physical phenomena that affect the defects after annealing.

The growth details of each set of samples are presented in each related experimental chapter.

3.2 MEASUREMENT DETAILS

This section provides the details of the experimental setup and equipment used for the measurements of the devices studied in this work.

3.2.1 PHOTOLUMINESCENCE MEASUREMENTS

The PL spectroscopy technique is a contactless and non-destructive method that is commonly used to probe the electronic structure of semiconductor materials. Low temperature photoluminescence measurements have been performed using a He closed-loop system which operates from T ~ 10 K to 350 K as described in section 3.3 in this chapter.

The optical excitation was generated using a solid-state blue laser having $\lambda = 473$ nm. The PL signal was collected using the following procedure. Laser light passes through a chopper which is operated at 90 Hz. Next, the light passes through a band pass filter (315-750nm) to eliminate the higher order harmonic lines which are present in the blue laser. A mirror then

deflects the light onto a 2nd mirror through a focusing lens. The laser light then falls onto the sample which is placed inside the cryostat. The incident light on the sample is established with such an angle that the laser light is deflected off-axis with respect to the entrance slit of the spectrometer. The luminescence from the sample is focused onto the spectrometer entrance slit by using two lenses. A line filter is placed inside the spectrometer to eliminate the laser light. The filtered signal is dispersed by the diffraction grating and then detected by a Photomultiplier (PMT) detector. Finally, PL spectrum is recorded in the computer. PL measurements have been carried out in the temperature range from 10 K to 300K.

3.2.2 I-V MEASUREMENTS

To perform DLTS and Laplace DLTS measurements, suitable devices should have leakage currents in the range of μA or lower because these techniques rely on the change of capacitance following an electrical excitation. A Keithley 236 source/measure unit, controlled by a computer software via GPIB interface, is used to obtain the devices I-V characteristics. The current values are measured at bias voltages ranging from -2.5 to 1.5 V with 50 mV increments depending on the quality of the diode.

3.2.3 C-V MEASUREMENTS

The C-V characteristics are acquired using a Boonton 7200 capacitance meter which operates at a fixed frequency of 1MHz and controlled by a computer in order to determine the built-in voltage and the background doping concentration of the structures investigated. Furthermore, as described in Chapter 4, the C-V characteristics are used to calculate the trap concentration.

3.2.4 DLTS MEASUREMENTS

The electrically active defects present in the material systems investigated in this thesis are probed by DLTS and Laplace DLTS techniques, which are discussed later in this chapter. In this section a brief description of the experimental procedures are given. Firstly, the samples are processed in the form of circular mesas with different diameters and mounted on 12 pins

TO5 headers which are fixed into a holder inside the closed-cycle cryodyne refrigerator, model number CCS-450 cryostat. The samples are cooled down to a temperature of 10 K and the DLTS measurements start by increasing the temperature at a rate of 2 K/min up to 450 K. A National Instrument Box generates a sequence of electrical pulses that are applied to the samples, and a Boonton 7200 capacitance meter is used to monitor the transient capacitance. At selected reverse biases (V_R) and filling pulse (V_P), the capacitance transients are recorded in the form of DLTS signal and stored in a computer.

3.2.5 LAPLACE DLTS MEASUREMENTS

High resolution Laplace DLTS measurements were performed in order to resolve the broad features detected in the conventional DLTS. As the Laplace DLTS is an isothermal process, the temperature of the sample is fixed during the measurements. The Laplace DLTS measurements are performed within the temperature range where the DLTS peak is observed. Further details of these measurements are explained in this chapter.

3.3 PHOTOLUMINESCENCE

Photoluminescence (PL) can be defined as the light emitted spontaneously from a material undergoing optical excitation. The term “luminescence” was suggested by Wiedemann in1888 [1-2], where the term means weak glow in Latin. Luminescence can be emitted in different durations and by different causes, thus being classified accordingly. If the material is excited due to photon absorption, the resulting luminescence falls into two main key classes, namely fluoresce and phosphoresce. If the emission duration is fast (~ns range) then it is known as fluorescence, while slow emission as in hours or even days the luminescence is termed phosphorescence. Photoluminescence is an approach used to determine the optical quality of material structure. In PL experiment, the light incident on a material has a photonic energy greater than the energy of the material’s bandgap. As a consequence, photons are absorbed by the material and result in the creation of electron-hole pairs which relax in time

and thus allowing the formation of excitons. By the end of the process, radiative or non-radiative carriers' recombination processes may occur. In case of radiative relaxation, the light emitted is called photoluminescence (PL). Fig 3.1 demonstrates the transition of an electron from the valence band to the conduction band by optical excitation (Fig 3.1 (a)), and then relaxation into band edge (Fig 3.1 (b)). An electron-hole pair is then formed and a photon is released (Fig 3.1 (c)).

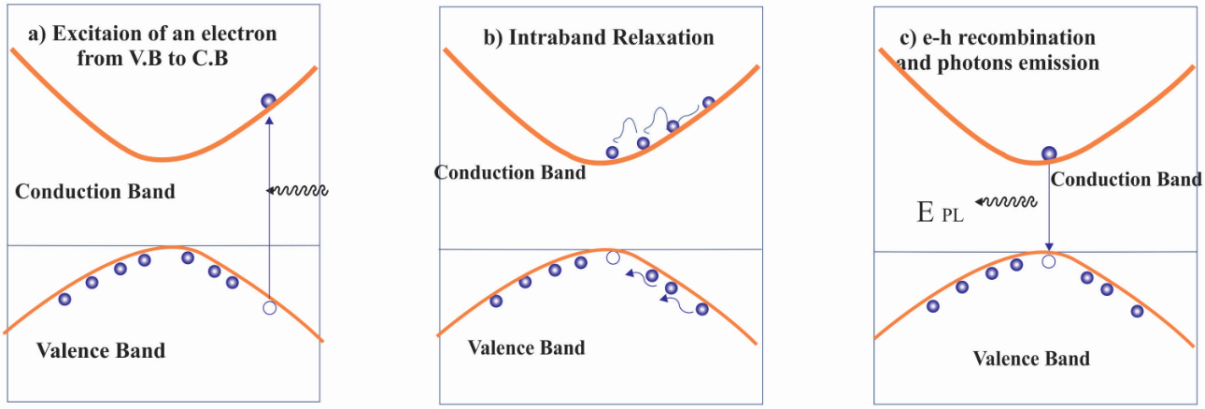


Fig. 3.1. Schematic illustration of the basic processes involved in luminescence emission from optically excited semiconductors.

Such emission can be detected and analysed to provide a rich source of information about the photoexcited material. A variety of PL investigations can be obtained in order to determine semiconductor parameters. The spectrum of PL gives the energies of photons emitted, which are a direct indication of the electronic energy levels. The radiative and non-radiative recombination centres can be probed by analysing the PL Spectra. Such intensities, beside the full width at half maximum (FWHM) of the PL signal, provides a measure of the sample optical quality. PL is basically a simple approach that is adaptable to many material systems in different forms and is non-destructive. Applying PL technique does not require complicated preparation of the sample. In addition, the PL technique is based on optical excitation of materials, thus it doesn't require junctions or electrical contacts. It is widely known that no practical complications are associated with high-resistivity materials, making

the PL technique suitable to investigate such materials. Further advantage of the PL is that the luminescence can be investigated at different regions on the sample surface. The main disadvantage of PL analysis originates from its reliance on optical transitions: the sample under investigation must emit photons. Some semiconductors have essentially very low PL efficiency, such as indirect bandgap semiconductors. Therefore, the relaxed states in these materials are based on non-radiative recombination processes. The density of traps and impurities states in general cannot be precisely estimated using PL, which represents another disadvantage of the technique. Nevertheless, when these states have radiative levels, they are readily identified in the PL spectrum, and the intensity of the associated PL peaks provides a relative measure of their presence in the sample.

3.3.1 SYSTEM HARDWARE IMPLEMENTATION

A PL system contains a number of hardware which are interfaced with a computer, providing a system capable of operation in the temperature range of 10K-350K. This section describes the required hardware for PL implementation, as well as the block diagram (Fig 3.2) and photograph (Fig 3.3) of the PL system used in this study.

3.3.1.1 SPECTROMETER

In this study, the emitted photoluminescence was scattered by a grating using the iHR 550 spectrometer from Horiba Jobin Yvon in order to obtain spectral analysis. It has a focal length of 0.55 m through an aperture of f/6.4. The spectrometer allows the holding of three different gratings via its motorized grating turret. The gratings adopted in this investigation are 1200 grooves/mm blazed at 500 nm, 600 grooves/mm blazed at 2000 nm and 300 grooves/mm blazed at 3000 nm. The slits of the input and outputs of the spectrometer can be adjusted 0.0mm to 2mm. The spectrometer has a motorized internal filter wheel at the entry slit holding six internal different filters. The iHR550 has two exit ports connected to a photomultiplier tube detector (PMT) and a dual Si/InGaAs detector.

3.3.1.2 LASERS, LIGHT CHOPPER AND OPTICS

The setup of PL is based on three excitation sources mainly of blue, green and red lasers with a tuneable incident power using a manual density filter. The setup contains a mechanical chopper in front of the laser that allows AC measurements using a lock-in amplifier. In addition, a band-pass filter is placed in the laser path to exclude the undesired higher order laser light. To achieve high focus of the light onto the sample the PL setup is equipped with a number of optics such as lenses and mirrors, which are used to ensure that the PL signal is focussed on the entry slit. The setup of the spectrometer is illustrated in Fig 3.2.

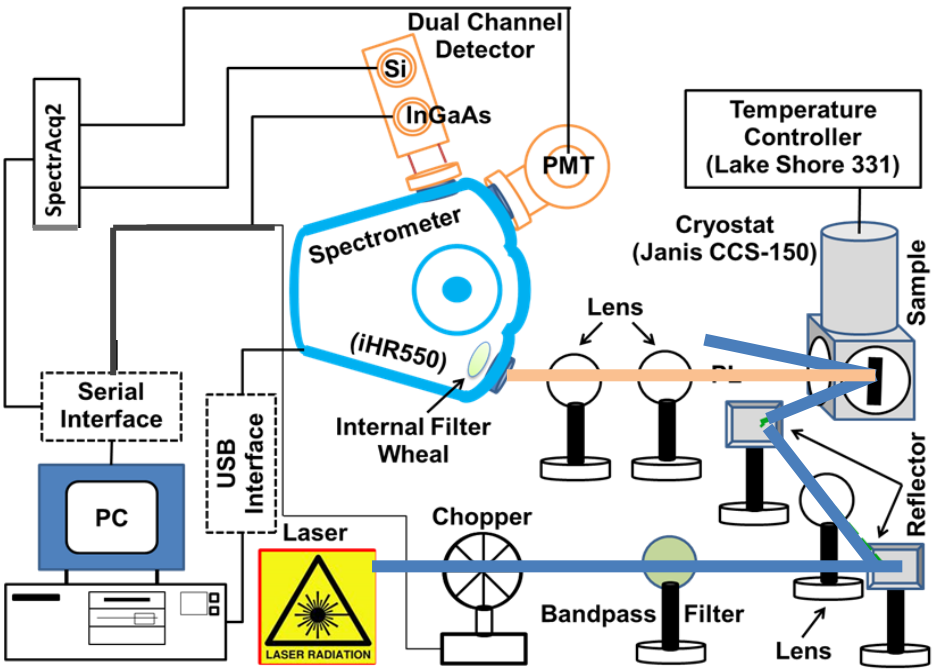


Fig. 3.2. A schematic diagram of photoluminescence (PL) apparatus.

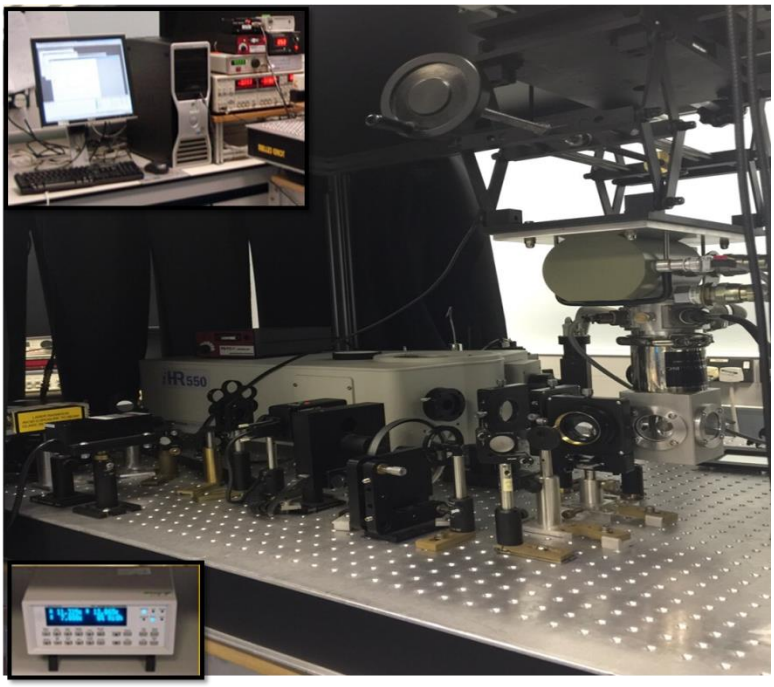


Fig. 3.3. Photograph of photoluminescence (PL) apparatus.

3.3.1.3 DETECTORS

The PL emissions are collected by optical detecting devices, which convert incident photons to electronic signals. The spectrometer incorporates two detectors installed in two different exits to cover a wide range of wavelengths. A Si/InGaAs dual channel solid state detector from Horiba Jobin Yvon (300 nm to 1700 nm) where silicon and InGaAs detectors can function from ~300 nm to ~1.1 μm, and ~1.1 μm up to ~1.7 μm, respectively. The second detector is a single channel photomultiplier tube (PMT). PMT detectors have the advantage of being highly sensitive in comparison to solid state detectors in addition to the efficient operation in the UV/VIS and NIR. However, PMT detectors have some disadvantages including their limited spectral coverage range (up to ~950 nm) and their high voltage power supply. The detected light by PMT is in the spectral range of 180nm to 900nm.

3.3.1.4 SPECTRACQ2

Data acquisition units are basically considered with the detected signals at processing and amplifying stages. The data acquisition module used is SpectrAcq2 from Horiba Jobin Yvon.

This module is of high speed allowing the collection and processing of 1000 data points per second and store up to 5000 data points, where the data are captured by the PMT or Si/InGaAs detectors. SpectrAcq2 configuration collects current or voltage inputs, and provides an output of high voltage to power the PMT (~ 950 Volts). The module is interfaced with the computer through a serial port RS-232.

3.3.1.5 LOCK-IN AMPLIFIER

Lock-in amplifiers (LIA) are usually employed when very small AC signals need to be detected and any other unwanted signals have to be removed. The function of the LIA is achieved through phase sensitive detection. Such detection is based on demodulation or rectification of the noisy signals which are usually mixed with reference signals such as the signal produced by the mechanical chopper which is used to chop the light with a fixed frequency.

The lock-in amplifier is fed with two signals; one is a control signal from a detector connected to the chopper, and the other is a response signal from the monitoring device. The purpose of the lock-in amplifier is then to selectively amplify only components of the response signal which oscillate at the same frequency as the control signal. The result is a very effective reduction of noise, and hence a large increase in the signal to noise ratio is obtained.

A Stanford SR830 digital lock-in amplifier with the capability to measure and amplify very small signals down to few nano-volts (nV) with a sensitivity of 2 nV was used.

3.3.1.6 CRYOSTAT AND TEMPERATURE CONTROLLER

A state-of-the-art cryostat model Janis CCS-150 combined with a temperature controller model Lake Shore 331 were used temperature dependent PL measurements. Additionally, it incorporates thermal sensors, radiation shield, and sample holder. The principle of

refrigeration is based on closed-cycle flow of helium gas (He) through a compressor. This refrigeration principle provides temperatures in the range from 10K to 350K.

3.3.1.7 COMPUTER INTERFACE

The computer used to interface with the PL system has 120MB RAM, 200MB hard disk, Windows XP as an operating system, a high speed USB port, and a serial port RS-232Data acquisition box spectrAcq2 and lock-in amplifier are connected to the computer by means of serial ports RS-232 and can be initialized and controlled from computer. A filter wheel fitted inside the spectrometer can also be controlled through high speed USB port.

3.3.1.8 SYSTEM CONTROLLING SOFTWARE

The SynerJY software supplied by Horiba Jobin Yvon was used to remotely control most of the components of the PL system including appropriate selection of grating and entry/exit slit sizes. Various parameters which are required to perform the PL measurement can be entered through software. The software is flexible in terms of recording and processing data simultaneously. The software can drive the turret containing three gratings, slits, and shutters. It also has control over the entrance and exit mirrors to select detector at axial and side positions. A filter wheel having different colour filters situated inside the spectrometer can also be controlled using the software.

3.4 CURRENT- VOLTAGE CHARACTERISATION

The current pass through the semiconductor due to thermionic emission of majority carriers is given by Richardson equation [3]

$$I_{ther} = AA^{**}T^2 \exp[-\frac{q\emptyset_B}{kT}] \qquad (3.1)$$

where A is the area of the junction and A^{**} is the effective Richardson's constant given for a semiconductor material, q is the electronic charge, ϕB is the height of the barrier, k is

Boltzmann constant, and *T* is the absolute temperature in Kelvin

The current flows from the semiconductor to the metal I_{sm} can be expressed as [3]:

$$I_{sm} = AA^{**}T^2 \exp[-\frac{q\emptyset_B}{kT}] \exp[\frac{qV}{kT}] \qquad (3.2)$$

where V is the applied voltage. At $V = 0$, the current flows from the metal to the semiconductor I_{ms} can be expressed by previous equation as:

$$I_{ms} = AA^{**}T^2 \exp[-\frac{q\emptyset_B}{kT}] \qquad (3.3)$$

Thus, the net current is:

$$I = I_{sm} - I_{ms}$$

Or:

$$I = I_s \left[\exp(\frac{q\emptyset_B}{kT}\right) - 1] \qquad (3.4)$$

Where I_s is the reverse saturation current, and given as:

$$I_s = AA^{**}T^2 \exp[-\frac{q\emptyset_B}{kT}] \qquad (3.5)$$

As the neutral area of the device offers a series resistance in pn junction, thus the previous equation becomes as:

$$I = I_S \left[\exp\left(\frac{q(V-IR_S)}{nkT}\right) - 1\right] \qquad (3.6)$$

Where R_S is a serise resistance and *n* is the ideality factor.

In the case of forward bias voltage for $V - IR_S >> kT$, the thermionic diode current is expressed as:

$$I = I_S \exp\left(\frac{q(V-IR_S)}{nkT}\right) \qquad (3.7)$$

The derivative of I with respect to V from Equation (3.7) is of the form:

$$\frac{dI}{dV} = I\left(\frac{q}{nkT} - \frac{\frac{qR_S}{nkT}dI}{dV}\right) \qquad (3.8)$$

By substituting dI/dV with the conductance (G) and rearranging the terms, the following form is obtained:

$$\frac{G}{I} = \frac{q}{nkT} - \frac{qR_S}{nkT}G \qquad (3.9)$$

Plotting the values of G/I vs G, values of n and R_S can be determined from the y-intercept and slope, respectively.

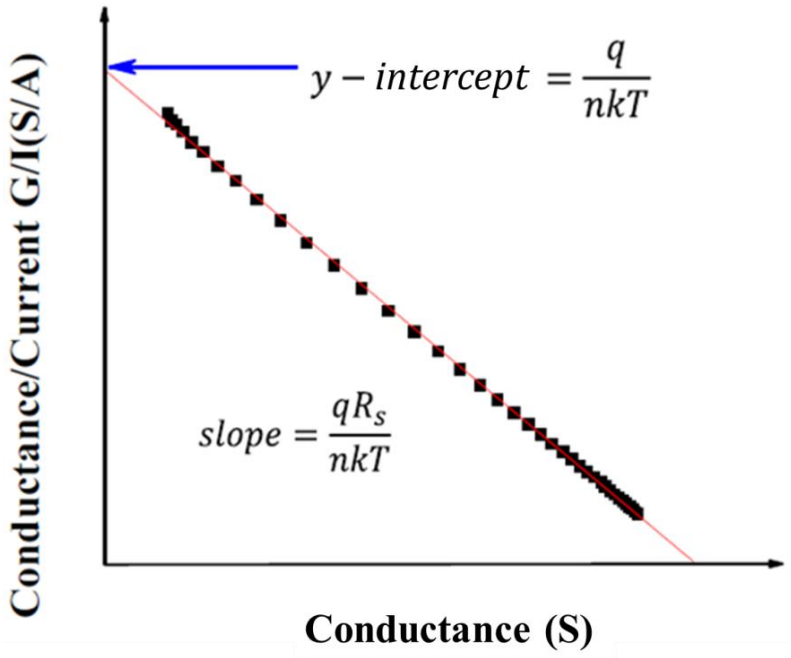


Fig. 3.4. A typical plot of G/I versus G used for extracting the I-V characteristics parameters [3].

To calculate I_S and ϕ_B, we take the natural logarithm of Equation (3.7):

$$\ln(I) = \ln(I_S) + \frac{q(V - IR_S)}{nkT} \qquad (3.10)$$

From the plot of $\ln(I)$ vs $(V - IR_S)$, I_S can be found from the y-intercept of the plot. Then, if the value of I_S is substituted in Equation (3.5), the value of $\emptyset_B$ can be found.

3.5 DEEP LEVEL TRANSIENT SPECTROSCOPY (DLTS)

Studying deep level defects in semiconductors experimentally can be done via microscopic defect analysis techniques [3]. Deep level transient spectroscopy (DLTS) is the most effective microscopic tool, and it is commonly used to characterize deep levels in semiconductors by the detection of charge carriers' emission [4]. DLTS technique was first realized by Lang in 1974 [5]. Such technique is based on the change in the depletion width with temperature. The measurement of the activation energies and capture cross-sections of defects can be found via DLTS, which is based on the concept of space charge capacitance.

3.5.1 CAPACITANCE TRANSIENTS

The DLTS method measures the capacitance transients which results from the change in the space charge region. For such a measurement to be carried out a Schottky diode or a p-n junction device is needed. Fig. 3.5 illustrates the changes in the charge occupancy of the defect level at various bias conditions in a Schottky diode. The occupancy of the defects is disturbed in the junction by the application of periodic bias pulses at a fixed repetition frequency. Such pulses are frequent between reverse bias V_R and filling bias V_P for a specific filling pulse width t_p (where $V_P < V_R$).

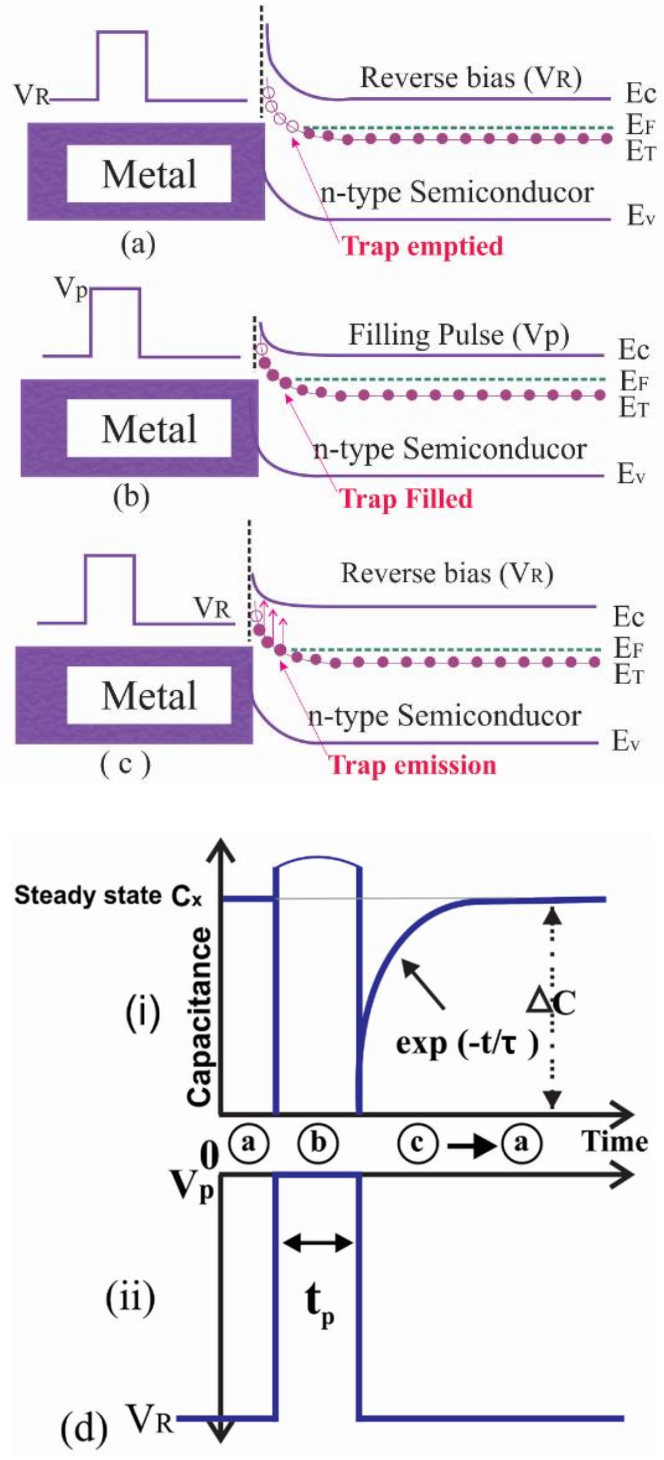


Fig. 3.5. Energy band diagrams of a Schottky diode illustrating the charge occupancy changes of the defects level during **(a)** emptying of traps at V=V_R bias condition, **(b)** filling of traps with filling pulse V=V_P, and **(c)** thermal emission of electrons due to the increase in the temperature at V=V_R. **(d)** DLTS pulse and the corresponding capacitance transient. t_p and E_T represent a pulse width and a trap energy level, respectively.

Fig. 3.5 shows the variation in the space charge region at four stages. At stage (a), firstly a reverse bias V_R is applied to the junction, thus a space charge region is established. Above the Fermi level, the traps are empty showing no charge carriers. At stage (b), the junction is exposed to a filling pulse V_P, causing the depletion region width to decrease. Consequently, the conduction band electrons flow to the region that was earlier depleted of carriers, where the traps in such region start capturing these electrons. By assuming no emission of charge carriers resulting from the capturing processes, the density of filled traps is given from the kinetics of the capture process as the rate:

$$\frac{dn_T}{dt} = c_n(N_T - n_T) \qquad (3.11)$$

where c_n is the capture coefficient of electrons, N_T is the total number of available trap states and n_T is the number of trap states occupied by electrons. The electron capture coefficient c_n can be given by the following relation:

$$c_n = \sigma_n < v_{th} > n \qquad (3.12)$$

where σ_n represents the electron capture cross-section, $< v_{th} >$ is the mean thermal velocity of the electrons, and n is the effective doping concentration which is equal to $N_D - N_T \approx N_D$. The traps will completely be filled by electrons if a filling pulse (t_p) is applied long enough, subsequently $n_T = N_T$. Nevertheless, in stage (c), the reverse bias is re-applied forcing the depletion region to move back to its original width, while the carriers starting to be emitted from the filled traps. Such emission is determined from the kinetics of emission process by the rate:

$$\frac{dn_T}{dt} = e_p N_T - n_T(e_n + e_p) \qquad (3.13)$$

where e_n is electron emission and e_p is hole emission.

If deep levels are anticipated to be just electron interacting centers, the calculation of the time dependences of n_T during capture (Equation (3.11)) and emission (Equation (3.13)) processes can be obtained, by [6]:

$$n_T(t) = N_T\{1 - \exp(-c_n t)\}, \;\; c_n \gg e_n, e_p, c_p \qquad (3.14)$$

and

$$n_T(t) = N_T \exp\left(-\frac{t}{\tau}\right), \;\; e_n \gg c_n, e_p, c_p \qquad (3.15)$$

where the capture coefficient of holes is given by c_p and the inverse of the electron emission rate is $\tau = \frac{1}{e_n}$.

Therefore, from the above equation, the reduction of the filled trap concentration has an exponential trend with a time constant τ and gives rise to a capacitance transient as presented schematically in Fig. 3.5 (d). The change of traps occupancy can be determined indirectly by controlling the capacitance variation of the diode. Hence, by adding the filled traps contribution $n_T(t)$ in the space charge region, Equation (3.4) can be modified as:

$$C = \frac{dQ}{dV_R} = \frac{A}{2}\left[\frac{2\varepsilon_S q N_D^*}{V_{bi}+V_R}\right]^{1/2} \qquad (3.16)$$

where $N_D^* = N_D - n_T$. In case $n_t \ll N_D$, then Equation (3.16) can be rewritten as:

$$\Delta C = C_\infty\left(1 - \frac{n_T}{2N_D}\right) \qquad (3.17)$$

where ΔC gives the amplitude of the capacitance transient and C_∞ is the steady state capacitance which can be written as $C_\infty = \frac{A}{\sqrt{2}}\left[\frac{2\varepsilon_S q N_D^*}{V_{bi}+V_R}\right]^{1/2}$.

Combining Equation (3.15) and Equation (3.17) provides the time dependence of the capaci-

tance for majority carrier traps emission as follows:

$$\Delta C = C_{\infty}\left[1 - \frac{N_T}{2N_D}\exp\left(-\frac{t}{\tau}\right)\right] \tag{3.18}$$

Hence, the deep level trap concentration can be obtained from the amplitude of the capacitance transient, while the emission rate of electrons is found from the time constant. Fig. 3.5 (d) shows the trap emission process and consequent change in the capacitance as a function of time. It is worth pointing out that, the sign of the capacitance transient for minority carriers traps is opposite to the majority carrier traps.

3.5.2 CONVENTIONAL DLTS

The principle of DLTS technique [5] is based on disturbing the occupancy of the deep states caused by capture and emission of carriers. DLTS detect the output of the variation in capacitance ΔC between two points in time t_1 and t_2 ($t_2 > t_1$). A DLTS spectrum can be constructed through the measurement of this transient as a function of temperature *T*. Thus, the produced spectrum leads to the calculation of the trap parameters such as capture cross section σ, the trap activation energy E_T, and density N_T. Equation (3.18) can be used to give the DLTS output signal as a function of temperature *S(T)*, as:

$$S(T) = C(t_1) - C(t_2) = \Delta C_0\left[\exp\left(-\frac{t_2}{\tau}\right) - \exp\left(-\frac{t_1}{\tau}\right)\right] \tag{3.19}$$

ΔC_0 is the variation in the capacitance at time *t = 0*, and it is expressed as:

$$\Delta C_0 = \frac{C_{\infty}N_T}{2N_D} \tag{3.20}$$

where N_T represents the trap concentration and C_{∞}represents the capacitance at a maximum reverse bias (when the trap is empty). The emission rate e_n varies with temperature as illustrated in Fig. 3.6 (a) and thus causing *S(T)* to change. If $\tau \ll (t_1 - t_2)$ and $\tau \gg (t_1 - t_2)$,

then the resulted DLTS signal is small, while if $\tau \approx (t_1 - t_2)$ then the DLTS signal is maximum.

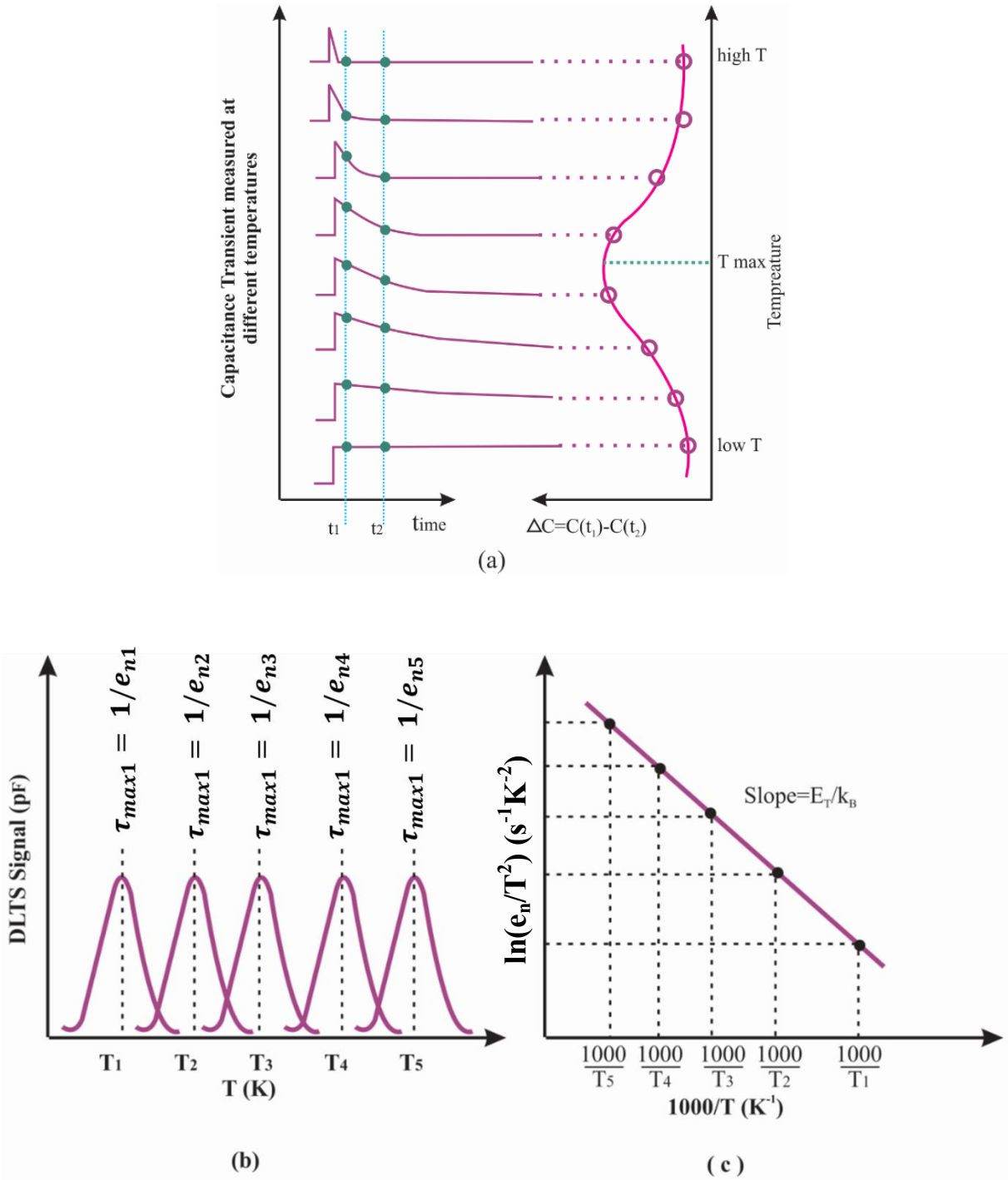


Fig. 3.6. Schematic diagram of the DLTS signal generation process: **(a)** the left side presents capacitance transients at different temperatures, while the right-side shows a DLTS signal resulting from the capacitance transient between the capacitance at time t_1 and time t_2 (fixed rate window) as a function of temperature, **(b)** DLTS signal at different rate windows and **(c)** the Arrhenius plot for the calculation of trap activation energy (E_T) [5].

The maximum signal of *S(T)* represents the maximum emission, which in turn corresponds to

the maximum amplitude of the DLTS signal. Such value can be obtained by using $\frac{dS(T)}{d\tau} = 0$. Consequently, the rate window equation can be written as:

$$\tau = \tau_{max} = \frac{(t_1 - t_2)}{\ln\left(\frac{t_1}{t_2}\right)} \qquad (3.21)$$

Changing the values of two points in times t_1 and t_2, the value of the rate window τ changes causing a shift in the DLTS peaks to higher temperatures (Fig. 3.6 (b)). Standard rate windows values are from 5 s^{-1} to 5000 s^{-1}. Therefore, a set of [T_{max}, e(T_{max})] data is generated to produce an Arrhenius plot as illustrated in Fig. 3.6 (c). The values of the trap activation energy E_T can be extracted from the slope of the Arrhenius plot, while the apparent capture cross-section σ_n of the trap is found from the intercept. Additionally, from Equation (3.20), the trap concentration N_T can be determined, where ΔC_o corresponds to the conventional DLTS peak amplitude. The maximum peak height of DLTS signal is independent of the absolute value of t_1 and t_2 as Equations (3.20) and (3.21) indicate, however it is related to the ratio (t_2/t_1).

3.6 LAPLACE DLTS SPECTROSCOPY

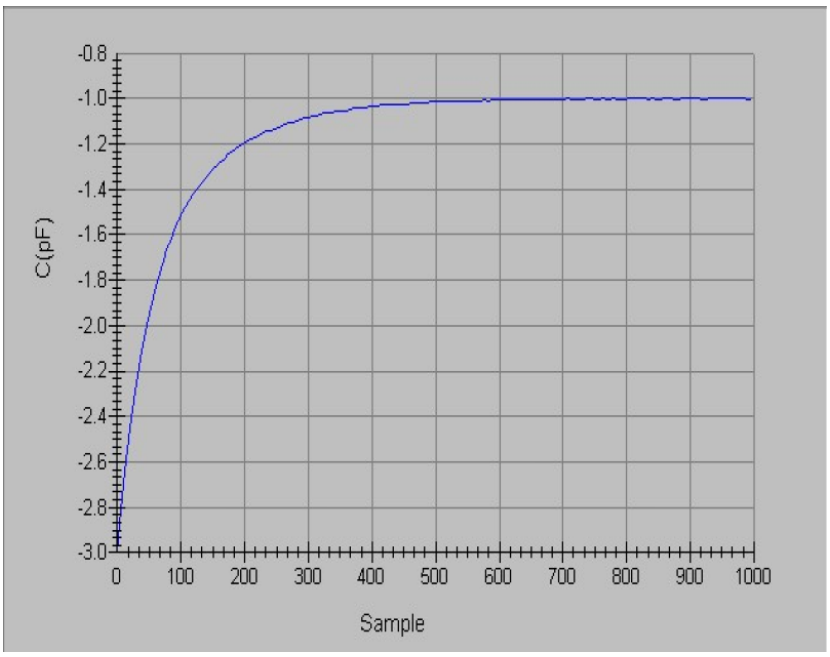
In semiconductor materials, the conventional DLTS technique is widely applied in order to characterize the deep levels by creating a series of peaks as a function of temperature [3]. These peaks are generated from the exponential behaviour of the emission transient of the deep levels. However, there are many issues correlated to the resolution of DLTS which arise from the scanning nature of the temperature. One of these issues is the accuracy of the temperature measurements related to the thermal scanning technique, since the temperature of the diode changes continuously. Consequently, this reduces the accuracy of obtaining the activation energies. Another issue arises from the difficulty of separating the time constants of exponential emission transients from various defect states which in turn causes a widening in

the DLTS peaks [7].

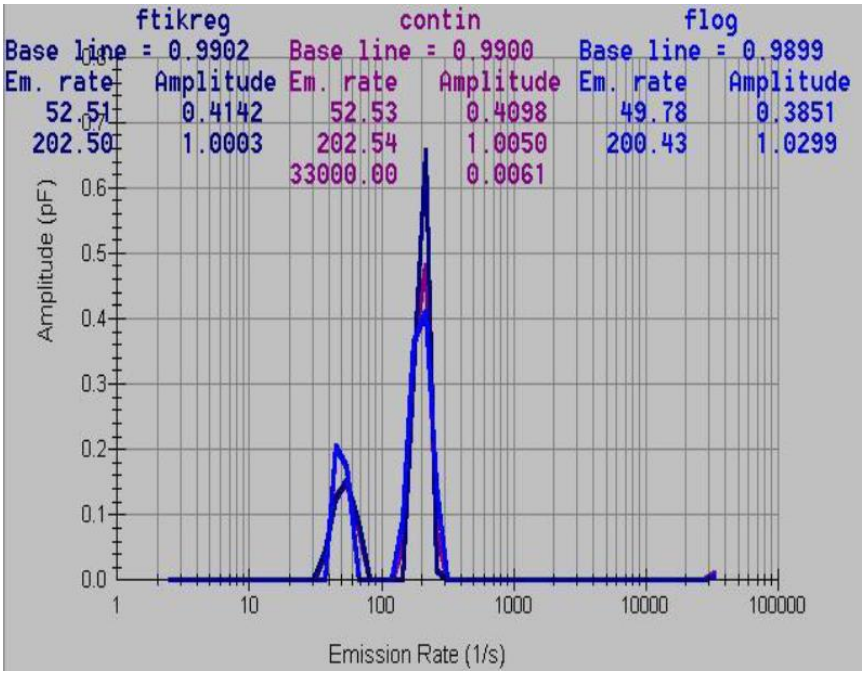
Accordingly, mathematical approaches have been designed to avoid such issues in the Conventional DLTS technique. One of the approaches is Laplace Inversion which is a calculation that aims to extract the emission spectrum F(s) from the capacitance transient. Laplace DLTS (or LDLTS) technique uses such mathematical method. In LDLTS, the temperature is fixed and therefore it is an isothermal technique [7-8]. Furthermore, in this technique the DLTS signal is shifted from time domain (conventional DLTS mode) to the frequency domain. Many digital schemes can be applied during the emission process to digitize and average the analogue transient output of the capacitance meter in order to increase the signal to noise ratio [9]. LDLTS transient can be mathematically expressed using the Laplace equation as follows:

$$f(t) = \int_0^\infty F(s)e^{-St}ds \qquad (3.22)$$

where $F(s)$ is the spectral function and $f(t)$ represents the Laplace transform of the true spectral function [$F(s)$]. An example of the capacitance transient which can be determined by Laplace DLTS is shown in Fig. 3.7 (a). In order to obtain a real spectrum of the emission rates show in the transient, $f(t)$, mathematical algorithms which apply the inverse Laplace transform for the function $f(t)$ are elected. These Laplace Inversion mathematical algorithms are FLOG, CONTIN and FTIKREG which are used in the Laplace method. To analyse the data, only one routine is used. The principle of all the three algorithms is known as the Tikhonov regularization method. Nevertheless, each one of them is based on a different method of determining the regularization parameters.



(a)



(b)

Fig. 3.7. (a) Diagram of the capacitance transient using Laplace DLTS at a fixed temperature; **(b)** delta-like peaks spectra output obtained from the capacitance transient with the use of three numerical routines.

The first algorithm (CONTIN) [10] and the second algorithm (FTIKREG) [11-12] codes are obtained from The Computer Physics Communication (CPC) Program Library at the Queen's

University of Belfast. These both algorithms have been adjusted for use in Laplace DLTS system. However, the last algorithm (FLOG) has been particulary established for the system. It is worth to mention that the parallel use of the three numerical algorithms enhances the confidence level in the spectra obtained. Moreover, the output of this technique gives a very well-defined, delta-like peaks spectra for multi-exponential transients as a function of emission rates as shown in (Fig. 3.7 (b)). Indeed, the trap concentration can be determined from the area under the peaks of LDLTS signal. Thus, the accuracy of the characterization of defects increases [8].

Fig. 3.8 illustrates the ability of the high resolution LDLTS technique in determining the signal of conventional DLTS for very closely spaced defects. The figure shows that conventional DLTS reveals the presence of only one broad peak in hydrogenated Si doped with gold [13-14]. However, the LDLTS measurements reveal two well resolved peaks associated with hydrogen and gold related defects.

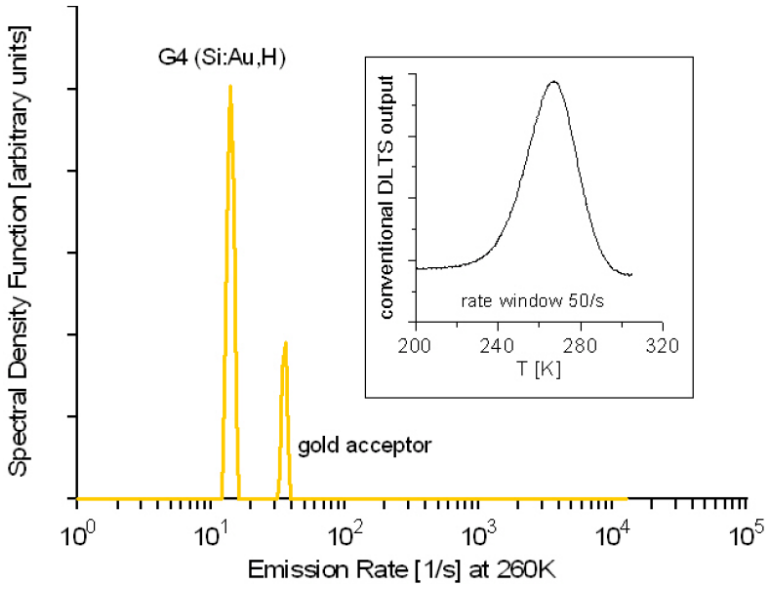


Fig. 3.8. LDLTS spectra of hydrogenated Si containing gold at 260 K. The inset shows the conventional DLTS spectrum at a rate window of 50 s^{-1} [14].

3.7 SYSTEM HARDWARE IMPLEMENTATION

3.7.1 DESCRIPTION OF SYSTEM HARDWARE

This section describes the conventional DLTS and Laplace DLTS experimental setup shown in Fig. 3.9. It consists of (i) Janis cryostat and temperature controller, (ii) capacitance meter, (iii) Current-Voltage meter, (iv) data acquisition and BNC connectors box for analogue Input (I)/Output (O). The setup is connected to a computer to control all this equipment via a GPIB interface.

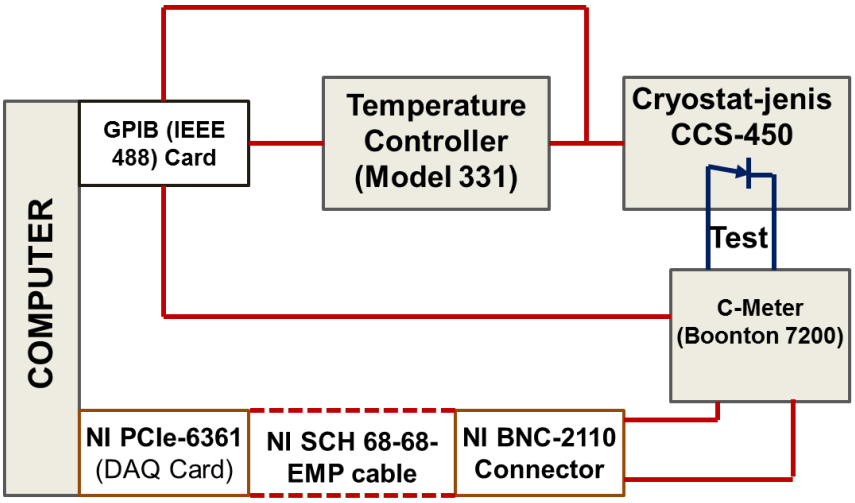


Fig. 3.9. Block diagram of DLTS and Laplace DLTS system.

3.7.1.1 CRYOSTAT AND TEMPERATURE CONTROLLER

Emission process from the traps depends on the thermal energy. Therefore, in the measurements of DLTS and Laplace DLTS the use of a cryostat (model Janis CCS-450) and a temperature controller (Model Lake Shore 331) is important to monitor the temperature of the sample. The internal configuration of the cryostat system is shown in Fig. 3.10. Such system contains a sample holder joined to a cold finger, thermal sensors, electrical ports for sample contacts, a radiation shield and aluminum vacuum shroud. The cryostat is connected to a compressor that consists a closed cycle cooling system with helium gas (He) flowing continuously through a six-feet high efficiency flexible cryogen transfer line. This cryostat is con-

trolled by Lake Shore 331 in the temperature range of 10 K - 450 K with stability of ±1 K. A temperature sensor is connected to Lake Shore 331 and placed very close to the sample for high temperature accuracy.

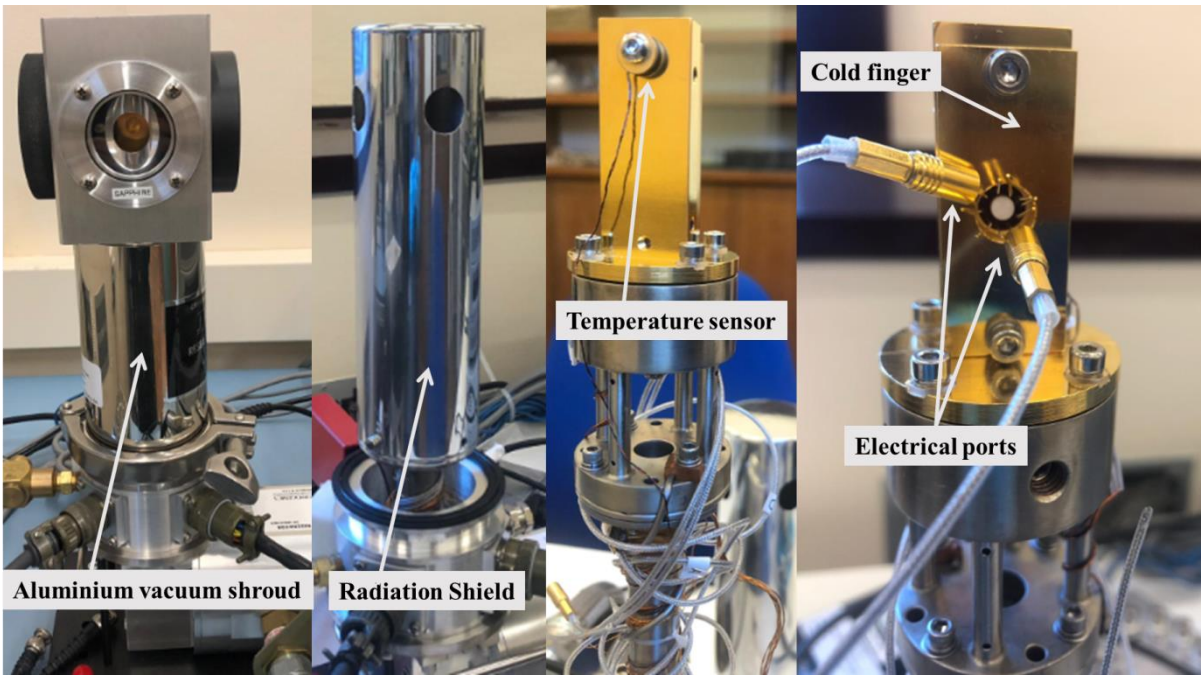


Fig. 3.10. Photograph of the external and internal structure of the cryostat system (model Janis CCS-450) used for the DLTS experiments.

3.7.1.2 CAPACITANCE METER

Measurements of the capacitance transient in DLTS requires a high response time capacitance meter. A good choice to obtain such measurements is the capacitance Boonton 7200 meter which has a response time of ~120 μs with 1 MHz sampling frequency. Furthermore, this meter is useful in measuring normal C-V at different temperatures.

3.7.1.3 CURRENT-VOLTAGE SOURCE METER

The sample requirement for capacitance-based DLTS and Laplace DLTS techniques is to have low leakage currents in the range of μA. The measurements of the current-voltage (I-V) characteristics are conducted using Keithley 236 current meter, which is operated by a computer software via GPIB interface. The source voltage provided by the meter is in the range

of 100 μV to 110 V with a sensitivity of ±10 μV, and a source current in the range of 100 fA to 100 mA, with a sensitivity of 10 fA.

3.7.1.4 DATA ACQUISITION AND BNC-2100 CONNECTOR

To apply biasing and pulsing to the diode, a National Instruments (NI) data acquisition (DAQ) card is employed. The provided input voltage by this card is up to ± 10.0 V and with pulse width from 0.5 μs. The DAQ card is connected to the computer by a SHC68-68-EPM matching cable with the BNC-2110 connector.

3.7.1.5 COMPUTER INTERFACE

To remotely control and monitor all the DLTS equipment a high speed general-purpose interface bus (GPIB) card and a dedicated software were used.

3.8 SYSTEM SOFTWARE

The development of the Laplace DLTS software was conducted under the joint project *"Copernicus Project CIPA CT-94-0172 and The Foundation for Polish Science Serial No: C3.2.041"* by two institutions, namely the Institute of Physics Polish Academy of Sciences, Warsaw, Poland (the late Prof. L. Dobaczewski) and University of Manchester (Prof. A. R. Peaker). This version of the software can operate in conventional DLTS and Laplace DLTS modes as described in the following section.

3.8.1 CONVENTIONAL DLTS MEASUREMENTS MODE

The conventional DLTS basic mode scans the sample by constantly changing the temperature. The measurements are performed within a range of two temperature points, with increasing steps of 2K/minute. The conventional DLTS uses Multi-Rate Window, TrapView and Exponential Fitting modes for measurements. Such modes run on the concept of rate window and are briefly described here. The "Multi-Rate" mode can operate on nine different rate windows which are:

$$5\ s^{-1}, 10\ s^{-1}, 20\ s^{-1}, 50\ s^{-1}, 100\ s^{-1}, 200\ s^{-1}, 500\ s^{-1}, 1000\ s^{-1}\ \&\ 2000\ s^{-1}.$$

The "TrapView" mode on the other hand can operate on one selected pair at a time out of 5 different pairs of rate windows, which are:

$$(4, 10)s^{-1}, (20,50)s^{-1}, (80,200)s^{-1}, (400,1000)s^{-1}\ \&\ (2000,5000)s^{-1}$$

The "Exponential Fitting" mode can operate only on one rate window. Running measurements in this mode, result in constructing an Arrhenius plot, which can be used to estimate the activation energies of defects and capture cross-section. Furthermore, "Exponential Fitting" mode can also operate in lock-in mode thus providing an improved resolution than the rate window mode. Nonetheless, the signal to noise ratio is poor in the lock-in mode. The DLTS experiment parameters can be customized and controlled remotely in all these three modes. These parameters are the reverse/forward bias, duration of pulses and range of temperature.

3.8.2 LAPLACE TRANSIENT PROCESSING MODE

Using the Laplace DLTS allows the increase of the S/N ratio. The measurements are performed using FLOG, CONTIN and FTIKREG algorithms at constant temperature to construct Laplace DLTS peaks.

REFERENCES

[1] H. Brito, O. Malta, M. Felinto, E. Teotonio. Luminescence Phenomena Involving Metal Enolates, (2010).

[2] T. Gfroerer, Encyclopedia of Analytical Chemistry R.A. Meyers, John Wiley & Sons Ltd, Chichester, 9209 (2000).

[3] S. Pandey, P. Middelkamp, Z. Li and V. Eremin, Nuclear Instruments and Methods in Physics Research Section A: Accelerators, Spectrometers, Detectors and Associated Equipment **426** (1), 109 (1999).

[4] A. Peaker and M. Brozel, III-Vs Review **12** (1), 44 (1999).

[5] D. Lang, J. of Appl. Phys. Lett. **45** (7), 3023 (1974).

[6] D. Schroder, Semiconductor material and device characterization. (John Wiley & Sons, 2006).

[7] L. Dobaczewski, I. Hawkins and A. Peaker, Mat. Sci. and Technol. **11** (10), 1071 (1995).

[8] L. Dobaczewski, A. Peaker and K. B. Nielsen, J. of Appl. Phys. Lett. **96** (9), 4689 (2004).

[9] L. Dobaczewski, P. Kaczor, I. Hawkins, and A. Peaker, J. of Appl. Phys. Lett. **76** (1), 194 (1994).

[10] S. Provencher, Computer Physics Communications **27** (3), 213 (1982).

[11] J. Weese, Computer Physics Communications **69** (1), 99 (1992).

[12] J. Weese, Computer Physics Communications **77** (3), 429 (1993).

[13] P. Deixler, J. Terry, I. Hawkins, J. Freeman, A. Peaker, L. Rubaldo, D. Maude, J. Portal, L. Dobaczewski and K. B. Nielsen, J. of Appl. Phys. Lett. **73** (21), 3126

(1998).

[14] V. Bormashov, S. Troschiev, A. Volkov, S. Tarelkin, E. Korostylev, A. Golovanov, M. Kuznetsov, D. Teteruk, N. Kornilov and S. Terentiev, physica status solidi (a) **212** (11), 2539 (2015).

CHAPTER 4: INVESTIGATION OF THE EFFECTS OF NITROGEN INCORPORATION AND THERMAL ANNEALING ON THE OPTICAL PROPERTIES OF $GaP_{1-x}N_x$ DILUTE NITRIDES

In this Chapter, the optical characterization technique, namely photoluminescence (PL) has been employed to study the effect of nitrogen incorporation and rapid thermal annealing (RTA) process on the optical properties of $GaP_{1-X}N_X$ alloys (x ranging from 1.4% to 2.7%) grown on (100) GaP substrates. In addition, High Resolution X-Ray Diffraction (HR-XRD) and X-Ray Specular Reflectivity (XSR) are performed to study the effect of RTA on the structural properties of the as-grown and annealed $GaP_{0.986}N_{0.014}$ samples.

4.1 INTRODUCTION

Dilute III-V nitride semiconductors are relatively a quite new material system, which has attracted a great deal of attention due to their anomalous properties. These are very promising materials for many technological applications such as solar cells [1], long wavelength lasers [2], terahertz emitters [3], optical amplifiers [4], and temperature-insensitive semiconductor band gap [5].

Incorporation of nitrogen in conventional III-V alloys, such as GaAs and GaP, strongly affects their electronic structure, leading to a wealth of fascinating physical properties inherent to the dilute III-V nitrides alloys. These include the giant bowing of the bandgap energy accompanied by the splitting of the conduction band (CB) states, the enhanced nonparabolicity of the CB energy dispersion, the unusually weak dependence of the bandgap energy on applied pressure and temperature, etc [6-7]. These properties have been found to be very desirable for various applications in optoelectronic and photonic devices, and therefore

attracting further interest in novel dilute nitrides. The N-induced modifications of the band structure have been attributed to a large mismatch of sizes and electronegativity between the N atom and another group-V element of the host lattice, which causes breaking of translational symmetry and thus promotes strong mixing of the CB states [8].

However, devices based on dilute nitride III-V materials such as long-wavelength lasers, heterojunction bipolar transistors (HBTs) and multijunction solar cells have generally shown less than optimum performance due to the poor quality of the material and presence of defect states with high concentrations [9]. In general, defects and impurities deteriorate the optical and electrical properties of semiconductor materials. In order to recover these qualities, it is common practice to subject the material to appropriate thermal treatments. The defect removal (also referred to as "healing") mechanisms which can occur upon the annealing procedure, involve diffusion and disassociation of the defect (also known as traps). In the diffusion process when the annealing temperature is increased, the defect could migrate towards the surface or grain boundaries (such as N related defects, N clusters and Ga vacancies [10-11]. In addition, the defect capability to diffuse through the crystal is determined by its charge state. The defect can be trapped by other impurities, for example, recombination of an interstitial with a vacancy. In the dissociation process, the intricate defect can break-up into separate defect complexes upon annealing.

Rapid thermal annealing experiments have shown that an improvement of the electrical and optical quality is possible [12-13], presumably due to the removal of some defect states [14]. There have been several studies reported in the literature about the annealing behaviour of dilute nitride semiconductor materials. A brief survey about the improvements in the material's quality and transport properties after annealing is given below.

An investigation of the effect of rapid thermal annealing on the optical properties of undoped GaNAs/GaAs multi-quantum wells (MQWs) was carried out by Buyanova et al. [15]. A

reasonable increase in the photoluminescence (PL) intensity and a substantial decrease in the PL linewidth were observed. Their magnetic resonance studies revealed a significant reduction in the concentration of non-radiative defects after the heat treatment with halogen lamp in a flowing N_2 ambient at 850 °C for 10s. They suggested that the reduction of the non-radiative defects after heat treatment leads to an improvement in the optical quality of GaAsN/GaAs MQWs.

In addition to the enhancement of the luminescence from the nitride materials upon annealing, several researchers have also observed a shift in the PL emission energy. Wang et al. [16] have reported PL experiments on GaAsN samples that reveal the existence of a red-shift in the PL peak energy after thermal annealing. Their observations have shown that the PL from GaAsN does not originate from band-to-band transitions, but rather from localized state excitonic recombinations. Furthermore, it was found that the thermal annealing process could effectively remove the interstitial N–As complex and the defects related to the broad energy-tail in the low-energy side of the PL spectrum. Another example of the redshift of PL emission is demonstrated by the work of Francoeur et al. [17]. Their PL measurements showed a redshift in the luminescence peak detected in MOCVD grown InGaAsN layers after annealing at 650°C for 5 minutes. A shift of 15 meV in a sample containing 0.7% N was observed. From the XRD measurements, they attributed this redshift to the increase of nitrogen incorporation.

Several other annealing studies of nitride materials reported in the literature show a blue shift of the PL emission upon thermal annealing [18,19,28]. For example, Tournie et al. [19] performed PL and X-ray diffraction experiments on Ga(In)NAs quantum wells and investigated the influence of post-growth annealing on their optical and structural properties. A blue shift in the PL emission was observed, which was attributed to the internal atomic rearrangement in the InGaAsN quantum well layer. Similarly, the annealing induced blue-

shift in InGaAsN materials observed by Kondow et al. [20] has also been suggested to be mainly due to the atoms' rearrangement in the material. Whereas the work of Li et al. [21], Damimano et al. [22], Kim et al. [23] and Albrecht et al. [24] attributed the blue shift of PL emission to the N diffusion.

There is tremendous interest in GaPN as an optoelectronic material and as a candidate for tandem solar cells with Si because of its ideal bandgap and lattice matching, and the optimisation of the thermal annealing procedures to remove the defects. Therefore, this work investigates the effect of nitrogen incorporation as well as the rapid thermal annealing (RTA) on the optical properties of Molecular Beam Epitaxy (MBE) grown GaPN layers with different nitrogen concentrations ranging from 1.4% to 2.7% using PL technique. The details of the samples used in this study and their preparation are given in Chapter 5.

4.2 SAMPLES DETAILS

The samples growth details are given in Chapter 5. Briefly, the GaPN structures are grown in a solid source Molecular Beam Epitaxy (MBE) system, which uses a valved RF plasma source to incorporate nitrogen into GaP lattice. The 100 nm thick $GaP_{1-x}N_x$ epilayer was grown on GaP (100) substrates. This was capped with 10nm GaP layer (see Fig. 4.1.). The growth temperature was 480 °C. These samples were grown under a high V/III flux with a Beam Equivalent Pressure (BEP) ratio of 25. The phosphorus flux was 5 µTorr.

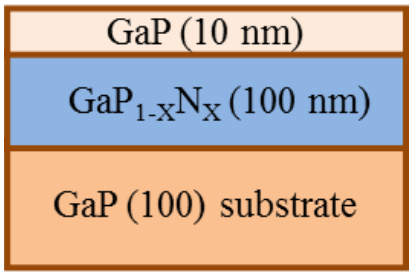


Fig. 4.1. Schematic diagram of the $GaP_{1-X}N_X$ dilutes nitride structure. Three samples were investigated with x=1.4%, 2.1%, and 2.7%.

Rapid thermal annealing (RTA) was performed at 800°C for 5 minutes.

4.3 RESULTS AND DISCUSSION

High-resolution X-ray diffraction (HR-XRD) and X-Ray Specular Reflectivity (XSR), which are important tools for structural characterization of thin epitaxial films, have been used only in one sample to understand the structural properties of $GaP_{0.986}N_{0.014}$ before and after RTA. In addition, the optical properties of both as-grown and RTA annealed $GaP_{1-x}N_x$ (x= 1.4%, 2.1%, 2.7%) epilayers were investigated using the PL technique.

4.3.1 INVESTIGATION OF STRUCTURAL PROPERTIES OF AS-GROWN AND ANNEALED $GaP_{0.986}N_{0.014}$

Very useful information about the vertical lattice parameters, layer thickness, roughness and strain in the epilayers can be obtained by using XRD technique. HR-XRD and XSR studies were performed in collaboration with the group at the Institute for Crystal Growth, Berlin, Germany. The HR-XRD measurements were carried out with a double-crystal diffractometer equipped with a parabolic (focusing) multilayer mirror. The x-rays are produced using the Kα1 transition of copper (λ= 1.54056 Å) and are monochromated with a four-bounce Ge 220 Bartels monochromator.

HR-XRD measurements were performed on $GaP_{0.986}N_{0.014}$ layer grown on (100) GaP substrate after centring and optimizing the (004) symmetrical Bragg reflection. The composition of GaPN ternary films on (100) oriented substrates can be determined by the x-ray reflection from the (004) plane. As the crystallographic parameters such as lattice constant and spacing between the planes of the substrate and epitaxial layer are different, an x-ray diffraction pattern as a function of angle should show at least two peaks corresponding to the satisfied Bragg conditions for the substrate and the GaPN epilayer. The Bragg's law for constructive interference is given by:

$$n\lambda = 2d\ sin\theta \qquad (4.1)$$

where n is an integer, λ is the wavelength of the incident photons, d is the interplanar spacing and θ is the Bragg angle of the substrate.

Differentiation of equation (4.1) allows the determination of the relationship between the peak-splitting $\Delta\theta$ and interplanar spacing d for coherently strained epilayer [25]. This is given as

$$\frac{\Delta d}{\Delta \theta} = -\frac{n\lambda}{2\,sin\theta}\,cot\theta \qquad (4.2)$$

From equation (4.1) and (4.2), the peak-splitting $\Delta\theta$ is given by

$$\Delta\theta = -\left(\frac{\Delta d}{d}\right)\frac{1}{cot\,\theta} \qquad (4.3)$$

where ($\Delta d/d$) is the deformation in the epilayer.

Now if we assume that the layer is in the non-relaxed state, the deformation ($\Delta d/d$) can be expressed as [26]

$$\left(\frac{\Delta d}{d}\right) = \frac{1}{P}\left(\frac{\Delta a}{a}\right) \qquad (4.4)$$

where ($\Delta a/a$) is the relaxed lattice mismatch between substrate and epilayer, and P is the distortion coefficient.

Once the mismatch strain is known, then the composition of $GaP_{1-x}N_x$ can be calculated using Vegard's law [27] (see equation 4.5).

$$a(GaP_{1-x}N_x) = (1-x).a(GaP) + x.a(GaN) \quad (4.5)$$

By rearranging equation (4.5) the N-concentration, x, can be extracted using equation (4.6)

$$x = \frac{\Delta a/a}{(\Delta a/a)_{GaP/GaN}} \qquad (4.6)$$

where

$$(\Delta a/a)_{GaP/GaN} = \frac{a_{GaP} - a_{GaN}}{a_{GaP}}$$

From equation (4.3) and (4.4) we can have the following relation.

$$\left(\frac{\Delta a}{a}\right) = P\left(\frac{\Delta d}{d}\right) = -P.\Delta\theta.cot\,\theta \qquad (4.7)$$

Thus, using equation (6.7), equation (6.6) for the composition *x* can be rewritten as

$$x = P\left(\frac{a_{GaP}}{a_{GaN} - a_{GaP}}\right)\Delta\theta.\cot\theta \qquad (4.8)$$

where θ is the Bragg angle for the GaP substrate reflections and $\Delta\theta$ is the angle shift of the GaPN reflections with respect to the GaP substrate.

The distortion coefficient *P* depends upon the elastic constants and on the surface orientation. For the sample grown on (100) GaP, *P* is given by [26].

$$P_{100} = \frac{C_{11}}{C_{11} + 2C_{12}} \qquad (4.9)$$

Given that the N content of our samples is low, the elastic constants (C) of GaP are used to calculate *P*. These are C_{11} = 140.4 GPa, C_{12} = 62 GPa and C_{44} = 70.3 GPa. The value obtained is P_{100}= 0.531.

XSR and HR-XRD curves (2θ scans) obtained from as-grown and annealed $GaP_{0.986}N_{0.014}$ epilayers grown under near-stoichiometric conditions on (100) GaP substrates are shown in Fig. 4.2.(a) and 4.2.(b), respectively.

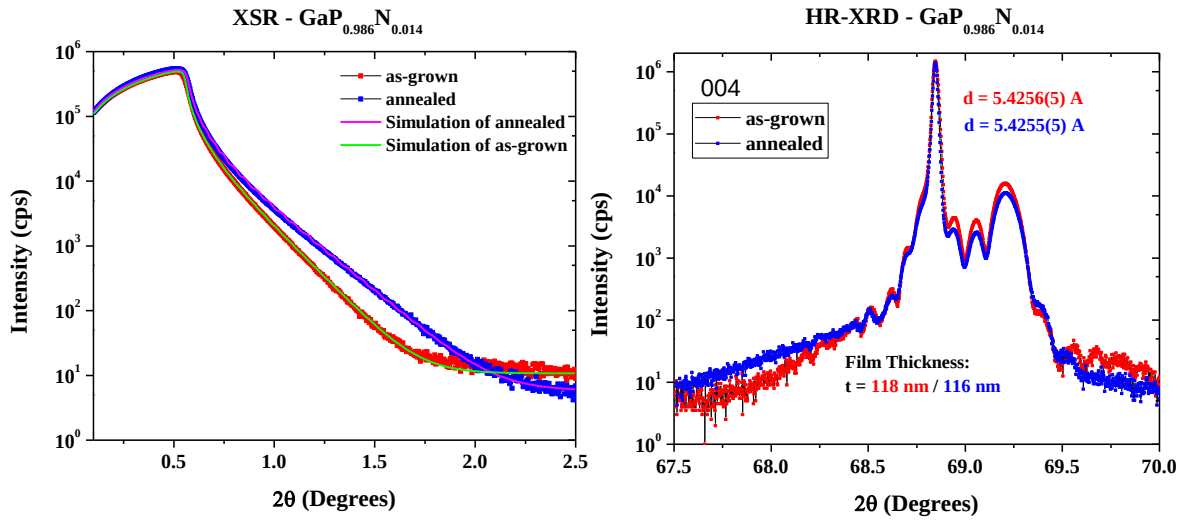


Fig. 4.2. (a) XSR spectra for $GaP_{0.986}N_{0.014}$ and simulation before and after RTA, **(b)** HR-XRD spectra for $GaP_{0.986}N_{0.014}$ before and after RTA.

Table 4.1: Main structural results from HR-XRD before and after RTA for $GaP_{0.986}N_{0.014}$.

Sample	Vertical lattice spacing (Å)	Root Mean Square (RMS) Surface Roughness (nm)	Thickness (nm)	Nitrogen induced change in vertical lattice spacing
$GaP_{0.986}N_{0.014}$ **as-grown**	5.4256	≈ 1.9	118	-0.0046
$GaP_{0.986}N_{0.014}$ **annealed**	5.4255	≈ 1.6	116	-0.0046

With regard to the XSR results shown in Fig. 4.2 (a) it is clear that no Kiessing fringes are observed. In other words, the surfaces of both as-grown and annealed samples are rough (i.e. have a roughness above a certain threshold from which Kiessing fringes cannot be observed). Moreover, it is clear that XSR measurements show different slopes for $GaP_{0.986}N_{0.014}$ before and after annealing. Therefore, one can conclude that the surface roughness changes after annealing. After RTA treatment a slight reduction in the surface roughness from ≈1.9 nm to ≈1.6 nm is noticed as indicated in Table 4.1. Furthermore, obviously there is no clear difference between as-grown and annealed samples in terms of vertical lattice spacing and

layer thickness. In addition, no measurable change was observed in the vertical lattice spacing after annealing.

The HR-XRD spectra in Fig. 4.2 (b) present slight damping of fringes and decrease of peak intensity after RTA annealing. This indicates an increase of disorder in the epitaxial layer. However, the 2θ values of layer reflections were very similar, meaning that the vertical lattice parameters of as-grown and annealed GaPN epilayers are identical.

4.3.2 INVESTIGATION OF THE EFFECT OF NITROGEN CONTENT ON THE OPTICAL PROPERTIES OF $GaP_{1-X}N_X$

The standard measurements of GaP proved that it has an indirect band gap with bandgap energy (Eg) equals to 2.26 eV at room temperature [27]. It was also reported that the incorporation of N into GaP, i.e. GaN_xP_{1-x} alloys with concentrations $x \geq 0.43\%$, changes the nature of the bandgap from indirect to direct [28]. In addition, N forms NN pairs such as NN_1 leading to the observation of a series of sharp PL emission lines [28]. With enhancing N concentration higher than 0.43%, the N pair bound states develop into an N-related impurity band. Thus, the GaNP alloy turns into a direct bandgap material and therefore a high efficiency room temperature (RT) PL from the epilayer can be achieved [28]. The $GaP_{1-X}N_X$ samples investigated in this work have N concentrations greater than 0.43%, namely x= 1.4%, 2.1%, and 2.7%, and therefore it is expected that the nature of the bandgap of our $GaP_{1-X}N_X$ should be direct. This is confirmed in Fig. 4.3 (a) and (b) which shows the spectral dependences of the PL intensity of $GaP_{1-x}N_x$ alloys and PL peak bandgap energy at 10 K respectively. This is in particular due to the well-known giant bandgap bowing effect in III-V-N alloys due to the nitrogen incorporation [29]. Therefore, the value of the observed reduction in the luminescence and emission peak energy with increasing N shown in Fig. 6.3 appears to depend on the N content in the alloys. From Fig. 4.3 (a) it can be seen that the luminescence intensity decreases with increasing nitrogen content from 1.4% to 2.7%. This

could be due to the fact that with an N concentration more than 1.3%, the PL intensity decreases due to reduced sample quality partly as a result of strain enhancement as well as an increase of the defects related to the nitrogen incorporation, resulting in a deterioration of the luminescence of dilute $GaP_{1-x}N_x$ [30].

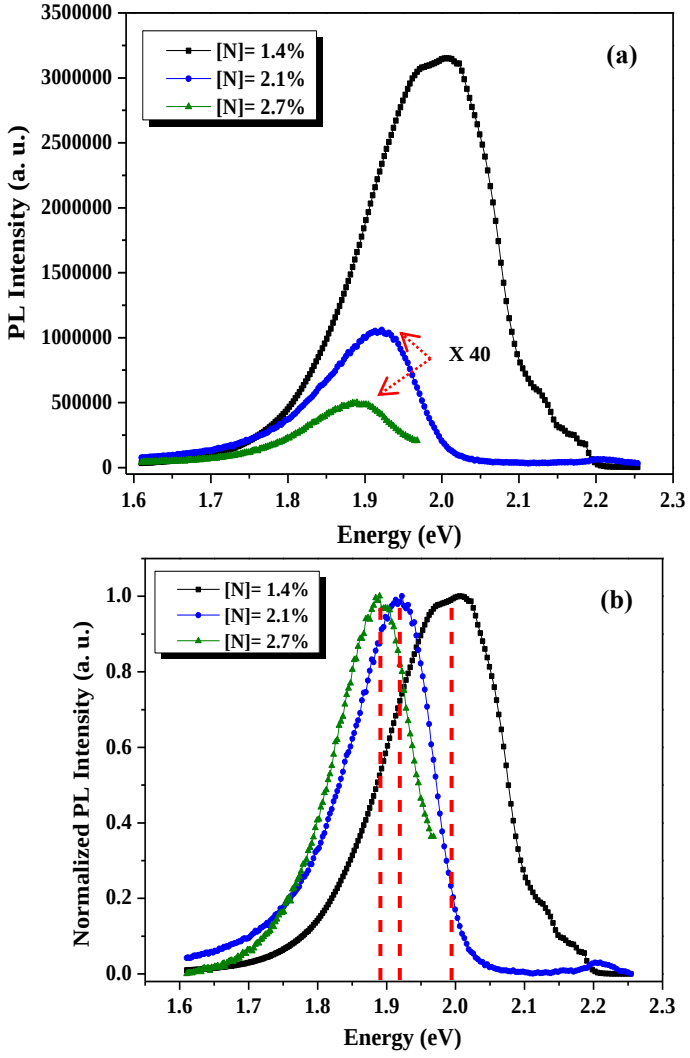


Fig. 4.3. (a) PL intensity vs photon energy for different N compositions at 10K, **(b)** Normalized PL intensity vs photon energy for different N compositions at 10K.

In addition to this, it is obvious that with increasing the amount of nitrogen incorporated into $GaP_{1-x}N_x$, the PL peak energy (Eg) decreases as illustrated in Fig. 4.3 (b). This decrease in bandgap energy has also been reported in dilute $GaAs_{1-x}N_x$ and was attributed to the large bandgap reduction as well as the heavy conduction band effective mass and its unusual

composition dependence to the formation of nitrogen related impurity band evolved from nitrogen pair bound states in heavily doped GaAs:N [31]. It is believed that a very similar situation happens in the $GaP_{1-x}N_x$ alloys studied in this work. Actually, in an earlier study of $GaP_{1-x}N_x$ alloys [32], it has been reported that the high nitrogen composition in GaPN leads to a band formation from the bound states of the isolated nitrogen centre which causes a bandgap reduction. The absorption peak reported in reference [32] was observed at the energy of NN_1 (as explained in Chapter 2) for concentrations up to x=2 %, thus it appears that the new conduction band of $GaP_{1-x}N_x$ alloys is a convolution of all the nitrogen related bound states, which are inhomogeneously broadened with enhanced N content. This conclusion was supported PL and the photoluminescence excitation (PLE) results [32]. The intercentre interactions or the formation of large nitrogen clusters cause band edge states to extend to the energy region below the lowest bound state NN_1, and therefore a further decrease of the bandgap of the alloy, producing the formation of a direct bandgap [28]. Subsequently, a very strong PL emission is expected in GaNP bulk layers.

Furthermore, it is obvious from Fig. 4.3 (b) that the PL peaks of all $GaP_{1-x}N_x$ alloys are broad. The broadening of the peaks observed in III-V-N is attributed to the effect of N incorporation. It is well-known that incorporating more than 0.5% of nitrogen leads to the creation of localized N-pairs and cluster levels in the bandgap of the host material GaP [33-34]. This means that the broadness of the PL peaks observed in GaPN layers indicates that N-levels in this material do not appear to be located within the forbidden gap of the host material and N localized levels could be lower than the conduction band (CB) of the host material [35-36].

Fig. 4.4 shows the temperature dependence of the PL peak energy for all three samples of as-grown $GaP_{1-x}N_x$ with an excitation wavelength of 473nm at a power of 20 mW. As it is expected, at high temperatures a red shift of the PL peak energy occurs. For the $GaP_{0.986}N_{0.014}$

alloy, a significant decrease of Eg from about 2.2 eV to 1.93 eV is observed over the temperature range 10-200 K. For the sample with 2.1% N concentration, the bandgap is first reduced from 1.92 eV to approximately 1.89 eV over the temperature range 10 -100 K and then remains almost constant from ~100 to 280K. At the highest N concentration (N= 2.7%), the bandgap energy reduction as a function of temperature is also observed from 1.89 eV at 10K to 1.87 eV at 80K and then the PL signal is quenched at ~120K.

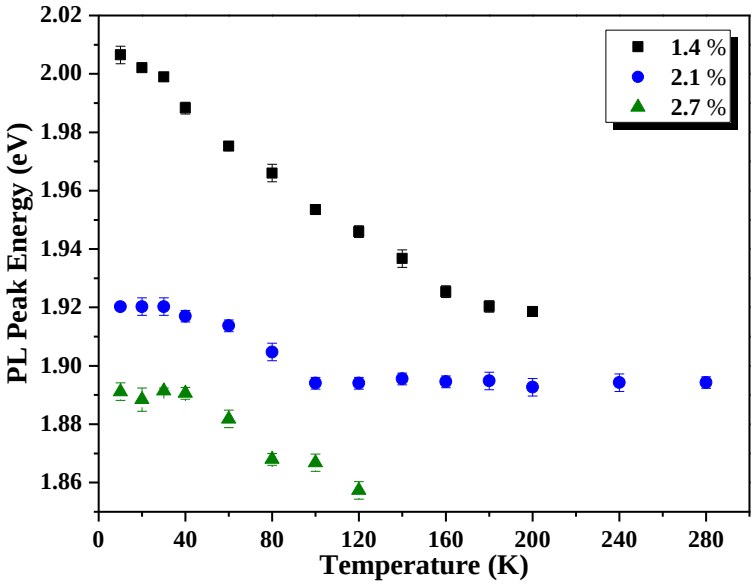


Fig. 4.4. Temperature dependence of the PL peak energy for as-grown $GaP_{1-x}N_x$ with x=1.4%, 2.1% and 2.7%.

It is worth noting that no PL signal was detected at RT in all samples studied in this work due to the poor quality of as-grown samples. It is important to point out that S-shape in the PL behaviour is observed in GaPN alloys with nitrogen compositions of 2.1% and 2.7% at low temperatures (from 10 to 100 K) (see Fig. 4.4). This confirms that increasing the nitrogen content above 2% causes an increase of the localized states in the dilute nitride alloys which leads to an S-shape behaviour. To understand the temperature behaviour of the alloy bandgap, one has to consider the temperature related properties of both types of states involved in the CB formation. It is known that the temperature-induced shift of the Γ minimum in GaP is larger than that for the X-minimum. On the contrary, the highly localized

N states are expected to be temperature insensitive. Thus, a simultaneous admixture of the delocalized Γ-like and localized N-related states will produce counteracting contributions [37].

Fig. 4.5 shows typical PL spectra for different laser power at low temperature (10K). For all samples, different broad bands were observed at lower energies and sharp PL peaks at higher energies (> 2eV) depending on laser power. These broad bands at lower energy are usually associated with exciton localization effects. The observed sharp emissions are due to NN_i (nitrogen-nitrogen interstitial) centers. Actually, these sharp peaks are usually observed in the doping regime at low incorporation of N in GaP and in non-intentionally doped GaP due to residual doping. In GaP crystal, all these states are localized below the conduction band. In this study, the observed sharp lines are associated with the emission in the GaP substrate. In addition, the observed asymmetry of the broad band is usually attributed with disorder effects such as random fluctuations in alloy composition which could result in a smearing of band edges and in an extended density of states into the band gap. This asymmetry of the PL spectrum is well known for dilute nitrides. Due to the fact that the high energy tail is enhanced by thermal filling of the bands, the asymmetric shape is more pronounced at lower temperatures than at room temperature and higher laser power. Particularly, it was observed a blue shift of the PL band with increasing laser power and a reduction of band tail at lower energy.

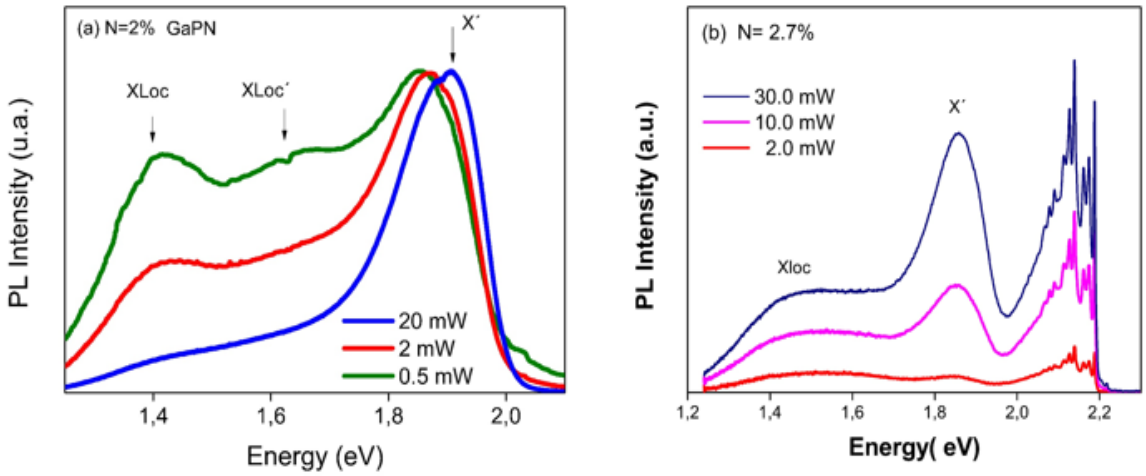


Fig. 4.5. Laser power dependence of the bandgap energy for as-grown $GaP_{1-x}N_x$ with **(a)** x= 2% and **(b)** x= 2.7% at 10K.

4.3.3 INVESTIGATION OF RAPID THERMAL ANNEALING ON THE OPTICAL PROPERTIES OF $GaP_{1-X}N_X$

In order to determine the effect of RTA on the luminescence properties of as-grown $GaP_{1-x}N_x$/GaP samples, PL experiments were performed for each nitrogen concentration (1.4%, 2.1% and 2.7%) at different temperatures ranging from 10 K to 300 K. The samples were excited with a 473 nm blue laser with 16 mW power. As explained in Chapter 3, the samples were annealed at 800°C for 5 minutes by a rapid thermal annealer.

Fig. 4.6 presents the PL intensity versus energy with for GaPN alloys with different nitrogen concentrations [N=1.4%, 2.1% and 2.7%] before and after RTA. A marked increase in the luminescence intensities is evidenced for all samples after the RTA annealing process (see Fig. 4.6 (b)). Some studies have attributed this enhancement in the PL intensity after annealing to the change in the deep levels defects originating from dislocations. However, in this work, the XRD results confirm that there are no differences between dislocation level before and after RTA, and therefore the improved PL intensity after RTA is attributed to another mechanism [38]. Tu et al. [38] suggested that the PL originated from defects related to N doping such as nitrogen clusters. Furthermore, it was found that these defects degraded

after RTA [38]. Subsequently, the decrease in the defects' density after RTA results in an increase of the luminescence peak intensity.

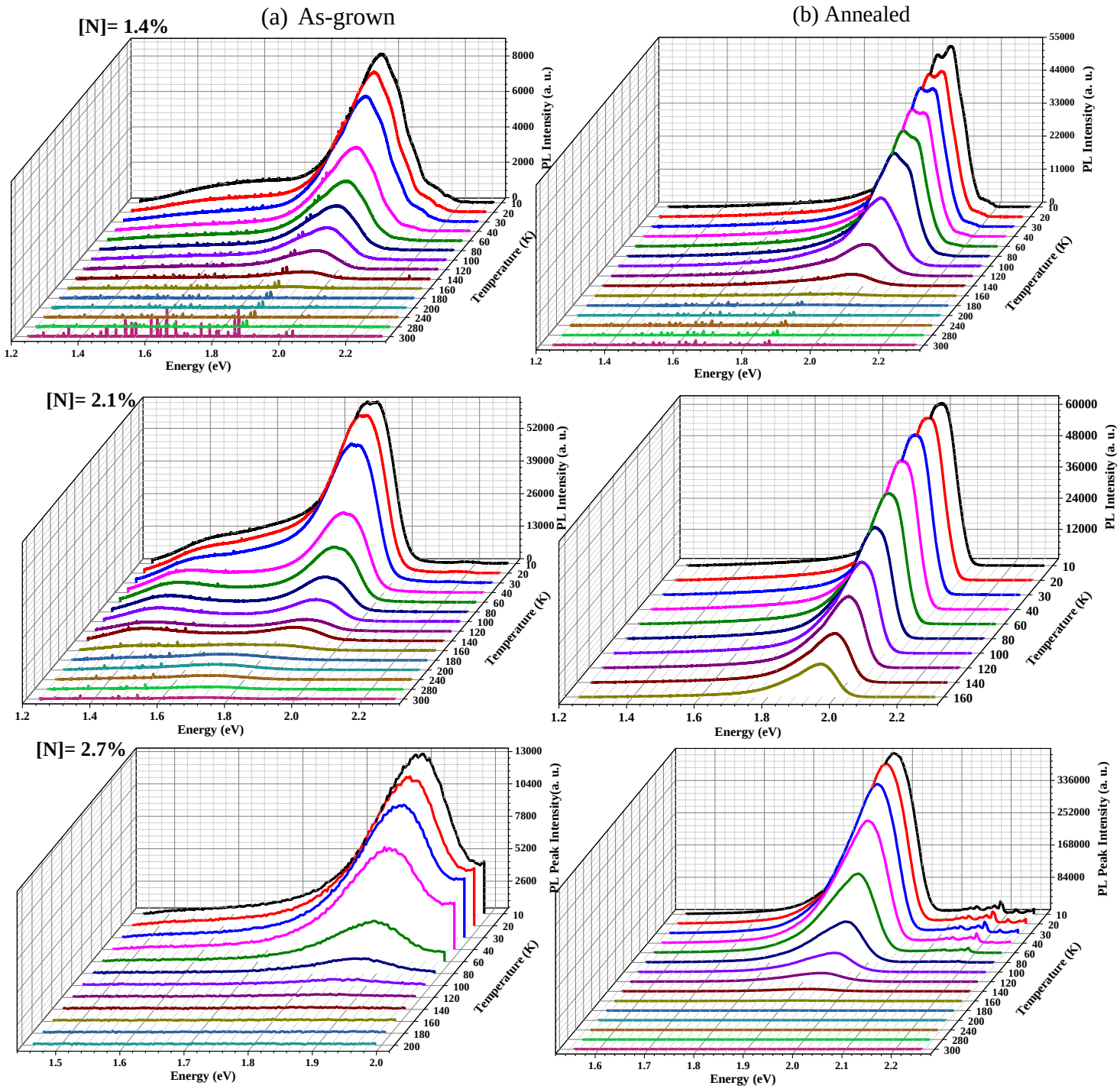


Fig. 4.6. Photon energy vs PL intensity spectra at different temperatures for **(a)** as-grown and **(b)** annealed of $GaP_{1-x}N_x$ with different nitrogen compositions [N= 1.4%, 2.1%, and 2.7%].

Moreover, it is obvious from Fig. 4.6 that the PL peak energy is blue-shifted after RTA for all $GaP_{1-x}N_x$ layers. This also shown clearly in Fig. 4.7 which illustrates the temperature dependence of the PL peak energy before and after RTA for all nitrogen compositions of $GaP_{1-x}N_x$ investigated in this work. It has been reported that the reduction of the defects after RTA in dilute nitrides leads to a blue-shift of the PL energy [39]. Therefore, the blue-shift of the PL peak energy observed in our RTA samples can be explained by the band-filling effect due to a decrease in the defects, such as nitrogen clusters and Ga vacancies [40]. Thus, RTA leads to an improvement of the uniformity of the nitrogen compositions and leading to an increase of the optical quality of the alloys.

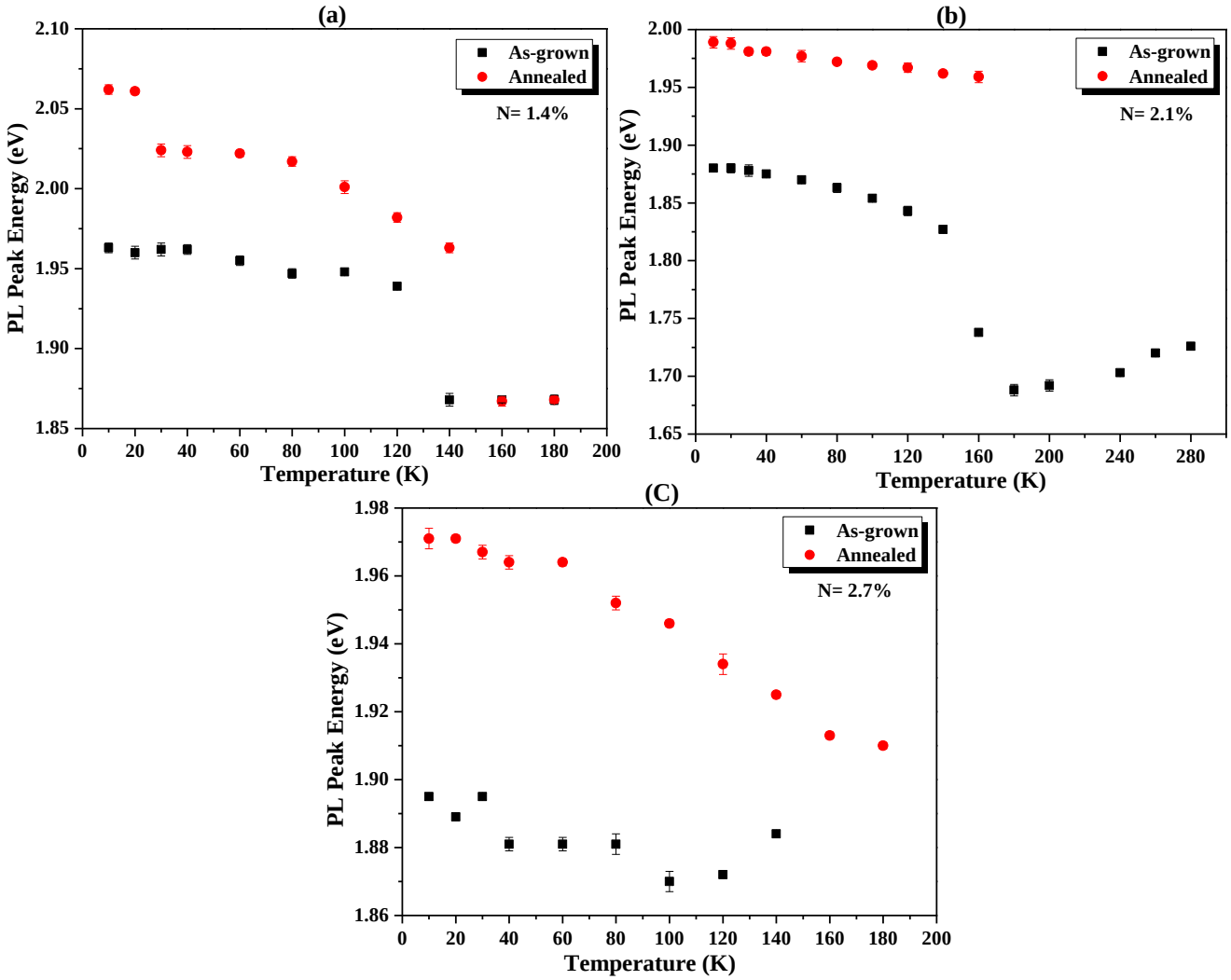


Fig. 4.7. Temperature dependence of the PL peak energy of GaPN layers before and after RTA for **(a)** N=1.4%, **(b)** N=2.1% and **(c)** N=2.7%

In addition, a clear S-shape behaviour is observed in as-grown GaPN layers with N=2.1% and 2.7%. As mentioned in the above section, this behaviour is due to carrier localization effect in the alloys after nitrogen incorporation. However, RTA significantly reduces this S-shape dependence. This means that the N localized states could be reduced by RTA due to the reduction of N related defects.

Figure 4.8 (a, b and c) illustrates the 10K and 100K PL spectra of the $GaP_{1-x}N_x$/GaP heterostructures with different nitrogen composition before and after RTA. The luminescence peak intensities for all $GaP_{1-x}N_x$ layers are increased by about 6.7 times after RTA in all samples, except for the GaPN sample with 2.1% of nitrogen, where no enhancement was noticeable at 10 K (see Fig. 4.8 (b). In the case of $GaP_{0.979}N_{0.021}$ shown in Fig. 4.8 (b), it is clear there are two peaks observed in the as-grown sample at 10K and 100K (inset). The peak which is in the range of 1.7 to 2 eV is related to the $GaP_{0.979}N_{0.021}$ emission, which is shifted after annealing to be in the range of 1.8 to 2.1eV at 10K. On the other hand, the second peak that is within the range of 1.6eV to 1.25 eV originates mainly from the N-N radiative defects [39]. These defects are annihilated after the RTA process as illustrated in Fig. 4.8 (b). In the inset of Fig. 4.8 (c) the PL signal of the as-grown $GaP_{0.973}N_{0.027}$ sample shows sharp emissions above 2 eV. These could be due to non-radiative defects [41] which are reduced after RTA (see Fig. 4.8 (c)).

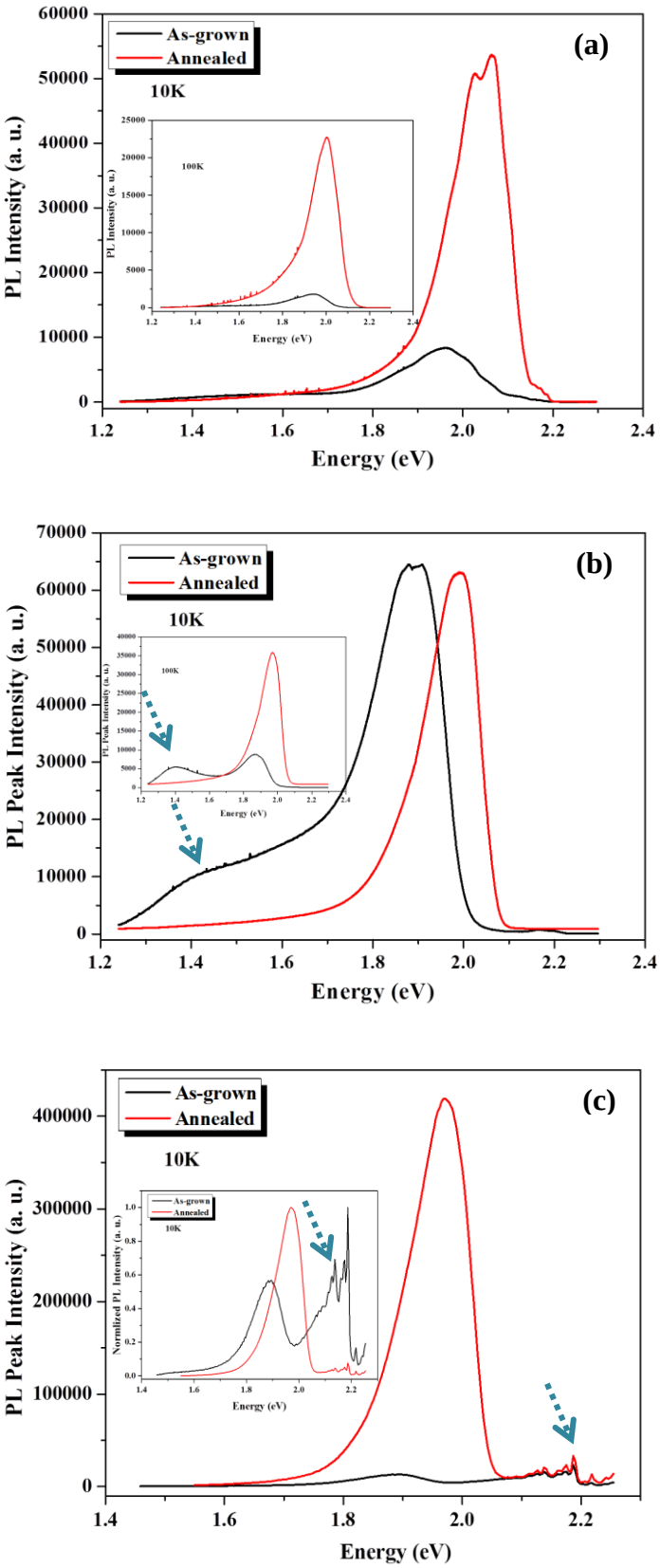


Fig. 4.8. PL spectra at 10 K and 100 K (inset) of $GaP_{1-x}N_x$/GaP heterostructures before and after RTA for **(a)** x=1.4%, **(b)** x=2.1% and **(c)** x= 2.7%.

Fig. 4.9 (a, b and c) illustrates the integrated PL intensities versus temperature for $GaP_{1-x}N_x$ alloys as well the Arrhenius fitting to assess the activation energies for PL thermal decay in different temperature regions.

The Arrhenius fitting expression is given by [41]:

$$I(T) = \left[\frac{I_0}{1 + \alpha_1 e^{\frac{-E_{a1}}{kT}} + \alpha_2 e^{\frac{-E_{a2}}{kT}}}\right] \qquad (4.10)$$

where I(T) and I_0 are the PL intensity at T, and PL intensity at the low temperature limit, respectively. E_{a1} and E_{a2} are thermal activation energies, α_1 and α_2 are the ratios between the radiative lifetime in the layer and the escape time from the layer by non-radiative processes at high temperature, and K is the Boltzmann constant.

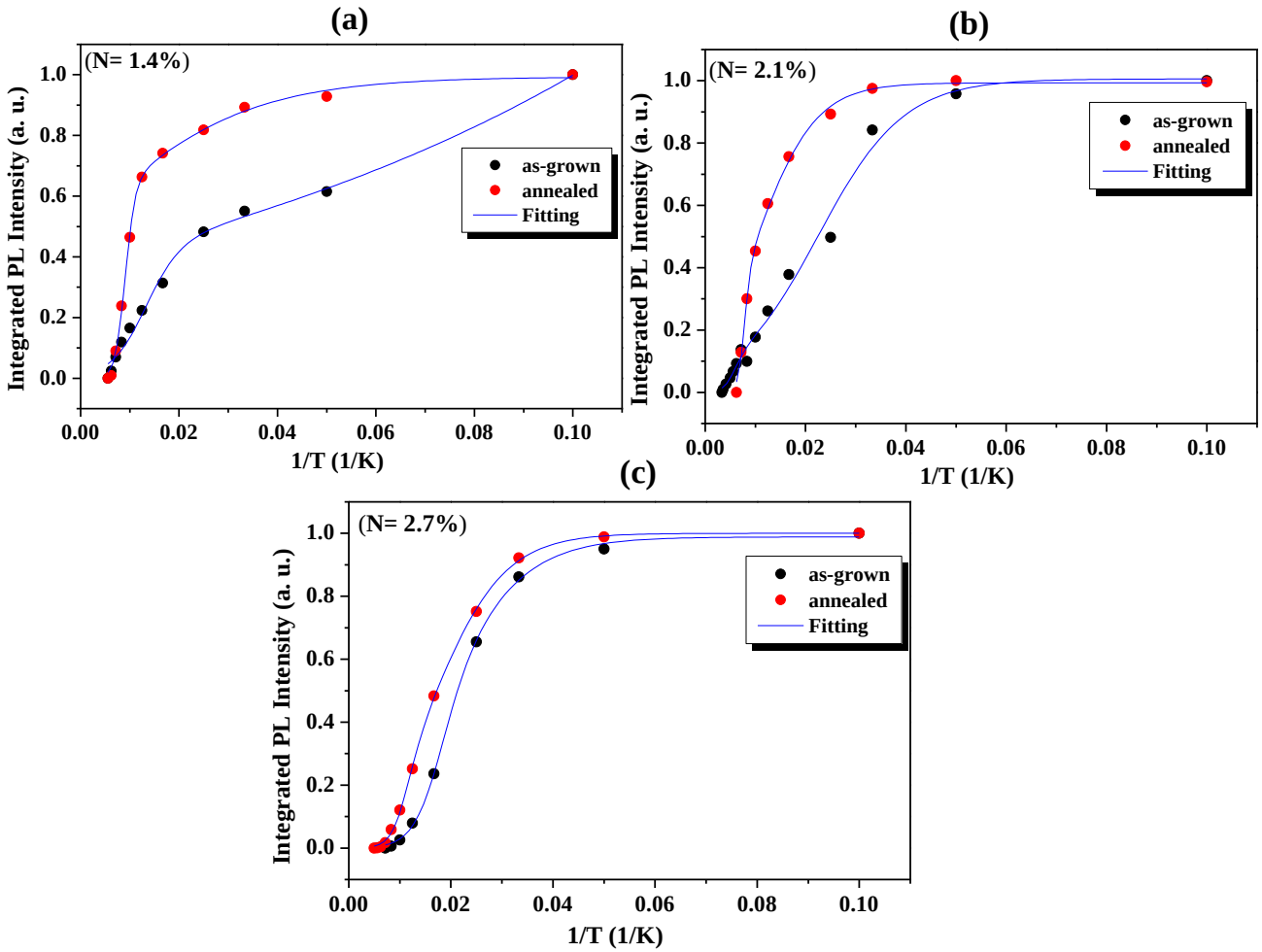


Fig. 4.9. Integrated PL intensity versus 1/T before and after RTA annealing of $GaP_{1-x}N_x$/ GaP epilayers with **(a)** x=1.4%, **(b)** x=2.1% [b] and **(c)** x=2.7%.

It is obvious that there are at least two sorts of non-radiative defects in as-grown and annealed $GaP_{1-x}N_x$ alloys indicating the presence of two quenching processes. Table 4.2 presents the values of E_{a1} and E_{a2} as well as α_1 and α_2.

After RTA the activation energy E_{a1} values for all samples increased. This could be due to a reduction of N related defects in the $GaP_{1-x}N_x$ alloy, which is confirmed by the enhancement of the optical quality of the annealed N samples. Up to the present time, there is still a lack of understanding of these types of defects and their quantities [42]. In the high temperature range, the calculated activation energy E_{a2} of all alloys increased significantly after RTA. Table 4.2 shows additionally, the corresponding ratios between radiative and non-radiative lifetimes α_1 and α_2 for all samples before and after RTA. Due to the enhancement of activation energy, these ratios have also enhanced after RTA.

Table 4.2: Arrhenius's parameters obtained from the integrated PL peak intensity versus 1/T results for as-grown and annealed $GaP_{1-x}N_x$ epilayers grown on GaP substrates.

Sample	**E_{a1} meV**	**E_{a2} meV**	**α_1**	**α_2**
as-grown $GaP_{0.986}N_{0.014}$	0.8	25.1	1	5
annealed $GaP_{0.986}N_{0.014}$	5.2	87	1	13708
as-grown $GaP_{0.979}N_{0.021}$	10.1	81.7	6	1496
annealed $GaP_{0.979}N_{0.021}$	14.6	140.1	14	711562
as-grown $GaP_{0.973}N_{0.027}$	10.3	34.9	8.5	1745
Annealed $GaP_{0.973}N_{0.027}$	12.4	59	11.6	4850

To further assess the effect of RTA on the optical quality of $GaP_{1-x}N_x$/GaP heterostructures investigated in this thesis, the full width at half maximum (FWHM) has been calculated for all samples (Fig. 4.10).

The remarkable improvement in the GaPN quality after RTA is evident from the substantial decrease in the PL line width for all samples. This considerable reduction is roughly from 200 meV down to 150 meV in $GaP_{0.986}N_{0.014}$ at low temperatures (10-120 K) (see Fig. 4.10 (a)). The FWHM data of $GaP_{0.979}N_{0.021}$ presented in Fig. 4.10 (b) before and after annealing demonstrates that annealing causes a decrease of FWHM line. In Fig. 4.10 (c) the FWHM of $GaP_{0.973}N_{0.027}$ sample shows a slight decrease in the temperature range below ~80 K. However, for temperatures above ~100K a large reduction is observed from 600 meV in the as-grown layer to approximately 100 meV in annealed samples. Such reduction in the FWHM values after RTA indicate superior material quality. The decrease of the FWHM lines observed in the annealed samples at different temperatures also indicates an improved compositional homogeneity upon annealing.

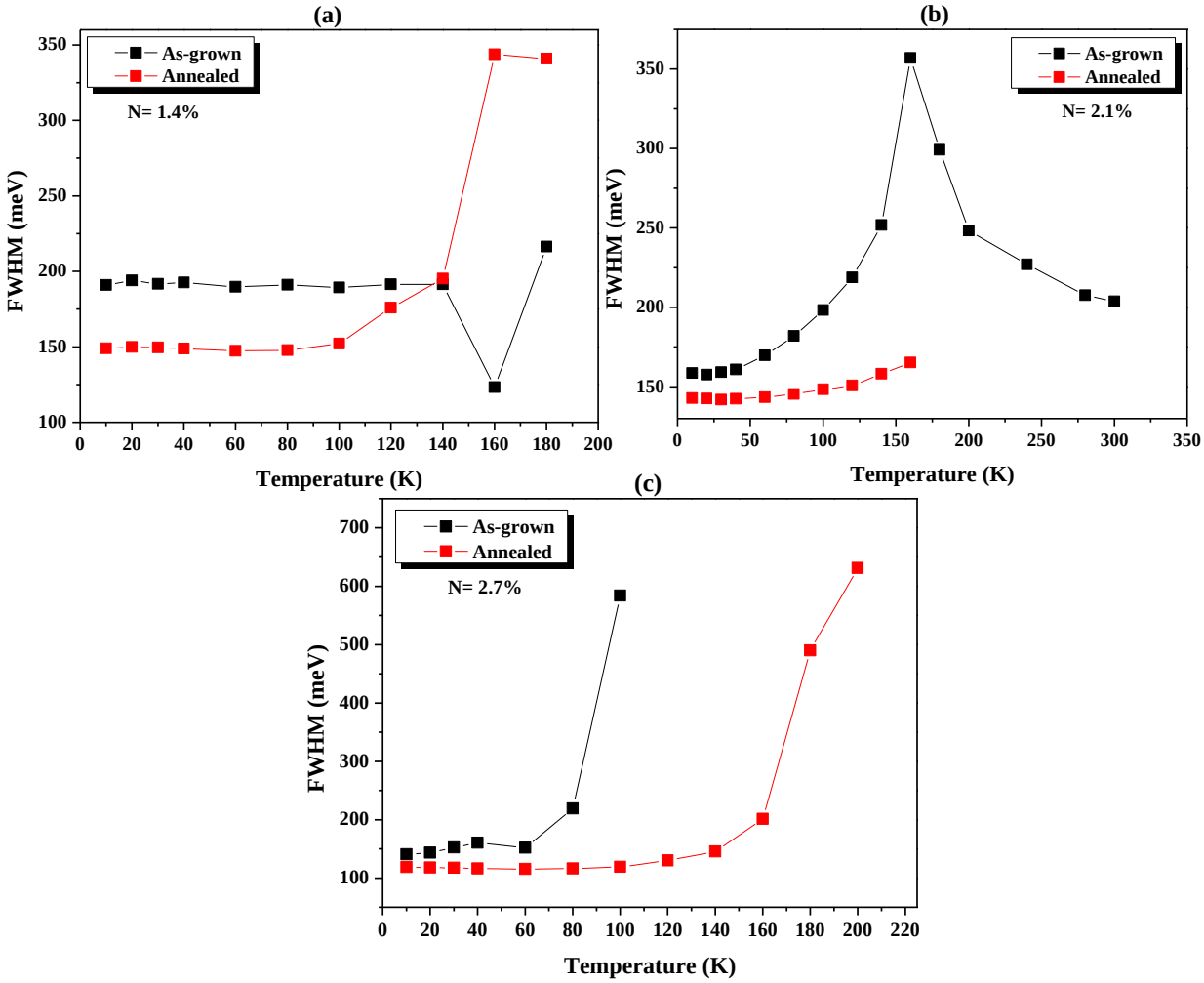


Fig. 4.10. FWHM lines of $GaP_{1-x}N_x$ epilayers before and after RTA for **(a)** x=1.4%, **(b)** x=2.1% and **(c)** x=2.7% alloys.

4.4 SUMMERY

In summary, photoluminescence (PL) measurements were performed to investigate the effect of nitrogen incorporation on carrier localization in $GaP_{1-x}N_x$ epilayers with x in the range 1.4 – 2.7%. Four main results were obtained. Firstly, GaPN has a direct bandgap after incorporating N into the GaP host lattice, due to the well-known giant bowing effect for III-V-N materials. Secondly, a redshift of the PL peak energy with increasing nitrogen content in GaPN was observed. This was attributed to the creation of N-pairs clusters and Ga defects near the CB after N incorporation. Thirdly, a decrease in the PL intensity was observed with increasing N content. This was explained by an increase in the defects related to nitrogen incorporation as well as a reduction in sample quality resulting from strain enhancement. Lastly, an S-shape behaviour has been seen in GaPN epilayers with nitrogen composition > 2%. This finding confirms the carrier localization phenomena caused by nitrogen incorporation in dilute GaPN materials.

In addition, the effect of the RTA thermal annealing at 800 °C for 5 minutes on the optical properties of GaPN with various N contents was investigated by PL technique. Primary, the PL intensity is increased after RTA for all samples. This is due to the reduction of the concentrations and or annihilation of some of the defects after heat treatment, such as nitrogen clusters and Ga vacancies. The observed blue shift after annealing was also assigned to potential fluctuations and a significant decrease in the defects which reduce the localized states. Additionally, RTA improved the optical properties of all GaPN alloys by reducing the PL linewidth and increasing in thermal activation energies. Carrier localization was reduced by RTA due to the reduction in N localized states. Generally, it was found that RTA improves the optical quality of the GaPN epilayers investigated in this study.

REFERENCES

[1] S. Kurtz, A. Allerman, E. Jones, J. Gee, J. Banas, and B. Hammons, J. Appl. Phys. Lett., **74**, 729 (1999).

[2] J. Wei, F. Xia, C. Li and S. R. Forrest, IEEE Photonics Tech. Lett. **14**, 597 (2002).

[3] G. RE, THz Workshop, Paris, France, (2008).

[4] P. Thijs, L. Tiemeijier, P. Kuindersma, J. M. Binsma and T. Van Dongen, IEEE J. Quantum Electron. **27**, 1426 (1991).

[5] I. Suemune, K. Uesugi, and W. Walukiewicz, J. Appl. Phys. Lett., **77**, 3021 (2000).

[6] I. Buyanova, W. Chen, and B. Monemar, MRS Internet J. Nitride Semicond. Res. **6**, 2 (2001).

[7] W. Shan, K. Yu, W. Walukiewicz, J. Wu, J. Ager, and E. Haller, Semicond. Sci. Technol. **17**, issue No. 8 (2002).

[8] P. Kent and A. Zunger, Phys. Rev. Lett. B **64**, 115208 (2001).

[9] S. Xie, S. Yoon and S. Wang, J. Appl. Phys. Lett., **97**, 073702 (2005).

[10] J. Geisz, D. Friedman, and S. Kurtz, IEEE, pp. 864 (2002).

[11] W. Chen, I. Buyanova, C. Tu, and H. Yonezu, Phys. B Condens. Matter , pp.376, 545 (2006).

[12] D. Friedman, J. Geisz, S. Kurtz, and J. Olson, Jornal of Crystal Growth **195**, 409 (1998).

[13] S. Spruytte, C. Coldren, J. Harris, W. Wampler, P. Krispin, K. Ploog and M. Larson, J. Appl. Phys. Lett. **89**, 4401 (2001).

[14] L. Grenouillet, C. Chevallier, G. Guillot, P. Gilet, P. Ballet, P. Duvaut, G. Rolland, and A. Million, J. Appl. Phys. Lett. **91**, 5902 (2002).

[15] I. Buyanova, G. Pozina, P. Hai, N. Thinh, J. Bergman, W. Chen, H. Xin and C. Tu, J. Appl. Phys. Lett. **77**, 2325 (2000).

[16] S. Wang, S. Yoon, W. Loke, C. Liu and S. Yuan, Jornal of Crystal Growth **255**, (2003).

[17] Y. Qiu, S. Nikishin, S. Francoeur, G. Sivaraman and H. Temkin. J. Appl. Phys. Lett., **72**, 1857 (1998).

[18] R. Kudrawiec, J. Misiewicz, E. Pavelescu, J. Konttinen, and M. Pessa. IEE. Proc.-Optoelectron., **151**, 323 (2004).

[19] E. Tournie, M. Pinault, and A. Guzman, J. Appl. Phys. Lett., **80**, 4148 (2002).

[20] T. Kondow and S. Shirakata, J. Phys. Cond. Matter, **16**, (2004).

[21] P. Melanen, P. Savolainen, P. Wei Li, J. Turpeinen and M. Pessa. J. Appl. Phys. Lett., **78**, 91 (2001).

[22] B. Damilano, J. Barjon, J. Duboz, J. Massies A. Hierro, J. Ulloa, and E. Calleja, J. Appl. Phys. Lett., **86**, 071105 (2005).

[23] T. Kim, J. Park, T. Cuong, H. Kim, H. Lee, E. Suh, and C. Hong, Jornal of Crystal Growth, **267**, 412 (2004).

[24] M. Albrecht, T. Remmele V. Grillo, H. Strunk, A. Egorov, Gh. Dumitras, and H. Riechert, J. Appl. Phys. Lett., **81**, 2719 (2002).

[25] P. Fewster, Cond. Sci. Technol., **8**, 11, 1915 (1993).

[26] J. Ibáñez, R. Kudrawiec, J. Misiewicz, M. Schmidbauer, M. Henini, and M. Hopkinson, J. Appl. Phys. Lett., **100**, 093522 (2006).

[27] http://www.ioffe.ru/SVA/NSM/Semicond/GaP/bandstr.html, [online 25/09/2017].

[28] H. Xin, C. Tu, Y. Zhang and A. Mascarenhas. J. Appl. Phys. letts. **76**, 10 1267 (2000).

[29] W. Bi, and C. Tu, J. Appl. Phys. letts. **69**, 3710 (1996).

[30] J. Baillargen, K. Chen, G. Holfl, P. Pearah, and K. Hsieh, J. Appl. Phys. Lett. **60**, 2540 (1992).

[31] Y. Zhang, A. Mascarenhas, H. Xin, and C. Tu, Phys. Rev. Lett. **63**, 161303 (2001).

[32] H. Yaguchi, S. Miyoshi, G. Biwa, M. Kibune, K. Onabe, Y. Shiraki, and R. Ito, Jornal of Crystal Growth **170**, 353 (1997).

[33] X. Liu, S. Bishop, J. Baillargeon, and K. Cheng, J. Appl. Phys. Lett. **63**, 208 (1993)

[34] L. Bellaiche, S. Wei. Phys. Rev. Lett. **56** (16) 10233 (1997).

[35] W. Shan, W. Walukiewicz, Y. KM, J. Wu, J. Ager, and E. Haller. J. Appl. Phys. Lett. **76** (22) 3251 (2000).

[36] K. PRC, A. Zunger. Phys. Rev. Lett. **86** (12) 2613 (2001).

[37] H. Xin and C. Tu, J. Appl. Phys. Lett. **77**, 2181 (2000).

[38] A. Utsumi, H. Yonezu, Y. Furukawa, K. Momose, and K. Kuroki, Physica Status Solidi (C) 0, No. **7**, 2741–2744 (2003).

[39] S. Almosni, Growth, structural and electro-optical properties of GaP/Si and GaAsPN/ GaP single junctions for lattice-matched tandem solar cells on silicon, PhD, INSA de Rennes, France, (2015).

[40] S. Olsthoorn, F. Driessen, A. Eijkelenboom, and L. Giling. J. Appl. Phys. Lett. **73** (1 l), 7798 (1993).

[41] H. Sun, S. Calvez, M. Dawson, J. Gupta, G. Aers, and G. Sproule, J. Appl. Phys. Lett. **89**, 101909 (2006).

[42] B. Kunert, D. Trusheim, V. Voßebürger, K. Volz, and W. Stolz, Physica Status Solidi (A) **205**, 114 (2008).

CHAPTER 5: INVESTIGATION OF THE EFFECTS OF ARSENIC AND INDIUM INCORPORATION AND THERMAL ANNEALING ON THE STRUCTURAL AND OPTICAL PROPERTIES of $GaP_{0.99}N_{0.01}$

This chapter reports the effect of arsenic (As) and indium (In) incorporation into $GaP_{0.99}N_{0.01}$, namely $GaAs_{0.1}P_{0.9}N_{0.01}$ and $In_{0.07}Ga_{0.93}P_{0.99}N_{0.01}$ quaternary alloys grown by Molecular Beam Epitaxy (MBE) on (100) GaP substrates, on their structural and optical properties using HR-XRD, XSR, and PL techniques. In addition, the effects of rapid thermal annealing (RTA) on the structural and optical properties of $GaAs_{0.1}P_{0.89}N_{0.01}$ and $In_{0.07}Ga_{0.93}P_{0.99}N_{0.01}$ are also investigated.

5.1 INTRODUCTION

Recently, III-V-N dilutes nitrides have received significant attention due to their unique optical and electrical properties. They have been used in optoelectronic and photovoltaic applications. For example, GaPN materials are used to develop high efficiencies solar cells [1-2]. Adding 2% of N into GaP host material resulted in a change of the nature of the bandgap, i.e. from indirect (2.26 eV) to pseudo-direct bandgap (1.9 eV) [3] at room temperature (RT). Thus, this allows the control of new optical and electrical properties of GaPN. In addition, various ions have been added to modify further GaPN's properties and reduce the band gap to reach near 1.8 eV [4-5]. The most attractive atoms are arsenic (As) and indium (In) which have been used for the fabrication of quaternary GaAsPN and InGaPN materials based solar cells with high photovoltaic efficiency. However, the composition of As and In in GaAsPN and InGaPN, respectively, have to be controlled in order to satisfy the lattice matching conditions [6]. In the following section the effect of the As and In

compositions on the bandgap of the GaAsPN and InGaPN quartenary materials and the critical thickness, known as the thickness above which misfit dislocations are created, will be discussed.

7.1.1 BANDGAPS OF GaAsPN AND InGaPN

By using sp3d5s*sN tight-binding calculations adjusted for the description of nitrogen incorporation in diluted regimes, the GaAsPN and InGaPN bandgaps are determined [7-8]. This model has been shown to agree with the experimental data with good accuracy [8]. The black lines (solid and dashed) in Fig. 5.1 present the nitrogen amount required for quaternary alloys to be lattice-matched with a (001)-oriented silicon substrate, as a function of As or In content. Moreover, the red lines (solid and dashed) show the bandgap calculation of the corresponding alloy. For example, the GaAsPN (InGaPN) alloy with an As (In) content equal to 18% would need 6% (10%) of N to be lattice-matched with Si, giving an alloy with an energy bandgap of 1.58 (1.32) eV [1]. It is clear from the calculated data shown in Fig. 5.1 that the optimized structure of lattice-matched $GaAs_xP_yN_{(1-x-y)}$ and $In_xGa_{1-x}P_{1-y}N_y$ is $GaAs_{0.122}P_{0.83}N_{0.048}$ and $In_{0.07}Ga_{0.83}P_{0.95}N_{0.05}$, respectively, to ensure a 1.8 eV bandgap energy. However, it is known that diluted nitrides layers with high N composition display poor structural quality because of the low solubility of N in GaP, however, these structural properties have been enhanced by annealing processes [9-10]. The main goal is to achieve a pseudomorphic growth by keeping the grown layers under critical thickness [3]. This could help increase the As incorporation in order to achieve the expected 1.8 eV bandgap while keeping the amount of incorporated nitrogen atom low.

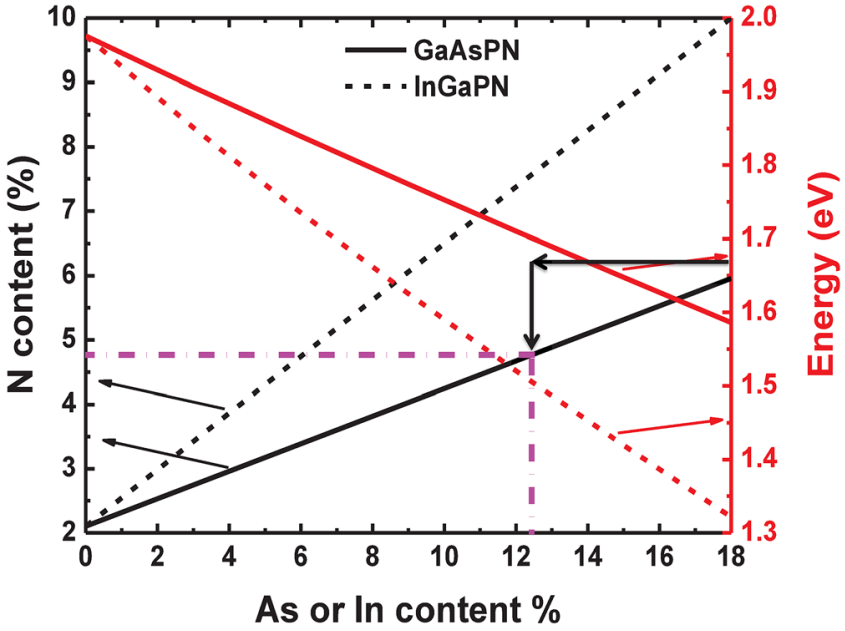


Fig. 5.1. Bandgap and composition of GaAsPN and InGaPN alloys lattice matched with Si. Black lines represent the evolution of nitrogen content in GaAsPN (solid line) or InGaPN (dashed line) alloys as a function of As or In content to get the exact lattice matching with silicon substrates. Red lines give the bandgap energy for the corresponding GaAsPN (solid line) or InGaPN (dashed line) alloys, as determined with sp3d5s*sN tight binding calculations [3].

5.1.2 CRITICAL THICKNESS OF GaAsPN AND InGaPN

The critical thickness of the film (h_c), is defined as the thickness beyond which dislocations are introduced [11].

Taking into consideration that the ideal thicknesses of deposited III-V layers on silicon in tandem solar cells are around 1μm, this value was considered in the following as a lower limit for the critical thickness. Matthews and Blakeslee reported a relationship that can be used to determine the critical thickness of those materials [12].

$$h_c \cong \left(\frac{b}{f}\right)\left(\frac{1}{8\pi(1+\nu)}\right)\left(\ln\left(\frac{h_c}{b}\right)+1\right) \qquad (5.1)$$

where f is the lattice mismatch, b is the intensity of the burgers vector, ν is the Poisson ratio of the thin layer, and h_c is the critical thickness (CT).This model with above equation has been shown to provide a good agreement with the experimental data [3] . Fig. 5.2 (a) and (b)

illustrates the iso-contour plots of the CT for GaAsPN and InGaPN between 100 nm and 1 µm, as a function of nitrogen concentration and As and In content, respectively. With the absence of N and As, the value for the GaP/Si CT has been found to be equal to 40 nm [3]. This value is coherent with the experimental findings [13-14].

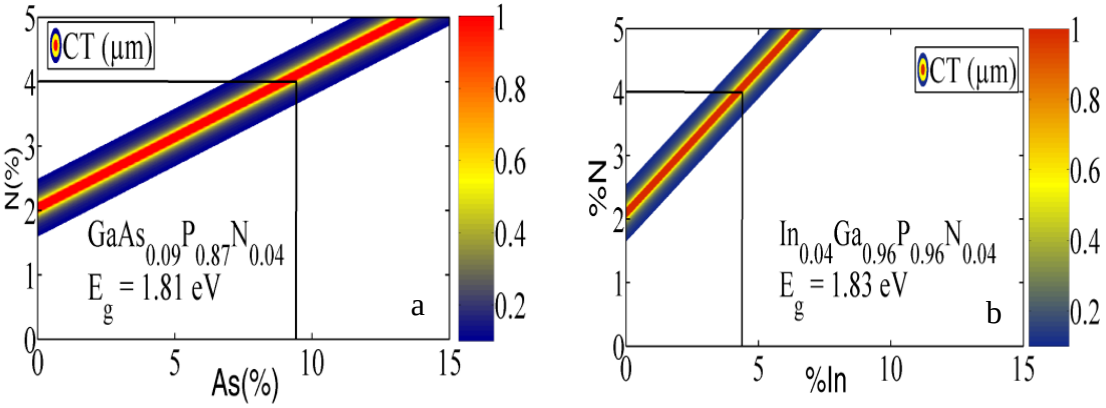


Fig. 5.2. Iso-contour plot of the critical thickness (CT) for **(a)** GaAsPN and **(b)** InGaPN alloys between 100 and 1000 nm [3].

Almosni [3] reported that in the case of the GaAsPN alloy, assuming a 1µm threshold of CT and a maximum of 4% nitrogen for a reasonable crystalline quality, the As content is equal to 9%. Thus, with regard to tight-binding calculations, this would grant a 1.81 eV bandgap for the $GaAs_{0.09}P_{0.87}N_{0.04}$ alloy, which is the ideal 1.8 eV energy bandgap [3]. Furthermore, for InGaPN case (see Fig. 5.2 (b)), keeping the same threshold and the same nitrogen limit of 4%, the indium content is equal to about 4%. However, for an In content of 6% in $In_{0.06}Ga_{0.94}P_{0.96}N_{0.04}$ alloy the calculations of tight-binding give a bandgap energy of 1.83 eV [3]. As a result, it is obvious that GaAsPN alloy reaches slightly lower bandgap than the InGaPN alloy.

In summary, incorporating a small percentage of nitrogen atoms, as well as arsenic and indium into the host lattice of dilute III-V nitride semiconductors allow the synthesis of novel materials with a bandgap energy of 1.8 eV, which are required for Si tandem solar cells [15]. In addition, these new materials could have unprecedented optical and electrical properties.

As mentioned in previous chapters, RTA has a strong treatment impact on III-V-N materials. Therefore, it is important to study the influence of RTA on the $GaAs_{0.1}P_{0.89}N_{0.01}$ and $In_{0.07}Ga_{0.93}P_{0.99}N_{0.01}$ quaternary compounds.

In this work, the effects of arsenic (10%) and indium (7%) incorporation in $GaP_{0.99}N_{0.01}$ and the RTA annealing process on the structural and optical of $GaAs_{0.1}P_{0.89}N_{0.01}$ and $In_{0.07}Ga_{0.93}P_{0.99}N_{0.01}$ will be investigated. All samples, namely $GaAs_{0.1}P_{0.89}N_{0.01}$ and $In_{0.07}Ga_{0.93}P_{0.99}N_{0.01}$, reported here are grown by Molecular Beam Epitaxy (MBE) on (100) GaP substrates. These experiments were performed by using HR-XRD, XSR and PL techniques.

5.2 SAMPLES DETAILS

The samples growth details are discussed in chapter 3. Briefly, the $GaAs_{0.1}P_{0.89}N_{0.01}$ and $In_{0.07}Ga_{0.93}P_{0.99}N_{0.01}$structures are grown in a solid source MBE with a 10 nm GaP capping layer on (100) GaP substrates. In the growth chamber, the fluxes of arsenide and indium are set in order to achieve 10% and 7%, respectively. A valved RF plasma source has been used to incorporate a 1% of nitrogen. The $GaAs_{0.1}P_{0.89}N_{0.01}$ and $In_{0.07}Ga_{0.93}P_{0.99}N_{0.01}$layers are 100 nm thick as shown in Figure 5.3 (a) and (b), respectively. The growth temperature was 480 °C with a growth rate equals to 0.5 monolayer (ML)/s. These samples are grown under V/III BEP flux ratio which is 10. Phosphorus flux is 7 µtorr.

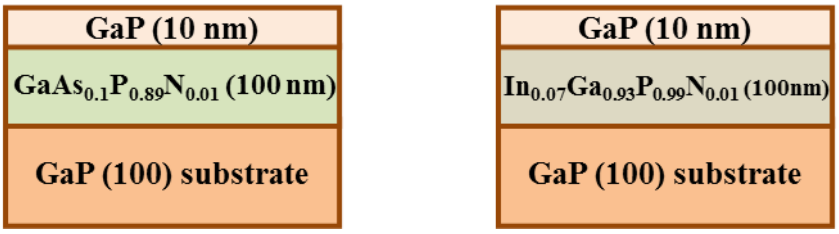


Fig. 5.3. Schematic diagram of **(a)** $GaAs_{0.1}P_{0.89}N_{0.01}$ **(b)** $In_{0.07}Ga_{0.93}P_{0.99}N_{0.01}$ dilutes nitrides.

These samples will be compared with $GaP_{0.99}N_{0.01}$ with N content of 1%. Rapid thermal annealing (RTA) process was carried out at 800°C for 5 minutes.

5.3 RESULTS AND DISCUSSION

In this section the structural and optical properties of the samples discussed in the above section using HR-XRD, XSR and PL measurements will be reported.

5.3.1 INVESTIGATION OF STRUCTURAL PROPERTIES OF AS-GROWN AND ANNEALED $GaAs_{0.1}P_{0.89}N_{0.01}$ and $In_{0.07}Ga_{0.93}P_{0.99}N_{0.01}$

For investigations of structural properties of thin epitaxial films, similar procedure has been used as explained in chapter 4 by performing HR-XRD and XSR.

HR-XRD measurements were performed on $GaAs_{0.1}P_{0.89}N_{0.01}$ and $In_{0.07}Ga_{0.93}P_{0.99}N_{0.01}$ layers grown on (100) GaP substrates after centring and optimizing the 004 symmetrical Bragg reflections. The composition of GaAsPN and InGaPN quaternary films can be determined by x-ray reflection from the (004) plane. As the crystallographic parameters such as lattice constant and spacing between the planes of the substrate and epitaxial layer are different, an x-ray diffraction pattern as a function of angle will show at least two peaks corresponding to the satisfied Bragg conditions for the substrate and the epilayer of $GaAs_{0.1}P_{0.89}N_{0.01}$ and $In_{0.07}Ga_{0.93}P_{0.99}N_{0.01}$.

If a(GaP) (a is a lattice constant)= 5.4505 Å (reference value), a(GaAs) = 5.65325 Å and a(InP) = 5.8687 Å , then the composition of ($GaAs_xP_{1-x}$) and (Ga_xIn_{1-x} P) can be calculated using Vegard's law [16] as following:

$$a(GaAs_xP_{1-x}) = a(GaAs) \cdot x + a(GaP) \cdot (1-x) = 5.4505\ Å + 0.20275\ Å \cdot x \qquad (5.2(a))$$

$$a(GaAs_{0.1}P_{0.9}) = 5.4505\ Å + 0.20275\ Å \cdot 0.1 = 5.4708\ Å$$

$$a(Ga_xIn_{1-x}P) = a(GaP) \cdot x + a(InP) \cdot (1-x) = 5.8687\ Å - 0.4182\ Å \cdot x \qquad (5.2\ (b))$$

$$a(Ga_{0.93}In_{0.07}P) = 5.8687\ Å - 0.4182\ Å \cdot 0.93 = 5.4798\ Å$$

Then distortion coefficient *P* for the sample grown on (100) GaP, as explained in equation (4.9) in previous chapter [17] and given that the N content of our samples is low, the elastic constants of GaAs are used to calculate *P*. These are C_{11} = 119 GPa, C_{12} = 53.4 GPa and C_{44} = 59.6 GPa. The value obtained are P_{100}= 0.527. For InP elastic constant are These are C_{11} = 101.1 GPa, C_{12} = 56.1 GPa and C_{44} = 45.6 GPa. Thus, the P_{100}= 0.474.

HR-XRD and XSR curves (2θ scans) obtained from as-grown and annealed ($GaAs_{0.1}P_{0.89}N_{0.01}$) and ($In_{0.07}Ga_{0.93}P_{0.99}N_{0.01}$) epilayers grown under near-stoichiometric conditions on (100) GaP substrates are shown in Fig. 5.4 (a) and Fig. 5.4 (b), respectively.

With regard to XSR results illustrated in Fig. 5.4 (a) pronounced Kiessing fringes were observed. In other words, the surfaces of both as-grown and annealed samples are rough. Moreover, it is clear that XSR measurements for as-grown samples exhibit peak at around 2θ=2, which disappears after the annealing process. Thus, the samples have different surface roughness before and after annealing. Fig. 5.4 (b) shows slight damping of fringes and a decrease of peak intensity after RTA. This gives an indication of increasing disorder in the epitaxial layer. All these results indicate that the vertical lattice parameters are not identical for as-grown and annealed $GaAs_{0.1}P_{0.89}N_{0.01}$ layers.

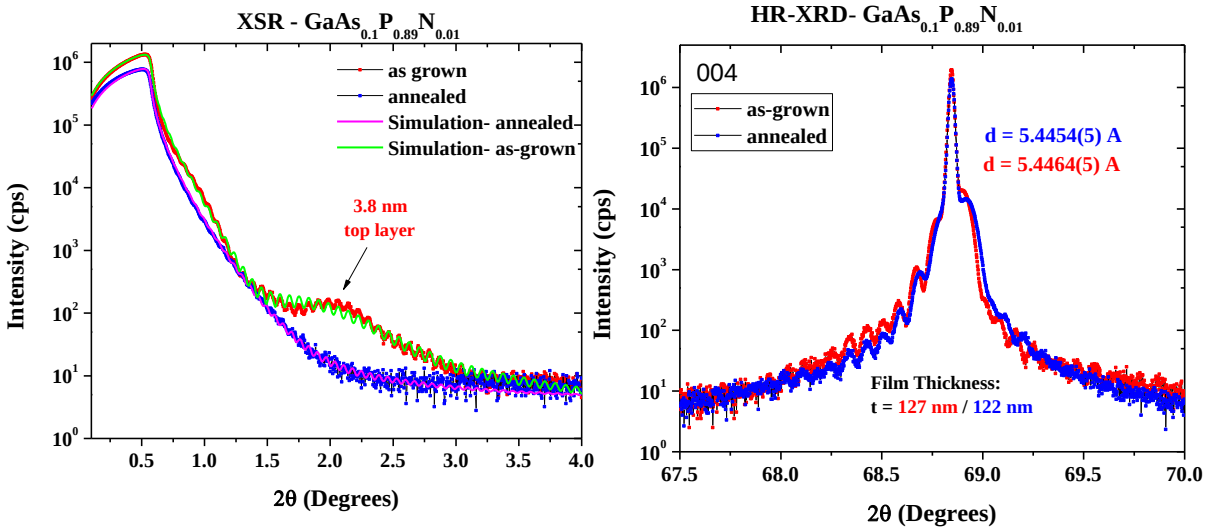


Fig. 5.4. (a) XSR measurements for $GaAs_{0.1}P_{0.89}N_{0.01}$, **(b)** HR-XRD measurements for $GaAs_{0.1}P_{0.89}N_{0.01}$.

It is noted that RTA leads to an increase of the surface roughness from ≈1.5 nm to ≈2.1 nm as shown in Table 5.1. Furthermore, it is obvious from Table 5.1 that there is a small reduction of the vertical lattice parameters after RTA which reduces the thickness from 127nm to 122nm. There is no significant N-induced change in the vertical lattice spacing after annealing.

Table 5.1: Main structural results from HR-XRD before and after RTA for $GaAs_{0.1}P_{0.89}N_{0.01}$.

Sample	**Vertical lattice spacing (Å)**	**Root Mean Square (RMS) Surface Roughness (nm)**	**Thickness (nm)**	**Nitrogen induced change in vertical lattice spacing**
$GaAs_{0.1}P_{0.89}N_{0.01}$ **as-grown**	5.4464	≈ 1.5	127	-0.0079
$GaAs_{0.1}P_{0.89}N_{0.01}$ **annealed**	5.4454	≈ 2.1	122	-0.0077

For as-grown and annealed $In_{0.07}Ga_{0.93}P_{0.99}N_{0.01}$ layers which are grown under near-stoichiometric conditions on (100) GaP substrates, XSR and HR-XRD curves are illustrated in Fig. 5.5 (a) and 5.5 (b), respectively. In Fig. 5.5 (a) no Kiessing fringes were observed indicating rough surfaces for both samples. Moreover, the measurements of XSR for both samples show similar slopes, evidencing the identical surface roughness for these samples.

Fig. 5.5 (b) shows that no measurable qualitative difference between as-grown and annealed samples. This means that there is no change in the epitaxial layer disorder. However, a very small difference in the 2θ value of layer reflections between as-grown and annealed $In_{0.07}Ga_{0.93}P_{0.99}N_{0.01}$. It is noticed that this could be accounted for by the experimental error.

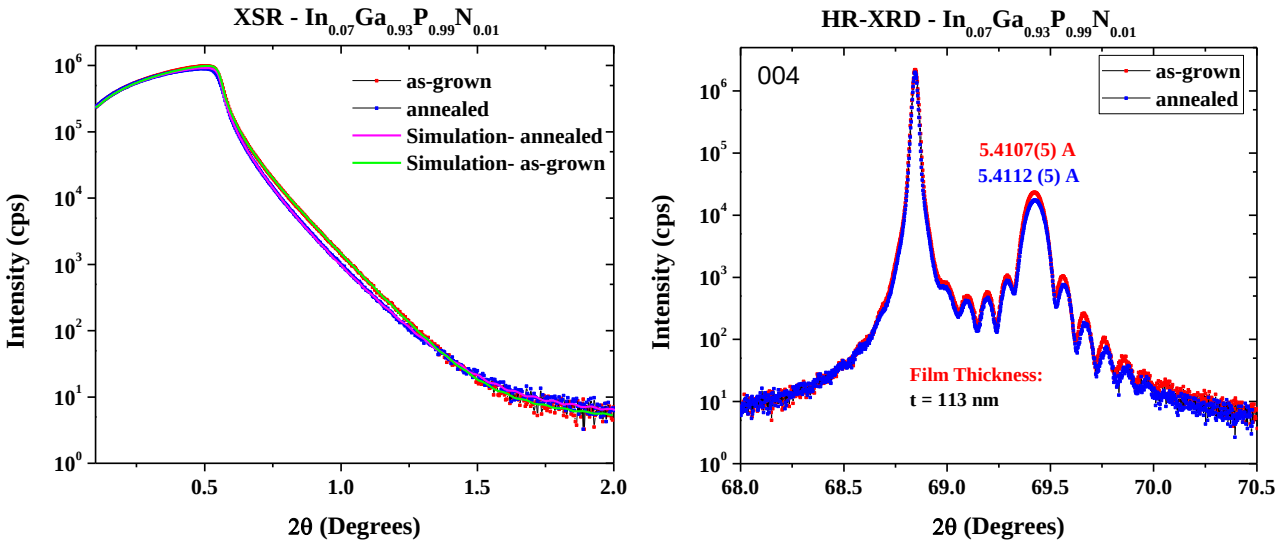


Fig. 5.5. (a) XSR measurements for $In_{0.07}Ga_{0.93}P_{0.99}N_{0.01,}$ **(b)** HR-XRD measurements for $In_{0.07}Ga_{0.93}P_{0.99}N_{0.01}$.

As a result, RTA leads to no measurable effect on the lattice parameter, and no noted nitrogen induced change in vertical lattice spacing, as well as no impact on surface roughness (see Table 5.2).

Table 5.2: Main structural results from HR-XRD before and after RTA for $In_{0.07}Ga_{0.93}P_{0.99}N_{0.01}$.

Sample	Vertical lattice spacing (Å)	Root Mean Square (RMS) Surface Roughness (nm)	Thickness (nm)	Nitrogen induced change in vertical lattice spacing
$In_{0.07}Ga_{0.93}P_{0.99}N_{0.01}$ **as-grown**	5.4107	≈ 2.5	113	-0.0173
$In_{0.07}Ga_{0.93}P_{0.99}N_{0.01}$ **annealed**	5.4112	≈ 2.5	113	-0.0172

5.3.2 OPTICAL PROPERTIES OF $GaAs_{0.1}P_{0.89}N_{0.01}$ and $In_{0.07}Ga_{0.93}P_{0.99}N_{0.01}$

The samples were excited using a blue laser with a wavelength of 473nm and a power of 16mW.

From previous studies, it was proven that adding a small number of atoms into III-V-N materials leads to a change of the bandgap energy [6]. For example, incorporation of arsenic

(As) and indium (In) into GaPN leads to a reduction of the bandgap from ≃1.9 eV to ≃1.8 eV at room temperature [1]. Fig. 5.6 illustrates the PL spectra of $GaP_{0.99}N_{0.01}$, $GaAs_{0.1}P_{0.89}N_{0.01}$ and $In_{0.07}Ga_{0.93}P_{0.99}N_{0.01}$ at 10 K.

It is clear that after adding 10% of As and 7% of In to $GaP_{0.99}N_{0.01}$, the peak PL energy shifts to lower value, namely from 1.96 eV to ≃1.8 eV and ≃1.82 eV, $GaP_{0.99}N_{0.01}$, $GaAs_{0.1}P_{0.89}N_{0.01}$ and $In_{0.07}Ga_{0.93}P_{0.99}N_{0.01}$, respectively (see Fig. 5.6). It is important to note that a lower In composition as compared to As (10%) results in an energy shift closer to the ideal 1.8 eV energy bandgap suitable for tandem solar cells using Si. In the case of $GaAs_{0.1}P_{0.89}N_{0.01}$, this result can be attributed to a lowering of the density of non-radiative (NR) centres [3]. Thus, this could be explained by the fact that the generation of NR traps is dependent on strain effects induced by N incorporation. This is confirmed by the fact that Ga_i has been created due to the incorporation of nitrogen, which could be decreased by adding As into $GaP_{0.99}N_{0.01}$ [18]. With regard to the energy reduction in $In_{0.07}Ga_{0.93}P_{0.99}N_{0.01}$, this could be because of the reported high degree of lattice mismatch between $In_{0.07}Ga_{0.93}P_{0.99}N_{0.01}$ on GaP substrate [3] that leads to increase the defects. In general, the Eg observed in both materials reaches the target energy value for solar cells based materials on Si which is 1.8 eV.

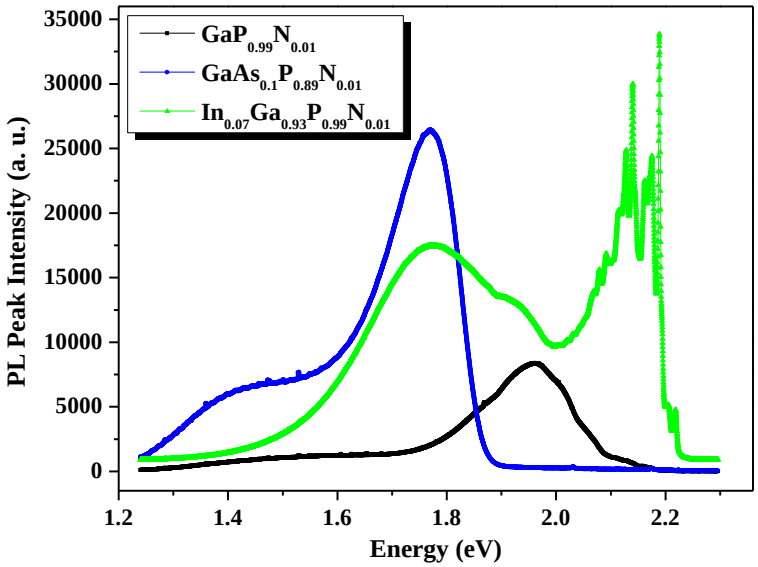


Fig. 5.6. PL intensity *vs* photon energy for $GaP_{0.99}N_{0.01}$, $GaAs_{0.1}P_{0.89}N_{0.01}$, and $In_{0.07}Ga_{0.93}P_{0.99}N_{0.01}$ at 10K.

It is clear from Fig. 5.6 that the PL intensity increases by incorporating arsenic and indium in $GaP_{0.99}N_{0.01}$ by roughly a factor of 3.2 times and 2.1 times, respectively. The nitrogen incorporation into GaP leads to a decrease of the crystal lattice constant and the formation of elastic stresses in the epitaxial layer upon pseudomorphic growth on GaP substrates [19]. Adding arsenic and/or indium in GaPN result in an increase of the crystal lattice constant and the compensation of elastic stresses originating by the incorporation of nitrogen [19]. As can be seen in Fig. 5.6 the PL peak intensity for the $In_{0.07}Ga_{0.93}P_{0.99}N_{0.01}$ layer is lower than that of the $GaAs_{0.1}P_{0.89}N_{0.01}$ layer by almost a factor of 1.6. This could be attributed to the fact that the concentration of defects in the $In_{0.07}Ga_{0.93}P_{0.99}N_{0.01}$ layer is higher [19]. The indium incorporation leads to the compensation of elastic stresses, but indium is incorporated in the sub-lattice of group III elements. Such a method of compensation is clearly worse than adding arsenic, which compensates elastic stresses caused by nitrogen in the sub-lattice of group V. The compensation of stresses by arsenic substitution into group V eliminates the formation of defects, which was reported in a previous study [20]. This means that $GaAs_{0.1}P_{0.89}N_{0.01}$materials could be better suited for solar cells application on Si substrates because of its higher quality than $In_{0.07}Ga_{0.93}P_{0.99}N_{0.01}$ based materials.

Moreover, Fig. 5.6 shows a broad peak in the energy range of 1.23-1.5eV for $GaAs_{0.1}P_{0.89}N_{0.01}$. This could be caused by the NR defects which originated after incorporating arsenic into GaPN [21]. These NR defects are reported in earlier study as defect complexes involving As_{Ga} antisite [21]. Fig.5.6 also displays sharp peaks for $In_{0.07}Ga_{0.93}P_{0.99}N_{0.01}$ in the energy range from 2eV to 2.2eV, which are also related to NR defects that are Ga_i self-interstitials after nitrogen incorporation [21].

It is very important to plot the temperature dependence for all samples for comparison purposed as shown in Fig. 5.7. Clearly, all three samples display the S-shape behaviour but over different temperature ranges. $GaP_{0.99}N_{0.01}$, $GaAs_{0.1}P_{0.89}N_{0.01}$ and $In_{0.07}Ga_{0.93}P_{0.99}N_{0.01}$

display the S-shape over the temperature range 40K-140K, 40K-160K, and 20K-300K, respectively. This is due to the carrier localization effect which causes by incorporating N into $GaP_{0.99}N_{0.01}$, $GaAs_{0.1}P_{0.89}N_{0.01}$ and $In_{0.07}Ga_{0.93}P_{0.99}N_{0.01}$ [3].

In the case of $In_{0.07}Ga_{0.93}P_{0.99}N_{0.01}$ alloys, the S-shape is also attributed to that incorporation of indium leads to a disturbance of the localized states caused by indium fluctuations [19].

This is also assigned for a broad peak of this material as it is shown in Fig. 5.6 in the energy range of 1.5-2eV.

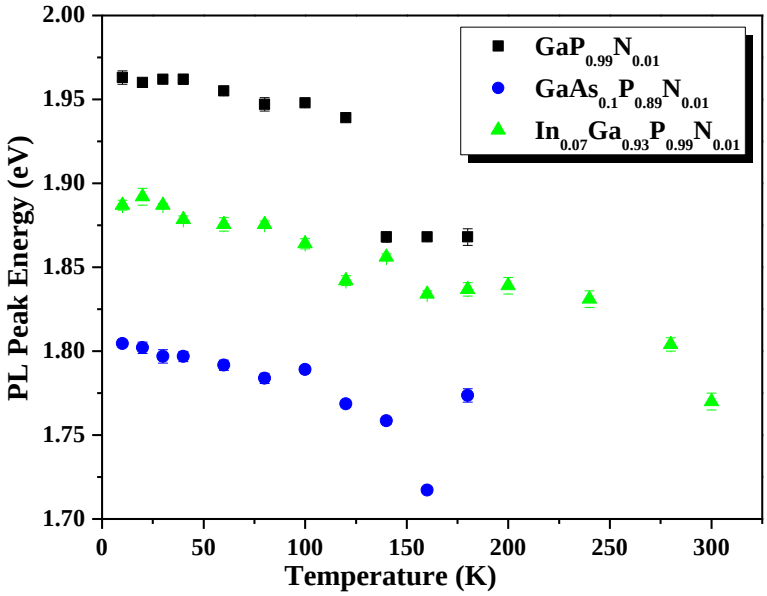


Fig. 5.7. Temperature dependence of PL peak energy of $GaP_{0.99}N_{0.01}$, $GaAs_{0.1}P_{0.89}N_{0.01}$, and $In_{0.07}Ga_{0.93}P_{0.99}N_{0.01}$.

Full Width at Half Maximum (FWHM) curves for $GaP_{0.99}N_{0.01}$, $GaAs_{0.1}P_{0.89}N_{0.01}$, and $In_{0.07}Ga_{0.93}P_{0.99}N_{0.01}$ alloys are presented in Fig. 5.8. It is clear from Fig. 5.8. that $GaAs_{0.1}P_{0.89}N_{0.01}$ has the narrowest linewidth (i.e. smallest FWHM values) in the low temperature range (under 140K). This means that the optical quality of $GaAs_{0.1}P_{0.89}N_{0.01}$ is higher than that of $GaP_{0.99}N_{0.01}$ and $In_{0.07}Ga_{0.93}P_{0.99}N_{0.01}$, indicating a good level of lattice matching between the $GaAs_{0.1}P_{0.89}N_{0.01}$ layer and GaP substrate.

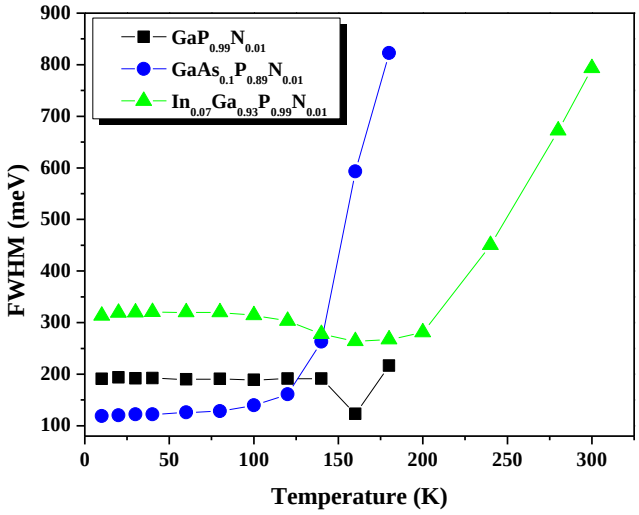


Fig. 5.8. Full Width at Half Maximum (FWHM) of $GaP_{0.99}N_{0.01}$, $GaAs_{0.1}P_{0.89}N_{0.01}$, and $In_{0.07}Ga_{0.93}P_{0.99}N_{0.01}$.

As shown in Fig. 5.8, $In_{0.07}Ga_{0.93}P_{0.99}N_{0.01}$ sample has the highest value of FWHM in the temperature range 10K-140K, which could indicate a large mismatch between $In_{0.07}Ga_{0.93}P_{0.99}N_{0.01}$ layer and GaP substrate, and therefore leading to a poor crystalline quality and a high rate of nonradiative recombination [1]. Therefore, all the above results obtained in this study indicate that $GaAs_{0.1}P_{0.89}N_{0.01}$ is the best choice to fabricate good efficiency solar cells-based materials on Si substrates.

5.3.3 INVESTIGATION OF RTA EFFECT ON THE OPTICAL PROPERTIES OF $GaAs_{0.1}P_{0.89}N_{0.01}$, AND $In_{0.07}Ga_{0.93}P_{0.99}N_{0.01}$

In order to investigate the effect of RTA on the luminescence properties of these quaternary alloys, photoluminescence measurements at different temperatures (10 K- 300 K) were performed for annealed samples using the same PL experimental conditions as the as-grown samples. The details of the annealing procedure were described in Chapter 3, however, briefly the samples were heat treated at 800°C for 5 minutes.

5.3.3.1 THE $GaAs_{0.1}P_{0.89}N_{0.01}$ CASE

Fig. 5.9 presents the photon energy with luminescence intensity for $GaAs_{0.1}P_{0.89}N_{0.01}$ and $In_{0.07}Ga_{0.93}P_{0.99}N_{0.01}$ alloys before and after RTA. It can be seen that the annealing process

leads to an enhancement of the optical properties as demonstrated by the PL intensity increase by approximately a factor of 13.

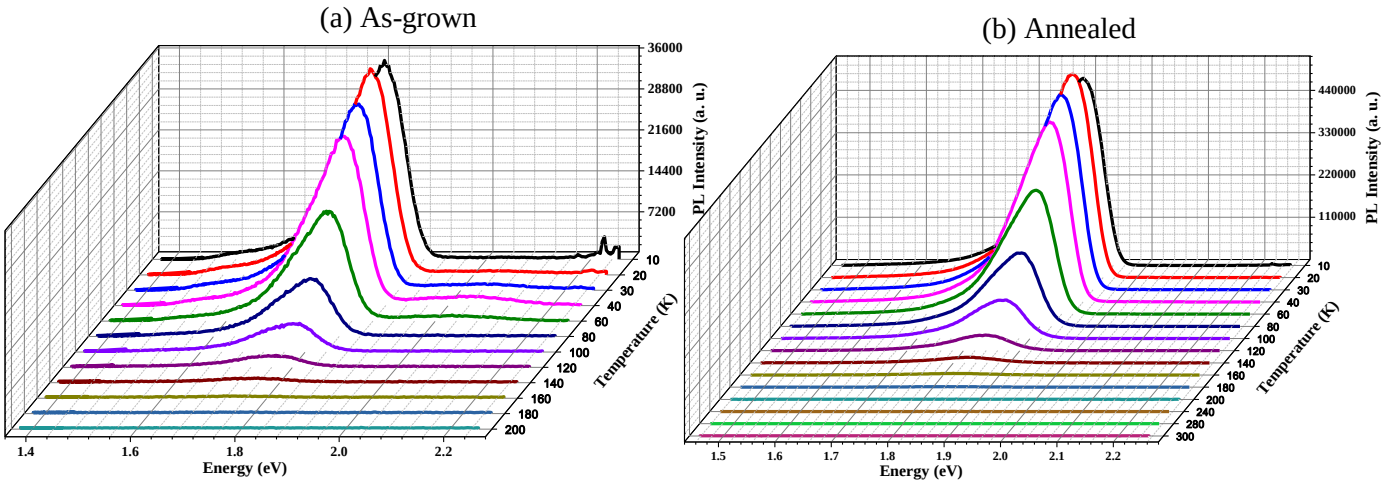


Fig. 5.9. Photon energy *vs* PL intensity spectra at different temperatures for **(a)** as-grown and **(b)** annealed of $GaAs_{0.1}P_{0.89}N_{0.01}$.

This is not a surprise in dilute nitride materials, as the N incorporation into GaAsP leads to the presence of a random distribution of nitrogen clusters and isolated nitrogen impurity states in the crystals [22-23]. By subjecting this alloy to an RTA temperature of 800°C, a thermal energy applied for the change in group V atom configuration i.e., a change in the nearest neighbour environment of Ga atoms [24]. This significantly results in a reduction in the defect density and an increase in layer absorption [24-25]

In addition, after RTA a blue-shift is observed at all temperatures as evidenced in Fig. 5.9. This is clearly seen in Fig. 5.10, which presents the normalized PL peaks with photon energy at 10 K, as well as in Fig. 5.11 (a), which presents the temperature dependence of the PL peak energy.

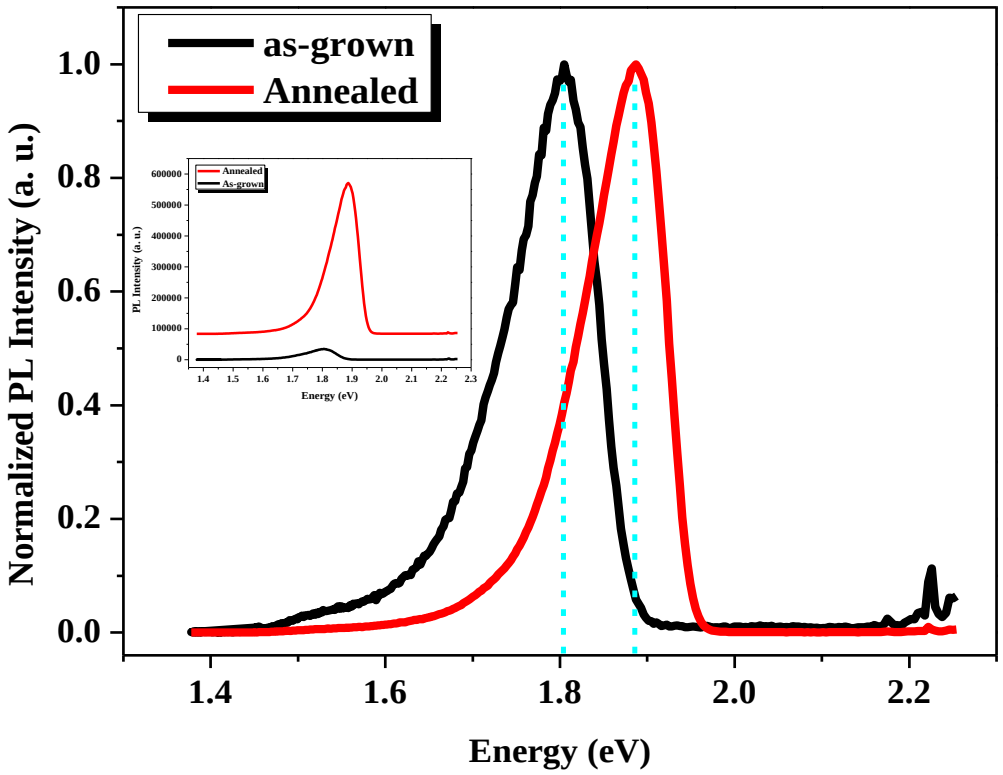


Fig. 5.10. Normalized PL intensity for $GaAs_{0.1}P_{0.89}N_{0.01}$ before and after RTA.

Obviously, the PL energy shifts to higher energy (from 1.8 eV to ≃ 1.9 eV) after annealing treatment. The mechanism of this could be attributed to the fact that by annealing the increase in the luminescence intensity evidences a decrease of point defects in the layers and /or radiative localised states in the bandgap [26]. The annihilation of these defects result in an enhancement in carrier concentration and radiative recombination processes at the band edges, which could lead to a luminescence shift towards higher energy.

The PL peak energy positions and FWHM of the as-grown and annealed $GaAs_{0.1}P_{0.89}N_{0.01}$ alloys over the temperature range 10-300K are plotted in Fig. 5.11 (a) and Fig. 5.11 (b), respectively. The S-shape behaviour is also observed in the annealed sample (see Fig. 5.11 (a)). This impact could be clarified by the effect of strain on N incorporation, as the increase of the N content leads to a strain reduction in samples with high As content. Additionally, the

N composition could be promoted by the higher surface roughness of the sample with high As content [27].

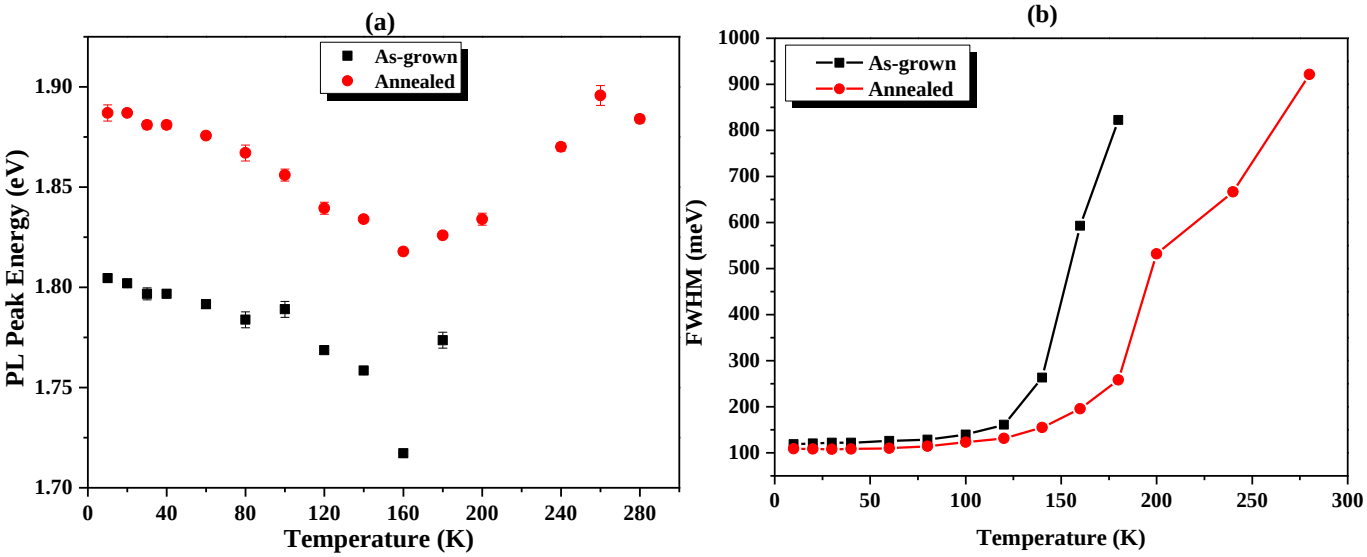


Fig. 5.11. (a) Temperature dependence of PL peak energy and **(b)** FWHM of $GaAs_{0.1}P_{0.89}N_{0.01}$ alloys before and after RTA.

In Fig. 5.11 (b), the FWHM results show a strong dependence on the annealing. After RTA, the FWHM decreases to almost a value of 150 meV from approximately 300 meV at 140 K, which indicates the enhancement of $GaAs_{0.1}P_{0.89}N_{0.01}$ layer quality after RTA.

For further evidence of the positive effect of the rapid thermal annealing treatment, it is very significant to plot the temperature dependence of the integrated PL intensity for as-grown and annealed $GaAs_{0.1}P_{0.89}N_{0.01}$, as illustrated in Fig. 5.12. In addition, the Arrhenius equation (introduced and explained in the previous chapter) is used to fit these data to calculate the activation energy (E) and the corresponding ratios between radiative and non-radiative lifetimes (α). It is very obvious from Fig. 5.12 that the integrated PL intensity decreases as the temperature is increased in both as-grown and annealed samples.

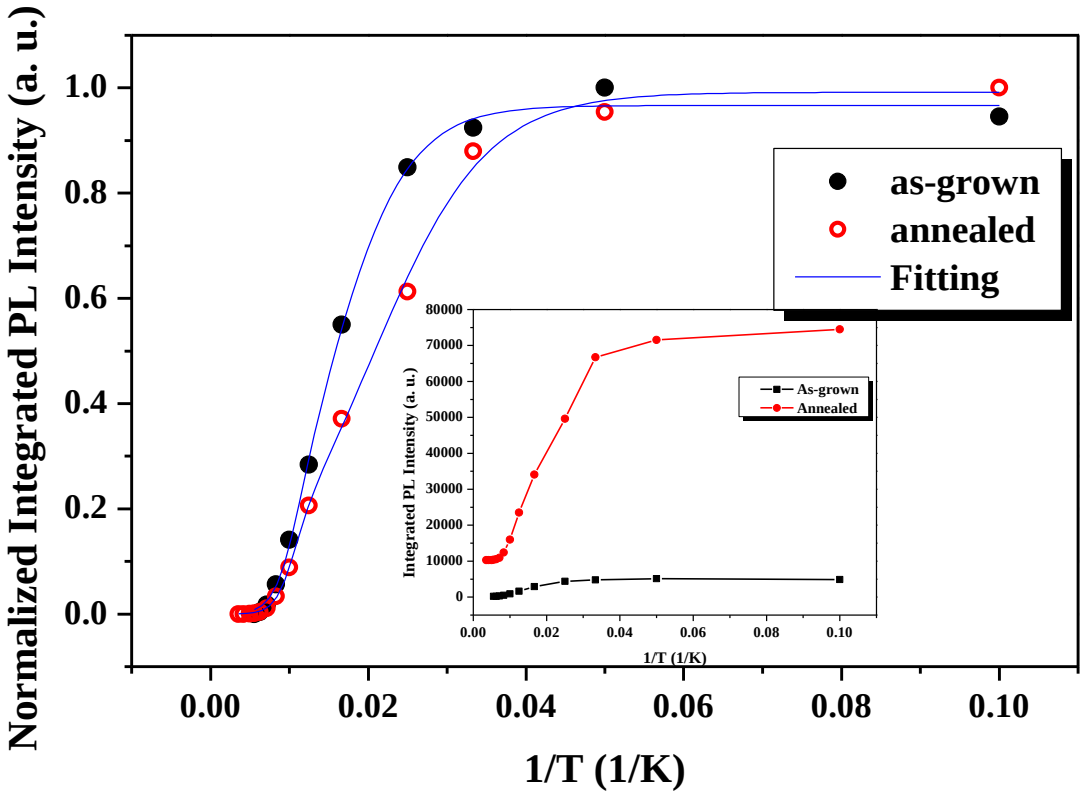


Fig. 5.12. Temperature dependence of the integrated PL intensity for $GaAs_{0.1}P_{0.89}N_{0.01}$ alloys before and after RTA, with Arrhenius fitting (blue lines).

It is very clear from the inset in Fig. 5.12 that the RTA treatment leads to an enhancement of the integrated PL intensity. Table 5.3 displays the values of thermal activation energies as well as the corresponding ratios between radiative and non-radiative lifetimes. The presence of two quenching processes indicates that there are at least two types of non-radiative defects in the sample. The thermal activation energies E_{a1} and E_{a2} are 17.2 and 65.8 meV, respectively, and the corresponding ratios between radiative and non-radiative lifetimes α_1, α_2 are equal to 28.5 and 51949 for as-grown $GaAs_{0.1}P_{0.89}N_{0.01}$ alloys. These values increased after annealing treatment. After RTA, the thermal activation energies E_{a1} and E_{a2} are found to be 21.1 and 78.5 meV respectively, and the corresponding ratios α_1, α_2 are also increased by increasing the activation energy to be from 21 and 7641 to 28.5 and 51949 after RTA. This means that RTA helps to increase the optical efficiency of the samples. Additional structural

studies need to be carried out in order to identify which defects correspond to these activation energies and also to measure the concentration of these defects [3].

Table 5.3: Arrhenius's parameters for the integrated PL peak intensity for as-grown and annealed $GaAs_{0.1}P_{0.89}N_{0.01}$ grown on GaP substrates.

Sample	E_{a1} meV	E_{a2} meV	α_1	α_2
as-grown $GaAs_{0.1}P_{0.9}N_{0.01}$	17.2	65.8	21	7641
annealed $GaAs_{0.1}P_{0.9}N_{0.01}$	21.1	78.5	28.5	51949

5.3.3.2 THE $In_{0.07}Ga_{0.93}P_{0.99}N_{0.01}$ CASE

Fig. 5.13 (a) and (b) shows the PL spectra versus PL peak energy of $In_{0.07}Ga_{0.93}P_{0.99}N_{0.01}$ before and after RTA, respectively. It is clearly observed that the optical quality in terms of luminescence intensity of this material is enhanced after RTA. However, RTA leads to shifting towards higher bandgap energy. A similar blue-shift caused by annealing has also been reported for (GaIn)(NAs) grown on GaAs substrates [28].

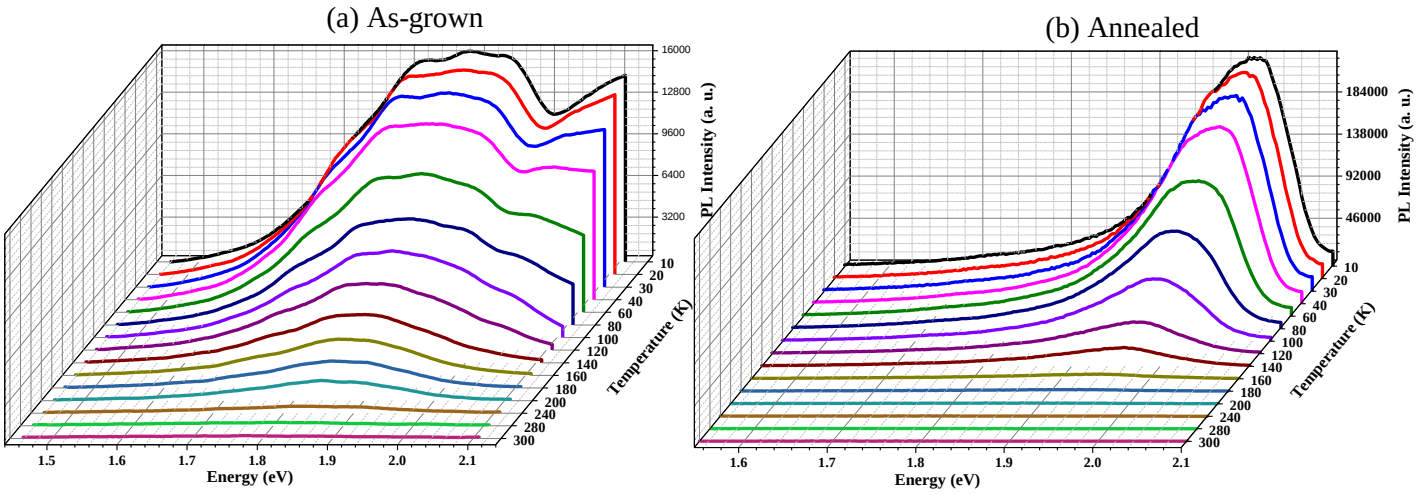


Fig. 5.13. Photon energy *vs* PL intensity spectra at different temperatures for **(a)** as-grown and **(b)** annealed of $In_{0.07}Ga_{0.93}P_{0.99}N_{0.01}$.

In MBE GaInNAs III-V-N grown samples, depending on the N and In concentrations and the annealing conditions, there are indications that the local N-environment changes. For example, the configuration of N-environment could have four Ga nearest neighbours or more In nearest neighbours [28]. This rearrangement of the N nearest-neighbour environment is caused by the competition between chemical bonding and local strain contributions to the site energies of the different N-environments. Over the growth process chemical bonding aspects dominate at the surface which forms Ga-N bonds instead of In-N bonds [29]. This surface state is frozen in during the non-equilibrium growth process. In contrast to the surface at equilibrium, In-rich nearest neighbour configurations of N are favoured in bulk because of the local strain dominance effects. Thus, the frozen non-equilibrium bulk state can be converted into the equilibrium bulk state by annealing under compatible conditions. The change of N to In-rich environments leads to reduced N-induced perturbation of the host semiconductor [30]. This decrease in the perturbation causes small changes in the band structure.

Thus, it is believed that the same mechanism could explain the observed blue-shift in the annealed $In_{0.07}Ga_{0.93}P_{0.99}N_{0.01}$ samples investigated in this work.

Moreover, the broadening in the as-grown photon luminescence is really minimized after annealing. This could be explained by the fact that RTA decreases the In fluctuation in the layer. The peak which was observed in the as-grown sample at energy range above 2eV (see Fig. 5.13 (a)), is not present after RTA, indicating a reduction of NR defects density (see Fig. 5.13 (b)).

Fig. 5.14 (a) shows the temperature dependence of PL peak energy of both as-grown and annealed $In_{0.07}Ga_{0.93}P_{0.99}N_{0.01}$ samples. An S-shaped curve (up-down-up), is clearly seen below 150 K for the as-grown sample (Fig. 5.14 (a)). However, this S-shape (up-down) is less pronounced for the annealed samples. The S-shape behaviour evidences the presence of

localized states in both as-grown and annealed samples due to the spatial distribution of local regions of N-induced fluctuations of the bandgap energy [31-32]. However, the less pronounced S-shape behaviour observed in the annealed sample indicates that the annealing process has been effective in decreasing the effect of localization. The composition non-uniformity of N and In in the $In_{0.07}Ga_{0.93}P_{0.99}N_{0.01}$ layer causes these various spatial regions. [31].

Assuming that there are three spatial regions in the potential as follows: (1) a shallow potential region in which N and In compositions are higher, (2) an intermediate potential region in which N composition is intermediate and In composition is lower, and (3) a deep potential region in which N and In compositions are higher. Therefore, the bandgap energy in the N- and In-rich region (3) is smaller than in the other spatial regions (1) and (2). After RTA, the S-shape curve was changed to the up-down curve. The disappearance of the up-phase above 150K means that the spatial density of the N- and In-rich region (3) has decreased with a relative increase of the other spatial regions (1) and (2). This phenomenon is similar to that observed in InGaAsN [31-33] alloys, which originates from partial elimination of the spatial fluctuations.

Narrower FWHM has been observed after RTA as demonstrated in Fig. 5.14 (b) in the temperature range from 10K-160K. However, in the temperature range 160K to 300K the energy of the PL peak of the annealed sample falls more rapidly than the as-grown sample (Fig. 5.14. (a)). In addition, the FWHM is larger than the as-grown sample (Fig. 5.14. (b)).

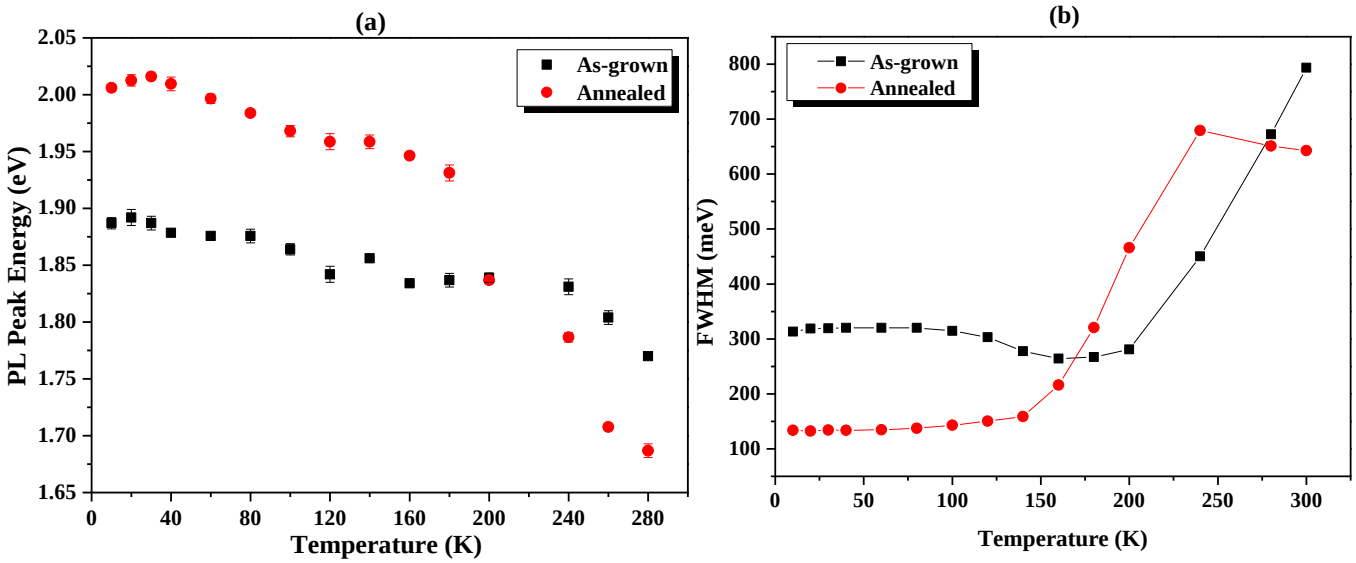


Fig. 5.14. (a) Temperature dependence of PL peak energy and **(b)** FWHM of $In_{0.07}Ga_{0.93}P_{0.99}N_{0.01}$ alloy before and after RTA.

Fig. 5.15 shows the integrated PL intensities over (1/T) with Arrhenius fitting for $In_{0.07}Ga_{0.93}P_{0.99}N_{0.01}$ before and after RTA. The integrated PL intensity decreased with the increase of the temperature for both as-grown and annealed $In_{0.07}Ga_{0.93}P_{0.99}N_{0.01}$ layers. This behaviour is similar to the one observed in InGaAsN alloys, which may involve a preferable formation of In-N bonds due to the local strain compensation of atomic size between In and N atoms [34-35]. The PL quenching in the annealed $In_{0.07}Ga_{0.93}P_{0.99}N_{0.01}$ layer became smaller than that in the as-grown layer (see inset in Fig. 5.15). This means that RTA could lead to a decrease in non-radiative centres resulting from the increase in the In-N bonds [36]. It could be expected that the more In atoms are incorporated, the more In-N bonds and fewer N-related defects [37-38] are formed. This reduction in N related defects will be of great help in the deactivation of non-radiative centers.

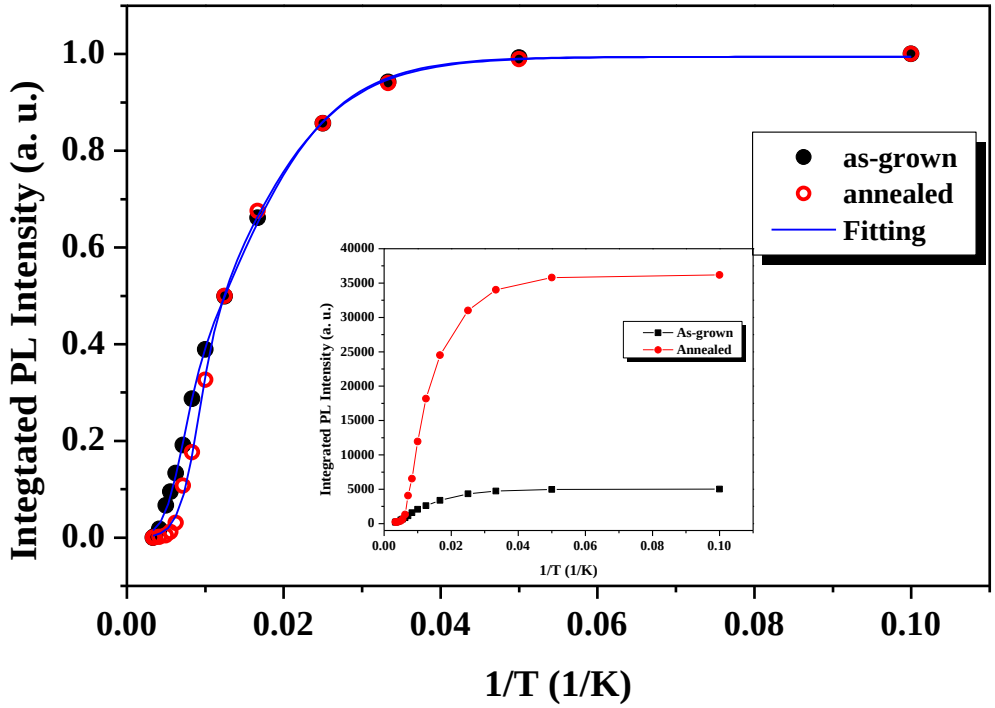


Fig. 5.15. Temperature dependence of the integrated PL intensity for $In_{0.07}Ga_{0.93}P_{0.99}N_{0.01}$ layer before and after RTA with Arrhenius fitting (blue lines).

Table 5.4 presents the Arrhenius fitted calculation of the activation energy for $In_{0.07}Ga_{0.93}P_{0.99}N_{0.01}$ alloys before and after RTA. It can be seen that there are two kinds of non-radiative defects in as-grown and annealed samples. Thermal activation energies E_{a1} and E_{a2} are 11.9 meV and 74.9 meV, respectively. The corresponding ratios between radiative and non-radiative lifetimes α_1 and α_2 are equal to 5 and 1369, respectively, for as-grown $In_{0.07}Ga_{0.93}P_{0.99}N_{0.01}$. These results suggest that there exists two different origins of PL in InGaPN layer, namely localized (P_L) and free (P_H) excitonic recombination [39]. The values of thermal activation energies are increased after annealing to 12.59 meV and 79.16 meV. These above ratios are also enhanced by thermal annealing to 6 and 4525. This increase of the activation energy after RTA indicates that the optical quality of the sample is more efficient after RTA.

Table 5.4: Arrhenius's parameters for the integrated PL peak intensity for as-grown and annealed InGaPN grown on GaP substrates.

Sample	E_{a1} meV	E_{a2} meV	α_1	α_2
as-grown $In_{0.07}Ga_{0.93}P_{0.99}N_{0.01}$	11.9	74.9	5	1369
annealed $In_{0.07}Ga_{0.93}P_{0.99}N_{0.01}$	12.59	79.16	6	4525

5.4 SUMMERY

In summary, experimental measurements have been carried out using PL to investigate the effect of RTA on the optical properties of $GaAs_{0.1}P_{0.89}N_{0.01}$ and $In_{0.07}Ga_{0.93}P_{0.99}N_{0.01}$ quaternary alloys grown on (100) GaP substrates.

With regards to the optical properties, the incorporation of As and In leads to a decrease in the bandgap of $GaP_{0.99}N_{0.01}$ and reach ≃1.8 eV for $GaAs_{0.1}P_{0.89}N_{0.01}$ and ≃1.83 eV for $In_{0.07}Ga_{0.93}P_{0.99}N_{0.01}$. This value of 1.8 eV is actually an ideal bandgap of solar cells-based materials grown on Si substrates. The incorporation of arsenic and indium resulted in an increase in the PL intensity in both quartenary alloys as compared to the ternary $GaP_{0.99}N_{0.01}$ alloy. However, the FWHM results evidenced poor quality of $In_{0.07}Ga_{0.93}P_{0.99}N_{0.01}$material, which could indicate lattice mismatching between $In_{0.07}Ga_{0.93}P_{0.99}N_{0.01}$ layer and the GaP substrate due to indium incorporation. On the contrary, As addition leads to lattice matching between $GaAs_{0.1}P_{0.89}N_{0.01}$ and GaP substrate, which means that this material has higher crystal quality than $In_{0.07}Ga_{0.93}P_{0.99}N_{0.01}$. In addition, compensation of elastic stresses and inhibition of defect formation occur because arsenic substitutes group V in the quaternary dilute nitride alloy. Furthermore, a comparison of the RTA impact on $GaAs_{0.1}P_{0.89}N_{0.01}$ and

$In_{0.07}Ga_{0.93}P_{0.99}N_{0.01}$ alloys have been investigated at 800 °C for 5 minutes. After RTA the PL peak intensities of both materials were increased, at the same time the bandgap energies shifted to higher values. In $GaAs_{0.1}P_{0.89}N_{0.01}$ alloy after RTA the blue-shift was attributed to the reduction of the crystal point defects that could lead to an increase in carrier concentration and radiative recombination processes at the band edges. For $In_{0.07}Ga_{0.93}P_{0.99}N_{0.01}$ alloy, the shift to higher energy after RTA could be caused by the modification of the electronic bandgap structure due to a reduction of the local perturbation associated with the modification of the N environment. Additional evidence of the enhancement of the optical properties of $GaAs_{0.1}P_{0.89}N_{0.01}$ and $In_{0.07}Ga_{0.93}P_{0.99}N_{0.01}$ alloys after RTA was demonstrated by narrower FWHM values and larger activation energies as compared with the as-grown samples.

REFERENCES

[1] S. Almosni, C. Robert, T. Nguyen Thanh, C. Cornet, A. Létoublon et al. J. Appl. Phys. Lett. **113**, 123509 (2013).

[2] A. Buyanova, W. Chen, Physics and Applications of Dilute Nitrides, Taylor & Francis Books, Inc., New York, (2004).

[3] S. Almosni, Growth, structural and electro-optical properties of GaP/Si and GaAsPN/ GaP single junctions for lattice-matched tandem solar cells on silicon, PhD, INSA de Rennes, France (2015).

[4] D. Friedman, Curr. Opin. Solid State Mater. Sci. **14**, 131 (2010).

[5] S. Kurtz, P. Faine, and J. Olson, J. Appl. Phys. Lett. **68**, 1890 (1990).

[6] M. Izadifard, I. Buyanova, J. Bergman, W. Chen, A. Utsumi, Y. Furukawa, A. Wakahara, and H. Yonezu, Semicond. Sci. Technol. **20**, 353 (2005).

[7] N. Shtinkov, P. Desjardins, and R. Masut, Phys. Rev. Lett. B **67**, 081202 (2003).

[8] C. Robert, M. Perrin, C. Cornet, J. Even, and J. M. Jancu, J. Appl. Phys. Lett. **100**, 111901 (2012).

[9] Y. Kuang, S. Chen, H. Li, S. Sinha, and C. Tu, J. Vac. Sci. Technol. B **30**, 02B121 (2012).

[10] I. Ho and G. Stringfellow, Jornal of Crystal Growth **178**, 1 (1997).

[11] Y. Liang, W. Nix, P. Griffin, and J. Plummer, J. Appl. Phys. Lett. **97** (4), p. 043519 (2005).

[12] J. Matthews and A. Blakeslee, Jornal of Crystal Growth **27**, 118 (1974).

[13] Y. Takagi, Y. Furukawa, A. Wakahara, and H. Kan, J. Appl. Phys. Lett. **107**, 063506 (2010).

[14] O. Skibitzki, F. Hatami, Y. Yamamoto, P. Zaumseil, A. Trampert, M. Schubert, B. Tillack, W. Masselink, and T. Schroeder, J. Appl. Phys. Lett. **111**, 073515 (2012).

[15] J. Geisz, J. Olson, D. Friedman, K. Jones, R. Reedy, and M. Romero, IEEE, pp. 695, (2005).

[16] http://www.ioffe.ru/SVA/NSM/Semicond/GaP/bandstr.html, [online 15/09/2018].

[17] M. Albrecht, T. Remmele, V. Grillo, H. Strunk, A. Egorov, Gh. Dumitras, and H. Riechert, J. Appl. Phys. Lett., **81**, 2719 (2002).

[18] X. Wang, Y. Puttisong, C. Tu, A. Ptak, V. Kalevich, A. Egorov, L. Geelhaar, H. Riechert, W. Chen, and I. Buyanova, J. Appl. Phys. Lett. **95**, 241904 (2009).

[19] M. Henini, Dilute Nitride Semiconductors (Elsevier, 2005).

[20] W. Chen, I. Buyanova, C. Tu and H. Yonezu. Acta Physica Polonica, Vol. **108** (2005).

[21] O. Rumyantsev, P. Brunkov, E. Pirogov, and A. Egorov, Semiconductors **44**, 893 (2010).

[22] H. Saito, T. Makimoto, T. Nishida, and N. Kobayashi, J. Appl. Phys. Lett. **70**, 2984 (1997).

[23] S. Francoeur, S. Nikishin, C. Jin, Y. Qiu, and H. Temkin, J. Appl. Phys. Lett. **75**, 1538 (1999).

[24] K. Volz, J. Koch, B. Kunert, I. Nemeth, and W. Stolz, Jornal of Crystal Growth **298**, pp. 126, (2007).

[25] O. Rubel, M. Galluppi, S. Baranovskii, K. Volz, L. Geelhaar, H. Riechert, P. Thomas, and W. Stolz, J. Appl. Phys. Lett. **98**, 063518 (2005).

[26] B. Kunert, D. Trusheim, V. Voßebürger, K. Volz, and W. Stolz, Physica Status Solidi (A) **205**, pp. 114 (2008).

[27] C. Cornet, T. Nguyen Thanh, T. Quinci, S. Almosni, T. Rohel, J. Kuyyalil, A. Rambaud, A. Létoublon, N. Bertru, O. Durand, and A. Le Corre, J. Appl. Phys. Lett. **101**, 251906 (2012).

[28] P. Klar, H. Grünning, J. Koch, S. Schäfer, K. Volz, W. Stolz, W. Heimbrodt, A. Saadi, A. Lindsay, and E. O'Reilly, Phys. Rev. Lett. B **64**, 121203 (2001).

[29] T. Matsuoka, T. Sasaki, and A. Katsui, Optoelectron. Devices Technol. **5,** 53 (1990).

[30] P. Klar, H.Gruning, J. Koch, S. Schafer, K.Volz, W. Stolz, W. Heimbrodt, A. Saadi, A. Lindsay, and Y. Oreille, Phy. Rev. Lett. B **64**, 121203 (R) (2001).

[31] S. Kim, Y. Furukawa, H. Yonezu, K. Umeno, and A. Wakahara, Japn. J. Appl. Phys., **44**, 12, pp. 8309 (2005).

[32] H. Xin, K. Kavanagh, Z. Zhu, and C. Tu, J. Appl. Phys. Lett. **74**, 2337 (1999).

[33] S. Shirakata, M. Kondow, and T. Kitatani, J. Appl. Phys. Lett. **80**, 2087 (2002).

[34] S. Kurtz, J. Webb, L. Gedvilas, D. Friedman, J. Geisz, J. Olson, R. King, D. Joslin, and N. Karam, J. Appl. Phys. Lett. **78** , 748 (2001).

[35] T. Tite, O. Pages, and E. Tournie, J. Appl. Phys. Lett. **85** (2004).

[36] S. Kim, Y. Furukawa, H. Yonezu, K. Umeno, and A. Wakahara. Japn. J. Apple. Phys., **45**, No. 12 (2005).

[37] W. Li, M. Pessa and J. Likonen, J. Appl. Phys. Lett. **78** (2001).

[38] T. Ahlgren, E. Ahlgren, W. Li, and M. Pessa, J. Appl. Phys. Lett. **80** (2002).

[39] D. Kaewket, S. Sanorpim, S. Tungasmita, R. Katayama, and K. Onabe. Physica Status Solidi (C) **7**, No. 7, 2079, (2010).

CHAPTER 6: INVESTIGATION OF THE EFFECT OF DIFFERENT THICKNESSES AND THERMAL ANNEALING ON THE OPTICAL PROPERTIES OF $GaAs_{0.1}P_{0.89}N_{0.01}$ ALLOYS GROWN ON GaP SUBSTRATES

In this Chapter, optical characterization technique, namely photoluminescence (PL), has been employed to investigate the effect of different epilayer thicknesses (i.e, 100 nm and 1 μm) on the optical properties of $GaAs_{0.1}P_{0.89}N_{0.01}$ grown on (100) GaP substrates. The effect of RTA on the optical properties of the thicker sample has also been investigated in this chapter.

6.1 INTRODUCTION

One of the most effective parameters in the growth of dilute nitrides is the thickness of the epilayer [1]. The thickness has been reported to influence the lattice matching of the materials as well as the structural, optical and electrical properties [2]. Moreover, it is very important to keep the thickness of the epilayer in the range of the critical thickness (CT) (1 μm within the CT range of GaAsPN alloy). In the following are a number of the reported studies on the impact of epilayer thickness on the various properties of semiconductors.

Chitra et al. [3] have studied the effect of different thicknesses (250, 300 and 500 nm) on the optical and electrical properties of gallium arsenide (GaAs) thin films [3]. They observed that by increasing the layer thickness, the optical transmittance peak was increased, while the luminescence bandgap was reduced from 3.2eV for thinner layer to 2.85eV for thicker one. Additionally, they reported that thicker layers lead to an enhancement of the refractive index from 1.8 to 2.5 at wavelength of 1800nm. On the contrary, the extinction coefficient (k_1)

which is related to the absorption coefficient ($\alpha = 4\pi k_1/\lambda$; λ is the wavelength of light), and the real and imaginary part of dielectric constant decreased.

S. Belahsene et al [4] studied two GaN p-i-n structures with different thicknesses of the (i-GaN) undoped layer (0.2 μm and 0.6 μm) after beta particle irradiation. One of their aims was to investigate the impact of the thickness of the (i-GaN) undoped layer on the number of generated electron-hole pairs (EHPs), therefore on the efficiency of betavoltaic conversion. It is worth noting that the operation principle of a betavoltaic microbattery is similar to that of a photovoltaic cell. They found that the irradiation had no effect on the measured capacitance of the thicker sample. On the other hand, a significant effect of β-particles was observed on the capacitance of the thinner sample compared with the as-grown sample. This result was explained by a variation of the free charge density in the depletion region due to a partial loss of charge carriers in the p-i-n junction upon irradiation. In addition, they reported that the irradiation has no effect on either deep electron traps ranging from 0.6 to 0.8 eV or deep hole trap at 0.8 eV. New shallow electron traps ranging from 0.06 to 0.08 eV were attributed to the effect of irradiation.

Another study has reported the epilayer thickness variation effects on the optical properties of AlN [5]. AlN epilayers were grown by metal organic chemical vapour deposition on sapphire substrates with three thicknesses 1.5 μm, 3 μm and 4 μm. Room temperature photoluminescence results showed that the PL emission increases linearly with increasing the epilayer thickness from 40 a.u to 125 a.u. The FWHM of free exciton emission decreased from 32 meV to ~ 27 meV as the layer thickness increased. The peak energies were also affected slightly by increasing the AlN epilayer thickness. The peak energy shifted from 5.975eV to ~ 5.99eV.

Additionally, the epitaxial layer thickness effect on the electrical properties of Ti/n-$Al_{0.33}Ga_{0.67}As$ Schottky barrier diodes was investigated in the temperature range of 300-420 K [6]. Comparing the current–voltage (I–V) characteristics of two samples with epitaxial lay-

er thicknesses of 2 μm and 1.5 μm showed that the device with the thinner epitaxial layer has a higher barrier height and thus a lower reverse current. Specifically, they found that increasing the $Al_{0.33}Ga_{0.67}As$ thickness leads to a reduction of the barrier height by ≃12% at 300 K. This degradation of the electrical quality was associated with the presence of deep level traps in the $Al_xGa_{1_x}As$: Si layer.

Lastly, Almosni [7] has investigated the effect of epilayer thickness of 100 nm and 1 μm on the structural properties of $GaAs_{0.1}P_{0.89}N_{0.01}$ samples grown at high growth temperature (480°C) by performing XRD [7]. An XRD peak splitting in the thicker layer (Fig. 6.1) was observed but not in the thinner sample. This indicates that phase separation has occurred in the thick layer. This was tentatively attributed to the higher growth temperature than normally used for these materials. However, it is still unclear the origin and the cause of this separation (e.g. spinodal decomposition of the metastable alloy is sometimes considered as reason for this), but a number of studies have demonstrated that phase separation was not present in the high efficiency solar cells based on dilute nitrides as well as in samples grown at low growth temperatures [7, 8, 9]. This peak splitting corresponds to a difference of 0.0012 nm of lattice parameter or a 0.13% difference in the nitrogen incorporation which was not observed in the thinner sample. This composition variation is assumed to be only due to an inhomogeneous distribution of the nitrogen content in the layer.

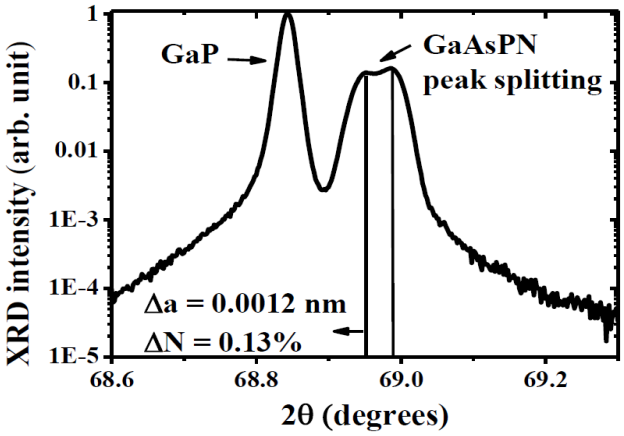


Fig. 6.1. XRD diagram performed for a 1 μm thick $GaAs_{0.1}P_{0.89}N_{0.01}$ layer grown on GaP substrate [7].

The reciprocal space mapping around the (224) reflection reported in [7] shows no evidence of any stress relaxation. In addition, no difference in surface morphology has been reported between the 1 μm and the 100 nm layer [7].

This work investigates the effect of the thickness on the optical properties of $GaAs_{0.1}P_{0.89}N_{0.01}$ epilayer (100nm and 1μm) grown by MBE on (100) GaP substrates using PL technique. The PL technique is performed also to study the effect of RTA on the optical properties of the thicker $GaAs_{0.1}P_{0.89}N_{0.01}$ layer. Further details of the samples used in this study and their preparation are given in Chapter 3.

6.2 SAMPLE DETAILS

The layer structure of the two samples investigated in this chapter are shown in Fig. 6.2.

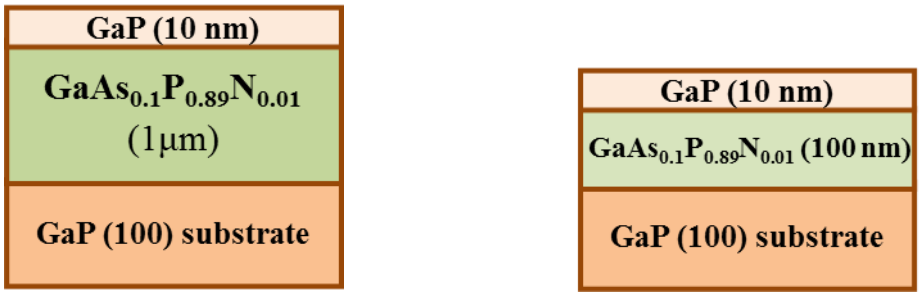


Fig. 6.2. Schematic diagram of $GaAs_{0.1}P_{0.89}N_{0.01}$ dilute nitride with two epilayer thicknesses **(a)** 1μm **(b)** 100 nm.

6.3 EFFECT OF EPILAYER THICKNESS ON THE OPTICAL PROPERTIES OF $GaAs_{0.1}P_{0.89}N_{0.01}$.

The first study in this section is to report the effect of increasing the $GaAs_{0.1}P_{0.89}N_{0.01}$ epilayer thickness from 100 nm to 1μm on the PL intensity as shown in Fig. 6.3.

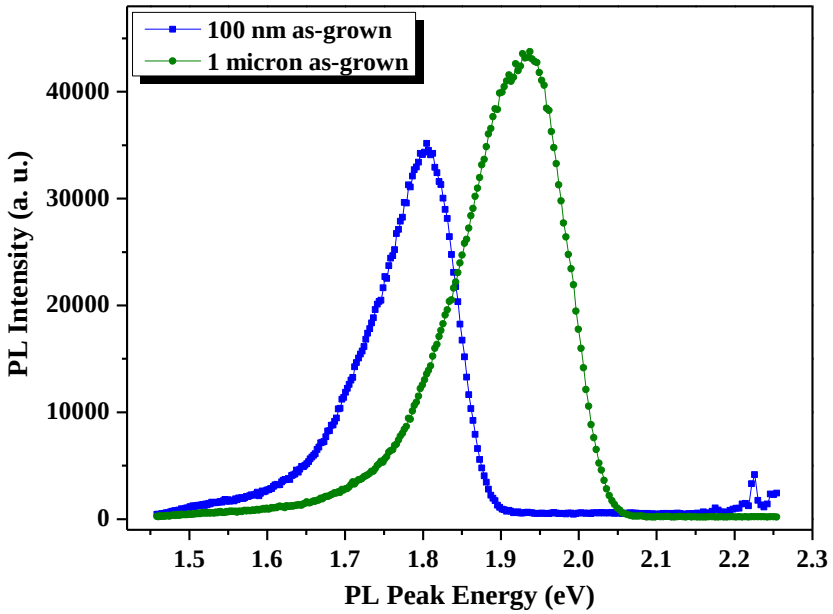


Fig. 6.3. PL peak intensity vs PL peak energy of 1μm and 100nm $GaAs_{0.1}P_{0.89}N_{0.01}$ at 10 K.

It is clear that $GaAs_{0.1}P_{0.89}N_{0.01}$ material with thicker epitaxial layer shows a higher luminescence intensity at 10 K than the thinner epilayer (~ 1.3 times higher). This possibly suggests that the 1 μm sample has a larger generation-recombination (GR) centres density than the 100 nm layer [10]. This finding supports the argument that the GR centres density might be strain related [10].

It was reported previously [10-11] that the investigation of the PL spectra at 300 K (room temperature RT) showed that increasing the thickness of $GaAs_{0.1}P_{0.89}N_{0.01}$ epilayer leads to two PL emission peaks at 1.73 eV and 1.84 eV. These two peaks seem to correlate with two regions of absorption, the first located roughly between 1.5 eV and 1.7 eV and the other over 1.7 eV, which could be a consequence of phase separation [7]. This could explain the slight broadening of the PL signal of the 1 μm thick $GaAs_{0.1}P_{0.89}N_{0.01}$ sample as compared to the 100 nm thick sample PL emission (see Fig. 6.3).

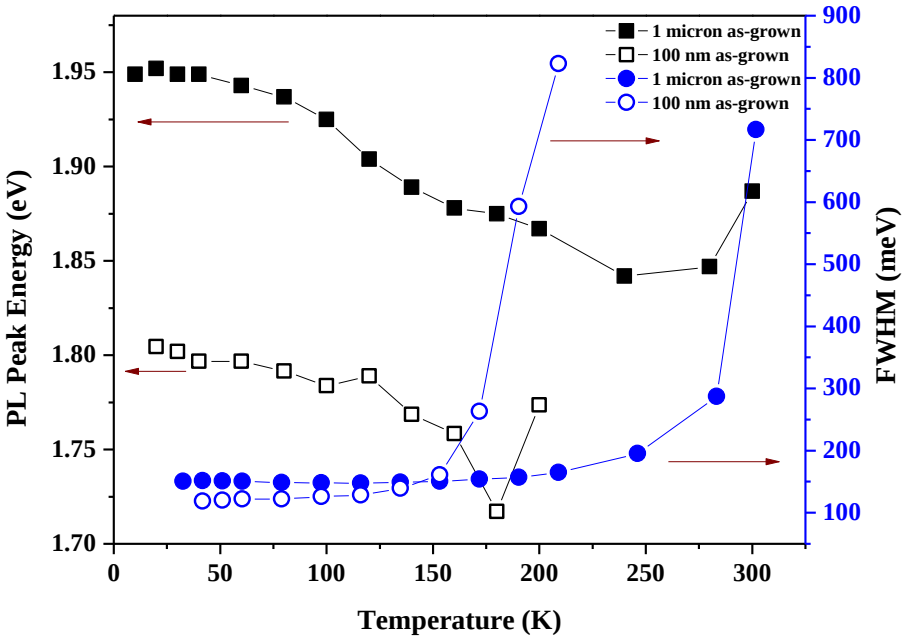


Fig. 6.4. Temperature dependence of the PL peak energy and FWHM for 1 μm and 100 nm of $GaAs_{0.1}P_{0.89}N_{0.01}$.

Fig. 6.4 shows the temperature dependence of the PL peak energy and full width at half maximum (FWHM) of 1 μm and 100 nm $GaAs_{0.1}P_{0.89}N_{0.01}$ epilayers. From Fig. 6.4 it can be seen that the bandgap energies of the thicker sample are higher than the thinner one throughout the temperature range 10 K- 300 K. This is because of the well-known fact that increasing the thickness of the layer leads to an increase of the absorption which helps to enhance the bandgap energy. In other words, the thicker the layer the more GR centres are created [12].

Moreover, in the low temperature range 10 K -140 K the FWHM values of the 100 nm thick sample are smaller than the 1 μm sample, while above 140 K to 300K the FWHM values of the 1 μm sample are smaller than the 100 nm sample . These results indicate that the optical efficiency of the thicker layer is better at high temperatures. However, the optically efficient thinner layer favours the low temperatures.

Fig. 6.5 shows the integrated PL intensity versus 1/T of 100 nm and 1 μm $GaAs_{0.1}P_{0.89}N_{0.01}$ epilayers and the Arrhenius fitting. The purpose of this investigation is to determine the PL activation energies as discussed in detail in Chapter 4.

As can be seen in Fig. 6.5, there are two straight lines in both 100 nm and 1 μm thick samples corresponding to two activation energies, and hence these are related to two types of non-radiative defects. Table 6.1 presents the values of E_{a1} and E_{a2} as well as α_1 and α_2 for 100 nm and 1 μm $GaAs_{0.1}P_{0.89}N_{0.01}$ samples.

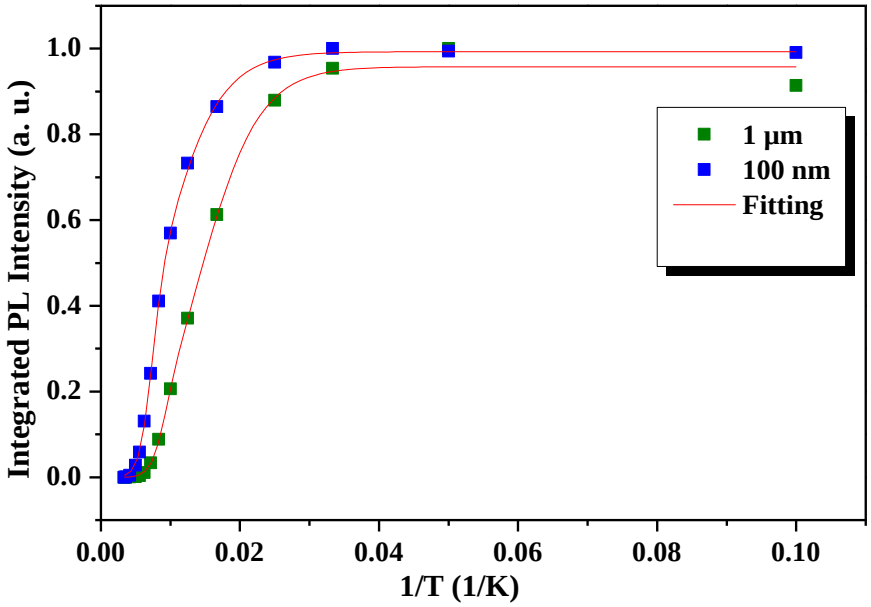


Fig. 6.5. Integrated PL intensity versus 1/T of 100 nm and 1 μm $GaAs_{0.1}P_{0.89}N_{0.01}$epilayers and Arrhenius fitting.

Table 6.1 shows clearly that the values of the two activation energies increase with increasing the epilayer thickness. The 100 nm $GaAs_{0.1}P_{0.89}N_{0.01}$ has activation energies equal to 17.2 meV and 65.8 meV with lifetimes ratios equal 21 and 7641, respectively. The activation energies and lifetimes ratios of the 1μm sample are found to be 20.5 meV and 110 meV, and 7 and 16070, respectively. Both the lifetimes ratio α_2 and the activation energies E_{a1} and E_{a2} increase, with increasing the thickness. However, α_1 decreases as the thickness increases. This

could be related to experimental error. The observed enhancement in the activation energies as well as the ratio α_2 with increasing the thickness could be related to the increase of the absorption in the thick layer.

Table 6.1: Arrhenius's parameters obtained from the integrated PL peak intensity versus 1/T results for as-grown 100 nm and 1 µm $GaAs_{0.1}P_{0.89}N_{0.01}$ epilayers grown on GaP substrates.

Thickness	E_{a1} (meV)	E_{a2} (meV)	α_1	α_2
100 nm	17.2	65.8	21	7641
1 µm	20.5	110	7	16070

Thus, all the above results show that increasing the thickness of the epilayer of dilute $GaAs_{0.1}P_{0.89}N_{0.01}$ material from 100 nm to 1 µm leads to an enhancement of the optical properties in terms of enhancing the PL intensity and activation energy, except the FWHM in the temperature range 10 - 140K. In addition, the bandgap shifts towards higher energy with increasing the thickness (from 1.8 eV to ≃1.95 eV). This makes thick $GaAs_{0.1}P_{0.89}N_{0.01}$ epilayers not suitable for solar-cells based materials grown on Si substrate.

6.4 EFFECT OF RAPID THERMAL ANNEALING ON THE 1 µm $GaAs_{0.1}P_{0.89}N_{0.01}$.

It is very important to study the effect of the RTA process on the thicker sample as has been done for a thinner sample in chapter 5 in order to understand the parameters that affect the optical properties. RTA could help improving the optical properties of thick $GaAs_{0.1}P_{0.89}N_{0.0}$ epilayers by annihilating defects.

Fig. 6.6 (a) and (b) illustrate the PL peak intensity for all temperatures before and after RTA for the 1 µm $GaAs_{0.1}P_{0.89}N_{0.01}$ sample. It can be observed that annealing at 800°C leads to an

increase in the PL intensity by a factor of 2.4 at 10 K. This is also confirmed in Fig. 6.7 which presents the PL signals at 10K for as-grown and annealed samples.

The observed enhancement in the PL intensity could be due to the fact that RTA helps reduce the density of the defects [13, 14, 15]. Moreover, it is clear from Fig. 6.7 that the energy of the $GaAs_{0.1}P_{0.89}N_{0.01}$ shifts to a higher value after annealing (from 1.95 eV to 2.1 eV). This strong blue-shift is a common behaviour in III-V-N dilute nitride after RTA treatment. In $GaAs_{0.1}P_{0.89}N_{0.01}$ material, this shift after annealing could be attributed to the modification of N clusters [3-16] as well as the removal of point defects. The reduction of the localized states radiative defects, which could also explain the blue shift, and leads to an increase in the recombinations and thus enhances the energy bandgap.

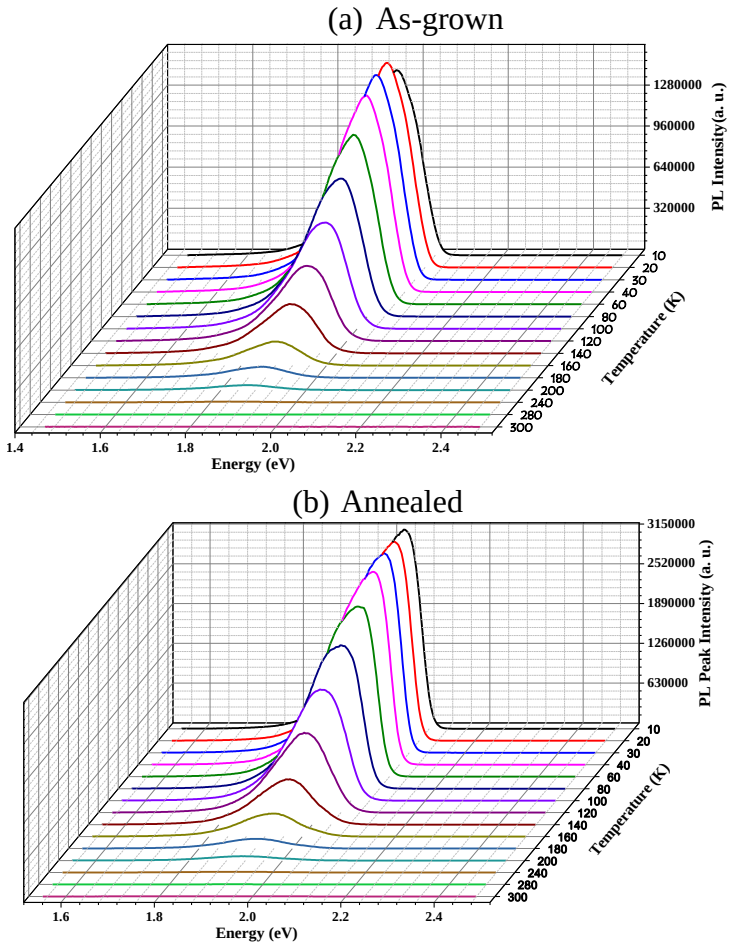


Fig. 6.6. Photon energy vs PL intensity spectra from 10 K to 300 K **(a)** as-grown and **(b)** annealed of $GaAs_{0.1}P_{0.89}N_{0.01}$ with epilayer thickness of 1 μm.

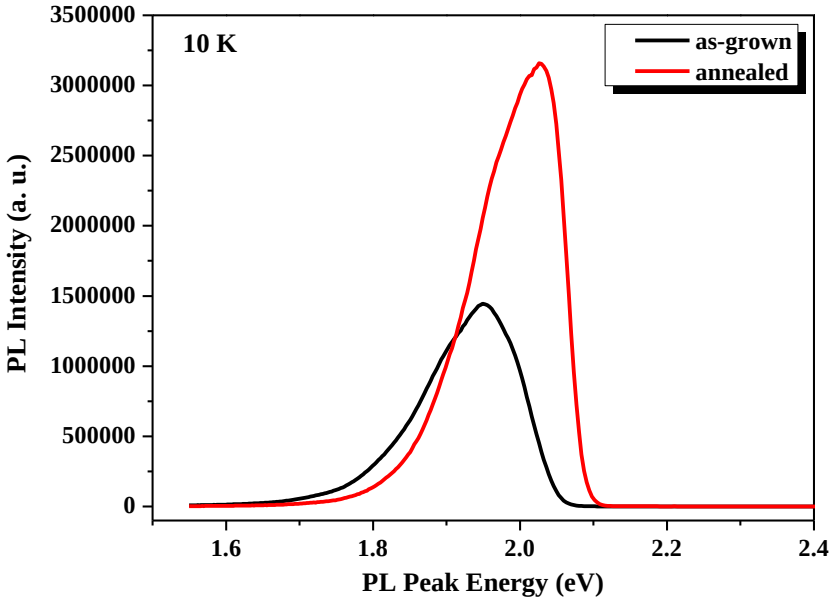


Fig. 6.7. PL spectra at 10 K of 1µm $GaAs_{0.1}P_{0.89}N_{0.01}$/GaP heterostructures before and after RTA.

In III-V-N dilute nitrides it is very significant to plot the temperature dependence of the PL peak energy before and after RTA in order to study the effect of localization on the bandgap. Fig. 6.8 shows the temperature dependence of the PL peak energy of the 1µm $GaAs_{0.1}P_{0.89}N_{0.01}$ before and after the rapid thermal annealing process. It is observed from Fig. 6.8 that the as-grown $GaAs_{0.1}P_{0.89}N_{0.01}$ bandgap energy has an S-shape (up-down-up) over the temperature range 10K- 300K. This means that the sample has been affected by the localized states phenomenon which is reported for a number of dilute nitrides materials. This phenomenon mainly happens due to the nitrogen incorporation and its effect on the conduction band of the materials as explained in Chapter 2 [17]. Furthermore, this S-shape is also observed in the annealed samples. This confirms that N incorporation has a strong effect on this sample as RTA has not led to a reduction or elimination of the S-shape as it is reported for other III-V-N dilute nitride semiconductors [18].

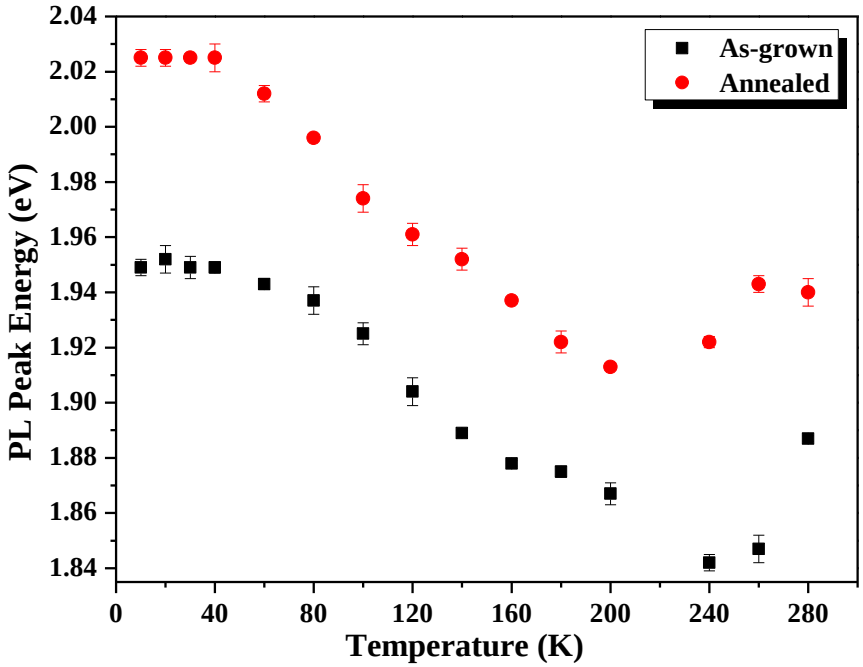


Fig. 6.8. Temperature dependence of the PL peak energy of 1μm $GaAs_{0.1}P_{0.89}N_{0.01}$ layers before and after RTA.

In terms of the temperature dependence of the FWHM of as-grown and annealed $GaAs_{0.1}P_{0.89}N_{0.01}$, it can be noted from Fig. 6.9 that the RTA treatment improved significantly the FWHM by narrowing its values throughout the temperature range 10 K-300 K. This reduction in the FWHM is indicative of a reduction of the point and radiative defects after RTA.

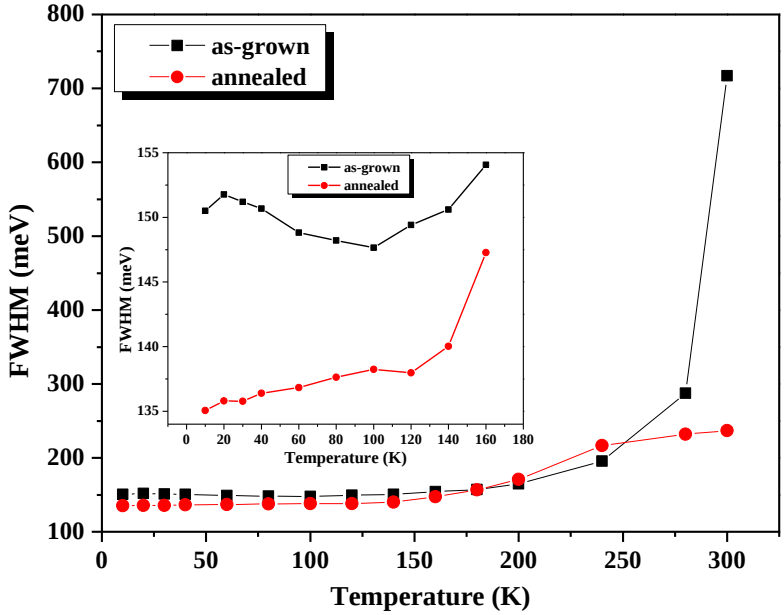


Fig. 6.9. FWHM lines of 1 μm $GaAs_{0.1}P_{0.89}N_{0.01}$ epilayers before and after RTA and inset for FWHM up to ≃150 K.

For a further understanding of the RTA effect on the optical properties, the PL integrated intensity as a function of temperature is plotted in Fig. 6.10. In addition, the Arrhenius fitting is performed to calculate the activation energies as well as the ratio between radiative lifetime and non-radiative escape time. Annealing leads to an enhancement of the integrated PL intensity by a factor ~2. This is could be related to the fact that thermal annealing treatment of $GaAs_{0.1}P_{0.89}N_{0.01}$ alloy reduces the non-radiative defects such as As_{Ga} antisites and Ga_i self-interstitials [19]. Table 6.2 summarises the values of the activation energy and the lifetimes ratio before and after the annealing process. The activation energies E_{a1} and E_{a2} for as-grown and annealed $GaAs_{0.1}P_{0.89}N_{0.01}$ alloy are found to be 20.5 eV and 110 eV, and 21.5 eV and 124.5 eV, respectively. This indicates that annealing leads to an enhancement of the activation energies which could be due to a reduction of N related defects that are not known up to the present [13]. Moreover, the lifetimes ratio also increased by RTA from 7 and 16070 to 10 and 39795, respectively as shown in Table 6.2. Therefore, annealing helps to improve the optical quality of the sample.

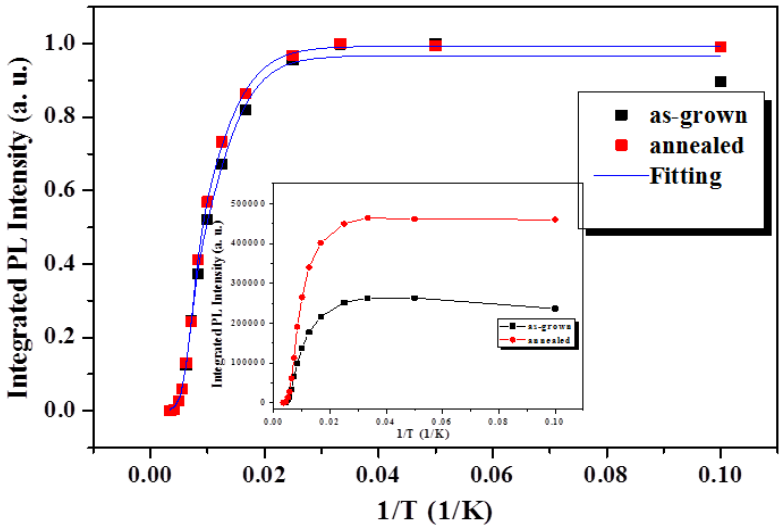


Fig. 6.10. Integrated PL intensity versus 1/T before and after RTA annealing of 1 μm $GaAs_{0.1}P_{0.89}N_{0.01}$ epilayers.

Table 6.2: Arrhenius's parameters obtained from the integrated PL peak intensity versus 1/T results for as-grown and annealed 1µm $GaAs_{0.1}P_{0.89}N_{0.01}$ epilayers grown on GaP substrate.

Sample	E_{a1} meV	E_{a2} meV	α_1	α_2
as-grown $GaAs_{0.1}P_{0.9}N_{0.01}$	20.5	110	7	16070
annealed $GaAs_{0.1}P_{0.9}N_{0.01}$	21.5	124.5	10	39795

It is worth comparing the activation energies of the annealed $GaAs_{0.1}P_{0.89}N_{0.01}$ samples having 100 nm and 1µm thickness. As can be seen in Table 6.3, the thicker layer has higher values of the activation energies E_{a1} (21.5 eV) and E_{a2} (124.5 eV) as compared to the thinner sample (E_{a1} = 21.1 eV and E_{a2} = 78.5 eV). This could be assigned to the reported fact that the thicker layer has large non-radiative centres density than the thinner one [7].

The lifetimes ratios decrease upon annealing from 28.5 and 51949 to 10 and 39795, respectively. This unexpected behaviour of reduced lifetimes ratio of the thicker sample after RTA might be related to experimental error.

Table 6.3: Arrhenius's parameters obtained from the integrated PL peak intensity versus 1/T results for annealed 100nm and 1000nm $GaAs_{0.1}P_{0.89}N_{0.01}$ epilayers grown on GaP substrates.

Sample	Thickness	E_{a1} meV	E_{a2} meV	α_1	α_2
annealed $GaAs_{0.1}P_{0.9}N_{0.01}$	100nm	21.1	78.5	28.5	51949
annealed $GaAs_{0.1}P_{0.9}N_{0.01}$	1µm	21.5	124.5	10	39795

6.5 SUMMERY

Photoluminescence (PL) measurements were performed to investigate the effect of the thickness of the epitaxial layer (100nm and 1μm) on the optical properties of quaternary $GaAs_{0.1}P_{0.89}N_{0.01}$ alloys. Furthermore, PL was used to study the effect of rapid thermal annealing on the thicker layer.

It was observed that increasing the epilayer thickness leads to an enhancement of the PL intensity as well as the energy bandgap which was shifted to higher energy (from 1.8eV in 100nm to 1.95eV in 1μm layer). This bandgap energy is not ideal for solar-cells based materials grown on Si substrate. The enhancement in the PL intensity and bandgap energy was explained by the fact that the thicker layer has larger generation-recombination (GR) centres density. This also confirmed by the smaller FWHM values in the temperature range of 150- 300 K for 1 μm $GaAs_{0.1}P_{0.89}N_{0.01}$ material as compared to the thinner sample.

The 1 μm $GaAs_{0.1}P_{0.89}N_{0.01}$ RTA heat treated samples exhibited an increase in their PL intensities as compared to the as-grown layers. The main reason for the improvement in the PL intensity was related to the fact that RTA caused a reduction in the density of defects. Moreover, the blue shift, which was observed after RTA treatment, was assigned with an increase of the recombination processes resulting from a decrease of the point defects and localized states radiative defects. An S-shape was observed for both as-grown and annealed 1 μm thick $GaAs_{0.1}P_{0.89}N_{0.01}$ samples. This is due to the effect of localization which is caused by N incorporation in $GaAs_{0.1}P_{0.89}N_{0.01}$ semiconductors. Furthermore, narrower FWHM from 10K to 300K and larger activation energies were obtained after RTA due to a reduction in the density of defects.

REFERENCES

[1] J. Olson, S. Kurtz, A. Kibbler, and P. Faine, AJ. ppl. Phys. Lett. **56**, 623 (1990).

[2] S. Kurtz, P. Faine, and J. Olson, J. Appl. Phys. Lett. **68**, 1890 (1990).

[3] Ch. Begum, T. Begum, and Sh. Choudhury. Journal of Bangladesh Academy of Sciences, **37**, No. 1, 83, (2013).

[4] S. Belahsene, N. Al Saqri, D. Jameel, A. Mesli, A. Martinez, J. Sanoit, A. Ougazzaden, J. Salvestrini, A. Ramdane, and M. Henini, Electronics, **4**, 1090 (2015).

[5] B. Pantha, R. Dahal, M. Nakarmi, N. Nepal, J. Li, J. Lin, H. Jiang, Q. Paduano , and D. Weyburne, J. Appl. Phys. Lett. **90**, 241101 (2007).

[6] N. Al-Ahmadi and H. Al-Jawhari, Results in Physics **6**, pp. 67 (2016).

[7] S. Almosni, Growth, structural and electro-optical properties of GaP/Si and GaAsPN/ GaP single junctions for lattice-matched tandem solar cells on silicon, PhD, INSA de Rennes, France (2015).

[8] J. Harris, R. Kudrawiec, H. Yuen, S. Bank, H. Bae, M. Wistey, D. Jackrel, E. Pickett, T. Sarmiento, L. Goddard, V. Lordi, and T. Gugov, Physics Status Solidi (B) **244**, 2707 (2007).

[9] A. Aho, A. Tukiainen, V. Polojärvi, J. Salmi, and M. Guina, 86201I (2013).

[10] S. Almosni, C. Robert, T. Nguyen, C. Cornet, A. Létoublon. J. Appl. Phys. Lett. **113**, 123509 (2013).

[11] A. Buyanova, W. Chen, Physics and Applications of Dilute Nitrides, Taylor & Francis Books, Inc., New York, (2004).

[12] C. Cornet, T. Nguyen , T. Quinci, S. Almosni, T. Rohel, J. Kuyyalil, A. Rambaud, A. Létoublon, N. Bertru, O. Durand, and A. LeCorre, J. Appl. Phys. Lett. **101**, 251906 (2012).

[13] B. Kunert, D. Trusheim, V. Voßebürger, K. Volz, and W. Stolz, Physics Status Solidi (A) **205**, 114 (2008).

[14] H. Saito, T. Makimoto, T. Nishida, N. Kobayashi, J. Appl. Phys. Lett. **70** (1997) 2984.

[15] S. Francoeur, S. Nikishin, C. Jin, Y. Qiu, H. Temkin, J. Appl. Phys. Lett. **75** (1999) 1538.

[16] P. Klar, H. Grünning, J. Koch, S. Schäfer, K. Volz, W. Stolz, W. Heimbrodt, A. Saadi, A. Lindsay, and E. O'Reilly, Phys. Rev. Lett. B **64**, 121203 (2001).

[17] R. Kudrawiec, M. Latkowska, M. Baranowski, J. Misiewicz, L. Li, and J. Harmand, Phys. Rev. Lett. B **88**, 125201 (2013).

[18] S. Mazzucato, R. Potter, A. Erol, N. Balkan, P. Chalker, T. Joyce, T. Bullough, X. Marie, H. Carrère, E. Bedel, G. Lacoste, A. Arnoult, and C. Fontaine, Phys. E Low-Dimens. Syst. Nanostructures **17**, 242 (2003).

[19] W. Chen, I. Buyanova, C. Tu, and H. Yonezu. Acta Physica Polonica, Vol. **108** (2005).

CHAPTER 7: INVESTIGATION OF THE EFFECT OF RAPID THERMAL ANNEALING ON THE ELECTRICALLY ACTIVE DEFECTS IN GaAsPN P-I-N SOLAR CELLS USING DEEP LEVEL TRANSIENT SPECTROSCOPY TECHNIQUE

This Chapter presents a detailed study of the effect of rapid thermal annealing (RTA) on the electrical properties of GaAsPN solar cell structures gown by molecular beam epitaxy (MBE) using Current - Voltage (I-V), Capacitance - Voltage (C-V), conventional Deep Level Transient Spectroscopy (DLTS) and Laplace DLTS measurements in the temperature range from 10 K to 450 K.

7.1 INTRODUCTION

Recently, III-V-N (dilute nitrides) materials classify as a new class of semiconductors due to their unusual and fascinating new physical properties that are rarely seen in other conventional alloys as well as their intriguing potentials for device applications [1]. For example, the band gap energy of III-V semiconductors can be tuned by changing the nitrogen content. Dilute nitride semiconductors can be grown by incorporating small amounts of nitrogen (1-4%) into the III-V host lattice to form a ternary compound (III-V-N). In addition, for example by adding As into GaPN quaternary (GaAsPN) alloys can be fabricated [2]. These materials which can be grown by molecular beam epitaxy (MBE) and metalorganic vapor phase epitaxy (MOVPE) are very attractive for light emitting and light absorbing devices [3,4,5]. These materials have highly desirable optical properties and crystal structure for lattice matching to common substrate such as Si [2] and GaP [6] substrates. For instance, the band gap energy of GaAsPN alloy with 6% nitrogen composition is 1.8 eV which is ideal for efficient GaAsPN/Si tandem solar cells [7]. With the absence of a window layer and non-

optimum band gap, a conversion of 7.9% was achieved for GaPN- based solar cells on GaP substrates with N =1.8% (E_g=2.05eV for $GaP_{0.982}N_{0.018}$). Most researches on III-V-N alloys including GaAsPN depend on low nitrogen composition less than 3% because of low solubility of nitrogen in III-V compounds at thermodynamic equilibrium [8]. Theoretically, by adding Al, As, In or Sb and controlling N content in the layer lattice-matched GaAsPN alloys having bandgap around 1.8 eV can be fabricated allowing the current matching with the Si-cell [9]. However, dilute III-V nitride layers with high N content are known to have poor structural quality due to the low solubility of N in GaP. However, structural optimization has been demonstrated through annealing processes [10].

The crystal defects especially misfit dislocations, generated in the matrix during metamorphic growth is responsible of carriers' lifetime shortening and thus the reduction of the current extraction. These effects affect the efficiency of multi-junctions solar cells. However, post growth annealing process [11-12] has been used to reduce and remove these generated defects. Therefore, the optimization of the dilute nitride material growth and annealing conditions are key points for improving their photoelectric properties [13,14,15].

In this chapter, a detailed investigation is carried out on the electrically active defects in as-grown and annealed GaAsPN solar cell structures. The devices investigated are p-i-n based solar cells. This study will help to get a better understanding of the physical phenomena that affect the efficiency of the above solar cell structures using current-voltage (I-V), capacitance-voltage (C-V), conventional DLTS and Laplace DLTS characterisation techniques.

7.2 SAMPLE DETAILS

In this study, p-i-n GaAsPN based solar cells were grown by molecular beam epitaxy (MBE). The epitaxial growth sequence is illustrated in Fig. 7.1, and consisted of 500 nm thick n^+ GaP ($n=1x10^{18}$ cm^{-3}) buffer layer on 400 μm of (001) GaP substrate, followed by deposition of

300 nm p-type GaAsPN (p= $1x10^{17}$ cm^{-3}) layer. A further 30 nm p^+ GaP (p=$1x10^{18}$ cm^{-3}) layer was deposited.

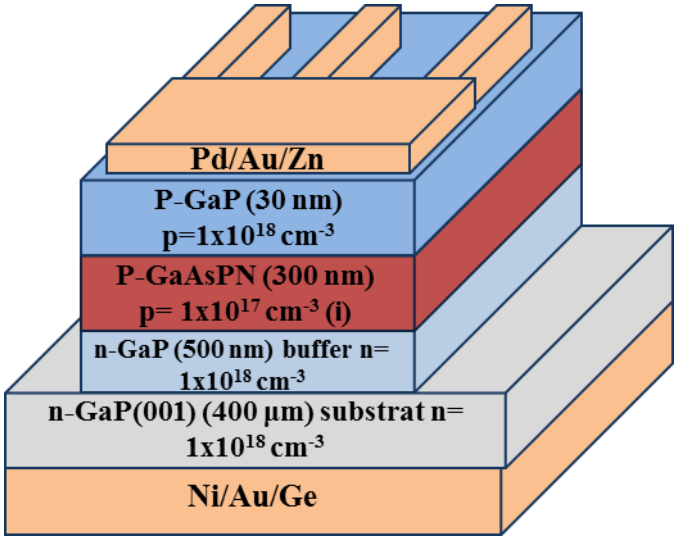


Fig. 7.1. Schematic diagram of the PIN solar cell structures.

Si and Zn are used as the n-type and p-type dopant for the n^+ and p^{++} epitaxial layers, respectively. Nitrogen was incorporated using a valved radio frequency (RF) plasma source with nominal 0.5 sccm N_2 flow and a 400 W RF power. The growth rate was 0.2 monolayer/s (ML/s). The V/III beam equivalent pressure (BEP) ratio has been set at 14. In order to obtain a GaAsPN compound lattice matched to the GaP substrate, the As flux has been set at 0.2 µTorr. After growth, the samples were annealed by using a JetFirst (Jipelec) rapid thermal annealer at 800^{o}C for 5 mins under forming gas (mixture of N_2 and H_2) ambient in a rapid thermal annealing (RTA) system, and the ramp-up temperature used is 100^{o}C/s.

Pd/Au/Zn and Ni/Au/Ge metallisation was performed to the front and back of the solar cell structures, respectively, to form Ohmic contacts [5-16]. The metallic contacts have been deposited using an electron gun and a joule evaporator with a pre-deposition residual pressure below 10^{-6} Torr. The front contact mesa is composed by a 2.5x0.5 mm^2 bus bar linked with 2.5x0.005mm^2 fingers spaced each 300 µm. The solar cells area is 2.5x3 mm^2. The cells area has been defined using a HCl 40:H_2O_2 2: H_2O 1 mesa-etch during 1 min.

7.3 RESULTS AND DISCUSSION

I-V, C-V, DLTS and Laplace DLTS techniques were performed in order to investigate the effect of RTA on the electrical properties of p-i-n GaAsPN based solar cells described in Fig. 9.1.

7.3.1 INVESTIGATION OF THE RTA EFFECT ON THE CURRENT (I) – VOLTAGE (V) CHARACTERISTICS OF P-I-N GaAsPN SOLAR CELLS

The I-V measurements were performed at room temperature for as-grown and annealed samples as shown in Fig. 7.2. It can be seen that the reverse current is reduced considerably when the sample is annealed. The leakage current of the annealed p-i-n solar cells is one to two orders of magnitude lower than the as-grown sample. The lower reverse current observed in the annealed cell indicates that there is a reduction of the concentration of the defects which act as generation recombination centers [17].

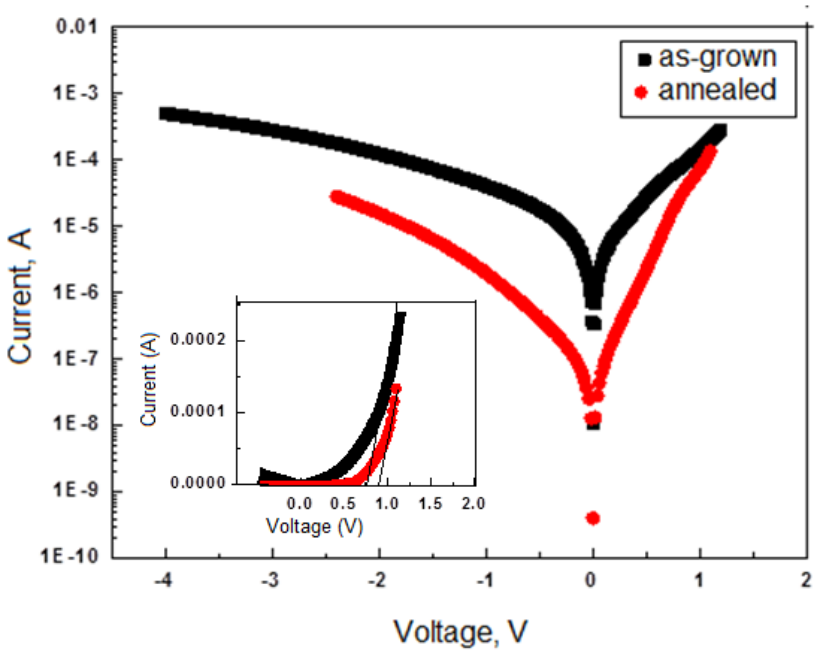


Fig.7.2. I-V characteristics of p-i-n GaAsPN based solar cell at room temperature.

The annealing process decreases the concentration of major defects and consequently contributes to the decrease of the leakage current [18]. Similar observation has been reported by Xie et al [19].

The thermal annealing process is therefore an efficient way to improve the electrical properties of these devices. This improvement could be attributed to a decrease in the defects concentration and /or their transformation. This effect will be investigated further using DLTS measurements as described below. In addition, the turn on voltage (V_{on}) increases when the samples are annealed. V_{on} is 0.7 V and 0.9 V for as-grown samples and annealed samples, respectively. This behavior can be attributed to the increase of the excess capacitance due to the interface states [20].

The p-i-n junction current–voltage (I-V) characteristics can be described by the thermionic emission (TE) model with a series resistance (R_S) as given previously by equation (3.6) [21-22]. Additionally, the expression of the saturation current I_s is given by equation (3.5). Furthermore, the barrier height (ϕ_B) can be determined also from equation (3.5). A is the effective diode area and A^{**}= 98.2 $Acm^{-2}K^{-2}$ is the effective Richardson's constant for n-GaP [23]. The ideality factor (n) can be calculated using equations (3.8) and (3.10).

The semi-logarithmic I-V characteristics of the p-i-n solar cells at room temperature are illustrated in Fig. 7.2. Fig. 7.3 (a) shows the temperature dependence of the ideality factor calculated from the semi-logarithmic I-V curves for as-grown and annealed samples over the temperature range 110 - 440K.

For all samples, it is evident that the ideality factor (n) increases with decreasing temperature. Similar trends have been reported by other researchers [24-25]. This is due to the current transport across the p-i-n interface which is temperature activated process [26-27]. For all samples in the temperature range 300K - 440K, the values of ideality factor are greater than

unity and close to 2 whichis the ideal factor of diode for solar cell. This behavior can be attributed to the generation-recombination mechanism, interface states, the series resistance and barrier height in- homogeneities [28]. However, the annealed samples have low ideality factor values compared with the as-grown samples indicating that the annealed samples are nearer to ideal diode for solar cells than the as-grown devices. For all samples, the higher values of ideality factor at low temperatures are caused by the presence of thermionic field emission, which contribute to the pure thermionic emission [29]. This phenomenon of the increase of the ideality factor with decreasing temperature is known as the T_o effect [30]. The ideality factor is inversely proportional with temperature as given by:

$$n(T) = n_o + \frac{T_o}{T} \qquad (7.1)$$

where here n_o and T_o are constants.

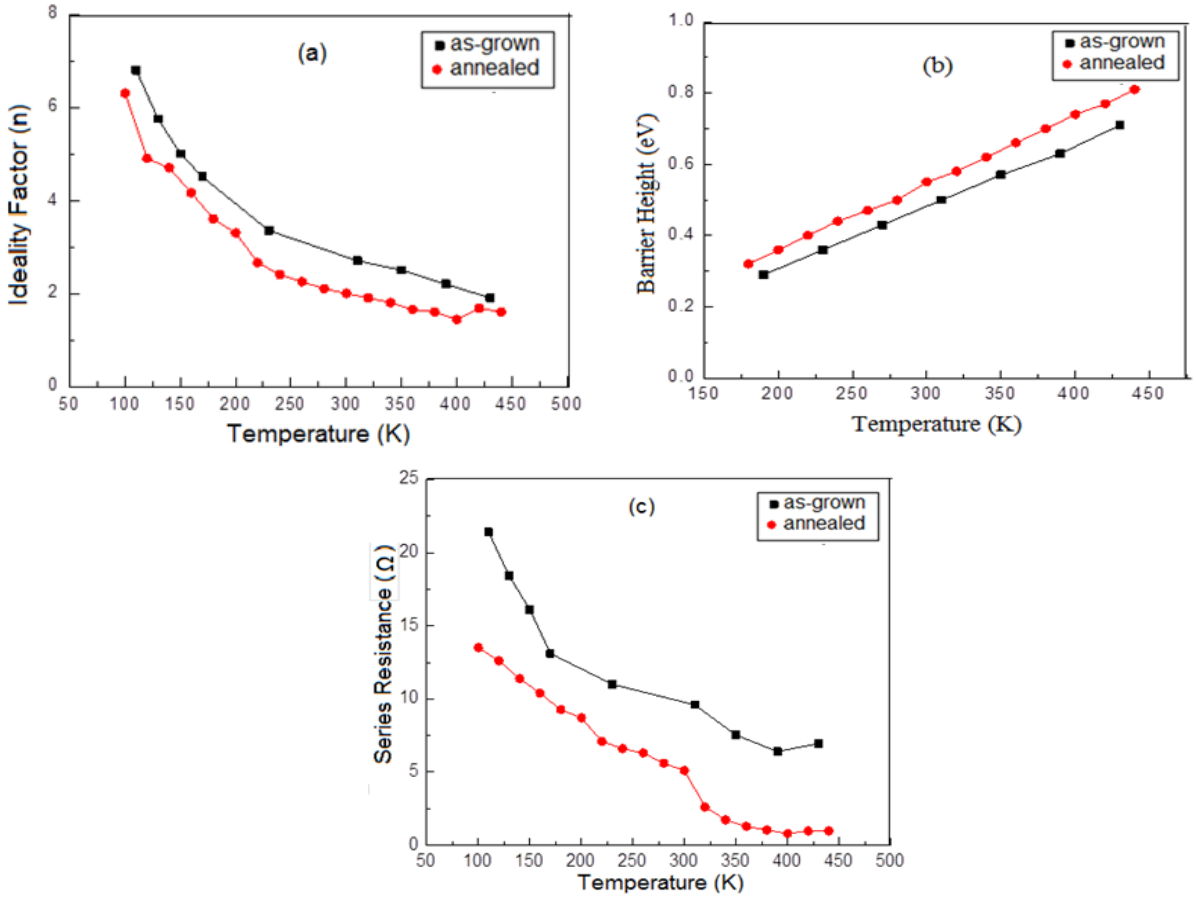


Fig. 7.3. (a) Ideality factor (n), **(b)** barrier height (ϕ_B) and **(c)** series resistance (R_s) were calculated from forward I-V curves for as- grown and annealed samples.

Fig. 7.4 shows that the ideality factor is temperature dependent. The calculated values of n_o and T_o for as-grown and annealed samples are 0.5 and 625 K and 0.25 and 366 K, respectively. The higher values of n_o and T_o of the as-grown samples indicate that the annealed samples deviate less from the thermionic emission model than the as-grown samples [31].

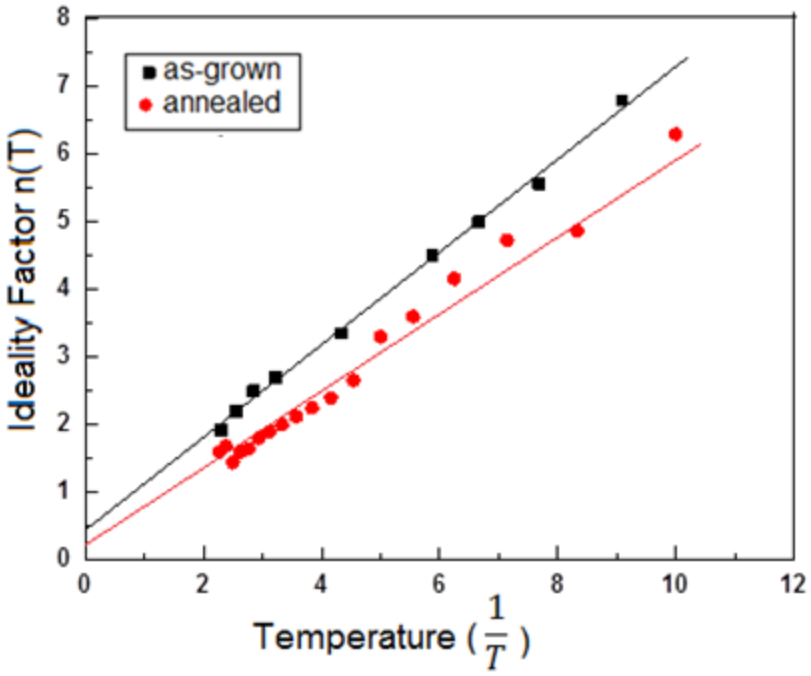


Fig. 7.4. Experimental n(T) versus $\frac{1}{T}$ plot of as- grown and annealed GaAsPN solar cells.

The values of the barrier height (ϕ_b) calculated from the I-V characteristics of our p-i-n GaAsPN based solar cell materials are shown in Fig. 7.3 (b). The barrier height increases with increasing temperature. This temperature dependence of the barrier height is due to the effect of barrier in-homogeneities at the p-i-n interface [32].

Fig. 7.5 illustrates a linear relation between the barrier height ϕ_b and ideality factor. As can be seen from Fig. 7.5, the lower ideality factor the higher the barrier height. This behavior can be explained by in-homogeneities of the barrier height which arise from different factors such as the surface defect density, the deposition process and surface cleaning [33-34].

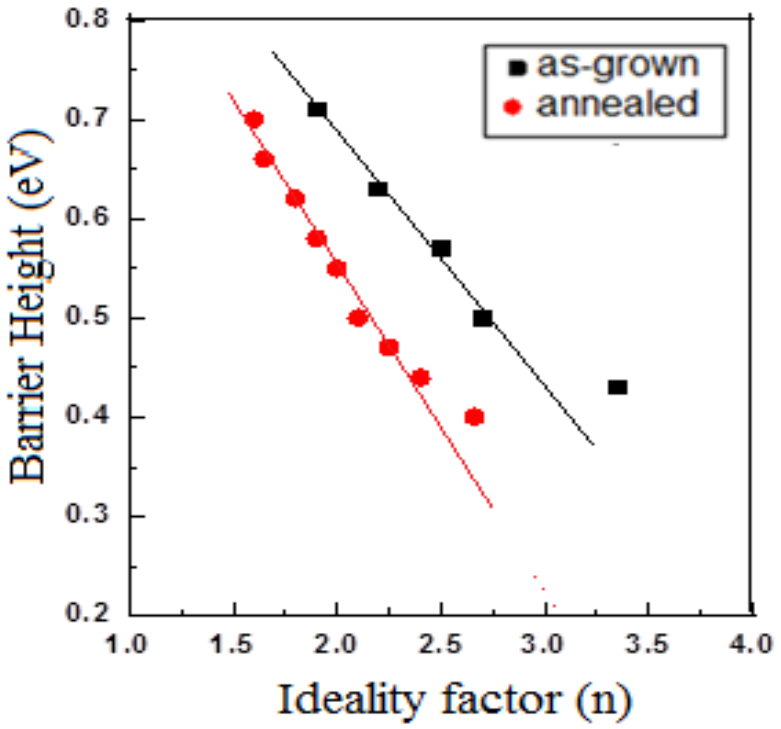


Fig. 7.5. The barrier height (ϕ_b) values versus ideality factor (n) for p-i-n GaAsPN solar cells before and after RTA.

The relation between barrier height ϕ_b and ideality factor n for as-grown samples exhibit high values than the annealed structures. Therefore, it can be concluded that the annealing act as important process for improving the electrical properties, and this can be attributed to several factors such as the lateral inhomogeneity along the barrier height, interfacial GaAsPN layer, grain boundaries and non-uniformly distributed dislocations (interfacial changes) [34,35, 36].

The effect of series resistance on the electrical characteristics of GaAsPN solar cell structure in the temperature range 110 K – 440 K is shown in Fig. 7.3 (c). The series resistance plays an important role in p-i-n solar cell devices. At low forward bias voltage, the semi-logarithmic I-V characteristics are linear and deviate significantly from linearity at high voltages. This behavior is attributed to the effect of series resistance (R_s) which is due to the interface states and the interfacial insulator layer when the applied voltage is large enough [37]. The lower values of (Rs) of the annealed samples as compared with the as-grown

sample at all temperatures indicate that the annealing process lowers the interfaces states density [38].

7.3.2 INVESTIGATION OF THE RTA EFFECT ON THE CAPACITANCE (C) – VOLTAGE (V) CHARACTERISTICS OF P-I-N GaAsPN SOLAR CELLS

Fig. 7.6 (a) presents the Capacitance -Voltage (C-V) characteristics of as-grown and annealed samples which will be used to determine the net acceptor concentration in the p^-GaAsPN layer. The plot of $1/C^2$ *vs* V in Fig. 7.6 (b) is a straight line for both diodes indicating that the doping is uniform throughout the measured region of p^-GaAsPN layer.

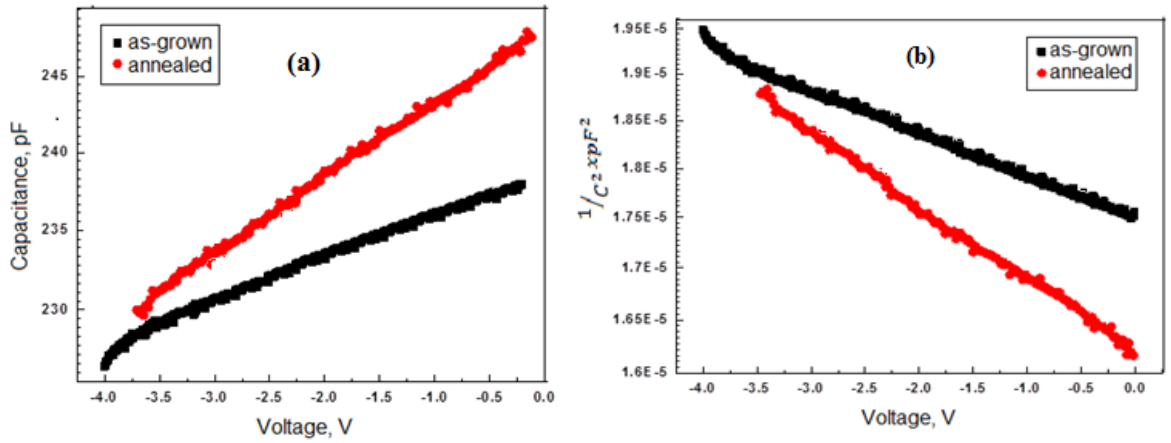


Fig. 7.6. (a) Plot of C-V characteristics and **(b)** $^1/_{C^2}$ *vs* V plots for as-grown and annealed GaAsPN based solar cells at room temperature (RT).

The net acceptor concentration was calculated to be 1.18 x10^{18} cm^{-3} and 2.11x10^{18} cm^{-3} for the as-grown and annealed GaAsPN absorber layers, respectively. The annealed layer exhibits higher value of free carrier concentration as compared with the as-grown layer. This increase in the net acceptor concentration could be attributed to a de-passivation of acceptors during thermal annealing [19].

7.3.3 DLTS AND LAPLACE DLTS CHARACTERISTICS

The DLTS measurements were performed to elaborate further on the role of rapid thermal annealing on the electrically active defects in p-i-n GaAsPN based solar cells. The DLTS spectra in the region close to the interface of the p-i-n junction are obtained by applying a small reverse bias of $V_r = -1\,V$, a rate window of 200 Hz, a filling pulse $V_p = 0\,V$ and filling pulse duration $t_p = 1\,msec$. The depletion width extends from 0.2 µm from equilibrium condition (0 V) to 0.63 µm at reverse bias $V_R = -1\,V$. For clarity Fig. 7.7 displays the peaks detected in the temperature range 150 K-450 K.

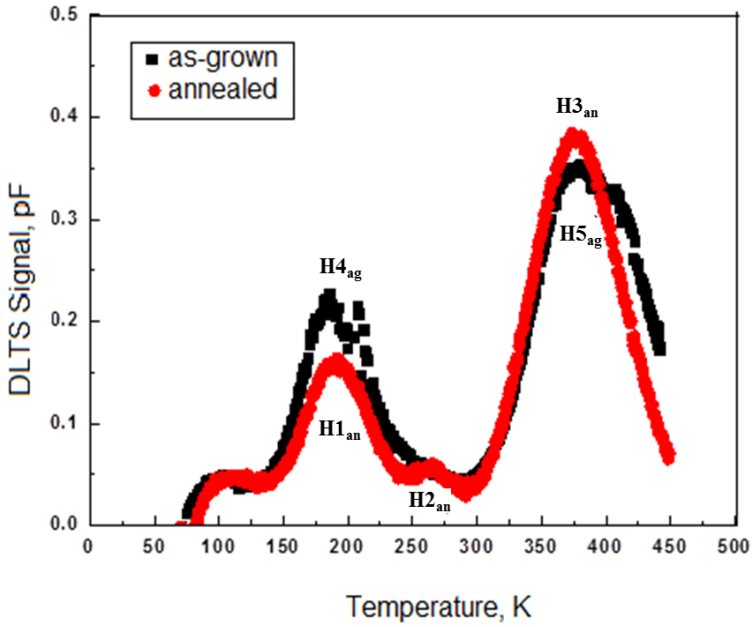


Fig. 7.7. DLTS spectra of GaAsPN based solar cells using a reverse bias of -1V, a rate window of 200Hz, a filling pulse V_p=0V and filling pulse duration is t_p=1msec before and after RTA.

It can be seen from Fig. 7.7 that the annealed and as-grown samples exhibit three and two hole traps labeled as $H1_{an}$, $H2_{an}$ and $H3_{an}$, and $H4_{ag}$ and $H5_{ag}$, respectively. These are related to hole emitting defect states [39]. As also seen in Fig. 7.7, $H4_{ag}$ and $H1_{an}$ traps, which are detected in the temperature range 150 K - 230 K could have the same nature. Similarly, $H5_{ag}$ and $H3_{an}$ detected in the temperature range 320 K- 450 K could originate from the same

defect. The $H2_{an}$ peak detected in the temperature range 250 K- 300 K in the annealed samples is absent in the as-grown samples.

High-resolution Laplace (DLTS) technique was used to analyze the DLTS peaks, which were obtained from DLTS measurements. The emission rates of carriers are given by [40]:

$$e_h = \left[\frac{\sigma_n < V_{th} > N_D}{g}\right] \exp\left\{\frac{\Delta E}{kT}\right\} \qquad (7.2)$$

where $< V_{th} >$ is the carrier average thermal velocity, N_D effective carrier density, k is Boltzmann constant and g is the trap degeneracy.

Arrhenius plot gives the activation energy of the corresponding deep level. Emission rate signatures of each trap are plotted in Fig. 7.8. Assuming that the capture cross section σ_n is temperature-independent, σ_n for each trap has also been calculated from the slope of the respective Arrhenius plots. The values of activation energies, capture cross-section and concentration of traps are given in Table 7.1.

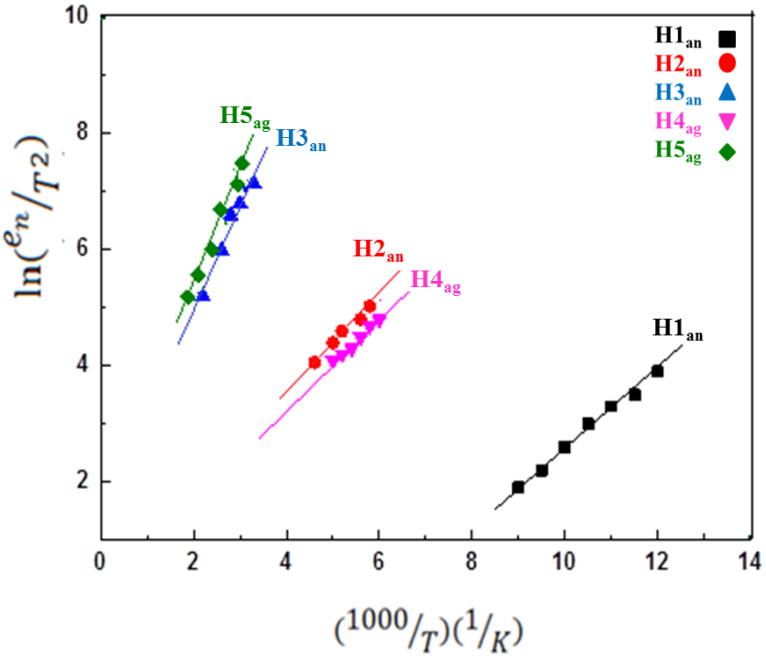


Fig. 7.8. Arrhenius plots of the peak data extracted from DLTS of as-grown and annealed GaAsPN based solar cells.

Shallow and deep traps were observed in the annealed and the as-grown samples in the temperature range 150 K - 450 K. The $H3_{an}$ and $H5_{ag}$ deep traps have activation energies of 0.23eV and 0.25eV, respectively. These values are close to nitrogen related hole trap with activation energy of 0.22 eV that was reported by Abulfotuh *et.al.* in [41]. Both samples exhibit shallow traps, namely $H1_{an}$ (0.06 eV), $H2_{an}$ (0.065 eV) and $H4_{ag}$ (0.07 eV).

Table 7.1. Summary of traps activation energies, capture cross-sections and concentrations for as-grown and annealed PIN GaAsPN based solar cells.

Trap Label	**Activation Energy (eV)**	**Capture Cross-Section (cm^2)**	**Trap concentration (cm^{-3})**
$H1_{an}$	(0.06 ± 0.01)	0.13×10^{-21}	2.4×10^{15}
$H2_{an}$	(0.07 ± 0.03)	0.1×10^{-21}	0.9×10^{15}
$H3_{an}$	(0.23 ± 0.07)	0.4×10^{-21}	3.5×10^{15}
$H4_{ag}$	(0.07 ± 0.02)	0.18×10^{-21}	2.7×10^{15}
$H5_{ag}$	(0.25 ± 0.05)	0.46×10^{-21}	7.2×10^{15}

To the best of our knowledge, no deep level studies have been reported on MBE grown GaAsPN/GaP. Therefore, our results can only be compared with those obtained for MBE grown GaPN/GaP structures without As. It is worth pointing out that our layers contain a very low As composition. In a previous study, Rumyantsev *et al*. [42] found two types of deep levels in lattice mismatched GaPN/GaP heterostructures with activation energies and capture cross-sections of (0.17eV, 0.08eV) and (5.5×10^{-15} , $4.8 \times 10^{-18} cm^2$). Incorporation of As atoms into group V- sub-lattice compensates for elastic stresses emerging during epitaxial growth of the nitrogen containing layer. Generally, the annealed sample exhibits traps with activation energies lower than those in the as-grown layers. It is important to point out that

the capture cross-section and the trap concentrations decrease when the samples are annealed. In general, the concentration of traps increases with nitrogen content or any impurity associated with it due to more defects created that behave as deep level centers [43]. It was also demonstrated that the concentration of defects decreases with annealing temperature due to the decrease of these traps in GaAsPN quaternary alloys [44-45].

7.4 SUMMERY

In summary, I-V, C-V, DLTS and Laplace DLTS were used to investigate the effect of rapid thermal annealing process on p-i-n GaAsPN based solar cells grown by solid source MBE. Deep and shallow traps were detected in the annealed and as-grown samples. However, an additional trap was generated after annealing. The improvement of the electrical properties of p-i-n GaAsPN based solar cells with annealing process can be attributed to the decrease of the concentration and /or capture cross-section values of major defects measured by DLTS and Laplace DLTS.

Using thermionic theory, the calculated I-V barrier height and ideality factor values showed that the ideality factor increases and the barrier height decreases with decreasing temperature. The observed correlation between barrier height and ideality factor values of the devices was explained by the lateral inhomogeneity of barrier height in these structures.

Additionally, the annealed samples showed an ideality factor lower than the as-grown solar cells and the barrier height increased after annealing process due to the effect of barrier in-homogeneities at the p-i-n interface. Using C-V characteristics, the net acceptor trap concentrations and turn on voltage were increased after rapid thermal annealing.

One can therefore conclude that rapid thermal annealing is an efficient treatment process to improve the electrical properties of solar cells based devices.

REFERENCES

[1] I. Buyanova, W. Chen, and B. Monemar, MRS Internet J. Nitride Semicond. Res. **6**, pp. 2 (2001).

[2] J. Geisz, J. Olson, D. Friedman, K. Jones, R. Reedy, and M. Romero, conference. Rec 31st IEEE photovoltaic, pp. 965, (2005).

[3] J. Geisz, J. Olson, W. McMahon, T. Hannappel, K. Jones, H. Moutinho, and M. Al-Jassim, Progress in Compound Semiconductor Materials III – Electronic and Optoelectronic Applications, pp. 27, (2003).

[4] A. Baranov, A. Gudovskikh, E. Nikitina, and A. Egorov, Tech. Phys. Lett. **39**, pp. 1117, (2013).

[5] O. Durand, S. Almosni, C. Robert, T. Nguyen, Y. Wang, C. Cornet, A. Létoublon, C. Levallois, L. Pedesseau, J. Even, J. Jancu, N. Bertru, A. LeCorre, A. Bondi, P. Râle, L. Lombez, J. Guillemoles, E. Tea, S. Laribi, J. Stodolna, A. Ponchet, and N. Boudet, Energy Harvest. Syst. **1**, pp. 147, (2014).

[6] J. Geisz, and D. Friedman, Semicond. Sci. Technol. **17**, pp. 769, (2002).

[7] K. Yamane, M. Goto, K. Takahashi, K. Sato, H. Sekiguchi, H. Okada and A. Wakahara, J. Appl. Phys. Exp. **10**, 075504, (2017).

[8] S. Sukrittanon, R. Lio, Y. Ro, J. Pan, K. Jungjohan, C. Ta and S. Dayeh, J. Appl. Phys. Lett. **107**, 153901 (2015).

[9] S. Kurtz, P. Faine, and J. Olson, J. Appl. Phys. Lett. **68**, 1890, (1990).

[10] I. Ho, and G. Stringfellow, Journal of Crystal Growth **178**, 1 (1997).

[11] B. Kunert, D. Trusheim, V. Volfeburger, A. Volz, and W. Stolz, Physica Status Solidi (A) **205** (1), pp. 114, (2008).

[12] K. Volz, D. Lckner, I. Nemeth, B. Kunert, W. Slolz, C. Baur, F. Dimroth, and A. Bett, **310**, pp. 2222, (2008).

[13] A. Aho, A. Tukiainen, V. Polojarvi, J. Salmi, and M. Guina, Journal of Crystal Growth **332,** pp. 862011, (2013).

[14] K. Volz, D. Lackner, I. Nemeth, B. Kunert, W. Stolz, and C. Baur, Journal of crystal growth **311**, pp. 2224, (2008).

[15] T. Quinci, J. Kuyyald, T. Thanh, Y. Wang, S. Almosni, and A. Etoublon, Journal of Crystal Growth **380**, 157-162, (2013).

[16] L. Baojun, L. Enke, and Z. Fujia, Solid State Electron. **41,** pp. 917, (1997).

[17] Z. Rebaoui, W. Bouiajra, M. Abid, A. Saidane, D. Jammel, M. Henini, and J. Felix, Microelectronic Engineering **171**, pp. 11, (2017).

[18] V. Polojarvi, A. Gubanov, A. Schramm, R. Koskinen, J. Paajaste, J. Salmi, S. Suomalainens, and M. Guina, Material Science and Engineering B **177** (13), pp. 1103, (2012)**.**

[19] S. Xie, S. Yoon, and S. Wang, J. App. Phys. Lett. **97**, (2005).

[20] M. Aziz, A. Mesli, J. Felix, N. AlSagri , D. Taylor, and M. Henini, Journal of Crystal Growth **424**, 5, (2015).

[21] H. Altuntas, and S. Ozcelik, Journal of Alloys and Compounds **577**, 143, (2013).

[22] O. Demircioglu, S. Karatas, N. Yıldırım, and O. Bakkaloglu, Microelectronic Engineering **88**, 2997, (2011).

[23] I. Orak, K. Ejderha, and A. Turut, Current Applied Physics **15**, 1054, (2015).

[24] S. Dogan, S. Duman, B. Curbulak, S. Tuzemen, and H. Morkoc. Physics E **41**, 646, (2005).

[25] B. Akkal, Z. Benamara, H. Abi, A. Talbi, and B. Gruzza, Mater. Chem. Phys. **85**, 27 (2004).

[26] S. Chand, and J. Kumar, J. App. Phy. A. Mater. Sci. Process **65**, 497, (1997).

[27] S. Zhu, R. Van, C. Detavernier, G. Ru, B. Le, and F. Cardon, Solid State Communication **112,** 611, (1999).

[28] J. Shan, Y. Li, Th. Gessman, and E. Schubert, J. Appl. Phys. Lett. **94** (4), pp. 2627, (2003).

[29] R. Tung, Materal Science Engeneering (R) **35**, pp. 1, (2001).

[30] V. Rajagopal, and N. Nanda, Superlattices and Microstructures **52**, pp. 484, (2012).

[31] M. Hudait, P. Venkateswarlu, and S. Krupanidhi, Solid State Electronic **45**, pp. 133, (2001).

[32] A. Chitnis, A. Kumar, M. Shatalov, V. Adivarahan, A. Lunev, J. Yang, G. Simin, M. Khan and M. Shur, J. Appl. Phys. Lett. **77** (23), pp. 3800, (2000).

[33] N. Yildirim, K. Ejderha, and A. Turut, J. Appl. Phys. Lett. **108,** 114506, (2010).

[34] J. Sulliva, R. Tung, M. Pinto, and W. Graham, J. Appl. Phys. Lett. **70** (12), pp. 7403, (1991).

[35] S. Altindal, H. Kanbur, A. Tataroglu, and M. Bulbul, Phys. B. Condense Matter **399,** pp. 146, (2007).

[36] G. Guler, O. Gullu, O. Bakkaloglu, and A. Turut, Physics B. Condense Matter **404**, pp. 2211, (2008).

[37] S. Karatas, and S. Altindal, Material Science and Engineering B **122** (2), pp. 133, (2005).

[38] A. Turut, M. Saglam, H. Efeoglu, N. Yalcin, M. Yildirim, and B. Abay, Physica B: Condense Matter **205**, pp. 41, (1995).

[39] R. Kaplar, A. Arehart, S. Ringel, A. Allerman, R. Sieg, and S. Kurt, J. Appl. Phys. Lett. **90**, pp. 3405 (2001).

[40] R. Mari, M. Shafi, M. Azizi, A. Khatab, D. Taylor, and M. Henini, Nanoscale Research Letters **6**, pp. 180, (2011).

[41] F. Abulfotuh, A. Balcioglu, D. Friedman, J. Geisz, and S. Kurtz, AIP Conference Proceeding **462**, pp. 492, (1999).

[42] O. I. Rumyantsev, P. N. Brunkov, E. V. PIrogov and A. Y. Egorov, Low Dimensional System **44** (7), pp. 923, (2010).

[43] C. Fischer, and P. Bhattacharya, J. Appl. Phys. Lett. **96,** pp. 4176, (2004).

[44] M. Aziz, F. Felix, D. Jameel, N. AlSaqri, F. AlMashry, H. AlGhamdi, H, Albalawi, D. Taylor, and M. Henini, Superlattices and Microstructures **8**, pp. 80, (2015).

[45] A. Tukiainen, J. Dekker, N. Xiang, and M. Pessa, Physics Scripta **114**, pp. 9, (2004).

CHAPTER 8: CONCLUSION AND FUTURE WORK

This chapter summarises the research work carried out on the effect of rapid thermal annealing (RTA) on a variety of advanced semiconductor systems and devices based on (100) GaP substrate, namely, $GaP_{1-x}N_x$ alloys with different N concentrations, $GaAs_{0.1}P_{0.89}N_{0.01}$ and $In_{0.07}Ga_{0.93}P_{0.99}N_{0.01}$ alloys. PL characterization technique was performed to investigate the optical properties of these heterostructures. It also includes the research study that was done on the effect of RTA on the electrical properties of GaAsPN p-i-n based solar cells material by using I-V, C-V, DLTS, and Laplace DLTS characterization techniques. Moreover, this chapter covers future work suggestions.

8.1 CONCLUSION

Gallium phosphide (GaP) has a good latticematted to silicon which makes it a very important material in solar cells world. Furthermore, Gallium arsnied (GaAs) has a direct bandgap which leads to huge usage of this material in semiconductore market. This thesis reports the optical properties of as-grown dilute nitride semiconductors, namely GaPN, GaAsPN and InGaPN grown by Molecular Beam Epitaxy (MBE) on (100) GaP substrates. The effects of rapid thermal annealing (RTA) on their optical properties have also been investigated. In addition, the electrical properties of as-grown p-i-n GaAsPN-based solar cells have been studied. The electrically active defects (known as traps and deep-levels defects) present in the as-grown photovoltaic devices were probed. The effects of post-thermal annealing on the deep-level defects are reported. The properties of these traps are of paramount importance for both the performance and reliability of these semiconductor devices. The principal objective behind the assessment of deep levels is to provide feedback information to improve the quality of the materials and understand the effect of deep states on the performance of devices.

Specifically, the work reported in this thesis deals with (i) the photoluminescence (PL) properties of ternary dilute GaPN epitaxial layers containing different nitrogen concentrations, quaternary GaAsPN and InGaPN heterostructure alloys and quaternary GaAsPN alloys with different epitaxial layer thicknesses, and (ii) the electrical properties of p-i-n GaAsPN-based solar cells grown by MBE using current-voltage (I-V), capacitance-voltage (C-V), deep level transient spectroscopy (DLTS), and Laplace DLTS measurements. The results of this work show that incorporation of nitrogen (N) into GaP ($GaP_{1-x}N_x$) with content x ranging from 1.4% to 2.7%, leads to high bandgap bowing and changes the nature of the GaP bandgap from indirect to pseudo-direct for all compositions x. With increasing N composition from 1.4% to 2.1% and 2.7%, the PL intensity degraded, and the PL peak energy shifted to lower values. Additionally, it was found that incorporation of 10% arsenic (GaAsPN) and 7% indium (InGaPN) into $GaP_{0.99}N_{0.01}$ affected the optical properties of these quaternary considerably in terms of PL intensity and energy bandgap. For example, the energy bandgap of $GaP_{0.99}N_{0.01}$ decreased from 1.97 eV to 1.8 eV and 1.83 eV in $GaAs_{0.1}P_{0.89}N_{0.01}$ and $In_{0.07}Ga_{0.93}P_{0.99}N_{0.01}$, respectively. An important key for obtaining an efficient solar cell is to minimize the heat losses due to the thermalization by choosing semiconductors with appropriate band gaps. Thus, for solar cells, the most effective materials for solar energy conversion have bandgap energies in the range of 1.0 to 1.8 eV. This is an important result for potential commercial two-junction solar cells made from Si (1.12 eV) substrates and $GaAs_{0.1}P_{0.89}N_{0.01}$ (1.8 eV) not only because their energies cover the efficient solar spectrum but also they are lattice matched. Lattice matching ensures perfect defect-free heteroepitaxy, as it avoids dislocations formations, which are known to be centers for non-radiative recombinations in III-V semiconductors. Lattice mismatching reduces the overall lifetime and efficiency of solar cells. Moreover, the PL intensities increased in both $GaAs_{0.1}P_{0.89}N_{0.01}$ and $In_{0.07}Ga_{0.93}P_{0.99}N_{0.01}$ alloys as compared to $GaP_{0.99}N_{0.01}$. In addition, all above materials have been annealed at 800°C for 5 minutes and it was observed that RTA

significantly improved the optical properties of all as-grown bulk dilute nitrides structures by (i) increasing the PL intensities of all samples; (ii) reducing the Full Width and Half maximum (FWHM) of the PL spectra. However, the PL energy peaks are blue-shifted (higher energy) in all samples after RTA. Epitaxial GaAsPN layers with small (100 nm) and large (1000 nm) thicknesses were also grown and investigated using PL. It was found that the thickness of the epilayer has profound effects on the PL spectra: as the epilayer thickness increased, the PL intensity increased and the PL peak energy blue-shifted, which is an undesirable effect for solar cell applications.

Current-Voltage (I-V), Capacitance-Voltage (C-V), Deep Level Transient Spectroscopy (DLTS) and LDLTS techniques have been used to investigate the effect of RTA process on the electrical properties of p-i-n GaAsPN-based solar cell devices grown on (001) GaP substrates. RTA treatment was found to improve their electrical characteristics. The annealed samples showed ideality factors lower than the as-grown samples for all temperatures. On the other hand, the barrier height increases, and the ideality factor decreases with increasing temperature for both as-grown and annealed samples. DLTS and Laplace-DLTS measurements detected three hole traps in the annealed samples as compared with two hole traps in the as-grown samples. After the RTA process, the concentration of the traps is reduced, however, an extra shallow trap is created. In addition, the annealed samples have the lowest leakage currents.

8.2 FUTURE WORK SUGGESTIONS

Proposals for future investigations according to the experimental results achieved in this thesis work are suggested in the following:

(i) In order to further improve the optical and bandgap properties of GaPN alloys, it would be more promising to investigate the effect of adding different ions such as antimony Sb or bismuth Bi to GaPN alloys, as the use of antimony has been prov-

en to improve the optical properties in dilute nitride material such as GaInAsNSb. Thus, this could also help to increase the optical efficiency of GaPN alloys.

(ii) For a further understanding of the effect of various thicknesses on GaAsPN alloys, it would be interesting to fabricate GaAsPN with different epilayer thickness (higher than 100 nm and less than 1 μm), therefore, this could help obtain 1.8 eV bandgap materials for solar cells based on Si with 1.1 eV.

(iii) In the case of annealed GaAsPN and InGaPN samples, it will be worth to carry out a systematic study to investigate the effect of different annealing temperatures. This could lead to a further reduction of the concentration of defects and/or annihilate completely defects. Therefore the optical and structural properties of the materials and devices will be improved.

(iv) For p-i-n GaAsPN solar cell structures, it is worth performing further studies on the effect of gamma (γ) irradiations. This type of irradiation indicated a great help to decrease the trap concentrations in III-V-N dilute nitrides. Therefore, this could increase the conversion efficiency solar cells.